



**HAL**  
open science

# Multifunctional magnetic and fluorescent nanoparticles for beta-amyloid targeting in neurodegenerative disease diagnosis

Francis Mpambani

► **To cite this version:**

Francis Mpambani. Multifunctional magnetic and fluorescent nanoparticles for beta-amyloid targeting in neurodegenerative disease diagnosis. Analytical chemistry. Université Claude Bernard - Lyon I, 2013. English. NNT : 2013LYO10080 . tel-01169688

**HAL Id: tel-01169688**

**<https://theses.hal.science/tel-01169688>**

Submitted on 30 Jun 2015

**HAL** is a multi-disciplinary open access archive for the deposit and dissemination of scientific research documents, whether they are published or not. The documents may come from teaching and research institutions in France or abroad, or from public or private research centers.

L'archive ouverte pluridisciplinaire **HAL**, est destinée au dépôt et à la diffusion de documents scientifiques de niveau recherche, publiés ou non, émanant des établissements d'enseignement et de recherche français ou étrangers, des laboratoires publics ou privés.

N° d'ordre : 80-2013

Année 2013

**THESE DE L'UNIVERSITE DE LYON**

Délivrée par

L'UNIVERSITE CLAUDE BERNARD LYON 1

ECOLE DOCTORALE DE CHIMIE DE LYON

SPECIALITE : CHIMIE

Laboratoire de Chimie de l'Ecole Normale Supérieure de Lyon

Pour l'obtention du

DIPLOME DE DOCTORAT

(Arrêté du 7 août 2006)

Présentée et soutenue publiquement le 28 mai 2013

Par **Francis MPAMBANI**

**Multifunctional magnetic and fluorescent nanoparticles for  
 $\beta$ -amyloid targeting in neurodegenerative disease diagnosis**

Directeur de thèse : Pr. Stéphane Parola

Co-directeur de thèse : Dr. Frédéric Chaput

JURY: Pr. Vadim Kessler, Université d'Uppsala, Rapporteur  
Dr. Thierry Gacoin, Ecole Polytechnique, Rapporteur  
Dr. Boudewijn Van der Sanden, Université Joseph Fourier, Examineur  
Dr. Chantal Andraud, ENS de Lyon, Examineur  
Pr. Marc Lecouvey, Université Paris 13, Président du jury  
Pr. Stéphane Parola, Université Lyon 1, Directeur de thèse  
Dr. Frédéric Chaput, Université Lyon 1, Co-directeur de thèse



N° d'ordre : XXXX

Année 2013

**THESE DE L'UNIVERSITE DE LYON**

Délivrée par

L'UNIVERSITE CLAUDE BERNARD LYON 1

ECOLE DOCTORALE DE CHIMIE DE LYON

SPECIALITE : CHIMIE

Laboratoire de Chimie de l'Ecole Normale Supérieure de Lyon

Pour l'obtention du

DIPLOME DE DOCTORAT

(Arrêté du 7 août 2006)

Présentée et soutenue publiquement le 28 mai 2013

Par **Francis MPAMBANI**

**Multifunctional magnetic and fluorescent nanoparticles for  
 $\beta$ -amyloid targeting in neurodegenerative disease diagnosis**

Directeur de thèse : Pr. Stéphane Parola

Co-directeur de thèse : Dr. Frédéric Chaput

JURY: Pr. Vadim Kessler, Université d'Uppsala, Rapporteur  
Dr. Thierry Gacoin, Ecole Polytechnique, Rapporteur  
Dr. Boudewijn Van der Sanden, Université Joseph Fourier, Examineur  
Dr. Chantal Andraud, ENS de Lyon, Examineur  
Pr. Marc Lecouvey, Université Paris 13, Président du jury  
Pr. Stéphane Parola, Université Lyon 1, Directeur de thèse  
Dr. Frédéric Chaput, Université Lyon 1, Co-directeur de thèse



# DEDICATION

À Papa Tshiama,  
Maman Lengo,  
Dasi et Micha,  
Claire,  
Toute ma famille et mes proches

*L'esprit est un produit de l'organisation du cerveau tout comme la vie  
est un produit de l'organisation des molécules. François Jacob*



## ACKNOWLEDGEMENTS

First all, I would like to thank my supervisor, Prof. Stéphane Parola, for introducing me to the research world, in particular to the field of nanotechnology. Thank you for guiding me during these years with enlightening ideas and kindness, thank you to trust to me.

I also want to thank my co-supervisor Dr. Frédéric Chaput, and Dr. Frédéric Lerouge, for all your help, your support, expertise and valuable ideas.

I thank Chantal Andraud; Director of laboratory for welcoming me into the laboratory. Thank you for the opportunity to be a member of the Functional Materials Division.

Special thanks to my collaborators from the laboratory, Dr. Cyrille Monnereau and Dr. Vinu Appukkuttan for material supply. I thank Dr. Julien Navarro for transmission electronic microscopy and Sandrine Denis-Quanquin for your help in nuclear magnetic resonance spectroscopy.

I would like to thank my collaborators from the consortium, Andeas Åslund from Linkoping University (Sweden) for chromophors supply. I thank also Marius Widerøe, Else Marie Huuse, Mikael Lindgren and Nina Reitan from NTNU (Norway) for relaxivity measurements, fluorescence characterization and imaging. Thanks to Bettina Braun and Susann Handrick, from Tuebingen University and Charité University (Germany) for beta-amyloid staining tests.

Thanks to Pr. Marc Lecouvey from Université Paris 13. Thank you for providing the bisphosphonate terminated polyethylene glycol supply.

I also want to thank my colleagues and friends at the laboratory. I have had a lot of fun times! Many thanks also to my family for your patience and for always being there for me.



## SUMMARY

Alzheimer's disease is the most common neurodegenerative disorder, affecting around 35 million people worldwide. One of the characteristic pathological hallmarks of AD is amyloid plaques; consist of  $\beta$ -amyloid ( $A\beta$ ) peptide aggregates. Today's diagnosis depends essentially on neuropsychological tests and in highlighting change in brain structure such as cortical atrophy. A major issue is that symptoms appear only at a developed stage of the disease. Then *in vivo* detection of  $A\beta$  deposits at an early stage could lead to earlier and more conclusive diagnosis of AD and help monitoring the effect of therapeutic interventions.

In this work, we develop an innovative and early diagnosis method, able to target and detect  $A\beta$  aggregates both by magnetic resonance and fluorescence imaging. Thus we develop a new kind of smart contrast agent for multimodal imaging, based on magnetic nanoparticles on which are grafted luminescent conjugated polythiophenes (LCPs). LCPs on the surface of the magnetic nanoparticles bound to  $A\beta$  aggregates selectively and specifically. Upon binding to  $A\beta$  aggregates the conformational freedom of the backbone is restricted, leading to specific conformation-dependent emission spectra from the LCPs, opening the way for magnetic resonance and fluorescence imaging of the  $A\beta$  plaques.

We synthesized three kinds of magnetic nanoparticles,  $GdF_3@PEG$ ,  $GdPO_4@PEG$  and  $TiO_2@DOTA-Gd(III)$ . The obtained particles show a strong stability in physiological condition and excellent magnetic properties leading to a good ability to create contrast as MRI contrast agents.  $GdF_3$  particles were successfully conjugated with LCPs and both fluorescence and magnetic properties of respectively LCPs and particles are conserved after conjugation. These LCPs labeled particles were tested *in vitro* and *in vivo*. Their ability to bind to  $A\beta$  fibers was revealed *in vitro* by transmission electronic and fluorescence microscopies. *In vivo* staining of  $A\beta$  plaques were shown by one and two-photon fluorescence microscopy. However,  $A\beta$  MRI after *in vivo* probes injection is not yet optimal because of the poor contrast due probably to the low concentration of the probes bound to  $A\beta$  plaques.

**KEYWORDS:** magnetic nanoparticles, surface functionalization, contrast agents, MRI, fluorescence imaging, multimodal imaging, Luminescent Conjugated Polythiophenes, Alzheimer's disease, amyloid plaques,  $\beta$ -amyloid targeting, Blood-Brain Barrier crossing

## RESUME

Avec 35 millions de personnes atteintes dans le monde, la maladie d'Alzheimer (MA) est la maladie neurodégénérative la plus répandue. L'une des caractéristiques pathologiques de cette maladie est l'apparition de plaques amyloïdes, composées d'agrégats de peptide  $\beta$ -amyloïde ( $A\beta$ ). Aujourd'hui, le diagnostic repose essentiellement sur des tests neuropsychologiques et sur la mise en évidence de changements dans la structure du cerveau tels que l'atrophie corticale (diminution du volume du cerveau). Cependant les symptômes de cette maladie n'apparaissent qu'à un stade très développé. Ainsi la détection *in vivo* des dépôts d' $A\beta$  avant le développement de la maladie pourrait conduire à un diagnostic plus précoce et plus probant. Elle pourrait également faciliter le suivi et l'évaluation des effets des interventions thérapeutiques au cours du traitement.

Dans ce travail, nous avons développé une méthode de diagnostic précoce innovante, capable de cibler et de détecter les plaques  $A\beta$  à la fois par l'imagerie par résonance magnétique et par l'imagerie de fluorescence. Nous avons développé un nouveau type d'agents de contraste intelligents pour l'imagerie multimodale, basé sur des nanoparticules magnétiques sur lesquelles sont greffés les polythiophènes luminescents (LCPs). Les LCPs à la surface des nanoparticules magnétiques se lient aux plaques  $A\beta$  de manière sélective et spécifique. Lors de cette liaison, la liberté conformationnelle des polythiophènes se trouve limitée, ce qui conduit à des spectres d'émission spécifiques dépendant de la conformation, et rend pertinent l'usage de l'imagerie par résonance magnétique et de fluorescence des plaques  $A\beta$ .

Nous avons synthétisé trois types de nanoparticules magnétiques,  $GdF_3@PEG$ ,  $GdPO_4@PEG$  et  $TiO_2@DOTA-Gd(III)$ . Les particules obtenues présentent une forte stabilité dans des conditions physiologiques et d'excellentes propriétés magnétiques. Ces caractéristiques leur assurent une bonne capacité à créer du contraste comme agents de contraste IRM. Les particules de  $GdF_3$  ont été conjuguées avec les LCPs avec succès : les propriétés de fluorescence et magnétiques des LCPs et des particules sont conservées après conjugaison. Les particules obtenues ont été testées *in vitro* et *in vivo*. Leur capacité à se lier aux fibres  $A\beta$  a été révélée *in vitro* par microscopie électronique à transmission et de fluorescence. Le marquage spécifique et l'imagerie de plaques  $A\beta$  *in vivo* ont été réalisés par microscopie de fluorescence à un et à deux photons. Cependant, l'IRM des plaques  $A\beta$  après injection *in vivo* des particules n'est pas encore optimale à cause du contraste assez faible. Ce dernier est probablement dû à la faible concentration des particules ayant passé la barrière hémato-encéphalique.

# TABLE OF CONTENTS

<b>GENERAL INTRODUCTION .....</b>	<b>1</b>
<b>CHAPTER I BACKGROUND AND PROBLEM DEFINITION .....</b>	<b>7</b>
<b>1 ALZHEIMER'S DISEASE .....</b>	<b>7</b>
1.1 Pathology and Etiology.....	7
1.2 Diagnosis of Alzheimer disease .....	13
<b>2 FLUORESCENCE MICROSCOPY AND MAGNETIC RESONANCE IMAGING.....</b>	<b>25</b>
2.1 Fluorescence microscopy .....	25
2.2 Magnetic resonance imaging .....	32
<b>3 AIMS AND OBJECTIVES .....</b>	<b>40</b>
3.1 Strategy of the study .....	40
3.2 Objective of the study .....	41
<b>CHAPTER II NANOPARTICLES SYNTHESIS AND SURFACE MODIFICATION .....</b>	<b>45</b>
<b>1 SYNTHESIS AND SURFACE MODIFICATION METHODS .....</b>	<b>45</b>
1.1 Top-down approach .....	45
1.2 Bottom-up approach .....	46
1.3 Examples of particles from conventional techniques .....	49
1.4 Colloidal stability and surface modification .....	54
<b>2 DEVELOPMENT OF NEW MAGNETIC CONTRAST AGENTS .....</b>	<b>61</b>
2.1 Isotropic system: spherical gadolinium fluoride nanoparticles ( $GdF_3$ ) .....	62
2.2 Anisotropic system: gadolinium phosphate nanorods ( $Gd_{1-x}La_xPO_4$ and $GdPO_4$ ) .....	64
2.3 Stabilization of the obtained systems by pegylation.....	66
2.4 Core-shell system: gadolinium chelate coated titanium oxide particle .....	68
<b>3 CHARECTERIZATION OF THE DEVELOPED CONTRAST AGENTS .....</b>	<b>72</b>
3.1 Physical measurements and instrumentation.....	72
3.2 Characterization of isotropic nanoparticles .....	74

3.3 Characterization of anisotropic nanoparticles .....	82
3.4 Characterization of the naked TiO <sub>2</sub> for core-shell system .....	90
3.5 Characterizations of the pegylated particles.....	95
3.6 Characterizations of the core-shell system: TiO <sub>2</sub> @DOTA-Gd(III) .....	103
3.7 Grafting density study .....	109
3.8 Colloidal stability study of the developed hybrid particles .....	112
3.9 Conclusion on surface modification .....	113
3.10 Magnetic signal enhancement effects of the developed particles .....	114
<b>4 Conclusion on nanoparticles synthesis and surface modification .....</b>	<b>121</b>
<b>CHAPTER III DEVELOPMENT OF MULTIMODAL CONTRAST AGENTS.....</b>	<b>125</b>
<b>1 MULTIMODAL CONTRAST AGENTS.....</b>	<b>125</b>
1.1 Multimodal contrast agent in diagnosis applications .....	125
1.2 Polythiophene and applications .....	126
<b>2 PREPARATION OF MULTIMODAL CONTRAST AGENTS .....</b>	<b>127</b>
2.1 Production of two luminescent conjugated polythiophene .....	127
2.2 Production of water soluble spacer: polyhydroxyethylacrylate .....	128
2.3 Attachment of the spacers with luminescent conjugated polythiophene.....	129
2.4 Preparation of LCP labeled nanoparticles .....	131
<b>3 CHARACTERIZATIONS OF LCP LABELED NANOPARTICLES .....</b>	<b>133</b>
3.1 Evaluation of the labeling by surface characterizations.....	133
3.2 LCP labeled particles behavior in solution.....	140
3.3 Photo-physic and relaxation properties in solution .....	143
3.4 Conclusion .....	146
<b>CHAPTER IV BIOLOGICAL EVALUATION OF THE PARTICLES.....</b>	<b>149</b>
<b>1 EX VIVO MRI EVALUATION OF PEGYLATED NANOPARTICLES.....</b>	<b>149</b>
1.1 Gadolinium fluoride as negative contrast agent .....	149
1.2 TiO <sub>2</sub> coated DOTA-Gd(III) as negative and positive contrast agent .....	150
<b>2 IN VITRO EVALUATION OF THE LCP LABELED NANOPARTICLES.....</b>	<b>151</b>

2.1 Selectivity of the LCP labeled particles to $\beta$ -amyloid fibrils cells .....	151
2.2 TEM visualization of the binding to $\beta$ -amyloid fibrils.....	152
2.3 <i>In vitro</i> binding of the particles to A $\beta$ in tissue samples .....	153
<b>3 IN VIVO EVALUATION OF THE LCP LABELED NANOPARTICLES.....</b>	<b>155</b>
3.1 Single photon fluorescence imaging of plaques in APP/PS1 mice brain .....	155
3.2 Two photon fluorescence imaging of plaque in APP/PS1 mice brain .....	158
3.3 Relaxation rate change and gadolinium concentration in brain tissues .....	164
3.4 Blood brain barrier crossing discussion.....	168
3.5 Conclusion .....	168
<b>GENERAL CONCLUSION.....</b>	<b>173</b>
<b>FUTURE WORKS .....</b>	<b>174</b>
<b>ANNEX.....</b>	<b>179</b>
<b>BIBLIOGRAPHY .....</b>	<b>197</b>



# GENERAL INTRODUCTION

Today, nanotechnologies represent a major area of technology development. Electronics, optics, environment and medicine are increasingly concerned by the development of "nano-objects". Nanobiotechnologies are promising because of the opportunity offered by multifunctionalization and miniaturization, to interact specifically with biological entities such as tissues, cells and molecules. Progress lie in three areas: (i) the earlier diagnosis of disease leading to a more personalized and more preventive medicine, i.e. taking into account the biological specificities of each organism, (ii) the therapy, including drugs vectorization and (iii) the compensation of deficits such as tissue engineering.

This research project aims to develop new hybrid contrast agents, made of magnetic inorganic particles functionalized with organic chromophores, capable of targeting  $\beta$ -amyloid (A $\beta$ ) proteins, one of the responsables of Alzheimer's disease. The originality of this work is the development of multimodal and smart probes for diagnosis both by fluorescence microscopy and by magnetic resonance imaging (MRI) for combined clinical applications.

This work is part of LUPAS project (*Luminescent Polymers for in vivo imaging of Amyloid Signatures*). A European integrated project, 7FP (seventh framework program), which aims to develop novel smart and multimodal contrast agents (fluorescence and magnetic resonance imaging) and methods for diagnostic of neurodegenerative diseases. The project is based on the unique capacity of LCPs i) to recognize amyloidotic molecules, ii) to possess a spectroscopic signature depending on their conformation, iii) to be functionalizable with magnetic moieties, leading to multimodal agent able to target amyloidotic molecules. The Table 0.1 shows the project participants.

This work aims to generate novel multimodal imaging agents for both fluorescence and magnetic resonance imaging. The approach involves the synthesis of a diversity of functionalized magnetic nanoparticles (MNPs) that can be further coupled to LCPs. Surface of the particles will be modified with water-soluble and biocompatible molecules (stabilizer) to ensure stability of the system in aqueous solution and their biocompatibility in biological media (Figure 0.1). The targeting molecules (LCPs) are attached to the particles via a water-soluble molecule (spacer), with possibility of varying spacer length and stabilizer/spacer-LCP ratio.

Table 0.1. LUPAS consortium

Participant	Country
<b>Linköping University</b> Departemt of chemistry	Sweden
<b>Université Claude Bernard Lyon 1 /ENS de Lyon / CRNS</b> Laboratoire de chimie	France
<b>University of Tübingen</b> Hertie Institute of Clinical Brain Research	Germany
<b>Norwegian University of Science and Technology</b> Dept of Physics and Dept of circulation and medical imaging	Norway
<b>Zürich University Hospital</b> Dept. Neuropathology	Switzerland
<b>Universitätsmedizin Berlin</b> Department of Neuropathology, Charité	Germany
<b>Genovis AB</b>	Sweden
<b>Applied Spectral Imaging</b>	Israel

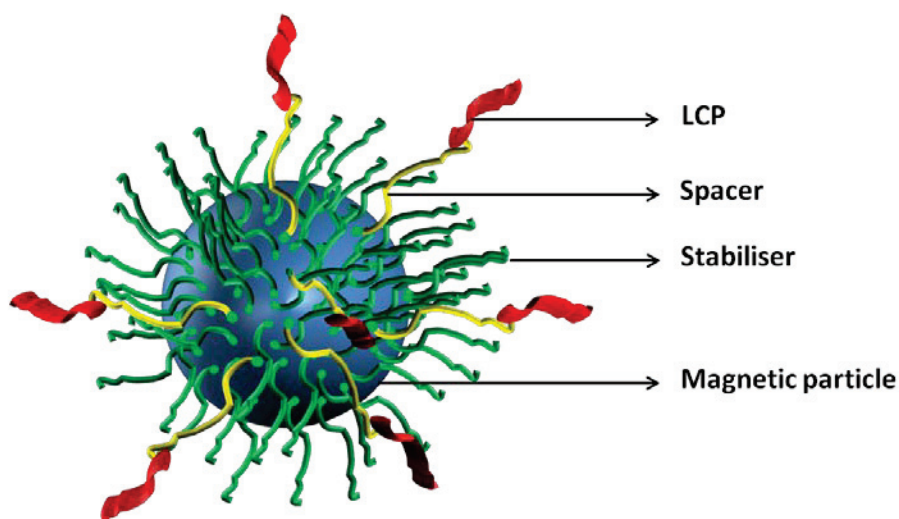


Figure 0.2. Schematic representation of the developed system

This manuscript is divided into four chapters; the first chapter briefly introduces Alzheimer's disease in terms of pathology, epidemiology and degeneration mechanism. The second chapter reports the synthesis of different magnetic nanoparticles, their functionalization with polyethylene glycol

(stabilizer) using bisphosphonates as anchoring groups and their physico-chemical characterizations. The third chapter presents the double functionalization of the particles by both polyethylene glycol and polythiophenes (LCPs) and physico-chemical characterizations, including photo-physic and magnetic properties of the resulting hybrid nanoparticles. The fourth chapter discusses the use of these particles as a contrast agent for fluorescence and magnetic resonance imaging. The particles are studied in biological environment to assess their abilities to create contrast, to specifically targeting A $\beta$  plaques by multimodal imaging.



# CHAPTER I



# **CHAPTER I BACKGROUND AND PROBLEM DEFINITION**

Before 20th century, the elderly dementia was considered as related to the time's wear. Alois Alzheimer presented for the first time in 1906 the clinical cases of one of his patients of 51 years, suffering from a progressive alteration of its capacity of understanding and memory, hallucinations and mental confusion<sup>1</sup>. The post-mortem examination of the patient's brain revealed two cortical lesions: intracellular fibrils tangles (neurofibrillary degeneration) and the accumulation of beta amyloid peptide in amyloid plaques<sup>2</sup>.

Today, this disease is known as Alzheimer's disease (AD) and is described as a progressive neurodegenerative, expressing by memory problems, cognitive decline, often associated with behavioral problems and moving towards a progressive loss of autonomy. This dementia, whose etiology remains poorly understood, is associated with characteristic histological lesions: amyloid plaques (A $\beta$  Pathology) and neurodegenerative tangles (Tau Pathology)<sup>3</sup>. AD is the most common cause of progressive cognitive decline in the aged population. Then great efforts are presently being made to find early diagnostic markers and hopefully a cure.

In this work we focus exclusively on diagnosis problems. Thus, in this first chapter, after describing the disease, we will present the clinically used diagnostic techniques, and those in development, before presenting our strategy for development of a multimodal tool for early diagnosis.

## **1 ALZHEIMER'S DISEASE**

### **1.1 Pathology and Etiology**

#### **1.1.1 Epidemiology**

In the context of ageing of population and the improvement of the general state of health, Alzheimer's disease affects an increasing part of the population. In 2010, the number of patients is estimated to approximately 900,000 in France and 35 million worldwide, with 250 000 and 4.6 million new cases each year in France and around the world. These figures can grow significantly in the increase of the living conditions in developing countries. It may double in 20 years to 66 million in 2030 and 115 million in 2050. Alzheimer's disease is characterized by numerous social and economic consequences. The worldwide cost of dementia was estimated at 421.6 billion US \$<sup>4</sup> in 2009. In France, life expectancy after the onset of symptoms is around 8.5 years; however that terminal

disease can last up to 20 years. The level of dependence is very variable and currently 40% of patients are supported in an institution and 60% in families. The major challenge of the current research is to delay the onset of the disease for at least five years, which would reduce by 50% the socio-economic burden of this disease.

## 1.1.2 Pathology

### 1.1.2.1 Clinical symptoms

Symptoms associated to AD are characterized by cognitive and behavioral problems generally simultaneously with cognitive impairment. The early affected cognitive function in AD is episodic memory<sup>5</sup> (autobiographical memories forgetfulness), working memory (difficulty to plan and execute multiple tasks), and amnesia that isolates the patient from its environment. Procedural memory is altered in the advanced stages of the disease. These memory disorders are associated with language disorders, disorders of executive functions (planning, realization of common gestures) that have a major impact on the autonomy of the subject<sup>6,7</sup>.

**Table I.1. Global Deterioration Scale (DTS, Reisberg scale)**

Stage 1	Normal	<b>Free of objective or subjective symptoms of cognition :</b> all right
Stage 2	Normal aged forgetfulness	<b>Complaint of cognitive and/or functional difficulties:</b> forgets names and locations of objects ...
Stage 3	Mild cognitive impairment (MCI)	<b>Concentration deficits:</b> difficulties to resolve new problems...
Stage 4	Mild Alzheimer's disease	<b>Decreased ability to manage instrumental activities of daily life:</b> decreased ability to manage finances, to prepare meals for guests...
Stage 5	Moderate Alzheimer's disease	<b>Incipient deficits in basic activities of daily life:</b> Need assistance for clothing selection
Stage 6	Moderately severe Alzheimer's disease	<b>Decreased ability to perform basic activities of daily life:</b> require assistance in putting on their clothing properly
Stage 7	Severe Alzheimer's disease	<b>Require continuous assistance for basic activities of daily life:</b> limited vocabulary, inability to sit, walk ...

Behavioral symptoms represent one of the major events of AD. In moderate and advanced stages, emotional disorders are observed. In advanced stages, psychotic disorders such as hallucinations and identification's difficulties make it very difficult to the end of life of the patients.

Dr. Barry Reisberg outlined the seven major clinical stages of Alzheimer's disease, and he developed the "Global Deterioration Scale" (Table I.1), now used in many diagnoses and care settings as the rating scale.

### 1.1.2.2 Brain change during Alzheimer diseases

During progression of AD, brain tissue shrinks and the ventricles enlarge. When the cells in the hippocampus begin to degenerate in early stages of AD, the short-term memory starts to decline. Then, AD spreads through the cerebral cortex (the outer layer of the brain), judgment worsens and language alters. The progression of the disease leads to the death of more neurons and subsequent changes in behavior, such as wandering and agitation. In the final stages, patients may lose the ability to perform basic activities, such as speak or recognize people and control of bodily functions. The memory can become almost non-existent and constant care becomes necessary.

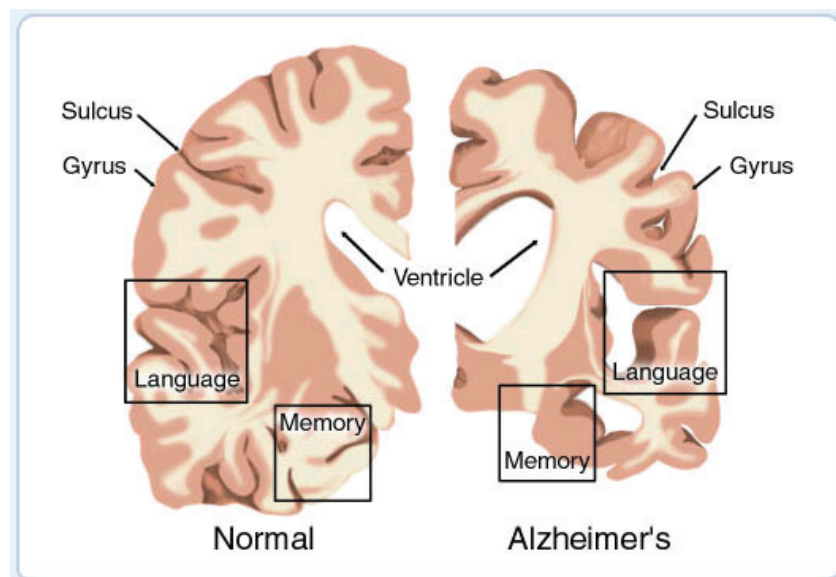


Figure I.1. Cross-section of the brain as seen from the front: normal brain (left) and brain with Alzheimer's disease (right). Image from *American Health Assistance Foundation*

### 1.1.3 Mechanisms of neuronal degeneration in Alzheimer's disease

Despite efforts on the elucidation of the molecular components of the brain lesions, mechanism of neuronal degeneration in AD remains unclear. However, recent advances in molecular genetics have focused attention to several pathogenic mechanisms. Two genes are known to confer

susceptibility to AD: genes for amyloid precursor protein (APP) and apolipoprotein E (ApoE). Multiple molecular pathways can lead to AD. Here, we discuss the potential pathogenic mechanism that emerges.

### 1.1.3.1 From amyloid precursor protein to amyloid plaques

#### (a) Amyloid precursor protein

Amyloid precursor protein (APP) is a transmembrane glycoprotein and the precursor of beta amyloid peptide (A $\beta$ ). A $\beta$  is a 40-42 amino acid peptide that is the principal constituent of senile plaques and cerebrovascular deposits in AD. APP is normally cleaved within the A $\beta$  domain to generate a 90–100kDa secreted form<sup>8</sup>. This secreted form of APP can function as an autocrine factor to stimulate cell proliferation and can promote cell–substratum adhesion<sup>9,10</sup>. An alternative processing pathway in which APP is cleaved at different sites in the extracellular and transmembrane domains generates soluble A $\beta$ , the putative source of amyloid plaque in AD<sup>8</sup>. APP can be processed by  $\alpha$ -,  $\beta$ - and  $\gamma$ -secretases. In the amyloidogenic pathway, APP cleavage by  $\alpha$ -secretases, the non amyloidogenic pathway, does not generate A $\beta$ . A $\beta$  protein is generated by successive action of the  $\beta$  and  $\gamma$ -secretases<sup>11</sup> (Figure I.2).

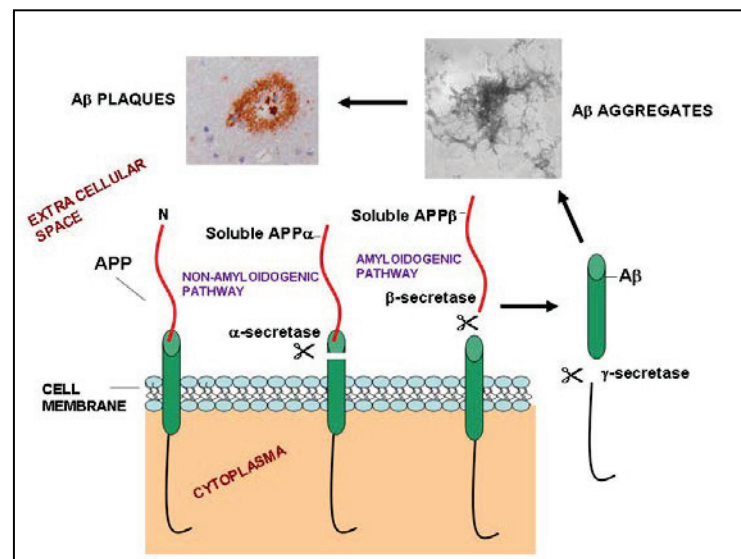


Figure I.2. Generation of A $\beta$  and formation of A $\beta$  aggregates and plaques

#### (b) Beta-amyloid peptide and amyloid plaques

A $\beta$  has several potential activities that are not associated with disease, including activation of Kinase enzymes, protection against oxidative stress<sup>12,13</sup>, regulation of the cholesterol transport<sup>14</sup> and anti-microbial activity, potentially associated with A $\beta$ 's pro-inflammatory activity<sup>15</sup>. It has a number

of isoforms of 36-43 amino acid residues in length; however the most common isoforms are A $\beta$ -40 and A $\beta$ -42. Both are present in the plaques, however the A $\beta$  42 is the major component of plaques in the human brain<sup>16</sup> while the A $\beta$ -40, is less prone to aggregation<sup>17</sup>. Amyloid fibrils are formed by normally soluble proteins A $\beta$  peptide, which assemble to form insoluble fibers that are resistant to degradation. Today research suggests that this A $\beta$  fibrillation is not the unique cause of AD. There are other probable influential factors.

### 1.1.3.2 A $\beta$ peptide, tau protein and Apolipoprotein E in Alzheimer disease

#### (a) Tau protein and Apolipoprotein E (ApoE)

One of the neuropathological hallmarks of AD is the intra-cellular neurofibrillary tangle, made of filaments of hyperphosphorylated tau, a microtubule-associated protein (MAP). During AD, these hyperphosphorylated Tau proteins are aggregated into paired helical filaments (PHFs) which are assembled in neurofibrillary tangles (NFTs), characteristic of degenerating neurons<sup>18</sup>. Research suggests that apolipoprotein E (apoE) may have a protective effect against the phosphorylation of Tau proteins.

ApoE plays an important role in the distribution and metabolism of cholesterol and triglycerides within many organs and cell types in the human body. It is the major carrier of cholesterol in the central nervous system (CNS) and is the strongest known risk factor influencing the incidence of AD.

Observations agree with the implication of tau protein and apolipoprotein E in AD. Here after, are presented some links between A $\beta$  and tau protein that can be found in literature.

#### (b) $\beta$ -Amyloid and tau protein relationship

A $\beta$  peptide and tau protein are characteristics of the AD (Figure I.3), they have been identified several decades ago. However the relationship between A $\beta$  and tau are still poorly defined. Many interactions were observed in various experiments. For example, research shows that A $\beta$  could directly or indirectly interact with the protein tau to accelerate the formation of neurofibrillary<sup>19,20</sup>, thus confirming the amyloid cascade hypothesis. For example, the accumulation of amyloid plaques preceded by a few months the development of tangles in triple mutated mice (APP, tau and PS1)<sup>20</sup>. It seems therefore that A $\beta$ , through various cellular and molecular mechanisms, facilitates phosphorylation, aggregation, and the accumulation of tau protein, resulting on the appearance of neurofibrillary. Several studies suggest that some of the pathological effects of apoE4 may be mediated by interactions with A $\beta$  cascade<sup>21</sup>.

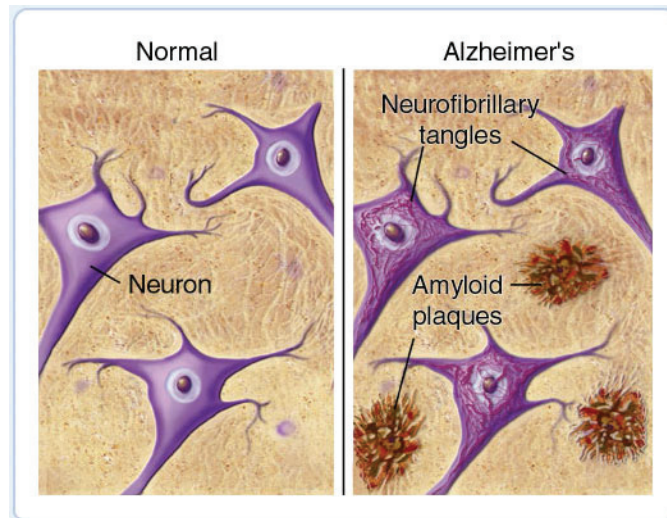


**Figure I.3. Schematic representation of normal (left) and Alzheimer (right) neuron with presence of plaques and neurofibrillary tangles. Image from *American Health Assistance Foundation***

However, until now, it is not clearly elucidated if apoE4, a variant of apoE has an active role in facilitating A $\beta$  aggregation and/or deposition or if, in contrast, apoE3 and E2 (others variants) have a protective role by inhibiting A $\beta$  aggregation or favoring A $\beta$  clearance. The neurotoxicity mechanism associated to A $\beta$  plaques is not definitively determined. Among all the hypotheses, the most advanced is amyloid cascade that we will explain briefly below.

### **1.1.3.3 Amyloid cascade hypothesis**

Amyloid cascade is the hypothesis that A $\beta$  deposition is a primary factor in the pathogenesis of AD. Thus pathologies associated to tau protein and other degenerative problems are secondary<sup>22</sup>. This hypothesis results in observation of amyloid plaques in the brains of AD patients and the finding of genetic mutations on genes for the APP, PS1 or PS2, responsible of familial form of AD. From this hypothesis, the abnormal aggregation of A $\beta$  would result in a series of imbalances and neurotoxic process leading to neuronal death and dementia (Figure I.4).

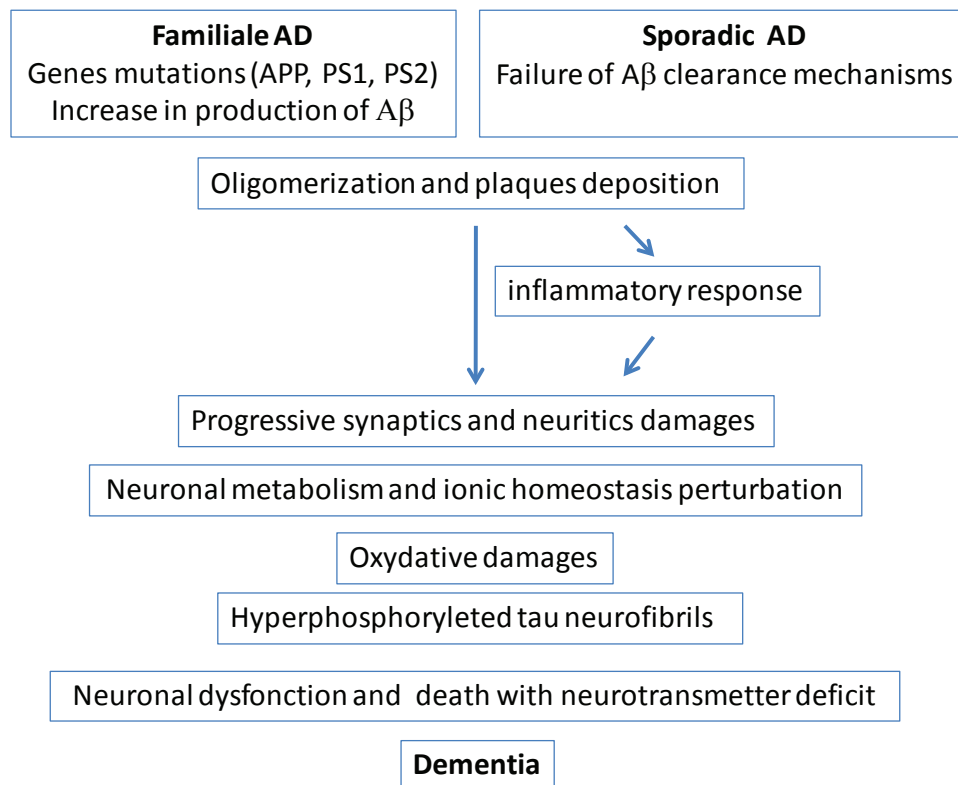


Figure I.4. Schematic representation of amyloid cascade hypothesis

If several hypotheses are today proposed to explain the mechanism of neuronal degeneration in Alzheimer's disease, diagnosis and early diagnosis techniques must be developed in order to improve drug management and therapy.

## 1.2 Diagnosis of Alzheimer disease

Today, the definitive diagnosis of the AD can be established only post-mortem via the autopsy of the patient's brain. Historically, the disease is clinically diagnosed by evidenced dementia and ruling out other specific causes thanks to neuroimaging. Thus, cognitive (neuropsychological) tests are used to evidenced dementia and neuroimaging to exclude other dementia of treatable causes such as tumor and hematoma or evidenced a cortex atrophy mainly associated to the advanced stage of AD. Today, neuroimaging is used as positive support for a clinical diagnosis of AD in symptomatic individuals by identifying characteristic patterns (signatures) of structural and functional cerebral alterations<sup>23</sup>.

Here after, we will present briefly the use of neuropsychological tests, neuroimaging tests in clinical diagnosis and the techniques in development for AD early diagnosis, including those of Aβ targeting.

## **1.2.1 Clinical diagnosis**

### **1.2.1.1 Neuropsychological tests**

In a first step, diagnosis was based on simple cognitive tests such as the scales of Blessed (1968), based on orientation, memory and concentration tests. There are also Pfeiffer tests (1975) and the Mini Mental Status Examination of Folstein (1975). These tests have been designed as indicators of severity of dementia and rapid screening tools; therefore they are not specific of the AD. In 1984, NINCDS-ADRDA, an American specialists work group, (now known as the Alzheimer's Association) offers the first criteria of diagnosis of the disease<sup>24</sup>. They are among the most used in the diagnosis of AD.

These criteria require that the presence of cognitive impairment and a suspected dementia syndrome be confirmed by neuropsychological testing for a clinical diagnosis of possible or probable AD. Histopathologic confirmation (microscopic examination of brain tissue) is need for the definitive diagnosis. Today is emerged a consensus for the development of performance assessment tools grouped around 4 axes:

- Cognitif tests : Mattis Dementia Rating Scale ; Alzheimer Disease Assessment Scale cognitive subscale (ADAS-cog) ; Syndrom Kurztest ...
- Functional assessment (activity of daily living): Instrumental Activities of Daily Living (IADL) ; Physical Self-maintenance Scale ...
- Behavioral assessment : ADAS-non cognitive subscale ; Behavioral pathology in Alzheimer Disease scale ; Neuropsychiatric, Inventory ...
- Global classification of severity scales: Global Deterioration Scale; Clinical Dementia rating Scale...

There is not yet a specific AD's marker able to be efficiently detected by biochemical tests and confirm definitively the AD diagnosis. These cognitive tests are always used and are accompanied by complementary tests including some biomarkers dosage and neuroimaging.

### **1.2.1.2 Biomarkers for biochemical test**

Today, AD cannot be diagnosed by only laboratory tests; however several biochemical markers have been investigated or are in investigation for their diagnostic utility or to distinguish the disease from other dementia types. Three main biochemical markers have been shown to have a good sensitivity and specificity and are used in clinical practice. These markers are considered to reflect the pathological processes of AD, including neuronal degeneration, formation of tangles, and

deposition of the A $\beta$ -42 peptide. There are measurements of the levels of total-tau (T-tau), phosphorylated tau (P-tau) and A $\beta$ -42 in cerebrospinal fluid<sup>25</sup>.

Concentrations of total tau, phosphorylated (tau<sub>181</sub>), and A $\beta$ -42 in cerebrospinal fluid (CSF) are strongly related with future development of Alzheimer's disease in patients with mild cognitive impairment (MCI)<sup>26</sup>. Low levels of A $\beta$ -42 and higher levels of tau are significantly associated with Alzheimer's disease. Moreover, these markers have also been evaluated as predictive markers of patients converting from MCI to Alzheimer's disease with increasing cognitive decline<sup>26,27</sup>. In the proposed revision of the NINCDS-ADRDA criteria, biomarkers analysis has been taken into account. Then presence of low A $\beta$ -42 as well high tau and phosphorylated tau levels in the cerebrospinal fluid have been added as supportive features of Alzheimer's disease.

Also the plaque-associated proteins have been suggested as potent markers of AD, such as serpin<sup>28</sup>. However, low sensitivity and specificity is a problem in establishing these markers.

### **1.2.1.3 Neuroimaging**

In addition to the cognition tests, the NINCDS-ADRDA criteria from 1984<sup>24</sup> and the recently revised version, have been added neuroimaging as supportive diagnostic features<sup>29</sup>. Imaging investigations such as structural neuroimaging with magnetic resonance imaging (MRI) is used to determine medial temporal lobe atrophy and molecular imaging with positron emission tomography (PET), is used to determine functional deficits such as reduced glucose metabolism.

Here after we will focus in the three main neuroimaging techniques used as complementary tests in clinical AD diagnosis.

#### **(a) Computerized tomography**

Computerized Tomography (CT) is based on capacity of different mater to absorb X-ray. Typically, an X-ray beam is sent through an object and is differentially attenuated by the various structures of the object according to their densities. For example, in living organisms, bones impede most of the incident X-rays, while soft tissues and fluids do not. X-rays absorption due to the object crossing is detected from multiple angles around the circumference of the scanner and a two-dimensional (2D) image of each slice of the object can be reconstructed by a computer. The spatial resolution is around 0.25 mm.

Early, the cerebral atrophy observed in CT in AD patients was attributed to the disease processes rather than to physiological aging of the brain<sup>30</sup>. It was the demonstration of its use for AD diagnosis. Today, CT is useful in the diagnosis of Alzheimer's disease because it allows the exclusion of other disorders such as brain tumor, hydrocephalus, and dementia associated with vascular

disease. Also quantitative CT can demonstrate the presence of greater brain atrophy and ventricular dilatation in patients with AD compared with controls<sup>31</sup>. It can delineate brain structure and quantify tissue densities, ventricular size, Cerebrospinal fluid (CSF) volume, and brain mass. However, these general patterns may not be particularly useful as diagnostic criteria in individual cases, because usually comparison with control is needed.

CT is one of the more used imaging technologies for various diseases including AD. Although the risks for any one person are not large, however the increasing exposure to radiation in the population may be a public health issue in the future<sup>32</sup>.

#### **(b) Positron emission tomography**

This technique is based in the observation of radio labeled molecules in vessels or in areas where they accumulate, i.e. areas where biological molecules are active. These molecules are injected intravenously and emits positrons ( $e^+$ ). The emitted positrons collide locally with electrons ( $e^-$ ) and lead to the emission of two photons at higher energy (gamma rays) captured outside the subject. When the photons reach a scintillator material in the scanning device, a burst of light is created and detected by photomultiplier tubes. This technique has a spatial resolution around 5-10 mm.

- **Fluorodeoxyglucose positron emission tomography:**

<sup>18</sup>F-2-fluoro-2-deoxy-d-glucose (FDG) positron emission tomography (PET) allows studying brain metabolism using fluorodeoxyglucose as probe. Because the brain use almost exclusively glucose as source of energy, the glucose analog FDG is a suitable indicator of brain metabolism and, when labeled with Fluorine-18 (half-life 110 min) is conveniently detected with PET.

Research identified a characteristic of limbic and association regions that are typically hypometabolic in clinically established AD patients<sup>33,34</sup> (Figure 1.5). Most patients with Alzheimer's disease show cerebral hypometabolism when compared with age-matched controls. Reduction in metabolism in neocortical areas is detected and metabolic deficits in AD gradually worsen throughout the course of the disease. These changes have been identified in MCI patients, some of whom were found on follow-up examination to have converted to AD<sup>35,36,37,38</sup>. Some works observed a high amyloid deposition in parietal regions and were associated with co-localized FDG hypometabolism that suggests a local toxicity.

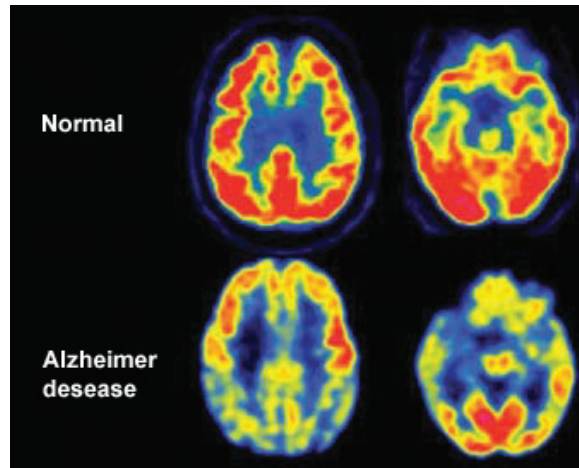


Figure I.5. Transaxial FDG-PET images of a normal control subject and a patient with mild AD<sup>23</sup>

- **Amyloid positron emission tomography**

Positron emission tomography (PET) with amyloid ligands is being used in the field of neuroimaging of aging and dementia in the last decade because it allows *in vivo* detection of amyloid plaques<sup>39</sup>.

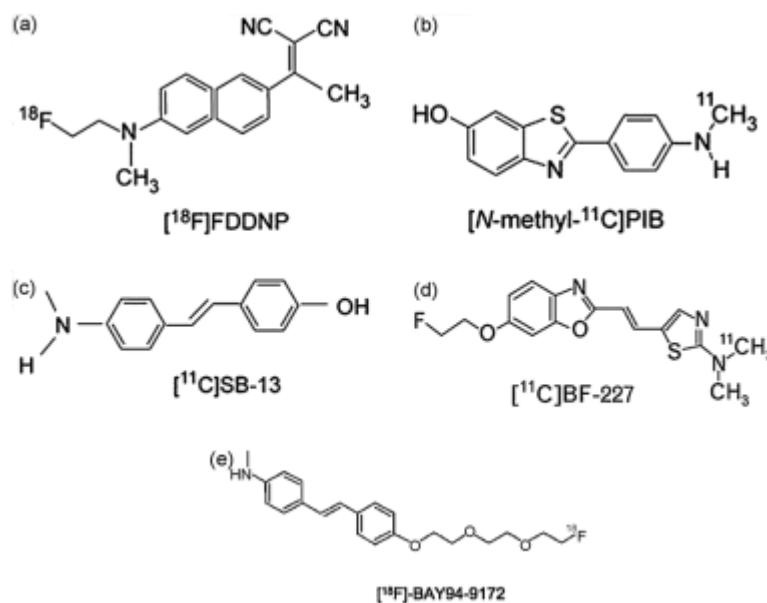


Figure I.6. Chemical structures of *in vivo* amyloid imaging PET ligands used in studies of Alzheimer patients

Recently, new radioactive tracers, which specifically mark the amyloid protein, have been developed<sup>40</sup> (Figure I.6), including the more used, PIB (Pittsburg Compound-B), a tracer-labelled with <sup>11</sup>C. These tracers allow obtaining quantitative information of the presence of amyloid deposits in the brain<sup>40</sup>. This technique is being evaluated and has high diagnostic interest.

Results, such as those from Ikonovic et al.<sup>41</sup> show that *in vivo* retention of PiB in brains of people with AD shows an A $\beta$  regional distribution similar to that of observed post-mortem.

Unfortunately the use of PET remains limited by the relatively low number of available devices and the cost of operation.

The main disadvantage of PET in general is that, it is relatively expensive with a limited availability, although it involves exposure to radioactivity.

### (c) Magnetic resonance imaging

MRI is based on the property that hydrogen protons will align and precess around an applied magnetic field,  $B_0$ . Upon application of a transverse radiofrequency (RF) pulse, these protons are perturbed from  $B_0$ . Then a relaxation phenomenon takes place where these protons return to their original state from the perturbed state. Two independent processes, called longitudinal relaxation (T1-recovery) and transverse relaxation (T2-decay), can be monitored to generate an MRI image. Local variation in relaxation, corresponding to image contrast, arises from proton density as well as the chemical and physical nature of the tissue under investigation. To obtain better images with well-defined mapping, contrast agents (CAs) are employed during the imaging recording procedure. These CAs and MRI mechanism are briefly presented respectively in the next section and in Annex A.

Today, structural MRI is used in clinical AD diagnosis in particular to assess atrophy<sup>42</sup> (volume of brain or brain's organisms) and changes in tissue characteristics as the result of vascular damage.

#### (i) *Utilization of structural MRI in Alzheimer disease diagnosis*

Structural MRI is used for atrophy assessment. Progressive cerebral atrophy is a characteristic feature of neurodegeneration, and can be visualized with MRI. See Figure I.7. Clinically, global brain volume, that of the cortex and the hippocampus of patients are followed on function of time to assess atrophy progression, because studies of hippocampal MRI volumes have shown that, there are closely related to neuronal counts at autopsy<sup>43,44</sup>.

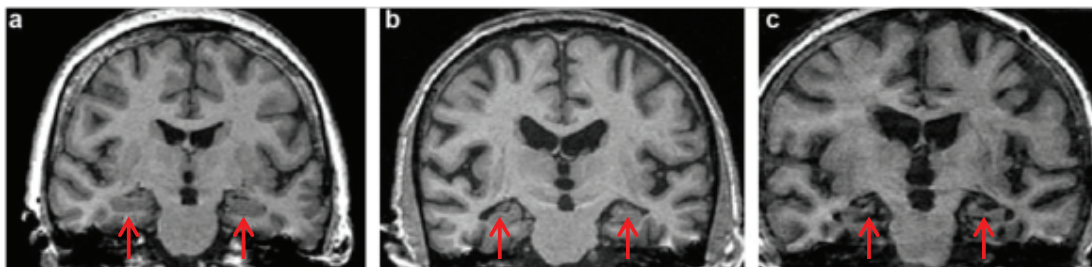


Figure I.7. MRI Coronal cuts weighted T1 showing hippocampal atrophy; a: normal hippocampus in healthy elderly subjects; b: beginning atrophy of hippocampal in an Alzheimer's patient. c: sharper hippocampal atrophy<sup>45</sup>.

Nowday, there is interest in automated pattern classification of MRI to predict AD at an early stage and to distinguish it from other dementias<sup>46,47</sup>.

## ***(ii) Utilization of functional MRI in the AD***

Functional MRI (fMRI) is used to probe the functional integrity of brain networks supporting memory and other cognitive domains in aging and early AD. It provides the indirect measure of neuronal activity, inferred from measuring changes in blood oxygen level-dependent (BOLD) MR signal<sup>36</sup>. The principle is based on the detection of a local reduction of deoxyhemoglobin in the capillaries and efferent veins during activation. Indeed, physiologically, there is a significant increase of local cerebral blood flow, while oxygen consumption is relatively weak, resulting in relative decrease of concentration of deoxyhemoglobin, detectable by MRI thanks to its paramagnetic characteristics. Images are acquired during cognitive tasks and compared to a control condition, such as encoding new information compared to viewing familiar information. fMRI has allowed to show changes in brain activity during the realization of specific cognitive tasks.

The main limitations of MRI for AD in general is the lack of molecular specificity, it cannot directly detect the histopathological hallmarks of AD (amyloid plaques or neurofibrillary tangles). Also with claustrophobia individuals MRI may not be tolerated whereas a rapid CT scan may be more feasible. Then, today in clinical practice, structural MRI can help support a clinical diagnosis, however unfortunately the techniques are not sufficient to establish a definitive diagnosis, as the overlap is great between atrophy associated with “healthy aging” versus AD<sup>48</sup> in early or medium stage.

### **1.2.1.4 Amyloid probe and early Alzheimer disease diagnoses**

Transgenic mouse lines developing amyloid plaques have been generated to produce animal models of AD, for AD research. The more used are mice overexpressing mutant amyloid precursor protein (APP) and both mutant APP and presenilin-1 (APP/PS1)<sup>49</sup>. At present it lacks sensitive *in vivo* method to assess amyloid burden in the brains of transgenic mice. There is no *in vivo* whole brain imaging method to detect A $\beta$  plaques efficiently and at high spatial resolution in mice or in men, to improve early diagnosis.

Then we are interested by multimodal smart contrast agents capable of recognize A $\beta$  plaques specifically and create contrast for both magnetic resonance and fluorescence imaging. Less works are published on multimodal contrast agent probe for A $\beta$  peptide; however some probes are developed for PET amyloid and for fluorescence imaging.

In recent years, several different strategies have been used to develop compounds suitable for amyloid imaging in different technique with different chemical structures and properties. These imaging ligands should meet several criteria:

- Cross the blood brain barrier (BBB) in sufficient amounts and nondestructively
- Be highly stable *in vivo*
- Moderately lipophilic
- Low uptake of metabolites to brain
- Bind specifically to plaques with high affinity
- High sensitivity (detection of small amount of A $\beta$ )
- Produce local changes in tissue contrast detectable (MRI, PET...)

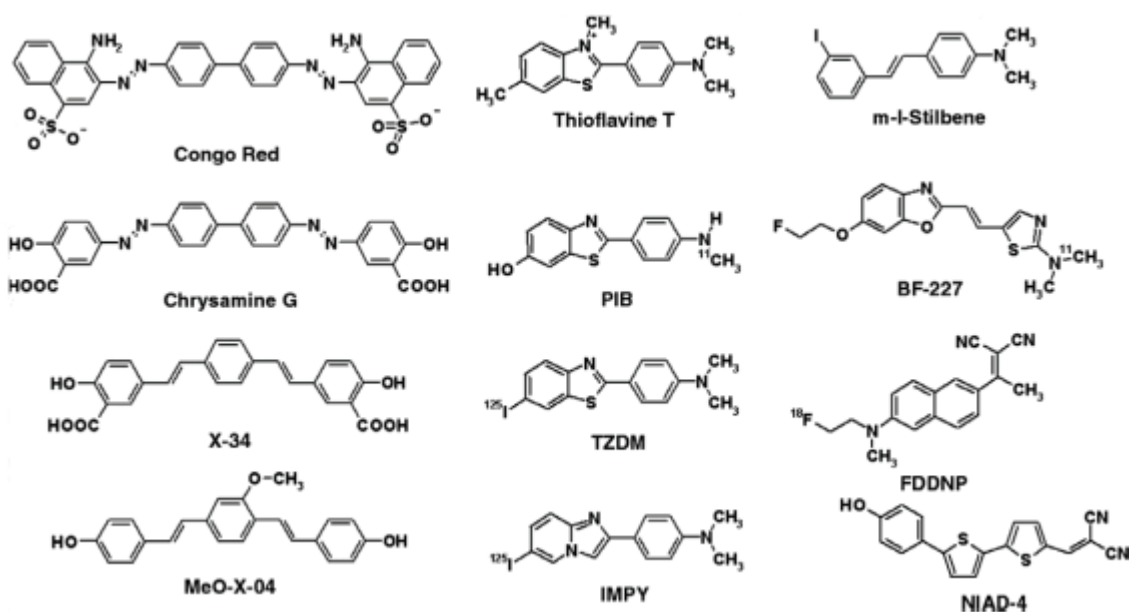


Figure 1.8. Examples of different amyloid imaging agents<sup>50</sup>

Several substances are developed as A $\beta$  plaques probe. Many of them failed due to highly unspecific binding and poor distribution in the brains of experimental animals<sup>51</sup>. These compounds include monoclonal antibodies against A $\beta$  peptide<sup>52,53</sup>, small radiolabeled analogues of Congo red, chrysamine-G, and thioflavin<sup>54,55</sup> that are applicable for single-photon emission computed tomography (SPECT) and PET. Some of these molecules are also used for MRI<sup>56,57</sup> and multiphoton microscopy<sup>58,59,60,61</sup>. The compounds fluorine-18-labelled FDDNP and the Pittsburgh Compound-B (carbon-11-labelled PIB) have been studied by PET in AD patients and are clinically used today<sup>39,62</sup>.

Today, researchers continue to develop and improve PET probes of AD. However, PET is limited by several problems, such as the poor spatial resolution with a detection limit of around 2 mm, the inability to visualize individual amyloid plaques, and the need for very short-lived radioisotope PET tracers and rapid synthesis. MRI is one of the best imaging techniques thanks to its availability and special resolution, even if the cost remains relatively high. This technique offers possibility to image individual amyloid plaques contrary to PET. Researchers develop techniques to

image amyloid plaques *in vivo* in human AD patients and AD transgenic mouse models using MRI with and without contrast agents.

## 1.2.2 $\beta$ -amyloid probes for MRI detection

### 1.2.2.1 $\beta$ -amyloid plaques detection without contrast agents

Over the last several years, some works were published on the development of techniques to image amyloid plaques in human AD patients and AD transgenic mouse models using MRI without contrast agents<sup>63,64,65,66,67,68,69</sup>. Only the large iron-containing plaques in certain brain region can be observed<sup>63</sup> and no correlation between AD plaque density with iron concentrations was observed<sup>64</sup>.

Magnetic resonance microscopy ( $\mu$ MRI) provides higher spatial resolution and higher signal-to-noise ratio than conventional MRI, and was used to detect A $\beta$  plaques<sup>70,71,72,57</sup>. It was applied in human brain autopsy tissue from patients with AD. A $\beta$  plaques were observed in the hippocampus of patients<sup>70</sup>. However, because imaging time was around 20 h, this technique is not suitable for *in vivo* imaging in humans. Also only the largest plaques can be seen using this technique<sup>71</sup> and structures within the cortex do not provide enough contrast to be appreciated<sup>72</sup>, confirming the necessity for special contrast for the target pathology.

Indeed, without contrast agent, contrast is due to the presence of metal ions in the plaque. This technique is problematic because endogenous iron contained in the hemoglobin of blood in blood vessels and microhemorrhages would create interfering artifacts. This technique lacks specificity and precision. Thus, it is difficult to distinguish A $\beta$  plaques to other brain anomaly, which constitute a major disadvantage.

### 1.2.2.2 $\beta$ -amyloid targeting probe labeled MRI contrast agent

$\beta$ -amyloid probes were associated with magnetic substances to target amyloid plaques in MRI<sup>56,57,65,73,74,75,57</sup>. Compound such as Putrescine-gadolinium-A $\beta$  peptide (PUT-Gd-A $\beta$ )<sup>56</sup> can label the APP mice's brain *in vivo* and be observed by *ex vivo* MRI in cortical tissue. Gadolinium-diethylenetriaminepenta-acetic acid (Gd-DTPA)<sup>57</sup>, monocrystalline iron oxide nanoparticles (MION)<sup>57</sup> and ultrasmall superparamagnetic iron oxide (USPIO)<sup>75</sup> can be conjugated to A $\beta$ -40 peptide to be used with mannitol as BBB crossing facilitator and detected by  $\mu$ MRI in transgenic APP and APP/PS mice *in vivo*. A significant correlation between densities of amyloid plaques in brains measured by MRI and by histological technique was found. MION-A $\beta$ -40 showed somewhat lower sensitivity to amyloid plaques than did Gd-DTPA-A $\beta$ -40, due to low permeability of the BBB for MION-A $\beta$ -40. Other works was published using Congo red-type compound shown in Figure I.9, able to cross the

BBB<sup>73</sup>. This compound labeled brain plaques and allows visualizing A $\beta$  in living mice by MRI using <sup>19</sup>F and <sup>1</sup>H nucleus.

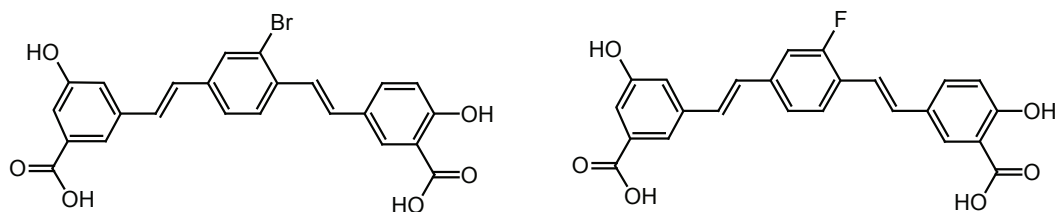


Figure I.9. Chemical structures of BSB (left) and FSB (right), the bromine (Br) of BSB is replaced with fluorine (<sup>19</sup>F) in FSB

However, these fluorine-containing probe molecules could be improved, to increase the specificity and avidity for A $\beta$  plaques as well as the number of <sup>19</sup>F atoms per molecule. These probes do not cross the BBB naturally and need mannitol or A $\beta$  peptide grafting for that.

### 1.2.2.3 Polythiophenes as $\beta$ -amyloid probe

Development of more sensitive methods for early detection and better understanding of the processes involved in amyloid fibril formation is necessary. The affinity of the traditional amyloidotropic dyes Congo Red (CR) and Thioflavin T (ThT) to A $\beta$  makes them the references in A $\beta$  staining. Today several compounds have been developed to increase affinity and contrast for *in vivo* applications as well as increasing blood-brain barrier permeability<sup>76,77</sup>. These derivatives of the traditional amyloidotropic dyes, like the PIB (a derivative of Thioflavin T), are at the forefront for *in vivo* amyloid imaging. These current compounds, all have a sterically rigid structure.

As research tools, Luminescent Conjugated Polythiophenes (LCPs) are superior since their spectroscopic signature depends on their conformation. Hence the LCPs molecules, which have been shown to reliably report on amyloid fibrillation *in vitro* and *ex vivo* tissue samples, provide unprecedented contrast of subtle changes of the molecular target due to conformational changes of the LCP during binding. LCPs contain a twistable conjugated polymeric backbone (poly-thiophene) whose geometry alters its spectroscopic properties. Molecules with low polymerization degree are identified as oligothiophene instead polythiophenes. However, for clarity and simplicity, they will be referred as LCPs, that is Luminescent Conjugated Polythiophene. (Figure I.10).

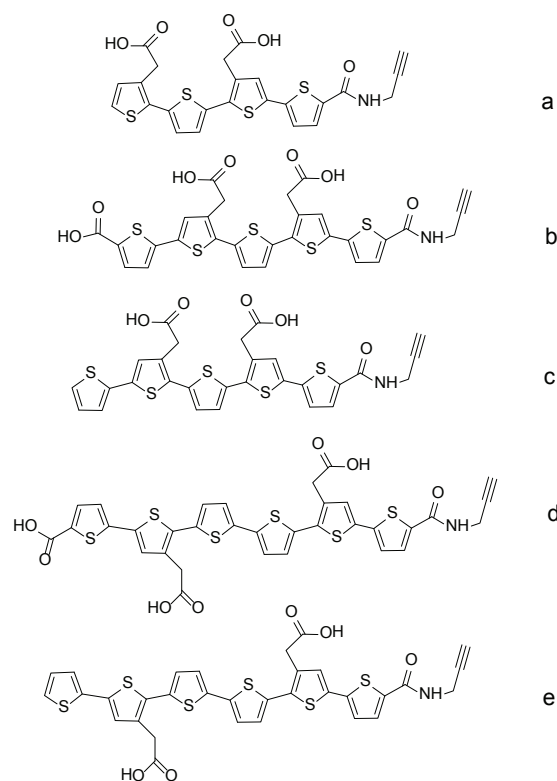


**Figure I.10. Example of different luminescent conjugated oligothiophene a) qHTAA, b) pFTAA, c) pHTAA, d) hxFTAA, e) hxFTAA**

The optical transitions of LCPs are tuned by interactions with certain peptides. Peptides force the LCPs to adopt a nonplanar conformation and the intensity of the emitted light is increased and shifted<sup>78,79,80</sup>. These transitions are related to a planar-to-nonplanar (from highly conjugated to less conjugated) conformational transition of the LCPs backbone. The highly conjugated form is associated with intermolecular aggregates. Molecular forces influencing this conformational change are hydrogen bonding, and nonpolar and electrostatic interactions, leading to aggregation<sup>81,82</sup>. The optical fingerprint obtained from the LCPs that reflects the conformational differences in distinct protein aggregates, is a unique property for the LCPs and is not offered by any of the commonly used amyloidotropic dyes<sup>83</sup> (Figure I.11). They have been demonstrated as conformational sensitive optical probes to detect conformational changes in  $\beta$ -amyloid<sup>84,85,86,87,50,80</sup>. Herland et al.<sup>84</sup> and Nilson et al.<sup>85</sup> have shown that LCPs can be used to monitor amyloid fibril formation *in vitro* for the histological labeling of amyloid deposits in *ex vivo* tissue samples and conformational mapping of amyloid deposits<sup>85</sup>.

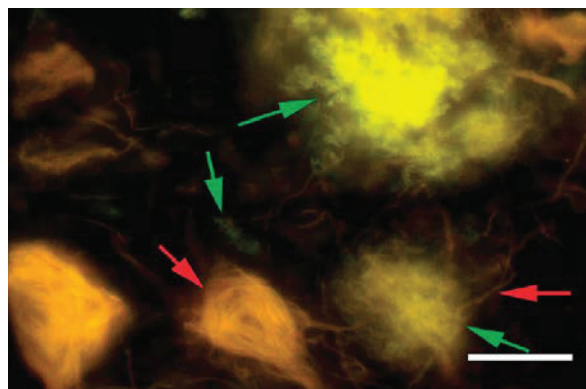


**Figure I.11.** High resolution fluorescence images showing the details of the interplay between A $\beta$  deposits (green), neurofibrillary tangles and dystrophic neurites (yellow red). Scale bar = 10  $\mu\text{m}$ <sup>83</sup>

LCPs are suitable for fluorescence detection, using mono or two-photon imaging technique. They can be activated by visible light and by infrared light (two-photon excitation) when bound to protein aggregates. These imaging agents can not only improve the quality of diagnosis of neurodegenerative diseases but also be of great advantage for monitoring and understanding the disease progression, especially from a biochemical research perspective. As optical probes are not the preferable agents for non-invasive imaging in humans, due to the limitations of multi-photon imaging, the development of novel multimodal contrast agent that can be used for both optical imaging and magnetic resonance imaging (MRI) hold great promise for AD diagnosis, since MRI is today a standard technique for imaging of pathological conditions in humans.

Thus, in this work, we propose new smart contrast agent, using particles capable to create contrast in MRI. Interestingly for the first time, these particles are chemically coupled with oligothiophenes. These oligothiophenes are both  $\beta$ -amyloid probe and fluorescent probe, paving the way to efficiency multimodal smart contrast agent for  $\beta$ -amyloid imaging.

The following section deals with the principle of fluorescence; the advantages and disadvantages associated with its use *in vivo* imaging. Then we will introduce briefly various nanoparticles used as contrast agent in MRI. Finally, we will end up with a presentation of our strategy for development of multi-modal contrast agents for both fluorescence and magnetic resonance imaging specifically suited to the recognition of A $\beta$  plaques for diagnosis of Alzheimer's disease.

## 2 FLUORESCENCE MICROSCOPY AND MAGNETIC RESONANCE IMAGING

### 2.1 Fluorescence microscopy

Fluorescent microscopy is an imaging technique that is widely used to study biological samples stained with particular fluorescent moiety that enhanced the contrast and allow the localization of specific cell structures or biomolecules. This technique is one of the more used in the biomedical field, including at the molecular level such as DNA and protein or at cell level in histological staining. Fluorescence imaging is the quickest and least expensive technique. It is a highly sensitive method with a high spatial resolution using two-photon absorption. In addition, this technique has a low acquisition time which makes it the current best adapted molecular imaging technique of screening.

#### 2.1.1 Principle of photoluminescence

Photoluminescence is the emission of light after the absorption of a photon by a molecule or material. Following this absorption, the substance passes from excited state (highest energy, due to the change of orbital of electrons). After this very rapid phenomenon (in order of fs), the molecule will return in its ground state (relaxation). This return involves two types of processes (Figure I.12).

- **Radiative relaxation processes:**

In these processes, molecule move from excited energy state  $E_n$  to a lower energy state  $E_{n-1}$  by emitting a photon of with  $\lambda = h.c / (E_n - E_{n-1})$ . There are transitions between the same spin states ( $S_1 \rightarrow S_0, \Delta S = 0$ ) in the fluorescence process and the transitions between different spin states ( $T_1 \rightarrow S_0, \Delta S \neq 0$ ) in the phosphorescence process.

- **Nonradiative relaxation processes:**

In these processes the molecule return to lower energy states without emitting photons. The energy is then dissipated as heat or transferred by the molecule in its environment. For a change in electronic state, there are non-radiative transitions between states of same spins (internal conversion) or different spins (Inter-system conversion). There is also the process of non-radiative relaxation inside of the same electronic state: vibrational transitions.

In the case of fluorescent or phosphorescent molecules, radiative relaxation processes are more probable than non-radiative relaxation processes.

Table I.2 shows characteristic times related to the various processes. Absorption is almost instantaneous and fluorescence, faster than the phosphorescence, is used in imaging. Subsequently, we are interested in fluorescence properties of molecules.

Various electronic processes caused by the absorption of light can be represented by the Jabłoński diagram (Figure I.12). The electronic energy levels and their vibrational substructure are shown with horizontal lines, and the physical processes that cause transitions between these levels are shown by vertical arrows. The singlet ground, first and second electronic states are labeled  $S_0$ ,  $S_1$  and  $S_2$ , respectively, and the first triplet state is labeled  $T_1$ . For each of these electronic states, the molecule can exist in a multitude of vibronic states indicated by the dashed lines (the rotational states are not represented).

**Table I.2. Characteristic time of the different processes in photoluminescence process**

Processes	Characteristics time
Absorption	$\sim 10^{-15} \text{s}$
Fluorescence	$\sim 10^{-10} - 10^{-7} \text{s}$
Phosphorescence	$\sim 10^{-6} - 1 \text{s}$
Internal conversion	$\sim 10^{-11} - 10^{-9} \text{s}$
Inter-system conversion	$\sim 10^{-10} - 10^{-8} \text{s}$
Vibrational transitions	$\sim 10^{-12} - 10^{-10} \text{s}$

At room temperature, the thermal energy is not sufficient to populate the energy states  $S_1$  and  $S_2$ . The absorption of light energy brings by photons allows to populate these excited states. Absorption usually takes place from the lowest vibrational levels of the ground state (they are the most populous). A fluorophore is usually excited to higher vibrational levels, either  $S_1$  or  $S_2$ .

The excited molecules then relax quickly by internal conversion to the lowest vibrational level of the excited state  $S_1$ . Return to the ground state  $S_0$  from the lowest vibrational level of the  $S_1$  state can then take place by emission of a photon (fluorescence), or by non-radiative relaxation (mainly by heat release during collisions with surrounding molecules). On the other hand, competing phenomena such as energy transfer between fluorophores, or to an inhibitor of fluorescence can also take place in the excited state. These concurrent processes of fluorescence emission lead the fact that the number of emitted photons is lower than the number of absorbed photons. Thus, the energy released in the fluorescence emission is generally lower than that caused by excitement.

The wavelength is inversely proportional to the energy of the photon, the emission wavelength is therefore red-shifted (towards the largest wavelength) compared to the wavelength of excitation.

The difference between the wavelength where absorption is maximum and that where there is the most intense fluorescence emission is called Stokes shift.

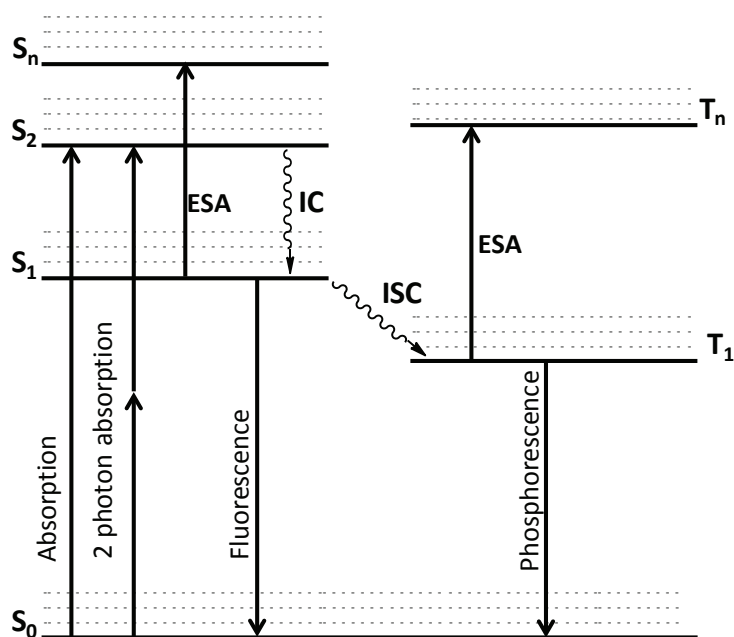


Figure I.12. Jablonski diagram of single-photon and multi-photon excitation

For some substances, an inter-system conversion process allows the population of the excited triplet  $T_1$  state from the excited singlet state  $S_1$ . Returning to the  $S_0$  state can in this case be carried out either by emission of light, known as phosphorescence or by non-radiative relaxation. The  $T_1$  triplet excited state is less energy than  $S_1$ , and energy released by phosphorescence is lower than that released by fluorescence. Phosphorescence emission is thus shifted to higher wavelengths compared to the fluorescence emission.

Two-photon absorption (TPA) is a nonlinear third-order effect, by which two photons of identical or different energy are absorbed simultaneously in order to excite a system from a state of lower energy (or ground state) to a state of higher energy (excited state). This phenomenon is widely employed in various applications including two photons microscopy that we will discuss later.

Also under the excitation, the two photon excitation process may be accompanied by excited-state absorption (ESA). The two-photoninduced ESA can be considered as a three-photon process, although three photons are not absorbed simultaneously; because the excited state is an effective state with finite lifetimes.

## 2.1.2 The main physical characteristic of fluorophores

- **Absorption and fluorescence emission wavelength:** they are the wavelengths for which the absorption and fluorescence emission are maximum.
- **Extinction coefficient  $\epsilon$  (or molar absorption):** This coefficient linking the amount of light absorbed over a length of cuvette  $l$  (cm) for a given wavelength to the concentration  $C$  (M) of the fluorophore in solution, according to the Beer-Lambert law:  $Absorbance = A = \epsilon l C$ . ( $\epsilon$  is expressed in  $M^{-1}.cm^{-1}$ ). This factor is a direct measure of the probability to absorb a photon of wavelength  $\lambda$  for a molecule.
- **Quantum efficiency:** is the ratio of number of photons emitted by the number of photons absorbed. It represents the relative fluorescence efficiency compared to other relaxation pathways.
- **Fluorescence lifetimes or lifetime of the excited state  $S_1$ :** this is the average time during which the molecule remains in the excited state before returning to its ground state. This period is in the order of nanosecond for an organic fluorophore. A short life time increases the sensitivity of the molecule, by allowing it to return more quickly in its ground state and therefore to a greater number of fluorescence cycles.
- **Photobleaching:** molecule in excited state, can participate in chemical reactions (photochemical reactions), in particular with oxygen. The fluorophore loses its fluorescence properties. Certain proportion of them can be destroyed by photobleaching, resulting in a decrease in the intensity of fluorescence with time during continuous exposure.

## 2.1.3 Parameters influencing fluorescence properties of fluorophores

In experimental conditions, the molecules are in a complex local environment, which will affect their fluorescence properties. It can promote the non-radiative relaxation and thus reduce the fluorescence. It will also modify the energy levels of the molecule and its spectra. The properties of fluorescence of a molecule are therefore related to its environment.

### 2.1.3.1 Dynamic quenching

In solution, once in their excited state, fluorescent molecules can collide with other molecules. In the case of collisions, electronic energy is converted into kinetic energy and vibration's energy, this is dynamic quenching. Thus, an increase in temperature and the concentration of the species in solution will reduce the fluorescence by increasing the probability of collisions.

### **2.1.3.2 Effect of solvent, pH and ions in solutions**

Salvation of the molecule can modify their spectra and their fluorescence properties. The polarity of the solvent will affect the stability of the molecular structure at the ground state and the excited state; leading to the change of the energy levels of the molecule and the transition probabilities. Molecules containing acidic or basic functions will be sensitive to the pH. They will be presented in different structure depending on the pH, thus depending on the protonation or deprotonation of the molecule. Finally, some fluorescent molecules will be sensitive to the ions present in solution. Their molecular structures and their fluorescence properties can be changed when they are complexed.

### **2.1.3.3 Effect of the concentration and aggregation**

In high concentration, fluorescent molecules with a low Stokes shift, undergo a decrease of the fluorescence efficiency. This decrease is due to the effects of recovery between absorption and emission spectra. A part of the emitted fluorescence radiation is reabsorbed by the other molecules in solution. In addition high concentrations will increase collisions and give rise to dimerization or aggregation phenomena. These phenomena will greatly alter spectral properties and efficiency of fluorescent molecules.

### **2.1.3.4 Photobleaching**

As mentioned previously, in its excited state, the molecule can also react chemically with its environment (polymerizations, oxidation, dissociation, isomerization...) and lose its fluorescence properties. Most often, the molecules react with oxygen (in the form of free radicals). When molecules are excited continuously, a part of them is destroyed and thus the fluorescence intensity decreases. Resistance to photobleaching corresponds to the average number of excitations that can undergo a molecule before being degraded. A high photostability is required for the imaging applications.

## **2.1.4 Advantages and limitations of *in vivo* fluorescence microscopy**

This technique has many advantages such as small size devices, good sensitivity, stable contrast agents and do not need ionizing radiation. The current application is for the small animal, and help in the discovery of biomarkers for targeting tumors or protein plaques, and secondly the discovery and evaluation of new therapeutic. Fluorescence imaging applications are in development for human, for example as a tool for diagnosis of breast cancer and detection of metastases.

Moreover, the use of fluorophores for *in vivo* experiments creates additional constraints compared to the *in vitro* experiments, due to the presence of organic tissues in the path of excitation and fluorescence light radiation. Then, the main problems encountered in fluorescence imaging *in vivo* are:

- Propagation of excitation and emitted light during the crossing of the tissue causes a significant loss of intensity (scattering phenomenon), thus a loss of information, makes it harder the exact localization of the fluorophore in the body.
- The absorption of the excitation and emitted light by the tissues leads also to a loss of intensity of the fluorescence signal.
- The autofluorescence of tissue, which is the source of a significant decrease in the contrast of the image, is the natural fluorescence emitted by many constituents of tissues (hemoglobin, Porphyrin...)

From instrumental point of view, these drawbacks can be limited, by increasing the sensitivity of detection and filtering the scattered excitation radiation. And fluorophores must have highest quantum efficiency and Stokes shift. Two-photon absorption method is suited to improve *in vivo* fluorescence imaging.

## **2.1.5 Two-photon microscopy**

### **2.1.5.1 Principle**

As mentioned previously, two-photon absorption is the simultaneous absorption of two photons in energy  $h\nu_1$  and  $h\nu_2$  via a virtual energy level. The sum of energy ( $h\nu_1 + h\nu_2$ ) is greater than or equal to the energy of transition  $h\nu_s$  in the absorption band. When the laser with visible or UV excitation of confocal microscope is replaced by femtosecond pulse laser emitting in infrared, transitions probability is too weak, because one infrared photon is not sufficiently energetic to excite fluorescence. Two photons need to team up and join their energies for that<sup>88</sup>. Then fluorescence emission, takes place only at the point where the photon density is highest (in the focal plan) of the microscope objective, contrary to classical (single-photon) absorption. This point is illustrated in Figure I.13. The excitation is linear for single photon absorption, and fluorescence is excited on the entire course of the beam, while in the case of two photon, the fluorescence is confined to the focal point.

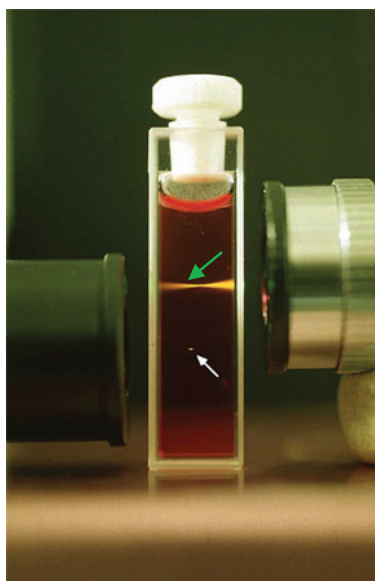


Figure 1.13. Difference between single-photon (green arrow) excitation and two-photon excitation (white arrow)

### 2.1.5.2 Advantage of two-photon microscopy

Two-photon fluorescence microscopy is characterized by high spatial resolution in three dimensions, it becomes an alternative technique to confocal microscopy and also offers additional advantages<sup>89</sup>:

- **Less background noise:** fluorescence signal come only from the focal point, no parasitic signal originates from others plans both lower and higher than the focal plane. This property of the two-photon microscope allows, thanks to the absence of hole of filtering, detection of all of fluorescence with very little background noise.
- **Well separated excitation and emission wavelength:** with two photon absorption, the excitation wavelength is almost twice compared to one photon absorption. Therefore the emitted fluorescence signal is easily and efficiently separate to the incident radiation.
- **Improvement of the depth of penetration:** the absorption coefficients of most biological components are lower in the infrared than in the UV. Therefore there is an enhancement of the penetration depth of the laser beam in the samples (at least doubled that obtained by confocal microscopy). This major advantage has already been verified experimentally and operated for the study of various thick samples<sup>90</sup>.
- **Reduction of samples degradation:** the main advantage of the fluorescence microscopy using two-photon excitation is the restriction of any damage at the focus point. The various issues encountered during the excitation of a molecule are limited to the micro focus volume (thermal effects, photo-bleaching, photo-degradation...).

### **2.1.5.3 Limitation of two-photon microscopy**

The main drawback of this technique for in vivo brain imaging for example, is the limitation of depth penetration and the need of skull opening<sup>91</sup>. That is an invasive surgical preparation which restricts its use in humans unlike MRI.

### **2.1.6 Conclusion**

Fluorescence imaging is of real interest for molecular imaging for the study and understanding of pathologies, but also for their detection and treatment. It has many advantages such as speed of acquisition, a low cost and a great sensitivity. However, molecular imaging is strongly linked to the fluorophores. It requires the injection of contrast agents. Among the molecules and fluorescent materials commonly used in fluorescence imaging, there are organic fluorophores, fluorescent proteins, and semiconductor nanocrystals. Due to its application little widespread in humans, one of the objectives of this work was to develop new magnetic nanoparticles associated with an organic chromophores for application in fluorescence and resonance magnetic imaging.

## **2.2 Magnetic resonance imaging**

MRI is based on the magnetic properties of the hydrogen nuclei of substances component biological tissues. The contrast of the image depends on essentially intrinsic parameters characteristic of the studied tissue such as proton density, longitudinal relaxation time (T1), transverse relaxation time (T2), magnetic susceptibility and extrinsic parameters which depend on the parameters of the sequences selected for the realization of the images and therefore adjustable by the operator. However the contrast between tissues is not always sufficient to allow clear differentiation of structures. Therefore, the use of contrast agents modifies the tissues characteristics, and allows increasing differential contrast of images.

In the following section, we will present different contrast agent for magnetic resonance imaging. Mechanism of MRI is briefly detailed in Annex A.

### **2.2.1 Contrast agents for MRI**

The magnetic resonance (MR) signal changes observed during the use of contrast agents are due to interactions of the later with the magnetic signal source, usually hydrogen nuclei. The contrasts enhancement depends on various parameters: the class of the contrast agent, its concentration in structures to be observed, the nature of these structures and the used MRI sequence. Contrast agents decrease T1 and T2 relaxation times and therefore accelerate the  $1/T1$  and  $1/T2$  relaxation rates. MR contrast agents can broadly be divided into two classes: those that

increase the T1 signal in T1-weighted images (positive contrast agent, bright contrast) usually paramagnetic moieties, and those that reduce the T2 signal in T2-weighted images (negative contrast agent, dark contrast) usually superparamagnetic nanoparticles. The effectiveness of these products on relaxation rates is proportional to their concentration, and is defined by its longitudinal (r1) and transverse (r2) relaxivities enhancement of water proton relaxation rates by 1 mmolL<sup>-1</sup> solutions of contrast agent. This effectiveness r1 and r2 correspond to the slopes of curves 1/T1 and 1/T2 as function of probe concentration.

The paramagnetic agents present a leading T1 effect. Relaxivities r1 and r2 of these agents are of the same order of magnitude. However because T1 in cells are much higher than T2 (on the order of 10 times), the T1 effect is predominant on the T2 effect. A decrease of T1 will enhance signal in T1- weighted sequence. Agents that have a major effect on T1, are positive contrast agents.

Superparamagnetic agents are agents with magnetic susceptibility and have a dominant T2 effect. Their high r2 value leads to spin dephasing and is expressed preponderantly to any T1 effect. A decrease in the T2 will decrease signal intensity on T2-weighted and on T1-weighted sequences. Therefore this effect depends less on the used sequence. Agents that have a major effect on T2, are negative contrast agents.

Paramagnetic nanoparticles can be used either positive or negative agents or both. The importance of this kind of particles as CAs can be emphasized by numerous research studies that have been done so far<sup>92,93,94,95</sup>.

### 2.2.1.1 Paramagnetic ions complex as positive (T1) contrast agent

These contrast agents decrease the proton longitudinal relaxation time (T1) and therefore increase the intensity of the MR signal, providing a positive contrast. These compounds often have several free electrons which the magnetic moment is very high than that of the proton. These compounds include oxygen, transition metals, and especially Lanthanide (III) including the most used Gadolinium (III). Gadolinium is a metal ion with 7 single electrons (Table I.3).

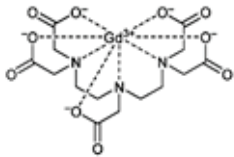
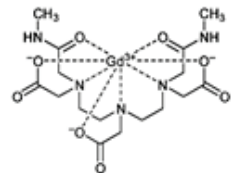
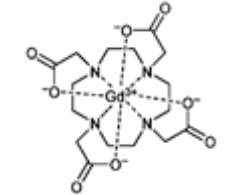
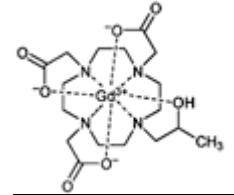
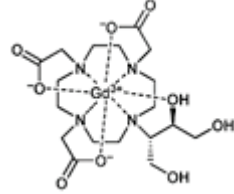
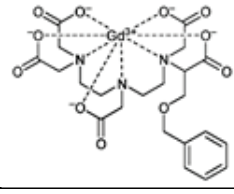
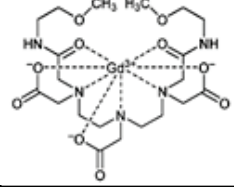
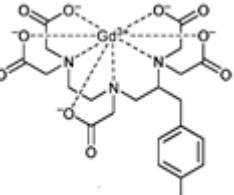
Table I.3. The main paramagnetic ions used in MRI

Atomic N	Ion	3d	4f	Magnetic moment (Bohr magneton)
24	Cr 3+	↑ ↑ ↑		3.8
25	Mn 2+	↑ ↑ ↑ ↑ ↑		5.9 (weak field)
26	Fe 3+	↑ ↑ ↑ ↑ ↑		5.9 (weak field)
29	Cu 2+	↑↓ ↑↓ ↑↓ ↑↓ ↑		1.7-2.2
63	Eu 3+		↑↓ ↑ ↑ ↑ ↑ ↑ ↑	(6.9)
64	Gd 3+		↑ ↑ ↑ ↑ ↑ ↑ ↑	7.9
66	Dy 3+		↑↓ ↑↓ ↑ ↑ ↑ ↑ ↑	(5.9)

**(a) Commercial agents**

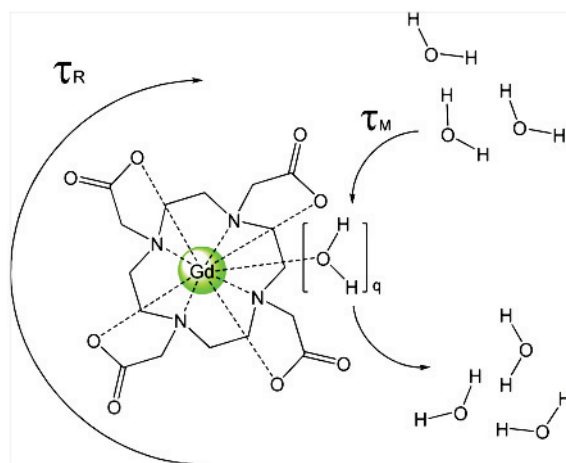
Gadolinium in his free ionic form (Gd(III)) is highly toxic for humans and animals. It precipitates in several tissues including liver, lymph nodes, and bones. Also Gd(III) obstructs passage of calcium through ion channels of muscle cells<sup>96</sup> and nerve tissue cells, thereby reducing neuromuscular transmission and interferes with intracellular enzymes and cell membranes. In order to avoid these toxic effects, Gd(III) is sequestered by non-toxic substances, by binding to chelate species. This type of compounds is the most used in clinical MRI as T1 contrast agents. The majority of these products are extracellular, don't cross the blood brain barrier and have r1 value in range 3-5 mM<sup>-1</sup>s<sup>-1</sup> (Table I.4). Therefore the major challenge in T1 probes development is, achieving the high sensitivity probes to reduce toxicity. Also the high sensitivity is required when the biological targets are present at very low concentrations.

Table I.4. Clinical gadolinium T1-agents<sup>97</sup>

Trademark	Generic name	Laboratory	Chemistry	Cyclic/Acyclic	$r_1(\text{mM}^{-1}\text{s}^{-1})$ (0,47 T)
Magnevist®		Bayer-Schering	Gd-DTPA	acyclic	3.8
Omniscan®		Amersham	Gd-DTPA-BMA	acyclic	3.8
Dotarem®		Guerbet	Gd-DOTA	cyclic	3.5
ProHance®		Bracco	Gd-HP-DO3A	cyclic	3.7
Gadovist®		Bayer-Schering	Gd-DO3A-butrol	cyclic	3.7
MultiHance®		Bracco	Gd-BOPTA	acyclic	4.8
OptiMARK®		Mallinckrodt	Gd-DTBA-BMEA	acyclic	4.1
Primovist®		Bayer-Schering	Gd-EOB-DTPA	acyclic	5.5

### (b) Development of new agents

According to Solomon-Bloembergen-Morgan theory<sup>98</sup>, relaxivity of a contrast agent is the result of the complex structure and dynamic parameters of the metal complex, among which the more relevant ones are the number of labile water molecules coordinated to the metal ( $q$ ), their residence lifetime at the metal site ( $\tau_M$ ), the rotational correlation time of the complex ( $\tau_R$ ), and the relaxation characteristics of the unpaired electrons of the metal ion (Figure I.14).



**Figure I.14. Schematic representation of a paramagnetic chelate complex in water and the structural parameters affecting the proton relaxivity**

When the water exchange rate is fast enough, the bulk solvent protons will relax as fast as the coordinated solvent protons. According to this theory, to increase the relaxivity  $r_1$  of a Gd(III) contrast agent, we need to design a compound able to have a greater number of inner-sphere water molecules,  $q$ ; an optimally short water residence time,  $\tau_M$ ; and a slow rotational correlation time ( $\tau_R$ ). New contrast agents are in development according to these requirements to improve T1 relaxivity.

One of the preferred strategies to improve relaxivity is to optimize rotational mobility. It is necessary to couple effectively the local motion of the Gd–OH<sub>2</sub> vector with the rotational motion of the whole complex, whilst maintaining fast water exchange on the Gd(III) ion. Theoretical predictions suggest that maximal relaxivity enhancement will occur when the water exchange rate is in the range 10 to 50 × 10<sup>6</sup> s<sup>-1</sup> (at 310 K) and when the rotational correlation time,  $\tau_R$ , defining the motion of the Gd–OH<sub>2</sub> vector, is in the order of a few nanoseconds<sup>99</sup>. Usually the rotational mobility of the paramagnetic agents is higher than that of the carrier molecule due to the flexibility of the linking between complex and carrier molecule<sup>100</sup>. Also the metal-water proton vector should not rotate independently and faster than the whole complex<sup>101</sup>. One of the solutions is the use of spherically

shaped carriers such as globular proteins or dendrimers to ensure an isotropic and slow tumbling motion. To limit the rotational freedom of the chelate, researchers used multisite binding chelate such proteins and macromolecules<sup>102</sup>. Thus Fulton et al.<sup>103</sup> developed dendritic gadolinium complexes with high relaxivity, by placing the metal ion at the barycentre of the molecular complex in order to improve motional coupling. Very high relaxivity values ( $20\text{-}40\text{ s}^{-1}\text{ mM}^{-1}$ ) were obtained.

Macrocyclic molecules are developed to complex gadolinium with more coordinated labile water ( $q>1$ ). Xu et al. designed a Gd(III) complex, Gd(TREN-1-Me-3,2-HOPO)(H<sub>2</sub>O)<sub>2</sub> (Figure I.15-1). The  $r_1$  value of this complex was  $10.5\text{ s}^{-1}\text{ mM}^{-1}$ , twice that of commercial agents. Raymond et al.<sup>104</sup> have designed optimized systems, the soluble tris-hydroxypyridonate Gd(III) complexes with  $q = 3$  characterized by a  $r_1$  value of  $13.1\text{ mM}^{-1}\text{ s}^{-1}$  at 0.5 T.

Several reviews treat various compounds in development using different strategies including effect of  $\tau_M$  and hydration<sup>105,97,106,107,108</sup>.

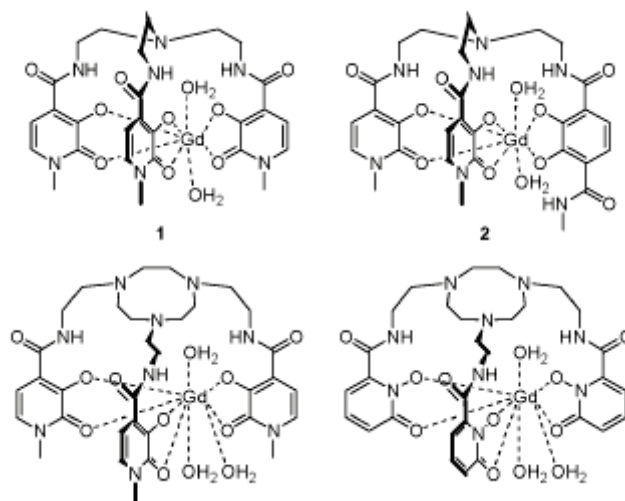


Figure I.15. Example of some Gd (III) complex with  $q>1$  for high  $r_1$  relaxivity<sup>104</sup>. Gd-TREN-1-Me-3,2-HOPO (1); Gd-TREN-bis-(1-Me-3,2-HOPO)-TAM (2); Gd-TACN-3,2-HOPO (3); Gd-TACN-1,2-HOPO (4).

### 2.2.1.2 Paramagnetic nanoparticles

#### (a) Superparamagnetic iron oxide nanoparticles as negative contrast agent

The previously described paramagnetic metal complexes have a low  $r_2/r_1$  value and give hyperintensity (bright contrast) in  $T_1$ -weighted MR images. The hypointense (dark) contrast could be obtained with contrast agents with high  $r_2/r_1$  ratios. Iron particles are the most negative agents used clinically. There are three kinds of iron oxides particles, according to the particles diameter  $d$ : *i*) ultra-small superparamagnetic iron oxide (USPIO) for  $d<50\text{ nm}$ ; *ii*) small superparamagnetic iron oxide

(SPIO) for  $1 \mu\text{m} > d > 50 \text{ nm}$  and *iii*) micron-sized particles of iron oxide (MPIO) for  $d$  around several micrometer.

**(i) Commercial agents**

Iron particles are commonly made of single crystals of magnetite ( $\text{Fe}_3\text{O}_4$ ) or maghemite ( $\gamma\text{-Fe}_2\text{O}_3$ ) phase<sup>109</sup>. They are modified on the surface usually with organic molecules including dendrimers phosphatic<sup>110</sup>, carboxylic acids (citric acid<sup>111</sup>, dimercapto-succinic acid<sup>112</sup>), polymers such as polyethylene glycol<sup>113</sup>, vinyl acetate polymer or dextran. They possess a very large transverse relaxivity ( $r_2$ ) from 30 to 300  $\text{mM}^{-1} \text{s}^{-1}$  (Table I.5).

**Table I.5. Clinical iron oxide T2-agents**

Trademark	Hydrodynamic diameter (nm)	Laboratory	$r_1(\text{mM}^{-1}\text{s}^{-1})$ (0,47 T)	$r_2(\text{mM}^{-1}\text{s}^{-1})$ (0,47 T)	$r_2/r_1$
Endorem <sup>®</sup>	120-180	Guerbet	10.1	120	11.9
Resovist <sup>®</sup>	50-65	Bayer-Schering	9.7	189	19.5
Sinerem <sup>®</sup>	20-40	Guerbet	9.9	160	16.2
Ferumoxytol <sup>®</sup>	30	Adv.Magnetic	15	89	5.9
Supravist <sup>®</sup>	21	Bayer-Schering	14	33.4	2.4
FeOdots <sup>®</sup>	30	Genovis	-	300	-

**(ii) Development of new agents**

Superparamagnetic relaxivity  $r_2$  depends mainly on magnetic proprieties of the particles such as susceptibility and magnetic moment, which depend on the particles size and crystallinity. Thus current challenges remain the development of monodisperse population of crystal cores in suitable controlled size and the design of optimized processes for improving the crystallinity degree of the ferrite core, which is proportional to the overall magnetization of the particle. Finally, a critical point deals with the selection of a reproducible procedure that should be industrialized without any complex purification procedure. Several procedures are used to produce magnetic nanoparticles from solutions, aerosol or vapor phase<sup>114,115,113,110</sup>.

T2 agents are highly sensitive; however sometimes they can suffer from poor contrast due to the dark contrast produced by hypointense areas developed from pathogenic conditions. Also, the “blooming effect” associated with T2 contrast agents makes imaging of lesions difficult, because the signal from abnormal areas are mixed with the background signal<sup>93</sup>. Thus, paramagnetic particles can be useful with high relaxivity values, able to create positive or negative contrast, or both for bimodal imaging.

**(b) Paramagnetic nanoparticles as positive or negative contrast agents**

Current literature shows that besides the efforts in improvement of traditional contrast agents, such as paramagnetic ion complexes<sup>107</sup> and iron oxide superparamagnetic particles<sup>109</sup>, there is a growing interest in the development of paramagnetic particles<sup>116,117,118</sup> and their characterization<sup>119</sup>. This will allow obtaining high contrast MR images even at a reduced dose and turn lower any danger coming from toxicity of MRI CAs<sup>92</sup>.

Recently vuong et al.<sup>95</sup> studied the aging mechanism of paramagnetic nanoparticles for MRI. They showed that, longitudinal relaxation of the paramagnetic particles is caused by an inner sphere mechanism between the surface exchangeable protons and bulk water protons. This process is similar to what happens for complexed paramagnetic ions, except for the correlations times of the modulation processes involved which are different and the core paramagnetic ions do not contribute to the inner sphere relaxation process, which can lowers the r1 relaxivity of the particles. Concerning paramagnetic particles, the paramagnetic ions belong to a large particle whose rotation correlation time is very large compared to paramagnetic complexes. However, this situation is also happening for paramagnetic complexes linked to a large molecule, such as macromolecules or protein.

The transverse relaxation can be due to a proton exchange between the particle surface and bulk water protons for some gadolinium particles<sup>95</sup> (as for hydrated iron oxide) in this case, r2 increase with the magnetic moment of the particles and consequently with the external field  $B_0$ . The transverse relaxation is more commonly caused by the diffusion of the water molecules in the gradients nearby the magnetic particles according to the outersphere relaxation mechanism.

The current developed particles are manganese oxide<sup>120,121,122</sup> and more widespread, particles made of gadolinium element, such as gadolinium hydroxide, oxide<sup>118</sup>, phosphate<sup>123,124</sup> and fluoride<sup>125,126</sup>, and also made of dysprosium, holmium, terbium and erbium<sup>119,92</sup>.

### 3 AIMS AND OBJECTIVES

#### 3.1 Strategy of the study

We have seen in the literature review that despite the number of people affected by AD and the need for diagnosis, the currently diagnostic techniques are insufficient. Combination of neuropsychological tests and neurological imaging do not meet the needs of the early diagnosis of AD. Neurological imaging includes mainly PET and MRI. MRI is clinically used without specific contrast agent to assess the brain volume. Thus diagnosis is only possible very late and lack specificity. PET can be used with specific contrast agent but resolution is very poor and individual plaques cannot be imaged.

We also have seen that there are several types of compounds used as MRI contrast agents, gadolinium complex-based or nanoparticles made of gadolinium or iron. With the development of nanotechnologies, these compounds can be functionalized by various molecules to ensure stability, biocompatibility and targeting. Specific contrast agents able to target A $\beta$  plaques in the brain for AD diagnosis are in development. Unfortunately until today, the BBB crossing remains an obstacle. According to literature, the main alternatives are the grafting of A $\beta$  fragments on the agents, in order to be used with mannitol to facilitate the BBB crossing. However, there are few fluorescence molecules capable of crossing the BBB and target A $\beta$ , and they are rarely associated to magnetic particles to make multi-modal contrast agents for A $\beta$  plaques imaging. Skaat et al. associated iron oxide to Congo red, however their investigation was restricted to the studies of A $\beta$  bending selectivity *in vitro*<sup>127</sup>.

We therefore chose this route; that is the development of the magnetic agents associated with LCPs. LCP is a fluorescent molecule, able to cross naturally the BBB and have been shown to efficiently bind to A $\beta$  *in vitro* and *in vivo* tissue samples. This structure should allow dispensing with the use of fragments of A $\beta$  or mannitol, as we exploit the ability of these LCPs to cross the BBB, to target the A $\beta$  and to create contrast in fluorescence imaging.

Regarding the magnetic agents, gadolinium was chosen because it wears seven unpaired electrons leading to a high electronic magnetic moment (7.9  $\mu_B$ ) and has a high electronic relaxation time ( $> 10^{-9}$  s). These two properties lead to an efficiency dipolar coupling between the magnetic moment of Gd (III) and the magnetic moment of the proton that induces an increase in the relaxation rate of protons. Also Gd (III) offers the possibility to develop both complexes and nanoparticles-based systems.

Nanoparticles will be functionalized with polyethylene glycol to provide water solubility and biocompatibility. The link between the nanoparticles and LCPs will be ensured by the bifunctional

spacer, with on the one hand a function for clicking to LCPs, and on the other hand a phosphonate group for a covalent binding with the nanoparticles. The spacer is a poly-hydroxyethylacrylate, chosen for its water solubility and the possibility that it offers in terms of the variation of the length of the spacer.

## **3.2 Objective of the study**

This work consists in the synthesis of various architectures of gadolinium-based magnetic nanoparticles and the grafting of PEG and LCPs on the surface of the particles. Particles will be characterized before and after functionalization. Finally we performed preliminary tests to evaluate these nano-objects such as contrast agents for fluorescence and magnetic resonance imaging, as well as their ability to pass the BBB and stain A $\beta$  plaques. The objectives of the work can be divided in three parts:

### **3.2.1 Synthesis of efficiency magnetic nanoparticles**

Here, we aim to develop various particles with different chemical composition and morphology. These particles will be functionalized and must be chemically stable and have efficiency magnetic properties for T1 and T2 relaxation. Three kinds of particles and structure will be synthesized. The isotropic system made of spherical gadolinium fluoride (GdF<sub>3</sub>), the anisotropic system made of gadolinium phosphate nanorods (GdPO<sub>4</sub>) and the core-shell system, titanium oxide coated with DOTA-Gd<sup>3+</sup> complex. They will be fully characterized before and after PEG coating and then tested *ex vivo* as MRI contrast agent.

We developed in the lab a versatile process for lanthanide fluoride (LnF<sub>3</sub>) synthesis. This process will be adapted for gadolinium fluoride using reflux and solvothermal process.

GdPO<sub>4</sub> nanorods are interesting, because adaptation and improvement of the literature process will lead to different size and chemically doped particles. Then influence of size, morphology and chemical composition on the relaxivity properties will be investigated. Also, contrary to the classical isotropic particles, biological activity of these anisotropic particles (rod) is little studied.

TiO<sub>2</sub>@DOTA-Gd<sup>3+</sup> will be developed to improve the T1 and T2 relaxivity of the commercial DOTA-Gd<sup>3+</sup> by increasing the local concentration and by decreasing the tumbling rate of DOTA-Gd<sup>3+</sup>, opening the way to a bimodal contrast agent, able to enhance both T1 and T2.

### **3.2.2 Functionalization of the particles**

The second objective is the functionalization of the particles. The first step is functionalization with PEG using bisphosphonate as the anchoring group. Phosphonate and

bisphosphonate have been shown to be an excellent coupling group for this kind of particles. After physico-chemical characterizations, the best particles will be selected according to their stability in physiological condition and ability to accelerate proton relaxation in aqueous solution. The second step is the co-functionalization with both PEG and LCPs on the surface of the selected particles. The anchoring group is bisphosphonate for PEG and phosphonate for LCPs. The resulting LCPs labeled particles will be characterized; their magnetic and fluorescence properties will be evaluated.

### 3.2.3 Biological evaluation of the particles

The last objective is the biological evaluation of the particles. Pegylated particles will be evaluated *ex vivo* MRI, while the LCPs labeled particles will be evaluated *in vitro* and *in vivo* as contrast agent for MR and fluorescence imaging. In this evaluation, capacity of the probes to cross the BBB, to stain A $\beta$  and create contrast will be assessed.

The generated novel multimodal imaging agents for both fluorescence and magnetic resonance imaging are presented schematically in Figure I.1. These final LCP labeled magnetic nanoparticles will be used *in vitro* and *in vivo*. Thus they must meet these main criterions:

- Covalent bound between organic molecules with inorganic particles
- Conserve magnetic and fluorescence proprieties of respectively the particles and LCPs after coupling
- Stable in aqueous colloidal solution
- Stable in biological environment after *in vivo* injection
- Cross the blood brain barrier and stain amyloid plaques
- Be detectable by fluorescence and magnetic imaging
- Be biocompatible and no toxic

In the following, chapter II will deals the synthesis and characterization of three different particles, gadolinium fluoride nanoparticles, gadolinium phosphate nanorods and titanium oxide nanoparticles. Then the particles will be functionalized with PEG and titanium oxide will be coupled with DOTA-Gd(III) complex. Chapter III will deals the functionalization of the particles with LCPs, followed by physico-chemistry characterizations including photophysics and magnetic, while chapter IV will be devoted to biological experiments, including magnetic resonance and fluorescence imaging tests.

# CHAPTER II



# CHAPTER II NANOPARTICLES SYNTHESIS AND SURFACE MODIFICATION

This chapter is devoted to the development of magnetic contrast agents. First of all, we will discuss the literature methods of synthesis of nanoparticles, their surface functionalization and stabilization in aqueous colloidal solution. Then we will present our methods and discuss the used processes.

## 1 SYNTHESIS AND SURFACE MODIFICATION METHODS

Nowadays several methods exist for the synthesis of nanoparticles. These methods can be divided into two large categories: Top-down and Bottom-up approaches. Top-down approach involves the breaking down of the bulk material into nano-sized particles, while Bottom-up starts with precursors at atomic or molecular state to assemble in nano-sized particles. In addition, depending on the desired application, nanoparticles need to be dispersed and stabilized in solvents. Their dispersibility and stability in different media depends on the synthesis method, the chemical nature of the particle, and their physico-chemical properties such as surface state, size and shape. Surface of the particles is the most flexible parameter that can be adjusted to adapt a particle in a media. Several surface modification techniques can be applied to adapt particles in the desirable media, and thus improve dispersability and stability without affecting the nanoparticles properties.

In this part, we are interested in the synthesis methods and particularly the Bottom-up approach. We will present examples of particles types that we are interesting on: oxides, phosphates and fluorides. Finally, we will focus on surfaces modification for biological applications, which result in water-soluble, stable and biocompatible nanoparticles.

### 1.1 Top-down approach

The breaking down of the bulk material into nanoparticles is performed using mechanical processes, to divide up bulk materials to nano-scale materials. Attrition or milling is a typical top-down method. The objectives of mechanical milling include particle size reduction, mixing or blending, particle shape changes and synthesis of nanocomposite<sup>128</sup>. Mechanical milling is a technique well developed towards the nanocrystalline structures. It is mainly a dry process at high-energy<sup>129</sup>, or using organic solvent and surfactant as the milling medium<sup>130,131</sup>, in which the basic powder (or pre-alloyed powder, oxides, nitrides, etc.) are crushed to obtain nanoparticles. This technique allows the production of several structures and microstructures including amorphous

alloys, meta-stable crystalline phases and nanocrystalline materials. Top-down methods process by introducing internal stress and result in particles with imperfection in the surface structure, random shape, impurities and heterogeneous chemical composition. These imperfections have a significant impact on physical properties and surface chemistry of nanostructure.

Here after, example of  $\text{Pb}(\text{Zr}_{0.52}\text{Ti}_{0.48})\text{O}_3$  nanoparticles prepared from the commercial  $\text{PbO}$ ,  $\text{TiO}_2$  and  $\text{ZrO}_2$  powders using the high-energy ball milling technique<sup>132</sup>.

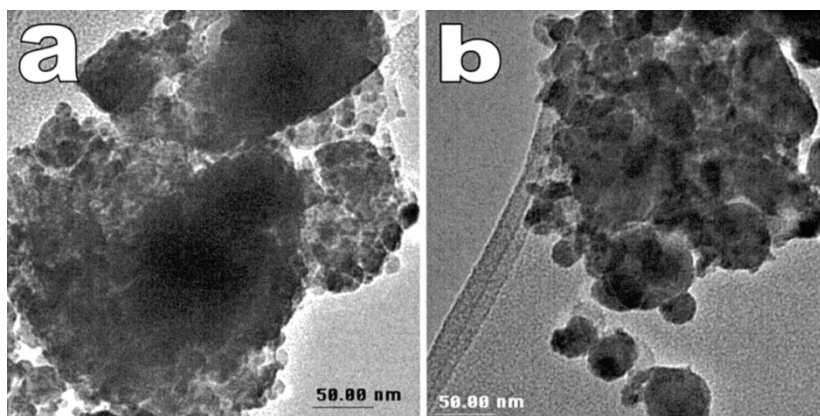


Figure II.1. TEM images of mixture milled for different times: (a) 20 h, (b) 40 h

On the contrary, bottom-up approach allows obtaining nanostructures with less defects with more homogeneous chemical composition and better short and long range ordering. This is because the bottom-up approach is driven mainly by the reduction of Gibbs free energy, thus the resulting nanostructures are in state closer to a thermodynamic equilibrium state<sup>133</sup>.

## 1.2 Bottom-up approach

Bottom-up approach consists in fabrication of nanoparticles atom-by-atom or molecule-by-molecule. The involved methods are mostly liquid phase synthesis techniques (colloidal chemistry). These techniques are particularly rich, both in term of the large number of compounds that can be fabricated and the flexibility of the processes which allow varying several numbers of parameters. The main advantages of these methods compared to top-down approach are low-cost methods, leading to uniform size distribution particles with control of morphology, several chemical composition and crystalline structure.

### 1.2.1 General mechanism

In liquid phase synthesis, mechanism of the formation of nanoparticles can be largely divided into three stages<sup>134</sup>: solid precursors' activation (1), nucleation (2) and particles growth (3). The first stage (stage I) consists in solubilization of the precursors which can precipitate at saturation, leading

to the nucleation stage (stage II). At this stage, precursors are consumed to form seeds. Nucleation is stopped when precursors' concentration becomes below saturation concentration, leading to growth stage (stage III). Stage II and III can be overlapped according to nature and reactivity of the precursors, synthesis media and methods. Polydisperse particles result mainly in this overlapping, because the growth of the first seeds overlaps to the formation of new seeds. To prepare particles with low size-dispersion, nucleation and growth stages should be separated.

Hereafter we present conventional techniques used for the synthesis of nanoparticles. We will then illustrate these methods by concrete examples of particles that can be developed by these techniques. We also highlight the advantages and limitations of each method for obtaining nanoparticles with various properties.

### 1.2.2 Synthesis techniques

#### ✓ **Co-precipitation**

Co-precipitation is one of the more used methods to synthesize nanoparticles. This method is widely developed for metal oxides. From aqueous salts solutions, metallic salts precipitate in presence of an alkaline compound. Precipitation is followed by germination and growth of particles. Iron oxide nanoparticles are usually prepared using this method. Size, shape, and composition of the particles depend on the type of the used salts (chlorides, sulfates or nitrates), the reactants ratio, the reaction temperature, the pH value and type of base. Today this method can be used for several materials such as compounds made of lanthanide phosphate<sup>135,136</sup>. Co-precipitation is a simple synthesis method; reaction temperature and time are lower than other methods such as thermal decomposition and hydrothermal. Also, solvent, usually water, is environmental friendly and the reaction yield is high and scalable. Size distribution is relatively narrow and the shape control is not better.

#### ✓ **Microemulsion**

Microemulsion is an isotropic and thermodynamically stable single-phase system that consists of three components: water, oil and an amphiphilic molecule (surfactant). Surfactant is important to lower the interfacial tension between water and oil resulting in the formation of a transparent solution. Water or oil nanodrop contains reagents as a nanoreactor. The nanodrop is surrounded by the surfactant molecules. It acts as cages for the growing particles and thereby reduce the average size of the particles during the collision and aggregation process. Thus, the size of the spherical nanoparticles can be controlled and tuned by changing the size of the micelles ( $W_0$  value: the water-to-surfactant molar ratio). Microemulsion is widely used for oxide particles such as silica,

titanium oxide<sup>137,138</sup> and also for lanthanide phosphate<sup>139</sup>. Microemulsion method allows obtaining monodispersed nanoparticles with various morphologies. However, this method requires a large amount of solvent, leads to amorphous particles and the reaction yield is low.

#### ✓ **Thermal decomposition**

Decomposition of organometallic precursors occurs at high-temperature using organic solvents and surfactants such as fatty acids. Principally the ratios of the starting reagents including organometallic compounds, surfactants, and solvents are the decisive parameters for controlling the size and morphology of the particles. The reaction temperature and time, as well as the aging period may also be crucial to control size and morphology<sup>140</sup>. Metal oxide<sup>141,142</sup>, sulfide<sup>143</sup> and quantum dot<sup>144</sup> can be synthesized with this method. Thermal decomposition is one of the best methods for size and morphology control of the particles. Also, the yield of production is high and scalable. However, one of the major disadvantages of this method is the production of organic soluble particles which limit the extent of application in biological fields. Then surface treatment is needed after synthesis. Also thermal decomposition methods require high temperatures.

#### ✓ **Hydro(solvo)thermal**

Solvothermal or hydrothermal when the solvent is water, is used to prepare several particles. Reaction occurs in an organic solvent or an aqueous media in reactors or autoclaves. Pressure is higher and temperatures usually higher than 200 °C. This method exploits the solubility of almost all inorganic substances in water at elevated temperatures and pressures and subsequent crystallization of the dissolved material from the fluid. The properties of the reactants, including their solubility and reactivity, change at high temperatures. Hydrothermal processing is one of the successful ways to grow crystals of many different materials. This is used to synthesize metal oxide particles such as Fe<sub>3</sub>O<sub>4</sub>, TiO<sub>2</sub><sup>145,146</sup>, lanthanide oxide<sup>147</sup>, lanthanide fluoride<sup>148,149</sup> and lanthanide phosphate<sup>150</sup> powder. The average particle size can increase with temperature and reaction time.

Microwave heating can be used during the hydrothermal synthesis because it increases the kinetics of crystallization<sup>151</sup>. The main advantage of the introduction of microwaves into a reaction system is the extremely rapid kinetics needed for synthesis. An increase in the reaction kinetics, up to two orders of magnitude, can be achieved by the microwave heating under hydrothermal conditions, due to the localized super heating of the solution. The microwave-assisted solution method is widely used today due to others advantages such as its rapid volumetric heating, higher reaction rate, reducing reaction time and increasing yield of products compared to conventional heating methods.

## 1.3 Examples of particles from conventional techniques

### 1.3.1 Synthesis of a metal oxide nanoparticles: TiO<sub>2</sub>

#### 1.3.1.1 Titanium dioxide applications

Titanium dioxide particles are of interest due to their unique properties and several potential technological applications. Titanium dioxide particles have found many important technological applications. It is used for anticorrosion, antimicrobial<sup>152,153</sup>, self-cleaning coating<sup>154,155</sup>, sensors<sup>156</sup>, solar cells<sup>157,158</sup> and photocatalysts<sup>159,160</sup>. The main applications of TiO<sub>2</sub> are due to its photo-activity properties. TiO<sub>2</sub> in the anatase phase is preferred as an photocatalyst for photodecomposition or solar energy conversion thanks to its high photoactivity<sup>161</sup> due to its lattice structure. Thanks to these technological applications, there are a lot of methods developed for TiO<sub>2</sub> preparation.

#### 1.3.1.2 Titanium dioxide preparations

TiO<sub>2</sub> exists in three polymorphic phases: rutile (tetragonal, 4.25 g/cm<sup>3</sup> of density), anatase (tetragonal, 3.894 g/cm<sup>3</sup>) and brookite (orthorhombic, 4.12 g/cm<sup>3</sup>). Both anatase and rutile have tetragonal crystal structures but belong to different space groups.

Sol-gel is one of the most common methods for TiO<sub>2</sub> and silica preparation<sup>162</sup>. It is based on the high chemical reactivity of the alkoxide<sup>158</sup> and titanium chloride<sup>162</sup> precursors toward hydrolysis that leads generally to aggregated particles, because of the lower charged surfaces or high ionic force. Peptization (increase surface charge) or dialysis (decrease ionic force) is required to separate the particles. A thermal treatment (reflux, hydrothermal, calcinations...) can be performed to improve crystallinity of the obtained particles. Hydrolysis of the titanium alkoxides precursors takes place with water or alcohols. Usually, a base is added to catalyze the precursor' hydrolysis. The mains stages of reaction are hydrolysis and condensation. Products purity, size control and homogeneity are the advantages of this method.

Micelles and inverse micelles are also used to synthesize TiO<sub>2</sub> nanomaterials<sup>137,163,138</sup>. Kim et al. studied the optimum experimental conditions for the preparation of TiO<sub>2</sub> nanoparticles.<sup>137</sup> He studied some parameters such as H<sub>2</sub>O/surfactant and H<sub>2</sub>O/titanium precursor ratio and ammonia concentration to control TiO<sub>2</sub> nanoparticles size and size distribution. Micelle method is also interesting for size control but leads usually to amorphous TiO<sub>2</sub> particles, which needs thermal treatment to be converted to crystallized phase.

Hydrothermal method can be used to enhance the crystallinity of amorphous or less crystallized particles from sol-gel method and micelle method<sup>164</sup>. This method is also used to synthesized crystallized particles from a peptized precipitates of a titanium precursor in water<sup>165</sup> or

from an aqueous solutions of titanium salts.<sup>166,162</sup> Precipitate from sol-gel method can be peptized and leads to different size and shape after hydrothermal treatment. Concentration of precipitate, the pressure and the autoclave degree of filling are the mains parameters for particles size and shape control. Solvothermal method is similar to the hydrothermal method except for the employed solvent (nonaqueous) and the temperature can be elevated higher than that of hydrothermal method, since a variety of organic solvents with high boiling points can be chosen.

### **1.3.2 Synthesis of lanthanide phosphate (LnPO<sub>4</sub>)**

#### **1.3.2.1 Lanthanide phosphate nanoparticles applications**

Here the term "phosphate" is used for orthophosphate LnPO<sub>4</sub>. Several other phosphate compounds have been identified in Ln<sub>2</sub>O<sub>3</sub>-P<sub>2</sub>O<sub>5</sub> systems<sup>147</sup>, including metaphosphates, such as Ln(PO<sub>3</sub>)<sub>3</sub> and pentaphosphates (LnP<sub>5</sub>O<sub>14</sub>)<sup>167</sup>. Lanthanide phosphate (LnPO<sub>4</sub>·nH<sub>2</sub>O) is useful for new wet sensor, phosphor<sup>167</sup> and refractory material due to their chemical and physical properties. Furthermore, lanthanide phosphate is useful for a host material making a composite with other lanthanide ions. The doped lanthanide salts, (La,Ce,Tb)PO<sub>4</sub>, are widely used as green-emitting phosphor for energy-efficient fluorescent and lighting<sup>168,169</sup>. Recently gadolinium phosphate particles are developed as MRI contrast agent<sup>170,171</sup>. Then preparation of monodisperse particles is necessary for this application.

#### **1.3.2.2 Lanthanide phosphate nanoparticles preparations**

Lanthanide orthophosphates LnPO<sub>4</sub>·nH<sub>2</sub>O ( $n = 0-3$ ) (Ln<sup>3+</sup> = lanthanide ion) have different structure: monazite (monoclinic), xenotime (tetragonal), rhabdophane (hexagonal), weinschenkite (monoclinic). The following Table II.1 lists the crystalline species identified. The degree of hydration for the rhabdophane-type is variable. The monazite and xenotime structures have exceptional thermal stabilities compare to other phases. Several phosphates complex decompose to the orthophosphate on heating such as La<sub>5</sub>PO<sub>14</sub> => La(PO<sub>3</sub>)<sub>3</sub> => LaPO<sub>4</sub>. LnPO<sub>4</sub> compounds can be prepared by precipitation<sup>123,135,136</sup> from aqueous solution of lanthanide salt (chloride, oxide, nitrate or carbonate) and phosphate source such as phosphoric acid or ammonium phosphates. The used lanthanide-containing chemicals Ln(OH)<sub>3</sub>, LnCl<sub>3</sub><sup>135,172</sup>, Ln<sub>2</sub>O<sub>3</sub><sup>150,173</sup>, Ln<sub>2</sub>(CO<sub>3</sub>)<sub>3</sub>, Ln(NO<sub>3</sub>)<sub>3</sub><sup>139,170,174</sup> react with the phosphate sources H<sub>3</sub>PO<sub>4</sub><sup>174,175</sup>, NaH<sub>2</sub>PO<sub>4</sub><sup>139</sup> and (NH<sub>4</sub>)<sub>2</sub>HPO<sub>4</sub><sup>124</sup>.

Many preparation methods have been developed, such as solid state reactions<sup>176</sup>, spray pyrolysis<sup>177</sup>, combustion synthesis<sup>173</sup>, sol-gel techniques<sup>178,179</sup>, coprecipitation<sup>180</sup>, mechanochemical methods<sup>181</sup> and hydrothermal synthesis<sup>182</sup> to prepare high quality LnPO<sub>4</sub> nanoparticles.

**Table II.1. Name and crystalline structure of some lanthanide orthophosphates**

Lanthanide orthophosphates				
Lanthanide	Compound	Name as mineral	Structure	Stability
La to Gd	$\text{LnPO}_4$	monazite	monoclinic	Stable to 2000 °C
Dy to Lu, Y	$\text{LnPO}_4$	xenotime	tetragonal	Stable to 2000 °C
La to Gd	$\text{LnPO}_4, 0.5 \text{ H}_2\text{O}$	rhabdophane	hexagonal	Converts to monazite around 500 °C
Dy to Lu, Y	$\text{LnPO}_4, 0.5 \text{ H}_2\text{O}$	weinschenkite	monoclinic	Converts to xenotime around 500 °C

Hydrothermal synthesis is a versatile tool for the preparation of narrow particle size distribution and uniform morphology. It is known for the preparation of high-crystalline powders at mild temperature.

The main method is a classical hydrothermal or in presence of complexing lanthanide agent<sup>183</sup>, micro emulsion system<sup>139</sup>, or reflux methods<sup>167</sup>. Morphology of the lanthanide phosphates is related to their crystal structures, the preparation method and the ionic radius. Lanthanide phosphates nanoparticles with the larger ion centers are in monoclinic and hexagonal structure. In classical hydrothermal conditions (without complexing lanthanide agent) these particles grow anisotropically to form rods shape particles contrary to tetragonal which form sphere-shaped particles. Figure II.2<sup>184</sup> shows crystal structure of hexagonal  $\text{CePO}_4$ . Each cerous ion is coordinated to eight oxygen atoms; the phosphate group is coordinated to six cerous ions. This structure is described as columns built up of alternate cerous and phosphate ions, extending along the *c* axis, and each column linked to four neighboring columns<sup>185</sup>. Yue-Ping Fang et al.<sup>184</sup> described this structure as infinite linear chains, parallel to the *c* axis. They postulate that from a thermodynamic perspective, the activation energy for the *c* axis direction of growth of hexagonal  $\text{LnPO}_4$  is lower than that of growth perpendicular to the *c* axis<sup>186</sup>. And this means a higher growth rate along the *c* axis and a lower one perpendicular to the *c* axis, to form  $\text{LnPO}_4$  nanorods that grow preferentially along [001] direction.

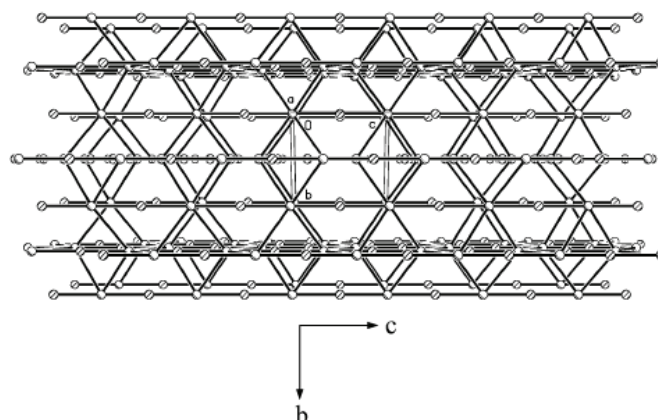


**Figure II.2.** Packing view of  $\text{CePO}_4$  along the  $a$  axis. Each column is built up of alternate cerous (shadow circles) and phosphate ions (open circles) and extends along the  $c$  axis. Oxygen atoms are omitted for clarity.

The anisotropic growth of nanocrystals has been shown to be strongly dependent on relative chemical potentials<sup>187,188</sup>. Ruoxue Yan et al<sup>189</sup> demonstrated it in case of lanthanide phosphate. They have successfully synthesized rod-shape particle of  $\text{LnPO}_4$  (Dy to Lu), in tetragonal structure which is supposed to don't have a preferred growth direction and to form spherical particle, according to the Yue-Ping Fang et al.<sup>184</sup>prevision. These nanocrystals obtained when  $\text{Ln}^{3+}$  was complexed with ethylenediamine tetra-acetic acid (EDTA) at various concentration prior to precipitate with  $\text{PO}_4^{3-}$ . They show that on increasing the amount of EDTA present in the original hydrothermal environment, the morphology of the nanocrystals varies from spherical to nanorods, related to increasing oriented growth. Several scientists show that the aspect ratio of the  $\text{LnPO}_4$  nanorods can be reduced in the alkaline environment<sup>123,150</sup>. Mainly because the  $\text{Ln}^{3+}$  ions are prone to precipitation as the hydroxide at higher pH values and their chemical potential is thereby reduced<sup>189</sup>. In an alkaline environment, when  $\text{Ln}^{3+}$  ions are chelated at the beginning (by a ligand), the precipitation of these cations by  $\text{OH}^-$  are suppressed, and their chemical potential is thereby increased, promoting the anisotropic growth.

### 1.3.3 Synthesis of lanthanide fluoride ( $\text{LnF}_3$ )

#### 1.3.3.1 Rare earth fluoride applications

Rare earths are the fifteen lanthanides plus scandium and yttrium. Rare earth fluoride nanoparticles have attracted more attention, due to the fact that they present great electronic, chemical, and optical characteristics because of the 4f electrons, combined with a good stability, thanks to the fluoride anions. These properties make them interesting systems for applications in fields such as biotechnology or optics. Thus rare earth fluoride nanoparticles were used for x-rays therapy<sup>190</sup> thanks to the capacity to absorb X-rays and emit visible light and for fluorescence

imaging<sup>191,192</sup>. Lanthanide fluoride particles were also developed as MRI contrast agents<sup>193,194</sup> for radio-opacity<sup>195</sup>, nanophosphors<sup>196,197</sup> and scintillators<sup>198,199</sup>.

However, today rare earth fluorides are much less developed compared to rare earth oxide and remain problematic to achieve.

### 1.3.3.2 Rare earth fluoride nanoparticles preparations

Development of solution phase based methods such as thermal decomposition and solvothermal reaction allowed a great progress in the synthesis of fluoride rare earth with size and shape control. Here a brief description of some methods.

Inspired by the synthesis of high-quality semiconductor nanocrystals and oxides, rare earth fluoride nanoparticles were synthesized in non-aqueous media by thermal decomposition process. This process involves organics precursors in high-boiling organic solvents in the presence of surfactant. Decomposition of the precursors occurs in high temperature<sup>140</sup>. The most organometallic precursor used is trifluoroacetate in octacene as solvent without surfactant<sup>200</sup> or with oleic acid and oleylamine as surfactant<sup>201</sup>. Thermal decomposition of trifluoroacetate precursors at 300 °C under argon was used to achieve hydrophobic particles of fluoride and oxyfluoride nanocrystals<sup>201</sup> through the mechanism proposed by sun et al<sup>201</sup>. In addition to the fact of requiring hard synthesis conditions, this method is limited to the preparation of hydrophobic particles.

Hydro and solvothermal reaction involves the dissolution of the lanthanide and fluoride precursors in water or other solvent at elevated temperature and pressure and subsequently crystallizing the dissolved materials from the fluid. This method can lead to the water dispersible particles<sup>192</sup>. An appropriate organic additive with functional groups acts as complex agent or structure-directing can be used to control the shape and size of the particles. Reaction temperature is relatively low, usually less than 250 °C. The commonly used organic additives for the fabrication of rare earth fluorides are oleic acid<sup>148</sup>, ethylenediamine tetraacetic acid (EDTA)<sup>202,203</sup>, cetyltrimethylammonium bromide (CTAB)<sup>204</sup>, and trisodium citrate (TSCi)<sup>205,206</sup>. Concentration of the precursors, complex agent and temperature and time of thermal treatment influences the size, shape and crystalline structure of the particles<sup>206</sup>. For example NaF/Ln ratio is important for the crystallization and the structure of the particles. When the ratio increases, crystallinity of the nanoparticles is improved with more regular shape and smoother surface. Structure change from cubic to hexagonal. This process use NaF as a fluoride source and involve the incorporation of sodium ions (Na<sup>+</sup>) into the matrix of Ln-F to form a lanthanide/sodium fluoride mixture (NaLnF<sub>4</sub>) for Ln = Eu to Lu<sup>207</sup>. To obtain a pure lanthanide fluoride, Li et al.<sup>207</sup> use lanthanide chloride, NaBF<sub>4</sub> and trisodium citrate as respectively lanthanide and fluoride source and complex agent. They obtain different morphology, spherical excepted.

Ionic liquids based synthesis is a solvothermal process using an ionic liquid (IL) as co-solvent, template or reactant. ILs are non-volatile, non-flammable and thermally stable organic salts. The main advantages of using ILs as solvents or additives in inorganic synthesis is their superior capability for the dissolution and stabilization of metal cations, which gives them the possibility of acting as capping agents or surfactants. In the synthesis method developed by zand and Guo<sup>208</sup>, [bmim]BF<sub>4</sub> ((1-butyl-3-methylimidazolium tetrafluoroborate) was added to the Ln(NO<sub>3</sub>)<sub>3</sub> solution and treated in autoclave. Fluoride anions are provided by BF<sub>4</sub><sup>-</sup> anions from the ILs<sup>209,210</sup>. When the temperature of [bmim]BF<sub>4</sub> IL solvent exceeds its boiling temperature, it decomposes. The BF<sub>4</sub> anions undergo fast hydrolysis: BF<sub>4</sub><sup>-</sup>(IL) + H<sub>2</sub>O → BF<sub>3</sub>·H<sub>2</sub>O (IL) + F<sup>-</sup>. The main limit of this method is the larger particles size estimated at 500 nm. Different nanosized metal fluorides (oval shaped) were synthesized by Jacob et al. (FeF<sub>2</sub>, CoF<sub>2</sub>, ZnF<sub>2</sub>, LaF<sub>3</sub>, YF<sub>3</sub>, and SrF<sub>2</sub>) via a general microwave-assisted ionic liquid route, however they obtained products contain carbon as impurity<sup>210</sup>.

Coprecipitation method was also developed to produce rare earth fluoride. An example of polyol method<sup>196,211</sup> consists in heating a mixture of Ln(NO<sub>3</sub>)<sub>3</sub> and NH<sub>4</sub>F in diethylene glycol (DEG) in a oil bath under argon. Small (10 nm) and bigger (100 nm) particles are obtained according heating time but they are heterogeneous shape. Coprecipitation in aqueous phase was employed<sup>212,213,214</sup>. Lanthanide source is dissolved in polar solvent (water and alcohol), mixed to fluoride source and heat (90 -200 °C) for several days. This method takes too much time.

Some of these methods need post-heat treatment, lead to hydrophobic and mixed particles, and have very toxic by-products. They are also hard to scale up and expensive. We develop in the lab a process involving rare earth salts and a solvent able to form a charge transfer complex with a fluorinated acid at low temperature, leading to highly crystallized and monodisperse nanoparticles. Details of this method are discussed in the experimental section and in our previously published work<sup>215</sup>.

## 1.4 Colloidal stability and surface modification

### 1.4.1 Colloidal stability of the suspension

Previously, we have described the mechanism of particle growth by three main stages, the precursors' activation, germination and growth. However after this last stage, colloidal system is not systematically at equilibrium. The formed particles can change to minimize their surface energy and tend to thermodynamically stable systems. Two phenomena can occur: the Ostwald ripening (1) corresponds to the transport of material, i.e. the smallest particles move into larger, leading to the increase in the average size of the initial particles. Initial particles aggregation (2) leads also to larger

particles. The used techniques to stabilize the particles in solution are based on the control of the interaction of the particles with each other.

#### 1.4.1.1 Attractive and repulsive forces

Stability of particles in solutions is described by the DLVO theory<sup>216,217</sup> (Dejarguin, Landau, Verwey and Overbeek). This theory is based on the balance between two opposing forces responsible of stability or flocculation of colloidal suspension: attractive and repulsive forces<sup>218</sup>.

##### ✓ **Attractive forces (Van- der-Waals forces):**

Van- der-Waals forces result from dipole fluctuations at molecular level and depend on the nature of the materials and the distance between particles. Detail on this attraction energy variation is described by Jolivet<sup>219</sup>. Between two particles with radius  $R$ , and  $r$  the distance between particles' centers, the interaction potential is:

$$V(r) = -\frac{A}{6} \left[ \frac{R^2}{r^2 - 4R^2} + \frac{2R^2}{r^2} + \ln\left(1 - \frac{4R^2}{r^2}\right) \right]$$

$A$  is the Hamaker constant, characteristic of material.

##### ✓ **Repulsive forces (electrostatic repulsion):**

Electrostatic repulsion results in the charge present on the surface of the particles due to adsorption of one type of ions. In fact, this repulsion force is due to the Coulomb repulsion and especially to the electric double layer made of counter-ions. The first layer (Stern layer) is made of ions with a particular affinity to the surface. Because they strongly interact with the surface, they preserve the local order and are therefore closer to the surface. In the second layer (diffuse layer) the counter-ions are attracted from the surface but interaction is weaker and the layer is subject to thermal movement.

#### 1.4.1.2 Stabilization of the colloidal suspension

##### ✓ **Electrostatic stabilization:**

Van der Waals forces coupled to the Brownian motion are the origin of flocculation of colloids. For stable suspensions, could be used charged particles. In a polar medium such as water, ion-pairs dissociate and counter-ions with charged surfaces form an electrochemical double layer, resulting in an electrostatic repulsion of the particles leading to stabilized suspension. The DLVO theory describes the balance of attractive and repulsive interaction (Figure II.3). The total interaction between two particles electrostatically stabilized, is the combination of van der Waals attraction and electrostatic repulsion. The electrostatic repulsion leads to an energy barrier that prevents the

particles to move closer to the distance where the attractive Van der Waals interactions are strong. Thus, Van der Waals forces are decreased and the system is dominated by the repulsive forces.

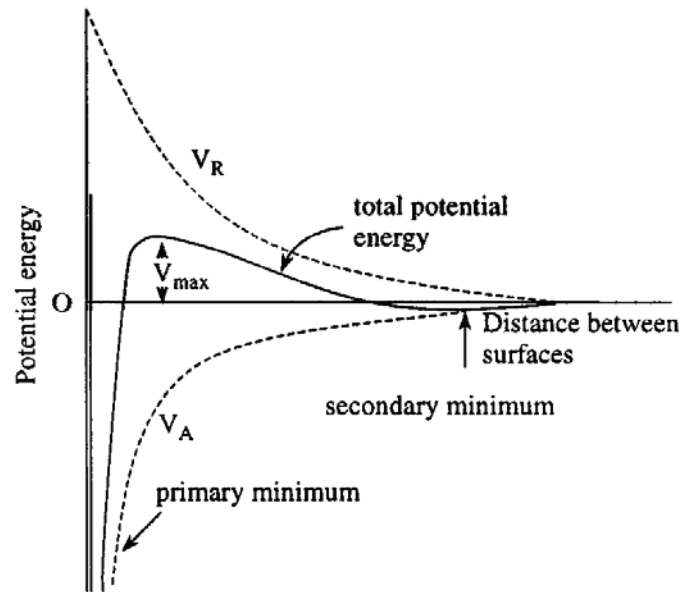


Figure II.3. Total interaction resulting in the combination of van der Waals attraction and electrostatic repulsion;  
 $V_A$  = attractive van der Waals potential and  $V_R$  = repulsive electrostatic potential

Electrostatic stabilization has certain limitations. It is a kinetic stabilization method employed for diluted system and hard to apply to multiple phase systems, because of different surface charge and electric potential of different solid in a given condition. Electrostatic stabilization can be applied only to particles with sufficiently charged surface and to solvent with sufficient dielectric constant to allow counter-ions moving to the vicinity of the surface of the particles.

✓ **Steric stabilization:**

The steric stabilization is an alternative method, which consists in adsorption or grafting of macromolecules at the surface of the particles, thus preventing the particles to come closer because of steric hindrance, limiting Van-der-Waals attraction. The absorbed macromolecules must be soluble in the desired solvent to repel one another and generate the repulsive force between particles. The steric repulsion is the result of osmotic effect due to high concentration of macromolecule in a limited region and the volume restriction from the conformations of the macromolecules. This technique needs an active surface for reversible or irreversible adsorption, and has several advantages such as there is a thermodynamic stabilization method, thus the particles are always dispersible, a very high concentration can be accommodated, and it is suitable to multiple phase systems.

### 1.4.2 Surface modification for biological applications

For biological applications, the preferred colloidal stabilization strategy is the steric repulsion. Today, beyond notion of stabilization, functionalization is used to bring new properties to the particles. This can be water-solubility (1), biocompatibility (2) or other functions such as fluorescence (3), magnetic properties (4) and targeting probes (5). A general structure of how various particles can be functionalized is presented below (Figure II.4). There are therefore four different parts with various functions: surface passivation (P), anchoring group (C), spacer (R) and functional group (F).

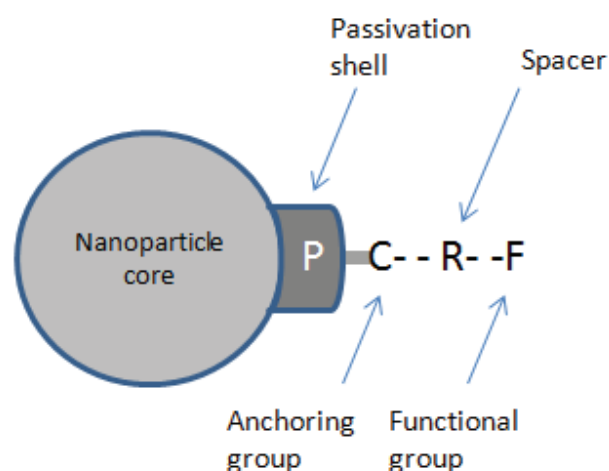


Figure II.4. Strategy for nanoparticles functionalization, see examples in Table II.2

Table II.2. Examples of modified nanoparticles for biological applications

NP	P	C	R	F	Ref
Fe <sub>2</sub> O <sub>3</sub>	-	Succinimidyl ester	PEG	Aβ <sub>40</sub>	220
Fe <sub>2</sub> O <sub>3</sub>	Silica	Thioisocyanate	-	Dye	221
Fe <sub>2</sub> O <sub>3</sub>	Au	-	-	-	222
MnO	Silica	Silane	-	PEG	223
Ag	Silica	-	-	-	224
Fe <sub>2</sub> O <sub>3</sub>	-	Phosphonate	-	Dye	225
Fe <sub>2</sub> O <sub>3</sub>	-	Carboxylate	-	Dye	225
Gd <sub>2</sub> O <sub>2</sub>	-	Carboxylate	-	PEG	226
SiO <sub>2</sub>	-	Carboxylate	Alkyl	DOTA-Gd(III)	227
ZnO <sub>2</sub>	-	Phosphoric acid	Alkyl	DOTA-Gd(III)	227
TiO <sub>2</sub>	-	Phenyl alcohol	Dopa mine	DOTA-Gd(III)	228
Au	-	thiol	-	PEG	229
Au	-	thiol	-	Polystyrene	230
GdF <sub>3</sub>	-	Carboxylate	-	Poly(acrylic acid)	194

#### 1.4.2.1 Surface passivation

Passivation is defined here as coating of nanoparticles by an inorganic shell made of other material, chemically different to confer new properties. The targeted properties are usually biocompatibility, stability in water and preparation for post-functionalization. Silica is the most used coating shell. Due to negative charge on the surface of silica, iron particles were coated with silica to obtain a core-shell particles as a very stable colloidal suspension without using surfactant<sup>221</sup>. In the obtained core-shell particles can be incorporated in silica shell an organic dye to make magnetic and fluorescent nanoparticles<sup>221</sup>, or graft an amine ended polymer for DNA separation application<sup>231</sup>. The interest of the silica is also based on the possibility of using the anchoring functions that react with amine on its amino surface, such as thiocyanate<sup>221</sup>. This method is also used to coated metallic particles such as gold<sup>232,222</sup>, silver<sup>224</sup> and MnO<sup>223</sup>. Gold coated iron particles was also prepared<sup>222</sup>.

#### 1.4.2.2 Anchoring group

The most commonly used particles for biomedical applications include iron oxide, silica and gold particles<sup>233</sup>. Functionalization techniques are initially adapted to these particles, essentially oxide and metallic particles. Today these developed techniques are extended to other materials families and more anchoring groups were developed to optimize the grafting. Typically, anchoring group must respect some requirements:

- They must contain a leaving group able to form a stable compound with proton or metal ion from the particle surfaces
- The anchoring group should have a valance of at least of two to be bound both to grafted molecule and the particle surface.
- The reaction between the group at the surface particle and the anchoring group should proceed faster
- The formed chemical bound must be stable under operational and storage conditions.

The main coupling agents that meet this requirements and used to attach the desired molecules to the particles surface are carboxylate groups<sup>225,234</sup>, silane derivate<sup>235,236,237</sup>, thiol<sup>238,229,239</sup> and more recently phosphonate<sup>225,240,241,242,243</sup>. Thiol groups are mainly used to stabilize and functionalized gold<sup>229,239,244</sup> and silver particles<sup>244,245</sup>. In the presence of thiols, Au(III) is reduced to Au(I) by oxidizing the thiols to disulfides. If more than 2 equiv of thiol are present, the resulting Au(I) and excess thiol will combine in an Au(I)-thiolate complex<sup>246</sup>. In the presence of some reducer such as sodium borohydride, all gold species present are reduced to clusters of gold atoms surrounded by thiolates. They were also developed for semiconductor particles<sup>247</sup> and silica particles<sup>248,249</sup>.

Organosilicon compounds are mainly used for silica particles surface modification and other oxide metallic compounds<sup>250,235</sup>. The interaction of these groups with the surface hydroxyl groups of the particles results in the formation of a hydrolytically stable system of chemical bonds M-O-Si-C, with M a metallic atom.

Carboxylate group is certainly the most used anchoring group to modify various surfaces particles. Vittadini et al.<sup>251</sup> showed that chemisorption at oxides particles through COOH groups can occur through a variety of binding modes (Figure II.5). One is prevalent depends on the structure of the molecule, the binding groups, the pH and the particles preparation<sup>251</sup>.

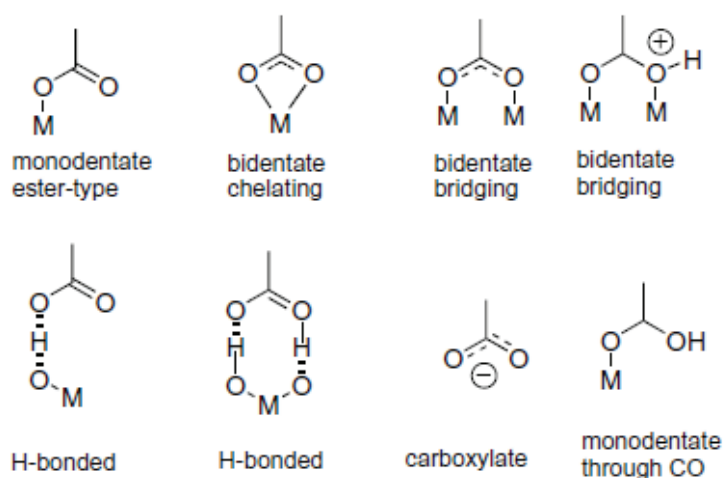


**Figure II.5. Possible binding modes of carboxylate group to metal oxide surface**

Phosphonate group has been first involved in self-assembled monolayers (SAM) formation on metallic and metal oxide surfaces as protective films or for biomedical applications<sup>252,241</sup> and recently in the grafting of bioactive molecules<sup>253,254</sup>. Phosphonate group is used as a coupling agent and provides a covalent grafting and a high recover rate of organic molecules at the surface. This covalent grafting and stability in aqueous media lead to the development of nanoparticles functionalization with phosphonates groups for medical applications.

The interaction of phosphonic acid with silica was studied<sup>255,256,257</sup>. Boiling silica with phosphonic acid in certain organic solvent such as chlorobezen, results in grafting of the acid to the surface. The granulo- metric composition of the support remained unchanged after modification and the grafted layer is hydrolytically stable in a neutral medium. The grafting density decreases after storage of the modified samples in distilled water for several days at room temperature; however, its stability in acidic and alkaline media is much lower. Phosphonic acids interact with the silica surface much less readily than with the surfaces of most metal or metallic oxide.

Phosphonic acids offer several advantages in the modification of other particles surface such as metallic oxide. It is first due to the presence of strong acid sites on the surface, which significantly facilitates the donor-acceptor interaction of phosphoryl group with the Lewis acid sites. This interaction makes the phosphorus atom more electrophilic and facilitates reaction between the molecule and the surface hydroxyl groups.

For example close to room temperature, treatment of  $\text{TiO}_2$  surface with phosphonate leads to the coordination of the phosphoryl oxygen atom to acid sites of the oxide surface followed by condensation of P-OH and Ti-OH groups. Modification of  $\text{TiO}_2$  with phosphonic acid derivate under severe conditions such as boiling in water or toluene at higher temperature, results in the formation of a bulk phase of titanium phosphonate<sup>252</sup>. Photolysis of P-C bonds on the surface of the modified particles under the action of soft UV radiation (350 nm) was also investigated<sup>252</sup>. It was found that irradiation of the samples placed in water causes cleavage of the P-C bonds whereas these bonds are retained upon irradiation of the samples placed in toluene. However, most of the experiments indicate a strong fixation of phosphonate group on the particles via a bidentate or tridentate bonds.

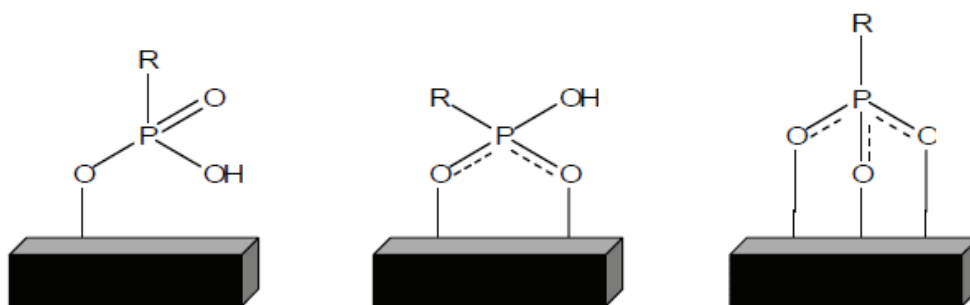


Figure II.6: possible binding modes of phosphonate group on surface particle

Due to the efficiency surface modification of several particle, the facile formation and the stability of M-O-P bounds (Figure I.6), organophosphorus coupling molecules are highly attractive<sup>258</sup>. They are the best anchoring groups for metal oxides followed by carboxylic acids and their derivatives, such as esters, acid chlorides, carboxylate salts, or amides<sup>259</sup>.

Few investigations have been conducted on bisphosphonate group<sup>260,261</sup> and demonstrate a real interest on this molecule which seems to be higher than that of phosphonate thanks to presence of two phosphonate group per molecule. The most interesting investigation from Yoann Lalatonne et al. compares bisphosphonate and carboxylic group. They demonstrate clearly that the more interesting fixation moiety is bisphosphonate<sup>261</sup>.

### 1.4.2.3 Spacer and functional group

Spacer is used to separate particle to the functional group to prevent interactions and then conserve the properties of each. It can separate an inert, fluorescent, magnetic or radioactive particle to an organic, fluorescent or magnetic probe for example. In biological applications particles are usually in aqueous media and in contact with biological organisms. Thus the first properties of these spacers are hydrophilicity and biocompatibility. Also they have to be capable to reduced uptake by reticulo-endothelial system (RES) and enhanced retention time. Polyethylene glycol (PEG)<sup>262,263</sup>, polyvinyl alcohol (PVA)<sup>264,112</sup>, poly(acid methacrylique) and or dextran<sup>123</sup> are the most used particles.

Depending on the application, spacer and functional group can be confused. For the magnetic particles used as magnetic contrast agent such as pegylated  $Gd_2O_3$ <sup>265</sup>; functionalization with organic molecules such as PEG that brings the above mentioned properties, can be considered as a functional group. Also PEG can be used as spacer to support a functional group, such as a fluorescent molecule, magnetic and targeting moieties. The main used magnetic moieties are chelated gadolinium<sup>266</sup> and targeting moieties are classified as proteins, peptides, nucleic acids or small molecules<sup>266</sup>.

The next section is devoted to the particles preparation and functionalization. The employed methods will be discussed and experiment detailed. Characterizations of the obtained nanoparticles will be discussed further.

## 2 DEVELOPMENT OF NEW MAGNETIC CONTRAST AGENTS

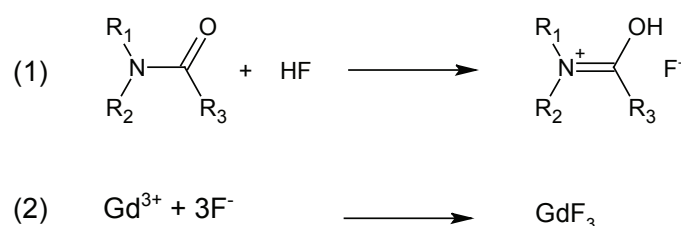
In this section, different types of inorganic crystalline nanoparticles are prepared, namely gadolinium fluoride, gadolinium phosphate and titanium oxide. The obtained particles will be characterized and afterwards functionalized to lead to efficient magnetic contrast agent. The obtained modified particles are divided into three types according to their structure and morphology. There are (1) isotropic system made of pegylted sphere-shaped gadolinium fluoride, (2) anisotropic system made of pegylated rod-shaped gadolinium phosphate and (3) core-shell system made of DOTA-Gd(III) coated titanium oxid particle.

The process of synthesis and functionalization are discussed here, following by physico-chemical characterizations of the prepared products.

## 2.1 Isotropic system: spherical gadolinium fluoride nanoparticles (GdF<sub>3</sub>)

### 2.1.1 Synthesis method

As mentioned previously, literature's methods for lanthanide fluoride synthesis present inconvenience such obtaining mixed fluorides or hydrophobic particles. We recently published our method<sup>215</sup> adapted for all rare earth fluoride particles. Here we will focus on gadolinium particles. This process involves rare earth salts and a solvent, able to form a charge transfer complex with a fluorinated acid. Usually the reaction process by heating in a balloon or schlenk tube connected to a condenser at atmospheric pressure (reflux heating). Several tests are conducted including change of the amide solvent (N,N-diméthylformamide (DMF) and N-méthyl-2-pyrrolidone (NMP)), heating time (few minutes to several hours) and temperature (from room temperature to 200 ° C), before to find the ideal conditions. During this synthesis, rare-earth chlorides were used as Ln(III) ions source and hydrofluoric acid as a fluoride source. Scheme II.1 shows reactions that happen in this synthese, in the specific case of gadolinium fluoride.



**Scheme II.1.** Reaction between an amide and HF leads to a charge transfer complex. In the case of DMF, R<sub>1</sub>=R<sub>2</sub>=CH<sub>3</sub>, R<sub>3</sub>=H.

The solvent forms a charge transfer complex with the fluorinated acid (1) and this charge transfer complex reacts at relative low temperature bellow 170 °C, with the rare earth salts (2) to grow small particles of fluoride in the nanometer scale (10-15 nm). The main used solvents are N,N-dimethylformamide (DMF) and N-methyl-2-pyrrolidone (NMP).

In the reflux method, reactions are carried out at relatively low temperatures (70 °C for DMF and 170 ° C for NMP) and the process is easily reproducible. One of the disadvantages of this method is therefore the HF handling, and also particles do not always have well-defined shape and sometimes less crystallized. To improve the crystallinity, we tested other heating conditions, such us solvothermal and microwave methods.

We are interested in the solvothermal method to take advantage of the pressure and temperature conditions. The mixture is put into autoclave, and placed in oven at 170 ° C under agitation. The heating and stirring are maintained for 3 h.

Microwave heating was also tested for the synthesis of lanthanide fluoride nanoparticles. The reaction mixture is identical to the reflux method. The heating time is extremely low and reaction occurs in a 20 mL glass reactor. Tests were performed for 1 min at 200 ° C and 3 min at 170, 80 and 50 ° C.

### 2.1.2 Experimental conditions

#### ✓ Reflux method

In a typical synthesis, 0.45 g of hydrofluoric acid (9 mmol HF) is mixed with 16 mL of N-methyl-2-pyrrolidone (NMP). A solution of 1.49 g (4 mmol) of  $GdCl_3 \cdot 6 H_2O$  in 3 ml of methanol is slowly added under stirring. A transparent solution is obtained. This solution is heated at 170 °C for 16 hours; to induce the anion exchange, nucleation and growth of nanoparticles. A stable colloidal suspension is obtained. The resulting suspension is purified through precipitation in acetone, centrifuged at 8000 rpm for 10 minutes and the supernatant was discarded. This step was repeated 3 times and then the precipitate was dispersed in distilled water (5 mL).

#### ✓ Solvothermal method

In a typical synthesis, 0.9 g of hydrofluoric acid (18 mmol HF) is mixed with 32 mL of N-methyl-2-pyrrolidone. A solution of 2.98 g (8 mmol) of  $GdCl_3 \cdot 6 H_2O$  in 6 ml of methanol is slowly added under stirring. 55 ml of the obtained transparent solution is put into an 80ml Teflon-lined stainless autoclave (filled at 70 %) and heated at 170 °C for 3h. Then solution is cooled at room temperature. The resulting suspension is purified through precipitation in acetone, centrifuged at 8000 rpm for 10 minutes and the supernatant was discarded. This step was repeated 3 times and then the precipitate was dispersed in distilled water (10 mL).

#### ✓ Micro-wave

In a typical synthesis, 0.45 g of hydrofluoric acid (9 mmol HF) is mixed with 16 mL of N-methyl-2-pyrrolidone (NMP). A solution of 1.49 g (4 mmol) of  $GdCl_3 \cdot 6 H_2O$  in 3 ml of methanol is slowly added under stirring. A transparent solution is obtained. The resulting solution is put into 20 mL glass reactor and heated at desired temperature for desired time. Then solution is cooled at room temperature. The resulting suspension is purified through precipitation in acetone, centrifuged at 8000 rpm for 10 minutes and the supernatant was discarded. This step was repeated 3 times and then the precipitate was dispersed in distilled water (10 mL).

## 2.2 Anisotropic system: gadolinium phosphate nanorods (Gd<sub>1-x</sub>La<sub>x</sub>PO<sub>4</sub> and GdPO<sub>4</sub>)

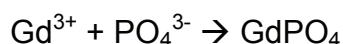
### 2.2.1 Synthesis methods

GdPO<sub>4</sub> and Gd<sub>1-x</sub>La<sub>x</sub>PO<sub>4</sub> nanoparticles were synthesized according to the method from Wang et al.<sup>135</sup> (reflux) and GdPO<sub>4</sub> in different size according to the method from Hifumi et al.<sup>123</sup> (hydrothermal). These co-precipitation methods are interesting because they are versatile, environmentally-friendly and don't need high temperature. They result in relative narrow particle size distribution and uniform morphology. Also, they can be easily adapted to prepare doped particles, with different chemical composition and morphology to study the influence of these parameters on physicochemical properties including relaxivity.

#### ✓ Reflux method

We synthesized pure gadolinium phosphate (GdPO<sub>4</sub>) and lanthanum doped gadolinium phosphate (Gd<sub>1-x</sub>La<sub>x</sub>PO<sub>4</sub>) at the theoretical doping values of (0; 0.25; 0.50; 0.75 and 1.00). These doped nanoparticles were prepared in order to dilute gadolinium atom per particles and minimize Gd-Gd interactions and thus impact directly on the magnetic properties.

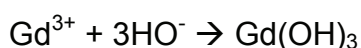
By adding the aqueous solution of phosphate precursor in that of lanthanide precursor, the resulting solution is very acidic (pH =1). Then the solvated lanthanide ion reacts rapidly with phosphate to form a white precipitate:



This precipitate crystallizes at moderate temperature (70 °C) even for relatively short reaction time. We observed that for better crystallized particles, 1 H reaction time was sufficient. For reproducibility, all syntheses were conducted for 5 H. A typical synthetic procedure to produce gadolinium phosphate nanorods will be briefly described below.

#### ✓ Hydrothermal method

As mentioned previously, this reaction depends strongly on the pH. Thus, the aspect ratio of the GdPO<sub>4</sub> nanorods can be reduced according to pH, which influences chemical potential of the lanthanide ion. Then in alkaline environment, Gd<sup>3+</sup> precipitates as Gd(OH)<sub>3</sub> reducing chemical potential and leading to lower aspect ratio particles. By controlling pH (1, 6, 9 and 12) of solution, we synthesize particles with different size. The reaction involves in the first step the precipitation of the kinetically favored hydroxide Gd(OH)<sub>3</sub>.



This gadolinium hydroxide, in the second step, reacts with phosphate ions to form thermodynamically stable GdPO<sub>4</sub>.



The hydrothermal reaction occurs in a capped glass pressure tube. At pH 9 and 12, solution are sufficiently alkaline to precipitate a large amount of Gd<sup>3+</sup>, consequently reaction yield are lower compared to acidic pH. This reaction formed a solid Gd(OH)<sub>3</sub> as by product that can be dissolved at acidic pH. Then the resulting suspension is dispersed in acidic aqueous solution (pH=1) to dissolve Gd(OH)<sub>3</sub> and purify particles by centrifugation. The employed process is detailed below.

### 2.2.2 Experimental conditions

#### ✓ Reflux method

##### • Gadolinium phosphate synthesis (GdPO<sub>4</sub>)

GdCl<sub>3</sub>, 6 H<sub>2</sub>O (1.49 g, 4 mmol) was dissolved in distilled water (10 mL). The resulting solution is slowly added under stirring to a solution of NaH<sub>2</sub>PO<sub>4</sub> (0.55 g, 4 mmol) in distilled water (10 mL) previously heated at 70 °C. The mixture is stirred at 70 °C for 5 h. The resulting suspension is purified through precipitation in acetone, centrifuged at 8000 rpm for 10 minutes and the supernatant was discarded. The precipitate was dispersed in distilled water (5 mL). This step was repeated 3 times. A stable colloidal suspension is obtained.

##### • Gadolinium/lanthanum phosphate synthesis (Gd<sub>1-x</sub>La<sub>x</sub>PO<sub>4</sub>)

GdCl<sub>3</sub>, 6 H<sub>2</sub>O and LaCl<sub>3</sub>, 7 H<sub>2</sub>O was dissolved in distilled water (10 mL), in the requested ratio (Table II.3) with a total of 4 mmol of lanthanide ions (Gd<sup>3+</sup> and La<sup>3+</sup>). The resulting solution is slowly added under stirring to a solution of NaH<sub>2</sub>PO<sub>4</sub> (0.55 g, 4 mmol) in distilled water (10 mL) previously heated at 70 °C. The mixture is stirred at 70 °C for 5 h. The resulting suspension is purified through precipitation in acetone, centrifuged at 8000 rpm for 10 minutes and the supernatant was discarded. The precipitate was dispersed in distilled water (5 mL). This step was repeated 3 times. A stable colloidal suspension is obtained.

Table II.3. Molar ratio of the prepared nanoparticles

Number	Gd		La	
	m (g)	% molar Gd	m (g)	% molar La
1	1,49	100	0,00	0
2	1,12	75	0,37	25
3	0,74	50	0,74	50
4	0,37	25	1,11	75
5	0,00	0	1,49	100

✓ **Hydrothermal method**

• **Gadolinium phosphate synthesis (GdPO<sub>4</sub>) at various pH**

GdCl<sub>3</sub> · 6 H<sub>2</sub>O (0.999 g, 2.69 mmol) was dissolved in distilled water (10 mL). The resulting solution is slowly added under stirring to a solution of NaH<sub>2</sub>PO<sub>4</sub> (0.369 g, 2.60 mmol) in distilled water (10 mL) at room temperature. The pH of the solution is rapidly adjusted to the desired value through the addition of 4 M aqueous NaOH solution and poured into a glass pressure tube. The tube was capped and heated under stirring to 170 °C for 5 h. The resulting suspension was centrifuged at 8000 rpm for 10 min, and the supernatant was discarded.

Samples synthesized at pH 1 and 6 were dispersed in water, and precipitated using acetone 1:2 volume ratio, centrifuged at 8000 rpm for 10 min and dispersed in distilled water. This step is repeated 3 times, and then particles are dispersed in distilled water (5 mL).

In order to remove the Gd(OH)<sub>3</sub> formed as byproduct, samples at pH 9 and 12 were suspended in 0.1 M HCl (54 mL), kept at pH 1 and stirred for 1 day. The suspension was centrifuged at 8000 rpm for 10 min, and the supernatant was discarded. The precipitate was added to distilled water (30 mL) and centrifuged at 6000 rpm for 1 min, to discard by precipitation the possible aggregates. The supernatant was decanted, precipitate by adding acetone 1:2 volume ratio and centrifuged at 8000 rpm for 15 min. The precipitate was dispersed in distilled water (5 mL).

### **2.3 Stabilization of the obtained systems by pegylation**

The rapid elimination of nanoparticles from the blood stream after their injection is due to their recognition by macrophages. Nanoparticles tend to adsorb proteins from plasma and when they are covered with adsorbed plasma proteins, they are quickly cleared by macrophages before they can reach their target. Modify the particles with PEG is one of the best approach to increasing the circulation time of nanoparticles in the blood stream, because it allow to disperse particles and minimize protein adsorption. Surfaces covered with PEG are biocompatible because PEG has uncharged hydrophilic residues, and very high surface mobility leading to high steric exclusion<sup>267,268</sup>. Therefore, covalently immobilizing PEG on the surfaces of our nanoparticles is expected to effectively improve the biocompatibility of the nanoparticles. Also PEG is interesting because it is inexpensive, versatile and approved for many biological applications<sup>262</sup>.

We used a PEG molecule with 10 ethylene glycol units, because larger PEGs can increase substantially the hydrodynamic radius of the particles and then shorten the retention time or affects the BBB crossing. The used PEG molecule has methyl (–CH<sub>3</sub>) and bisphosphonate groups at opposite



## 2.4 Core-shell system: gadolinium chelate coated titanium oxide particle

### 2.4.1 Titanium oxide core synthesis (TiO<sub>2</sub>)

TiO<sub>2</sub> nanoparticles were synthesized by the known sol-gel method involving hydrolyze of titanium isopropoxide<sup>274</sup>. The use of titanium alkoxide precursor has the advantage unlike the titanium salts precursor to not release inorganic ions in the medium, which may require an additional step of purification. Firstly, titanium isopropoxide is mixed with isopropyl alcohol under inert atmosphere (Argon). Then the mixture is added to a large volume of water with vigorous mechanical stirring, without catalyst. Solution to gel processing is carried out through the inorganic polymerization in two-step mechanism: hydrolysis and (poly-) condensation of titanium isopropoxide. Titanium isopropoxide is strongly hydrolysable (1), and will first react with water:



With *OiPr*, isopropoxide group and *iPr-OH*, isopropanol molecule

At this neutral pH, condensation (2) of the species is faster than hydrolysis. This mechanism leads to the formation of dense particles. The aggregation between particles leads to a white and opaque solution. Isopropanol is discarded by distillation. Then a solution of nitric acid is added to acidify the solution, which will charge the surface of the particles positively and stabilize the solution. Finally the solution is heated by reflux to lead to a stable and transparent colloidal solution. This solution can be treated hydrothermally in autoclave before to be dialyzed for purification.

#### ✓ Reflux method

Typically, titanium isopropoxide (0.11 mol) and isopropanol (0.20 mol) were first collected under inert atmosphere (argon) and introduced in a funnel tightly capped. This mixture is then introduced dropwise into a large quantity of ultrapure water (13.9 mol) with vigorous mechanical stirring. It formed in the middle a white precipitate (titanium oxyhydroxide). After 20 min of stirring, 1.4 milliliters of concentrated nitric acid 69 % (0.022 mol) are introduced. Table II.4 summarizes the reacting ratio of the synthesis. The solution is then peptized for 1h and distilled to remove all isopropanol. After 24 hours at reflux at 90 °C, an aqueous solution of titanium dioxide nanoparticles is obtained. The obtained solution is purified by dialysis.

Table II.4. Ratio of reacting for the TiO<sub>2</sub> synthesis

	Molar ratio	Quantity (mol)	Masse (g)	Volume (mL)
Isopropanol	1,8	0,20	11,78	15
Titanium isopropoxide	1	0,11	30,72	32
Ultra-pure water	128,5	13,9	250	250
Nitric acid 69%	0,2	0,022	1,36	1,4

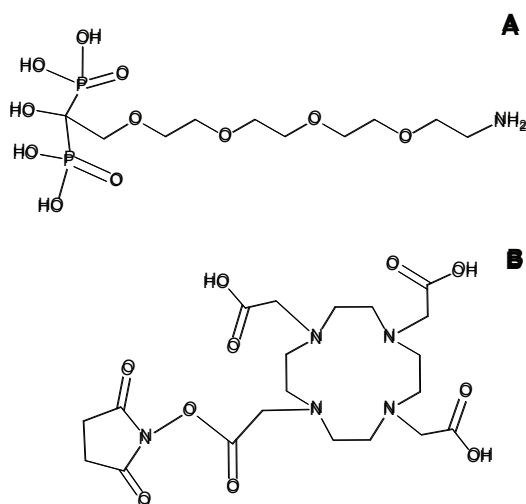
✓ **Hydrothermal treatment**

75 mL of suspensions from reflux method was charged into a 100 mL Teflon-lined stainless steel autoclave with a magnetic stirrer. The hydrothermal preparations were conducted at 250 °C for 4 h. After cooling in room temperature, this solution is purified by dialysis.

These naked titanium particles were first fully characterized (discussed in the next section) before surface pegylation.

**2.4.2 Magnetic shell coating on titanium oxide**

As mentioned previously, TiO<sub>2</sub> particles are diamagnetic and are used here as a support for DOTA-Gd(III) complex anchoring. The first stage of the coating is pegylation, to improve the water-solubility and biocompatibility. The used PEG possess bisphosphonate and amine (–NH<sub>2</sub>) groups at opposite ends (Scheme II.3-A) and was prepared by professor Lecouvey's group (Laboratoire de Chimie Structurale Biomoléculaire, Université Paris XIII).



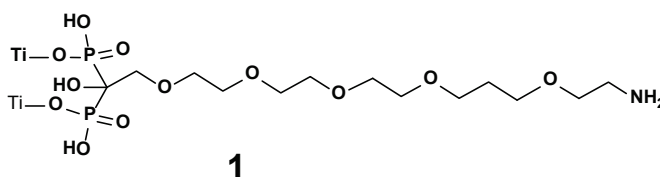
Scheme II.3. Bisphosphonate polyethylene glycol terminated NH<sub>2</sub> (A) and DOTA-NHS (B)

Then the pegylated TiO<sub>2</sub> will be further coupled with DOTA-NHS (Scheme II.3-B) via the amine group, using the peptide coupling. After all, lanthanide ions will be introduced within DOTA.

#### 2.4.2.1 Amino-Pegylation of titanium oxide (TiO<sub>2</sub>@PEG)

Pegylation of TiO<sub>2</sub> particles was carried out according to the grafting method discussed previously and employed for GdF<sub>3</sub> and GdPO<sub>4</sub>. We used a short PEG with 4 ethylene glycol units (Scheme II.3-A), to minimize the free motion of DOTA-Gd(III) moiety which will be attached on, in order to improve the relaxivity.

Typically, 2 mmol of bisphosphonate-PEG-NH<sub>2</sub> (BP-PEG-NH<sub>2</sub>) is dissolved in 10 ml of water and filtrated with 0.45 μm nylon filter if necessary. 5 ml of aqueous solution of previously prepared TiO<sub>2</sub> nanoparticles (4 mmol metal concentrations) is added to the BP-PEG-NH<sub>2</sub> solution previously heated at 70 °C under vigorous stirring. The suspension is sonicated and becomes transparent. The mixture is heated at 70°C for 5 hours, and the functionalized particles are purified through dialysis for 10 days.



Scheme II.4. Schematic representation of TiO<sub>2</sub> particle coated bisphosphonate-PEG-NH<sub>2</sub>: TiO<sub>2</sub>@PEG

These pegylated titanium particles were first fully characterized (discussed in the next section) before coupling with DOTA-NHS

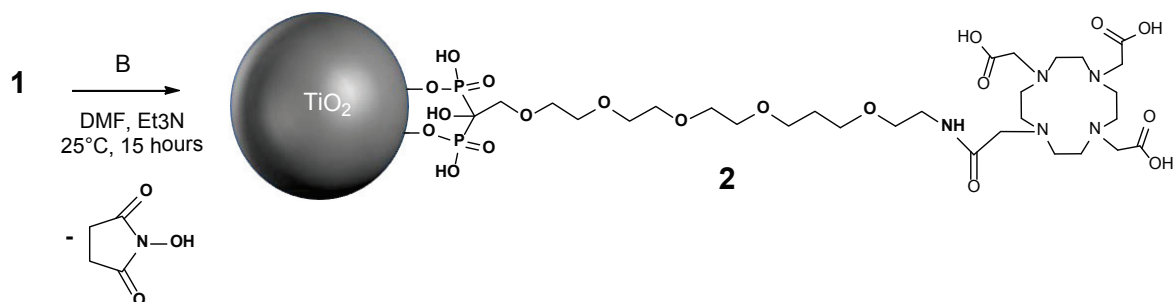
#### 2.4.2.2 DOTA-NHS ester coupling with pegylated TiO<sub>2</sub> (TiO<sub>2</sub>@PEG-DOTA)

The NHS (N-HydroxySuccinimide) ester contains an electrophilic active group that couples rapidly with the primary amine group to create a stable amide bond<sup>275,276</sup>. NHS ester is highly reactive compounds usually employed for the modification of amino groups in biochemical applications such as fluorescence and magnetic labeling<sup>277</sup>. The reaction of NHS esters with amines is strongly pH-dependent<sup>278,279</sup>. Thus at low pH, the amino group can be protonated. Consequently, no coupling takes place. At higher pH, above 9, hydrolysis of NHS ester takes places quickly, and coupling yield decreases. Optimal pH range for coupling is 7.5-8.5. pH can be adjusted by addition of an alkaline compound.

Here NHS ester group within DOTA-NHS will react with the primary amine group of the pegylated TiO<sub>2</sub> to yield stable amide bonds. Reaction takes places in DMF (*N,N*-Dimethylformamid).

Triethylamine was added to pegylated TiO<sub>2</sub> solution to adjust pH in range 8.0-8.5 and the mixture was added to a solution of DOTA-NHS in DMF. The obtained DOTA labeled particles are purified by dialysis and eventually centrifuged to remove *N*-hydroxysuccinimide before water dispersion.

Typically, to 6.7 mmol (4 ml) of colloidal suspension of pegylated TiO<sub>2</sub> (TiO<sub>2</sub>@PEG) in DMF, is added 0.16 mL (1.3 mmol) of triethylamine and 3.5 mL (1.3 mmol) of a DOTA-NHS solution in DMF. The suspension is stirred at room temperature over night. The nanoparticles are purified through dialysis and dispersed in 3 ml of water.



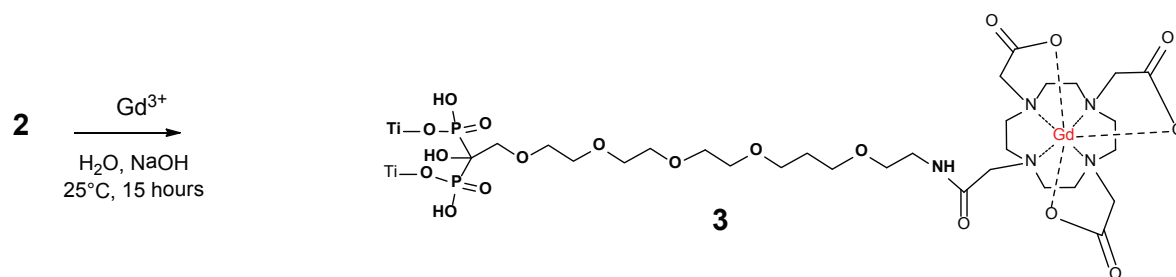
Scheme II.5. Schematic representation of DOTA labeled TiO<sub>2</sub> particle: TiO<sub>2</sub>@PEG-DOTA

#### 2.4.2.3 Chelation of gadolinium (III) on DOTA coated TiO<sub>2</sub>

Several ring or linear organic compound are used as Gd(III) complexing agent<sup>280,281</sup>. One of the advantages of the DOTA chelate is that it is clinically approved and has a higher binding coefficient to the Gd(III). Its stability constant ( $\log K_{\text{GdDOTA}}=18.6$ )<sup>282</sup>, superior to those of others chelating agent (14-17)<sup>280</sup> making it more stable *in vivo* over longer periods of time. Also, the rigidity and the pre-organization provided by the macrocyclic ring and the great correspondence between the macrocyclic cavity and the Gd(III) ionic radius, lead to the formation of a highly stable Gd(III) complex. Gd(III) has a coordination number CN = 9 and is coordinated to nitrogen and oxygen atoms from DOTA. In aqueous media, the coordination sphere is completed by a water molecule.

Chelating process is performed in aqueous solution, with Gd/DOTA ratio 3:1 to ensure Chelation for each DOTA molecule. A Gd(III) solution is added to DOTA coated TiO<sub>2</sub> and pH is adjusted at 10-11 by addition of NaOH, to deprotonate carboxyl groups within DOTA and then promotes Gd(III) chelation. Reaction occurs at room temperature because at high temperature, a competition between gadolinium hydroxides precipitation and chelation can occurs<sup>283</sup>.

A solution of GdCl<sub>3</sub>, 6 H<sub>2</sub>O (1.33 mmol) in 1 ml of water is added under stirring to the suspension of TiO<sub>2</sub> coated chelate DOTA (TiO<sub>2</sub>@PEG-DOTA). 5 drops of NaOH 1M are added to the suspension. The mixture is stirred overnight at room temperature. The nanoparticles are purified through dialysis and dispersed in water.



**Scheme II.6. Schematic representation of DOTA-Gd(III) chelate labeled particle: TiO<sub>2</sub>@BP-PEG-NH-DOTA-Gd<sup>3+</sup>**

The following section will focus on morphology, structural and physico-chemical characterization including stability, surface modification and magnetic properties of the naked and functionalized particles. These properties are investigated using various techniques.

### 3 CHARACTERIZATION OF THE DEVELOPED CONTRAST AGENTS

Magnetic properties and behavior of the particles as contrast agents depend strongly on size, morphology, structure and physico-chemistry properties of the particles. Full characterization of the nanoparticles is necessary to understand their properties. Also functionalization must bring the desired properties without affecting morphology, structure and magnetic properties of the particles.

Therefore this part is devoted to the characterization of the developed systems. This part will be articulated as follows. After a brief presentation of the various characterization techniques used (1), we will study the naked particles (before pegylation) of each system (2), afterwards we will see the pegylation of isotropic and anisotropic systems (3), before to look at the achievement of the core-shell system (4) i.e. the pegylation of titanium dioxide, DOTA coating and chelation of the lanthanide ions. Finally we will deal with the study of the behavior of all final systems in liquid solution (5). We will specifically look at their stability and their ability to enhance the relaxation rate of protons.

#### 3.1 Physical measurements and instrumentation

##### 3.1.1 Size and morphology characterization

✓ **Transmission electron microscopy (TEM)** is used to determinate the core size and morphology of the particles. It provides details on the size distribution and the particles shape. Typically, nanoparticles suspension was diluted and a drop was deposited on a copper grid covered with a holey carbon membrane to be examined by TEM (Topcon EM-002B, Akashi, Japan).

✓ **Photon correlation spectroscopy (PCS) or dynamic light scattering (DLS)**, is used to determine NPs size. This technique gives access to the hydrodynamic size and the polydispersity of

the colloidal solution. This hydrodynamic size is close to real size of the NPs in solution. DLS experiments was carried out using a MALVERN zetasizer nano ZS.

### 3.1.2 Structural and surface analysis

✓ **X-ray diffraction (XRD)** analysis is used to determine the crystallographic identity of the produced material and phase purity. Powder diffraction data are measured using the Bruker D8 ADVANCE X-ray diffractometer, which measures data in reflection mode using an X-ray tube with a Cu anode as the X-ray beam source. Phase identification was done using the EVA software (Bruker) and the JCPDS-ICDD PDF-2 database.

✓ **Inductively coupled plasma atomic emission spectrometry (ICP-AES)**

ICP measurements were performed for elementary analysis. ICP measurements were conducted on an axial Jobin-Yvon 138 Ultrace prototype spectrometer. Measurements represent the average of 3 measurements, and are back-calculated to offset the initial dilution. The individual measurements are typically obtained with a relative standard deviation of approximately 3% or less per sample.

✓ **FT-IR spectroscopy** is used in order to identify the functional group on the particle, to confirm the attachment of different functional groups in each step of functionalization, and to determine the coupling mode on the particle surface. This technique provides information about the interaction on the surface, chemisorption or physisorption. Infrared spectra in the range 500-4000  $\text{cm}^{-1}$  were recorded on a Perkin-Elmer spectrophotometer (spectrum 100 FT-IR with universal ATR sampling accessory)

✓ **Zeta potential.** Surface charge is characterized by zeta ( $\zeta$ ) potential analysis. The isoelectric point (IEP) or point of zero charge (PZC), is determined and compared to the size variation of the NPs, reflecting the stability of the NPs. This technique provides information about the stability of the particle and their surface state. Zeta potential measurements was carried out using a MALVERN zetasizer nano ZS.

✓ **Thermal gravimetric analysis (TGA)** has performed to study the surface chemistry of the naked particles and to confirm the organic coating formation on the surface of functionalized particles. TGA measurements can confirm the existence of various distinct populations of polymers coated on the particles. This analysis is based on measure of variation in mass of a sample undergoing a rise in temperature in a controlled atmosphere. Measurements were carried out using a Netzsch STA 409 PC.

✓ **Nuclear Magnetic Resonance spectroscopy (NMR)** is used in order to identify the functional group on the surface of the particle, study and determine the attachment of different functional groups in each step of functionalization.  $^{13}\text{C}$  and  $^{31}\text{P}$  NMR MAS spectra were recorded on a Bruker Avance 500 spectrometer.

### 3.1.3 Relaxivity measurements

✓ **Relaxivity measurements:** relaxivity measurements were performed using different instrumentations quoted in relaxivity discussion section. Samples were diluted in saline or PBS (phosphate buffered saline) into five different concentrations and filled in 2 mL tubes. These diluted concentrations were used for relaxivity measurements at different field strength. Typically concentrations prepared are 10, 5, 2.5, 1.25, 0.625, and 0.313 mM Gd. Concentrations 2.5, 1.25, 0.625, and 0.313 mM were used for  $T_1$  measurements. Due to low signal on T2 measurements, some samples were further diluted to 0.156, 0.078, 0.039 mM Gd for T2 measurements.

- Example of parameters for relaxivity measurement at 7 T (7T Bruker system)

2ml Eppendorf tubes at different concentrations in solution with 0.9% NaCl at room temperature.

T<sub>1</sub> was measured using:

- Spin echo sequence. TE 8.3 ms. Varying TR 13ms-6400ms.
- Relaxation curve was fitted based on signal intensity measurements in ROIs (region of interest) in the tubes with correction for incorrect saturation pulses.

T<sub>2</sub> was measured using:

- Spin echo sequence. TR 15000. 16 Echoes TE=11ms-176ms
- Relaxation curves fitted based on signal intensity measurements in ROIs in the tubes.

## 3.2 Characterization of isotropic nanoparticles

These particles were prepared according to the methods discussed previously, using three different heating methods: reflux, solvothermal and microwave. Because of the unsatisfactory results from microwave method, related to the size and morphology of the obtained particles, we focused at the particles from reflux and solvothermal methods.

### 3.2.1 Morphological and structural characterizations

These nanoparticles have been characterized by dynamic light scattering (DLS) and transmission electron microscopy (TEM) in order to determine the particle size and morphology. It

can be seen here (Figure II.7) that the nanocrystals from reflux and solvothermal methods have an average size of respectively 35 and 40 nm. These results show a relative narrow size distribution. We observed that these two heating modes lead to similar results in terms of size and size distribution. That is, higher temperature and higher pressure (in solvothermal method) do not influence the particle growth. However, we do not observe this similarity regarding the morphology of the particles.

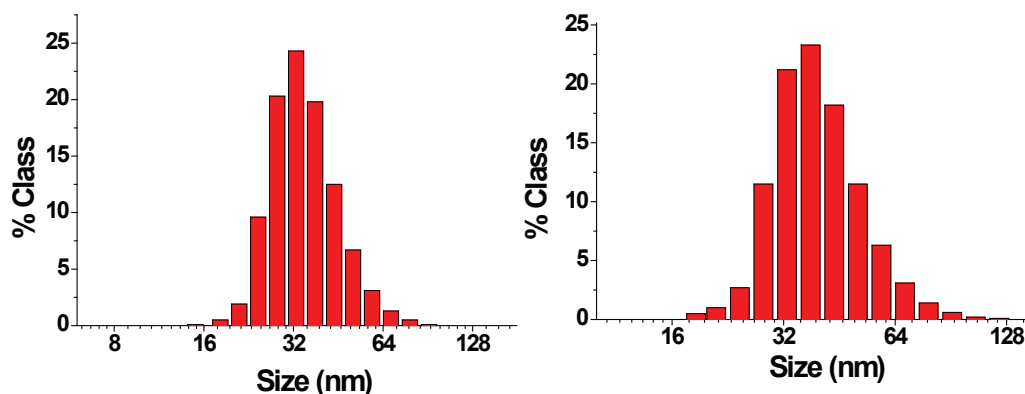


Figure II.7. Size distribution of  $GdF_3$  nanoparticles, from reflux (left) and solvothermal (right) methods

TEM images of the nanoparticles show that particles are not aggregated and are highly crystalline. Particles from solvothermal method (Figure II.8) are monodisperse and have an elongated shape with 10 nm of width and 15-20 nm of length. They have more well-defined and smoothed shape, contrary to the particles from reflux method (Figure II.9). The latter have mainly a spheroidal shape with 15-20 nm of diameter, however we can see also some particles in an elongated shape with the same dimension that the spheroidal ones.

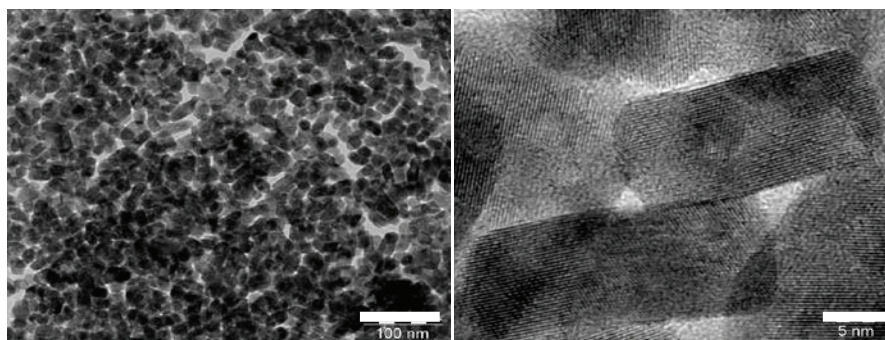


Figure II.8. TEM images of  $GdF_3$  nanoparticles from solvothermal method

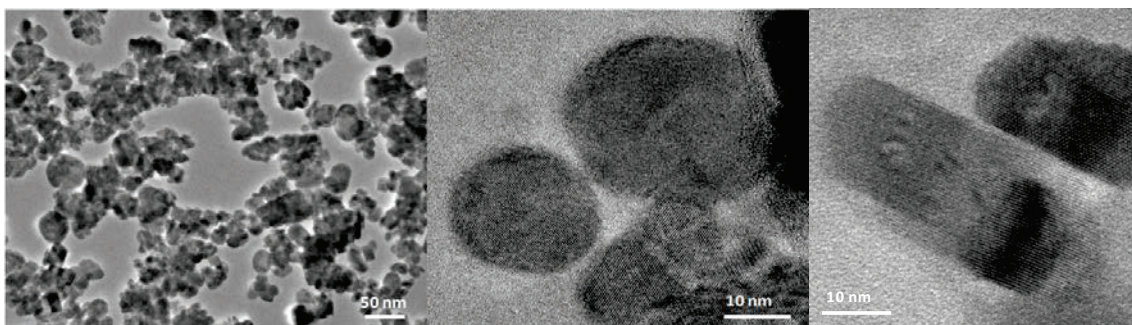


Figure II.9. TEM images of  $GdF_3$  nanoparticles from reflux method

Dimensions of these particles are similar in DLS (35-40 nm) and in TEM (15-20 nm). However, sizes determined from DLS are smaller mainly because it considers the hydrodynamic size, larger than effective size. There is also probably a reversible aggregation in solution that contributes in overestimation of the size in DLS. This eventual aggregation phenomenon must be reversible because no aggregated particles were observed in TEM.

Synthesis with microwave method was performed. The first test (50 °C/3 min) has not allows formation of nanoparticles. Temperature and pressure in the reactor were too low. On the others three tests (200 °C/1 min; 170 °C/3 min and 80 °C/3 min), higher temperature and pressure conditions have allowed reaction to take place; but resulted in bigger size particles with unexpected morphology (bone shape). Thus investigation on the microwave method was given up.

For *in vivo* applications, we aim particles below 100 nm. This method, leads to large particles around 300 nm, which seems to be aggregation of smaller units. The brutal rise of temperature during heating by microwave appears to be favorable to the rapid growth and aggregation of the particles. Absence of agitation during the heating could also affect the aggregation of particles.

Concerning reflux and solvothermal methods, DLS which calculates hydrodynamic size from diffusion constant measurement can't demonstrates difference in morphology observed at TEM images. This difference in morphology suggests a difference in crystallinity. XRD diagram of the particles were compared. In our previously published article<sup>215</sup>, we discussed crystallinity phase of lanthanide fluoride. We observed that lanthanide fluoride particles from reflux method can exhibit dimorphism and have a hexagonal structure for those from  $LaF_3$  to  $GdF_3$  and an orthorhombic one for those from  $GdF_3$  to  $LuF_3$ .  $GdF_3$  is the unique lanthanide fluoride to present both hexagonal and orthorhombic phase. Here diffraction peaks of  $GdF_3$  from reflux (Figure II.10-top) is in good agreement with the standard diffraction data for  $GdF_3$ , both JCPDS, Card No. 00-012-07-88 and 01-082-0689 corresponding respectively to orthorhombic and hexagonal phase with space group  $Pnma$  and  $P3c1$ . Peak (200) in red, come exclusively from hexagonal phase. Presence of two crystalline phases can explain coexistence of spheroidal and elongated shape for the particles from reflux

method. XRD patterns of  $GdF_3$  nanopowders from solvothermal method was indexed as only orthorhombic phase (JCPDS, Card No. 00-012-07-88) with space group  $Pnma$  (Figure II.10-bottom). The peaks shift between diagrams is due to the use of two different radiations:  $K\alpha$  Cobalt and  $K\alpha$  Copper.

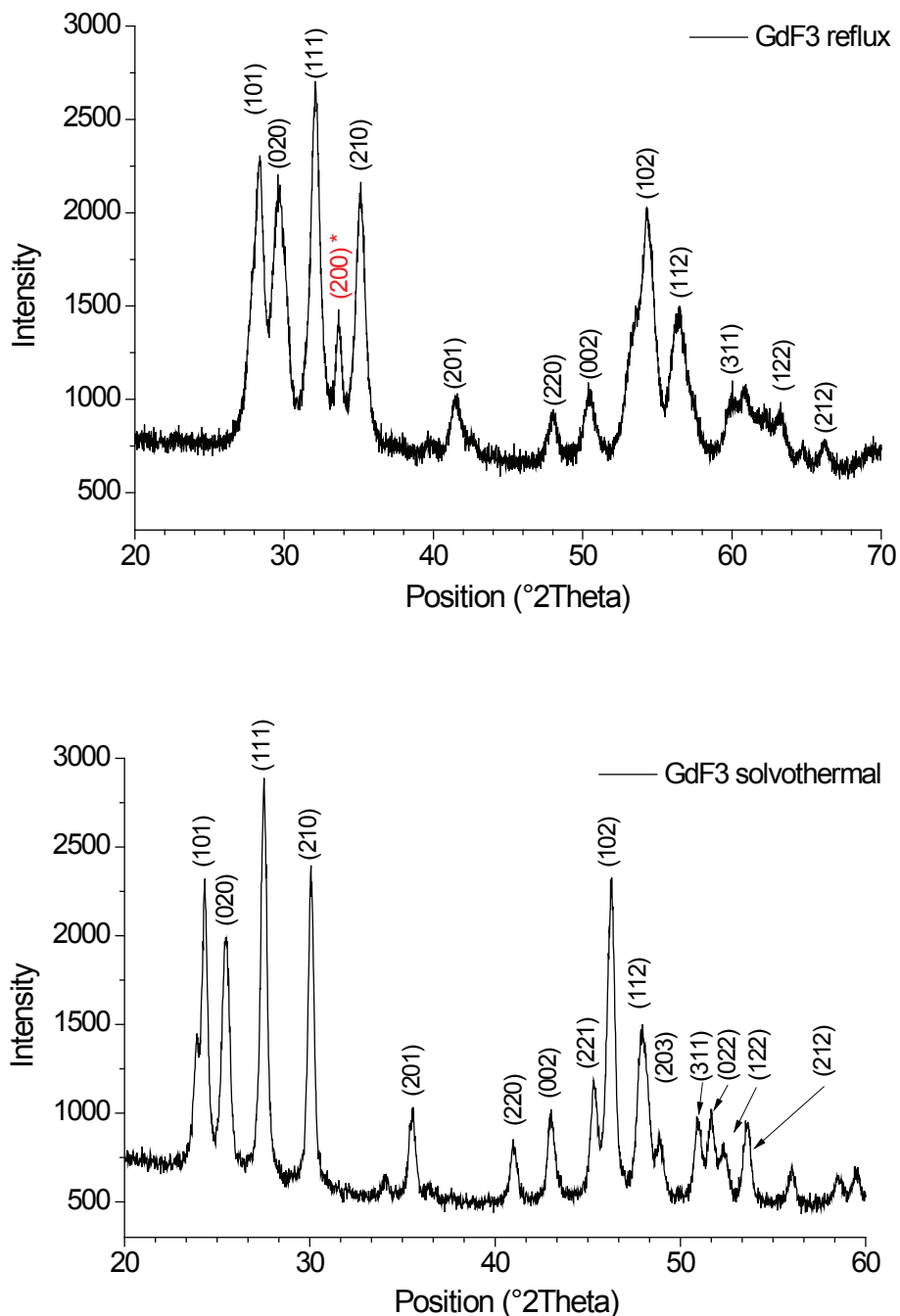


Figure II.10. XRD patterns of  $GdF_3$  nanopowders obtained using reflux method (top, Cobalt  $K\alpha$  radiation)) and solvothermal method (bottom, Cooper  $K\alpha$  radiation))

In our previous work, synthesis of several lanthanide fluorides ( $LnF_3$ ) was largely studied. Their crystallinity is highly depending on the solvent, heating time and temperature. For example, for

reaction times below 10h, the resulting particles are amorphous, while the pure crystalline orthorhombic  $\text{YbF}_3$  phase is obtained for reaction time above 10h in DMF. For comparison, we reported that  $\text{YbF}_3$  nanoparticles are more crystallized when they are prepared in NMP at 170 °C during 12 h than in DMF at the identical condition. The use of solvent with higher boiling point (NMP, bp = 202 °C) instead lower boiling point (DMF, pb =153 °C) allows preparation of better crystallized  $\text{LnF}_3$  nanoparticles using similar reaction times<sup>215</sup>. This observation evidence the influence of temperature and pressure in crystallization process. Thus in solvothermal method, the higher temperature and pressure impact directly the crystallization process, leading to more crystallized  $\text{GdF}_3$  particles and promoting the crystalline phase that leads to elongated and well-defined shape particles.

Also, surface of the particles and their colloidal stability were investigated using various techniques.

### 3.2.2 Surface characterizations

Surface of the particles is characterized using various techniques to determine the surface chemistry of the particles. First all infra-red spectroscopy revealed the adsorption of NMP molecules on the surface of dried nanopowders of  $\text{GdF}_3$  from both synthesis methods (Figure II.11). Presence of water in the particles surface is evidenced by its spectral features with a broad OH stretching band centered at  $3363\text{ cm}^{-1}$  and a signal at  $1595\text{ cm}^{-1}$  (more visible in the reflux particle spectra) due to the H-O-H binding. Adsorption of NMP molecules on the fluoride nanoparticles surface can be evidenced by a shift to lower frequency of the carbonyl band, from  $1673$  to  $1653\text{ cm}^{-1}$  with a lower intensity. The bands in the range  $1460\text{-}1425\text{ cm}^{-1}$  are assigned to C-H deformations (symmetric, asymmetric and wag). IR spectra show that the band at  $1400\text{ cm}^{-1}$  assigned to the C-N stretching vibration is shifted to  $1411\text{ cm}^{-1}$  with a great decrease of intensity as described by Fujiwara et al.<sup>234</sup> concerning the adsorption of NMP on the particles surface.

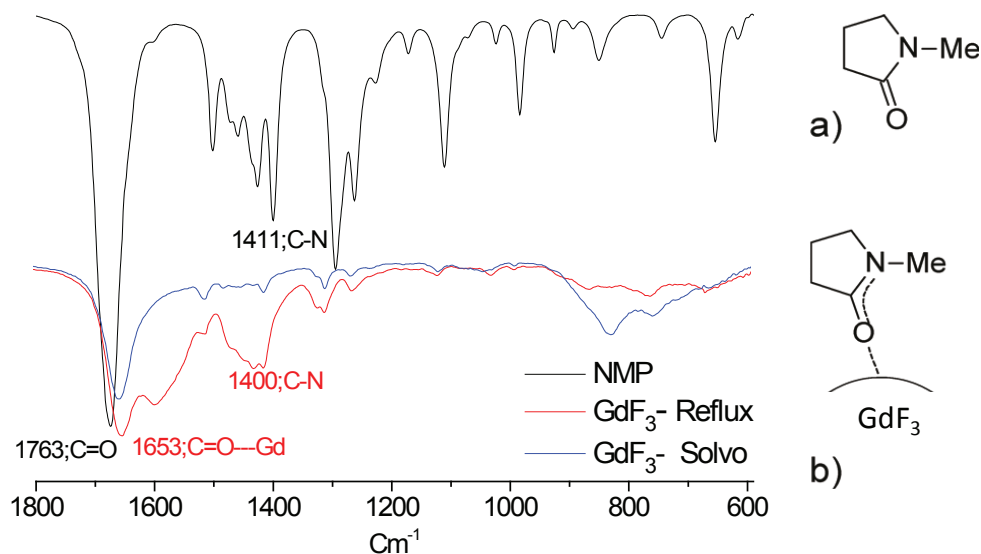


**Figure II.11.** IR spectra of free NMP (black),  $\text{GdF}_3$  powder from reflux (red) and Solvothermal method (blue).  
Schematic representation of (a) free NMP and (b) NMP adsorbed on  $\text{GdF}_3$  particle (right)

We can note the almost disappearance of the band at  $1501 \text{ cm}^{-1}$  assigned to C-N stretching (the carbonyl carbon) from free NMP on the spectrum of  $\text{GdF}_3$  nanoparticles, for which the surface is complexed by solvent molecules. This result suggests that the oxygen atom acts as an electron donor interacting with the Gd(III) ions on the surface of the particles, opening the possibility of achieving surface functionalization by ligand exchange.

The interaction of NMP molecules with the nanoparticles surface was also studied by  $^1\text{H}$  NMR spectroscopy, using tetramethylsilane (TMS) as a reference. The experiments were conducted on particles from reflux method (NMP,  $170 \text{ }^\circ\text{C}$ ). Since  $\text{GdF}_3$  is a paramagnetic ion that greatly influences the resolution of NMR spectra, we worked on lutetium fluoride ( $\text{LuF}_3$ ) nanoparticles dispersed in deuterium oxide. The  $^1\text{H}$  NMR spectrum of free NMP in  $\text{D}_2\text{O}$  shows signals at 2.08, 2.46, and 3.54 ppm assigned to methylene proton resonances. The peak at 2.86 is attributed to the resonance of methyl protons (Figure II.12-a). An upfield shift of these signals is observed in the presence of  $\text{LuCl}_3$ , 6  $\text{H}_2\text{O}$  as shown in Figure II.12-b. In the case of the system with the nanoparticles, the upfield shift of the signals is remarkably higher (almost 0.5 ppm in the case of signal 3 between Figure 10a and c) and a significant broadening of these signals is observed (Figure II.12-c).

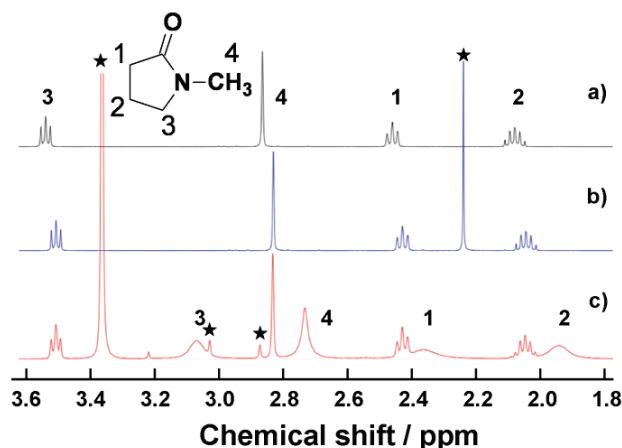


Figure II.12. NMR analysis of (a) free NMP, (b) NMP/LuCl<sub>3</sub>, 6H<sub>2</sub>O, and (c) LuF<sub>3</sub> nanocrystals in D<sub>2</sub>O (★: signals of residual solvents)

The signals of free NMP as well as residual solvents are also present on the spectrum of the colloidal solution. The NMR peaks are broadened and shifted as a result of the adsorption of NMP molecules on the LuF<sub>3</sub> nanoparticle surface<sup>234</sup>. The grafting of NMP on the surface of the particles is also evidenced by thermogravimetric analysis (TGA).

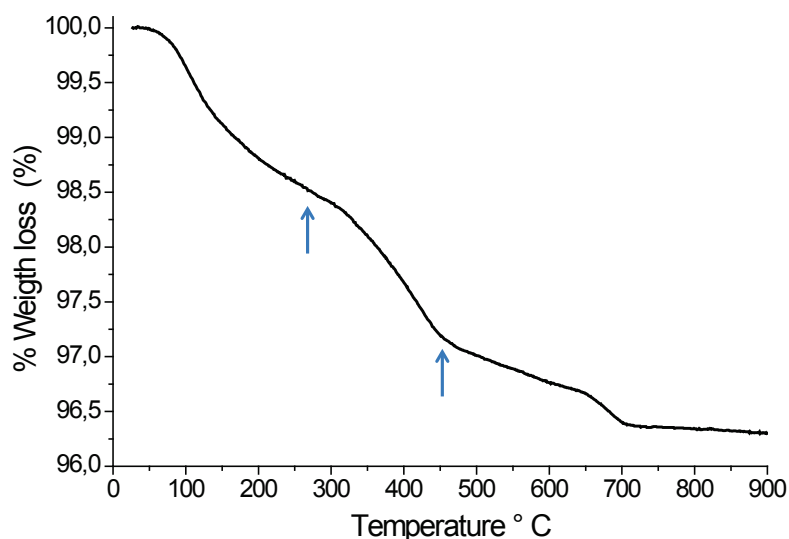


Figure II.13. TGA analysis of dried GdF<sub>3</sub> nanopowder from reflux method

The weight loss versus temperature of isolated and dried GdF<sub>3</sub> nanopowder is shown in Figure II.13. This curve is identical to that of particles from solvothermal. The measurements were carried out under oxygen atmosphere at a heating rate of 15 °C.min<sup>-1</sup> from room temperature (RT) to 900 °C. The weight loss profile can be divided in three parts. The first one, with a 2.5% loss in the range from room temperature to 260 °C, corresponds to the water molecules bound to the surface of the nanoparticles (evidenced also by IR analysis). The second part, with a total weight loss of about

1.5 % in the range 260-450 °C, corresponds to the loss of water molecules, subsequent to the dehydration of the lattice waters. The fifth part with a 1 % loss in the range 450-700 °C, corresponds to the loss of NMP molecules which complex the surface of nanoparticles. The presence of water can be explained by the process used to obtain the fluorides. In fact, these compounds can be partially hydrated. This remark is also true for all the methods, described in the literature, which use hydrated raw materials<sup>284</sup>. Presence of water is not detrimental for MRI applications, contrary to optics applications.

### 3.2.3 Colloidal stability

Zeta potential (ZP) measurement is an indicator of colloidal stability of colloidal suspension. Particles from reflux and solvothermal methods present identical behavior concerning zeta potential (Figure II.14). These particles are surprising because they don't have isoelectric point (IEP) in pH range 1-12. IEP is beyond pH 12, and they have a constant zeta potential at 37 mV from pH 2 to 10. They are very stable in this large pH range. ZP declines only beyond pH 10, from 35 mV to 12.5 mV at pH 12. This ZP decrease indicates a drop of surface charge leading to particles aggregation.

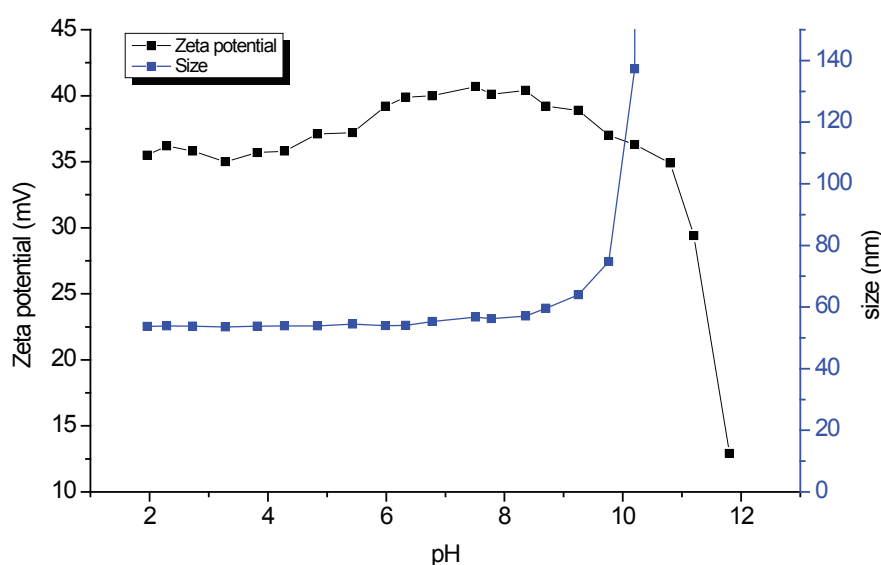


Figure II.14. Zeta potential versus pH of GdF<sub>3</sub> nanoparticles suspension

These particles are very stable in aqueous solution and in a large range of pH: acidic, alkaline or neutral solution without aggregation or precipitation. According to ZP curve, this stability is probably due to the positively charged surface due to the adsorbed water and presence of the hydrated adsorbed NMP.

### 3.2.4 Conclusion

Nanoparticles of  $GdF_3$  were synthesized using two heating methods, reflux and solvothermal. Microwave particles are bigger with unexpected morphologies, which do not fill the established requirements. Particles from reflux and solvothermal present smaller dimension, 15-20 nm (TEM). There is spheroidal and elongated shape in reflux method while only one morphology type, the elongated one was observed with solvothermal method. Solvothermal method results in higher crystallinity. However, particles are sufficiently crystallized, that is necessary to avoid gadolinium ions release and minimize their toxicity. Particles are especially stable in water and at a large pH range 2-10. Their surface is covered by adsorbed NMP. Presence of NMP at the surface of the particles can act as growth limitation agent during particles synthesis, allowing access to smaller particles in 15-20 nm range.

## 3.3 Characterization of anisotropic nanoparticles

We have prepared three kinds of anisotropic particles. Gadolinium phosphate ( $GdPO_4$ ) and lanthanum doped gadolinium phosphate ( $Gd_{1-x}La_xPO_4$ ) from reflux method; and  $GdPO_4$  at various sizes from hydrothermal method. Hereafter, the physico-chemistry characterizations of the obtained particles.

### 3.3.1 Morphological and structural characterization

#### 3.3.1.1 Particles from reflux method

##### (a) Gadolinium phosphate ( $GdPO_4$ )

Particle size and morphology of the prepared nanorods were examined by TEM, as shown in Figure II.15. All samples exhibited a homogeneous rod-like morphology with lengths in range 100-140 nm and a width in the range 20-25 nm. A typical HRTEM image is presented (Figure II.15) and indicates the single-crystalline nature of the particles. It is noteworthy that these particles have a large aspect ratio of around 5 and seem very thick, flat and squared-end.

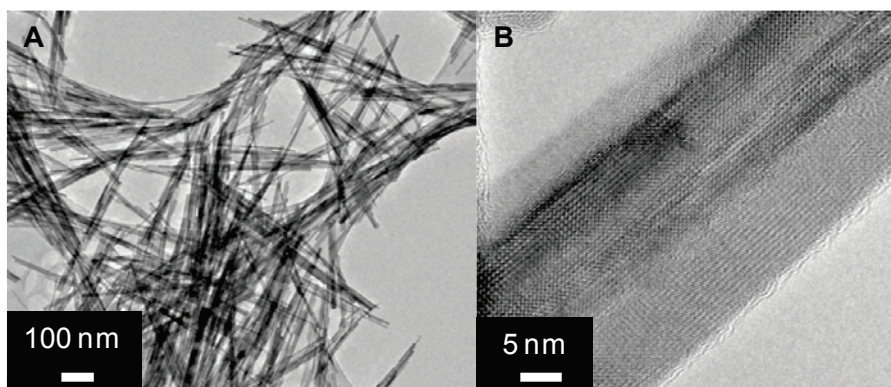


Figure II.15. TEM images of GdPO<sub>4</sub> nanoparticles formed using reflux method at pH 1 and 70 °C for 5 h.

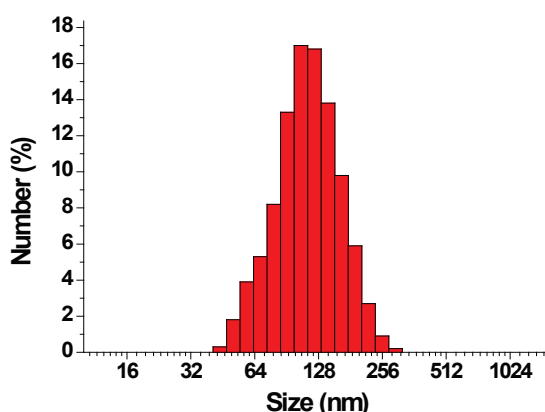


Figure II.16. Size distribution of GdPO<sub>4</sub> nanoparticles formed using reflux method at pH 1 and 70 °C for 5 h.

The size distribution is shown in Figure II.16, with 120 nm as the more represented size. This distribution size is in agreement with TEM observation. Here DLS size corresponds to the length of the rods particles, hence, the principal axis is too important that solvation of the particles don't influence significantly DLS size, contrary to spherical particles.

Figure II.17 shows the XRD patterns of the prepared samples. Diffraction peak is in good agreement with the standard diffraction data for GdPO<sub>4</sub>·H<sub>2</sub>O (JCPDS, Card No. 39-0232) and were indexed, in agreement with literature, to a pure hexagonal phase with space group P3121. These nanorods are obtained without using template; the rod shape is due to natural growth. In HRTEM (Figure II.15) the GdPO<sub>4</sub> nanorods appear as single crystals with a long axis assigned to the c axis (001) of the hexagonal structure, suggesting that particles growth preferentially in this axis, leading to high aspect ratio, consistent with literature<sup>184</sup>. This method consists in very mild preparation conditions and is well suited for preparation of high aspect ratio particles. The doped particles were also synthesized with similar method.

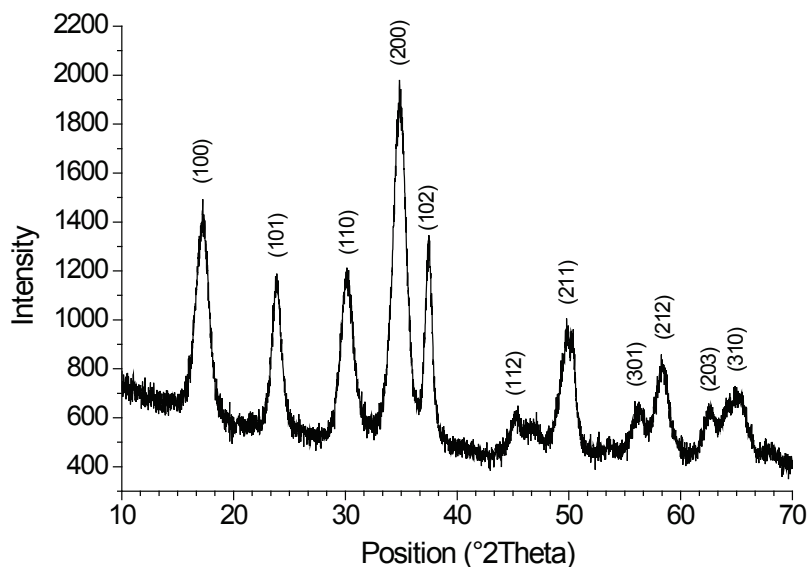


Figure II.17. XRD patterns (Cobalt K $\alpha$  radiation) of GdPO<sub>4</sub> nanopowders from reflux method

**(b) Gadolinium/lanthanum phosphate (Gd<sub>1-x</sub>La<sub>x</sub>PO<sub>4</sub>)**

The mixed phosphate of Gd<sub>1-x</sub>La<sub>x</sub>PO<sub>4</sub> (x=1.00; 0.75; 0.50 and 0.25) also consist of nanorods with a width around 10 nm and lengths ranging from 40 to 130 nm, precisely 40-110, 80-130, 60-100 and 60-90 nm respectively (Figure II.18). The size variation compared to the chemical composition is not clear, as the size distribution is wide enough. We observe that, statistically, the size of the doped particles made of 50% of Gd(III) and 50% of La(III) are smaller (60-100 nm), while the unmixed particles, i.e. particles with 100% of Gd(III) or 100% of La(III) have almost the same size (around 110).

Literature shows that gadolinium radii is smaller than lanthanum radii (0.0938 and 0.1061 nm respectively<sup>285</sup>), and the measured lattice parameters *a* and *c* of hexagonal LnPO<sub>4</sub> increase with crystal ionic radii of the lanthanide cations<sup>184</sup>. However hydrothermal synthesis has show that particles size is inversely proportional to ionic radii<sup>184</sup>. It is supposed to be related to the change of lanthanide ion radius, although the exact reason is not clear.

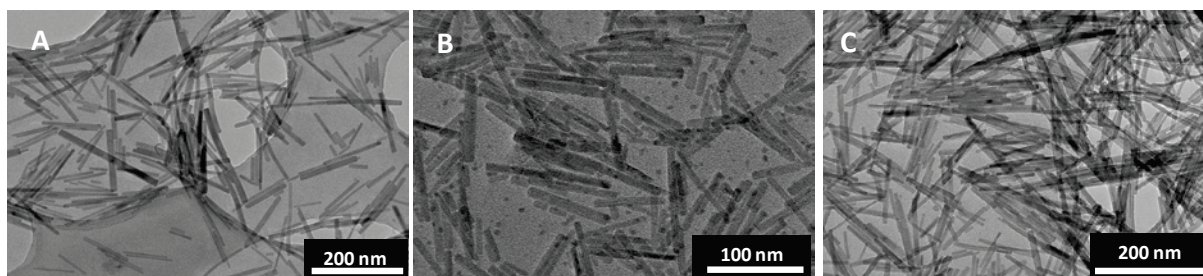


Figure II.18. TEM images of Gd<sub>1-x</sub>La<sub>x</sub>PO<sub>4</sub> nanopowders with different Gd molar ratio obtained using reflux method. Theoretical Gd molar ratio: 75% A); 50% B) and 0% C).

The XRD patterns in Figure II.19 indicate that the products are crystallized in hexagonal phase. Crystal phase of  $Gd_{1-x}La_xPO_4$  system do not vary with the molar ratio of the mixed lanthanide ions, however systematic shift of the diffraction peaks to lower angle is observed in comparison with those of the undoped  $GdPO_4$ . This result show the contraction of the ionic radii of the lanthanides, as it can be seen in XRD patterns of various  $LnPO_4$  ( $Ln=La, Ce, Nd...$ )<sup>286</sup>. This suggests that La(III) ions are doped into the  $GdPO_4$  matrix when Gd(III) are majority and reciprocally. There is no separate formation of  $GdPO_4$  particle on the one hand and of  $LaPO_4$  on the other hand.

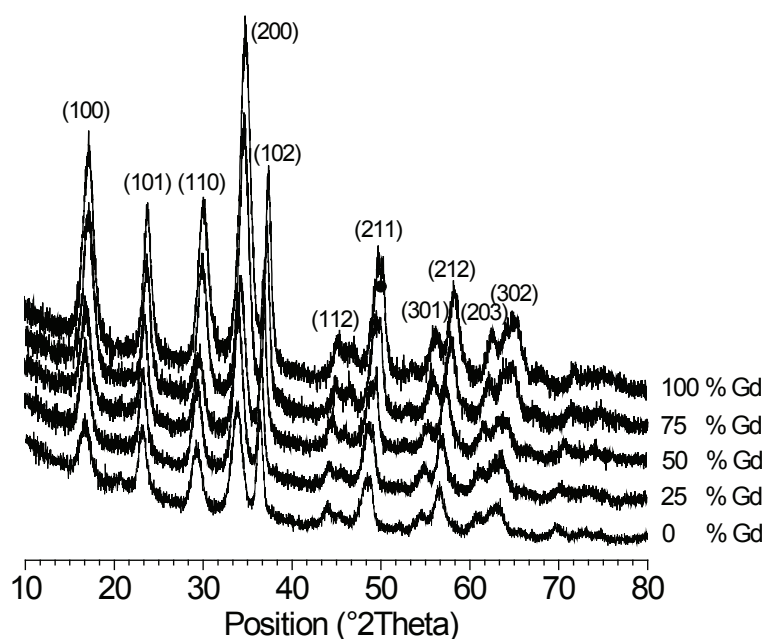


Figure II.19. XRD patterns (Cobalt  $K\alpha$  radiation) of  $Gd_{1-x}La_xPO_4$  nanopowders with different Gd molar ratio obtained using reflux method

The temperature-pressure conditions used here don't lead to crystal phase change with increase in the La(III) content (from hexagonal phase to monoclinic phase) as in hydrothermal conditions (autoclave, 200 °C)<sup>287</sup>. The obtained doped particles present the pure hexagonal phase, as in case of pure  $GdPO_4$ . Thus the replacement of Gd(III) by La(III) does not influence the final crystal phase structure of the product.

### 3.3.1.2 Particles from hydrothermal method ( $GdPO_4$ )

Hydrothermal method (capped glass pressure tube, 170 °C, 5 h) is the second method we employed to synthesized gadolinium phosphates nanorods. pH of the synthesis media was varied to modify the particles size. Figure II.20 shows TEM images of as-prepared  $GdPO_4$ . Images indicate that they all have a rod-shape and various dimension depending on the pH of the synthesis. Particles synthesized at pH 1 using hydrothermal method are longer than those synthesized at pH 1 using

reflux method (Figure II.15). They have a length in range 400-450 nm and the width around 30 nm. The length is almost 4 times larger while the width remains almost the same. The increase of pressure in the synthesis media enhances the growth capacity of the particles in the oriented direction; thus the aspect ratio is higher, around 15. Contrary to the reflux method, particles at pH 1 from Hydrothermal seem to be thicker with a round-end.

Evolution of morphology following pH of the starting solution is remarkable. Particles length decreases significantly with pH, while the width decreases slightly. We obtain 450, 150, 35 and 40 nm of length respectively for pH 1, 6, 9 and 12. The widths are around 30, 14, 7 and 10 nm respectively. Morphology changes from high aspect ratio (pH 1 and 6) to low aspect ratio (pH 9 and 12).

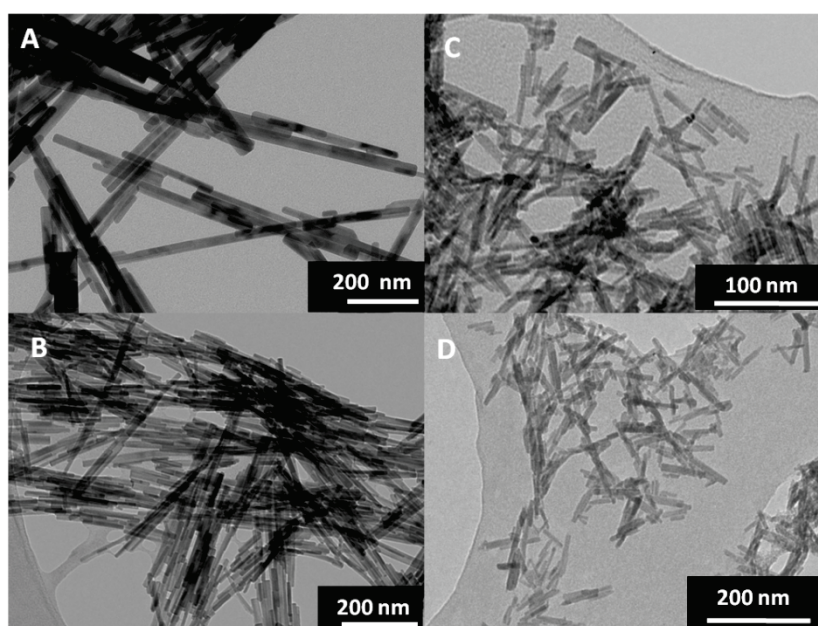


Figure II.20. TEM images of  $\text{GdPO}_4$  nanoparticles formed using hydrothermal method at pH 1 A), pH 6 B), pH 9 C), pH 12 D)

As discussed previously, the aspect ratio of the particles is reduced in the alkaline environment because the  $\text{Ln}^{3+}$  ions precipitation as the hydroxide at higher pH values. Therefore their chemical potential is reduced. It is interesting to note that the aspect ratio is proportional to the pH of the starting solution as shown in Figure II.21.

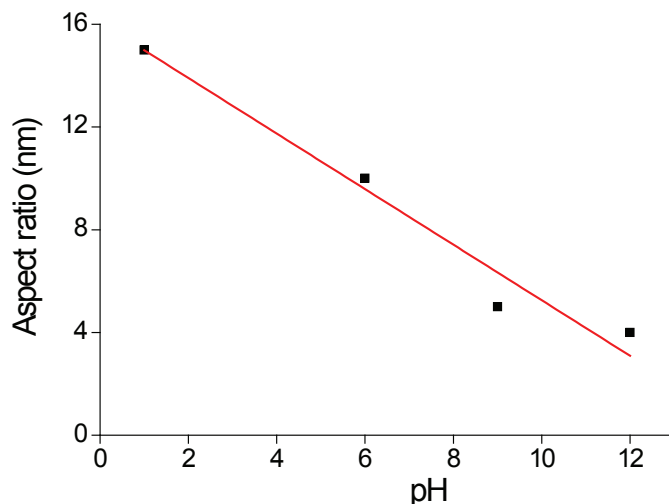


Figure II.21. Aspect ratio of  $GdPO_4$  particles versus pH of the synthesis

An XRD pattern of the as prepared sample (pH 1) is shown in Figure II.22. The diffraction peaks of sample from pH 1 were in good agreement with the standard diffraction data for  $GdPO_4 \cdot H_2O$  (JCPDS, Card No. 39-0232) and were indexed to a pure hexagonal phase with space group P3121. Samples from hydrothermal method at pH 6, 9 and 12 were indexed also to a pure hexagonal phase with space group P3121, however they are more hydrated (1.5 water molecule):  $GdPO_4 \cdot 1.5 H_2O$  (JCPDS, Card No 00-021-0337).

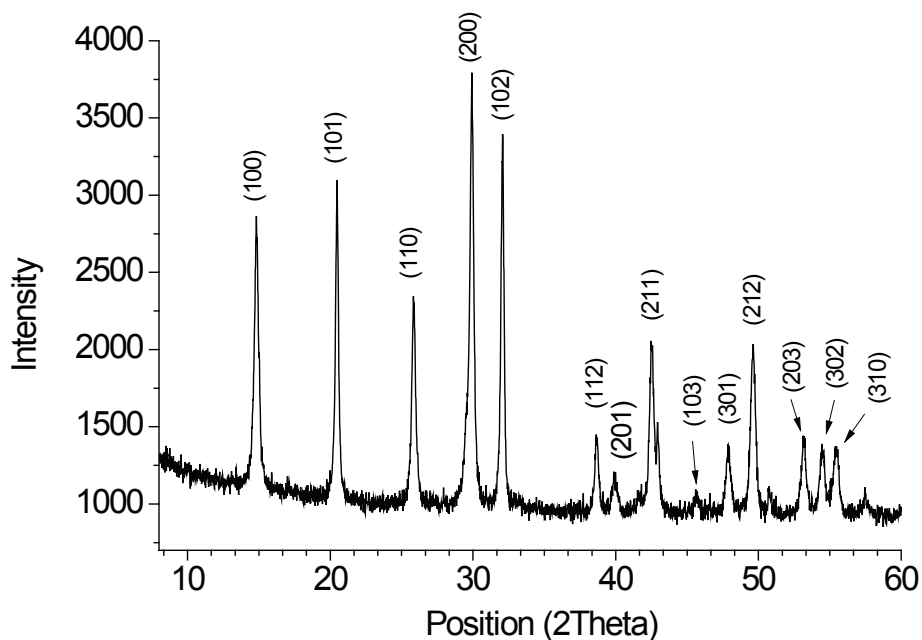


Figure II.22. XRD patterns (Cooper  $K\alpha$  radiation) of  $GdPO_4$  powders obtained using hydrothermal method (pH 1)

We can see that the sample obtained at pH= 1 in hydrothermal method, exhibited much defined diffraction peaks, than from reflux method, indicating a high crystallinity. Increasing the pH value lead to the slightly broadened diffraction peaks and the increased relative intensity of peak (1 0 2) (not shown). This phenomenon was previously observed by Heng Wang and al.<sup>150</sup> By estimating the particles size through Scherrer formula based on the widths of two main diffraction lines (2 0 0) and (1 0 0), they showed that the crystallite sizes decrease with pH, but obtains different crystallite size depending on whether they use diffraction line (2 0 0) or (1 0 0). These observations indicate that the morphology of particles is not spherical and the particle size can be tuned by tuning the pH values. Surfaces of all particles from the two methods are also investigated.

### 3.3.2 Surface characterizations

IR spectrum of particles from reflux method  $\text{GdPO}_4$  and  $\text{Gd}_{1-x}\text{La}_x\text{PO}_4$  (not presented here) are similar to that prepared using hydrothermal method at different pH (Figure II.23). The infrared spectra of rare earth phosphate were already studied<sup>288,289,172</sup>. The absorption bands observed in the range of 550 to 1500  $\text{cm}^{-1}$  are attributed to  $\text{PO}_4^{3-}$  vibration bands. The P-O stretching modes have been observed in the 1114-963  $\text{cm}^{-1}$  region. Band at 1000  $\text{cm}^{-1}$  is assigned to the stretching mode of P-O. Band at 619  $\text{cm}^{-1}$  is assigned to binding vibration mode of O=P-O. The binding vibration mode of O-P-O at 540  $\text{cm}^{-1}$  is not visible here<sup>179</sup>. The band at 1618  $\text{cm}^{-1}$  is associated with the deformation vibration of H-O-H bonds of the water molecules, while the broad band at 3460  $\text{cm}^{-1}$  is associated to the stretching vibration O-H.

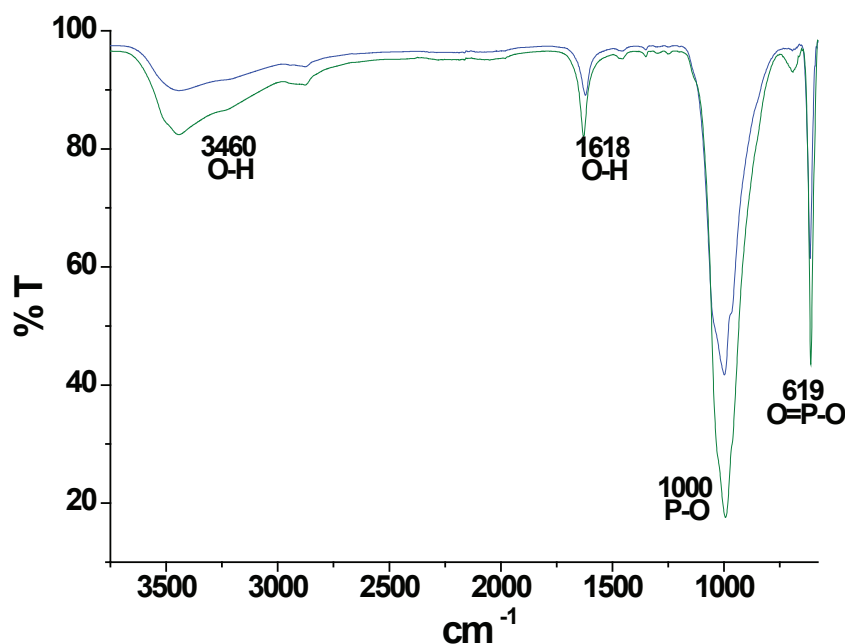


Figure II.23. IR spectra of  $\text{GdPO}_4$  (hydrothermal method) synthesized at pH 1 (blue) and pH 12 (green).

Since Ln-O bonds are not visible on these spectra, all particles with different chemical compositions from different methods have the same infrared feature. Only signals assigned to the phosphate group ( $\text{PO}_4^{3-}$ ) and water (in lattice and adsorbed in the surface) are visible. Also, the degree of hydration is not enough to make a difference on the IR signal. These results are consistent with the literature.

### 3.3.3 Stability of colloidal suspension

Zeta potential versus pH measurements of the colloidal solutions were taken and shown in Figure II.24. Solutions present all similar zeta potential curves, suggesting similarity in surfaces chemistry, despite their different synthesis conditions. Particles size does not influence remarkably their stability. Potential range is typically from 60 mV to -45 mV. The result shows that particles have all an IEP about 5.5, except for particle synthesized at pH 1, which has the PIE about 7. Nanoparticles suspensions with zeta potential out of range from +30 mV to -30 mV typically have high colloidal stability. Thus particles synthesized at pH 6, 9, and 12 are stable in pH range from 1 to 4.5 and above 11. The region of pH range 5-10 can be considerate as an instability zone. Particles synthesized at pH 1 are slightly more stable and present a larger range of stability from pH 1 to 5.5 and above 10.5.

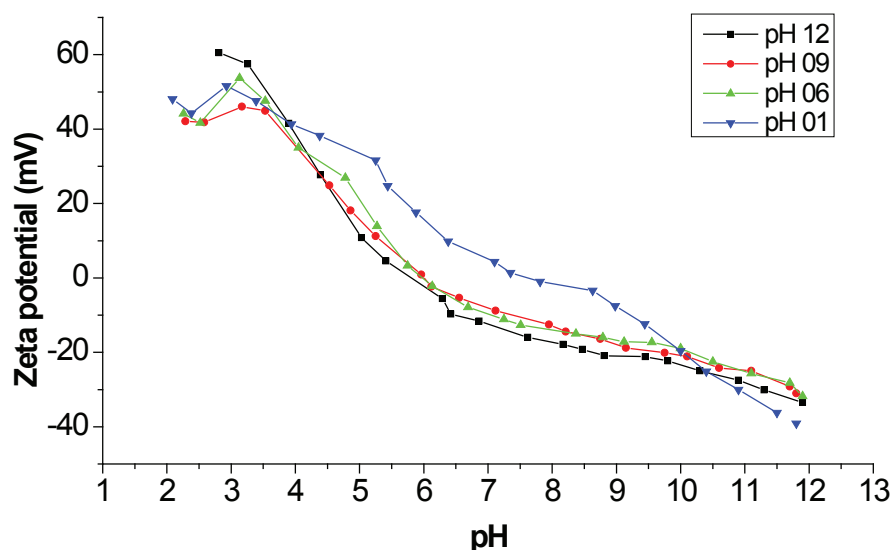


Figure II.24. pH versus zeta potential of various  $\text{GdPO}_4$  nanoparticles.

All these particles are stable in aqueous solution and can be kept in acid or alkaline solution without aggregation or precipitation. Moreover, they are not stable in neutral pH, close to the physiological conditions. One of the solutions to stabilize them is the surface functionalization.

### 3.3.4 Conclusion

GdPO<sub>4</sub> and Gd<sub>x</sub>La<sub>1-x</sub>PO<sub>4</sub> particles have been successfully synthesized by reflux and under hydrothermal conditions. They present all rhabdophane-type hexagonal phase and were obtained pure and well-crystallized. The synthesis method does not need catalyst, template or surfactant. It is simple, fast and clean. Size of the particles was adjusted according to temperature and pH of the synthesis, from 40 to 450 nm of length. Particles are stable in water in acidic or alkaline solution. Stability in neutral pH solution must be improved by surface functionalization.

## 3.4 Characterization of the naked TiO<sub>2</sub> for core-shell system

### 3.4.1 Morphological and structural characterization

Typical TEM pictures with the corresponding size distribution histograms are shown in Figure II.25 and Figure II.26. The average sizes of the nanoparticles is about 8-12 nm. We observed a relative narrow distribution size and when particles are treated hydrothermally (after reflux treatment), it was not observed an increase in the nanoparticles size or size distribution. Hydrothermal treatment doesn't lead to aggregation of the particles; they are well stabilized by peptization.

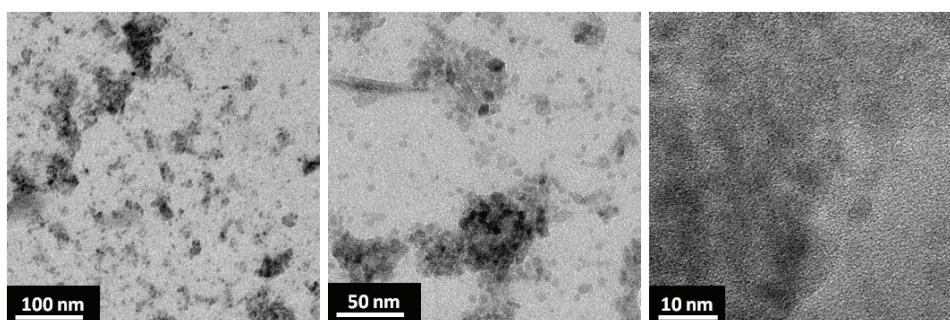


Figure II.25. TEM images of TiO<sub>2</sub> nanoparticles formed using reflux method, without hydrothermal treatment.

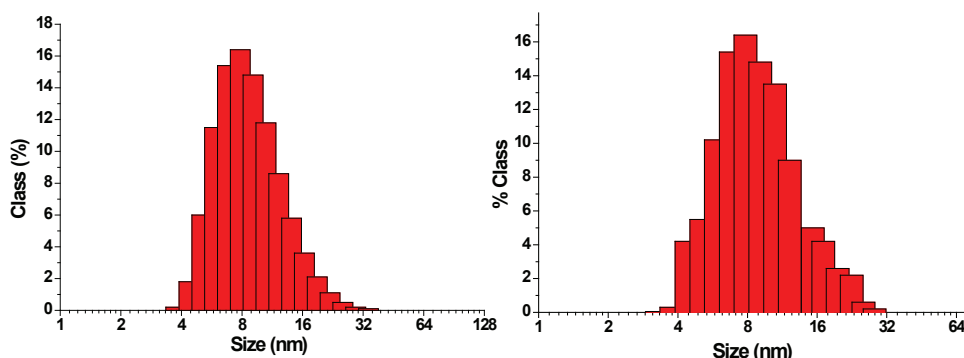


Figure II.26. Size distribution of TiO<sub>2</sub> nanoparticles, without (left) and with (right) hydrothermal treatment

Phase and crystallinity degree of the particles were evaluated by XRD (Figure II.27). As mentioned previously, titanium dioxide has three crystalline forms: rutile, anatase, and brookite.

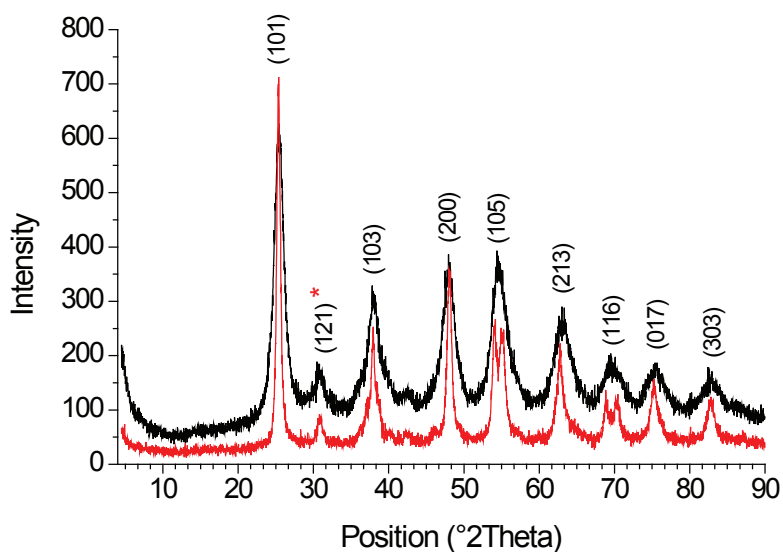


Figure II.27. XRD patterns (Copper K $\alpha$  radiation) of spherical anatase TiO<sub>2</sub>, (black) before hydrothermal treatment, (red) after hydrothermal treatment.

Brookite and anatase are metastable and can be transformed exothermally and irreversibly to the rutile over a range of temperatures, usually at 750 and 1000 °C, respectively<sup>290</sup>. Both samples from reflux and hydrothermal method are crystallized. However the peaks of hydrothermally treated particles are thinner and well defined than peaks of particles from reflux method, indicating a best crystallinity after hydrothermal treatment. The similitude of the both diffraction diagram shows that this hydrothermal treatment improve the crystallinity without leading to phase change. The diffraction peaks of both samples were in good agreement with the standard diffraction data for TiO<sub>2</sub> (JCPDS, Card No. 00-021-1272) and were indexed as anatase phase. Samples are mainly made of anatase phase; however we can note presence of the unique peak (121) which can be clearly identified as due to brookite phase (JCPDS, Card No. 00-016-0617). This peak has theoretically a relative intensity of 90 % in pure brookite phase and can be used to estimate the ratio of brookite phase in the particles. Peak (101) belongs to the both phases and theoretically represents 100 % of relative intensity according JCPDS, Card No. 00-021-1272 and 00-016-0617. From hydrothermal treated particles diffraction diagram, the weak peak (121) from brookite phase has 90 (u.a) intensity, then 100 % of intensity of (101) peak from exclusively brookite phase should has 100 u.a intensity, thus the intensity of (101) 715 u.a come mainly from anatase contribution:

$$\frac{100 \text{ u.a brookite)}}{715 \text{ u.a (anatase+brookite)}} \times 100 = 14 \% .$$

Particles are made of 86 % of anatase phase and 14 % of brookite phase.

### 3.4.2 Surface characterizations

IR spectrum of TiO<sub>2</sub> is shown in Figure II.28 . The large absorption bands observed at 3150 cm<sup>-1</sup> is attributed to O-H vibration bands from adsorbed water and hydroxyl group (Ti-O-H) in the particles surface. Presence of water is confirmed by the absorption band at 1634 cm<sup>-1</sup> corresponding to the bending vibration mode of H<sub>2</sub>O. The absorption bands at 1397 and 1329 cm<sup>-1</sup> can be assigned to N-O stretching and H-O-N binding mode<sup>291,292</sup> suggesting the presence of nitric acid used in the synthesis to peptize the particles solution. Peaks from N-O and H-O-N vibration are more intense in particles without dialysis (purification) than in the dialyzed particles. Indeed, dialysis is efficiency to remove nitrate ions from the colloid solution and from the surface of the particles.

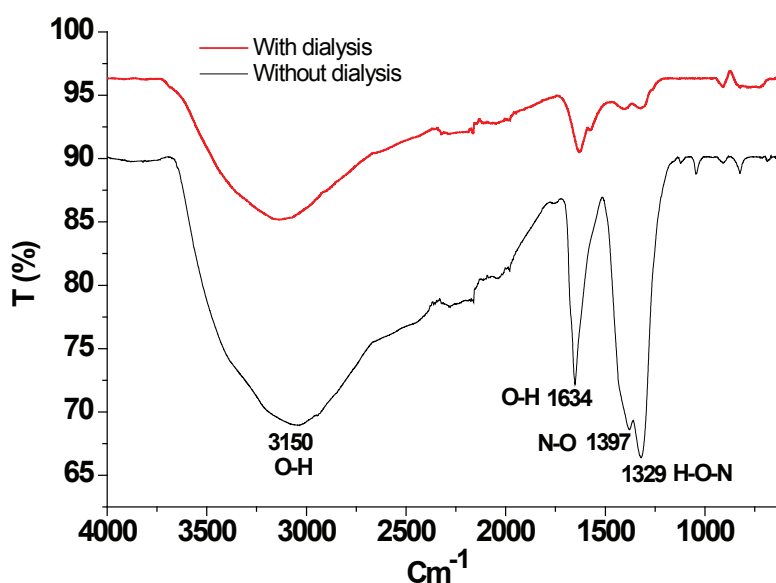


Figure II.28. IR spectra of TiO<sub>2</sub> without hydrothermal treatment

It is interesting to note the absence of bands at 2970, 1460 and 1130 cm<sup>-1</sup> corresponded to C-H stretching and C-O vibration respectively, observed for alkoxygroups in many alkoxide-derived particles. In our particles, there is no signal from isopropanol, suggesting that it is not adsorbed on the particle surface. The particles from hydrothermal treatment present a similar IR spectrum. The intensive band of OH-group evidences a large amount of water molecules adsorbed on TiO<sub>2</sub>. Thus water and nitrate are both adsorbed on the surface of the particles.

A typical TGA curve from RT to 1000 °C of TiO<sub>2</sub> nanopowders (without hydrothermal treatment) is shown in Figure II.29. This TGA curves demonstrate a unique weight loss of 7 % from room-temperature to 400°C. This weight loss is mainly attributed to dehydration (adsorbed water and lattice waters) and probably also the loss of nitric acid from the particles surface.

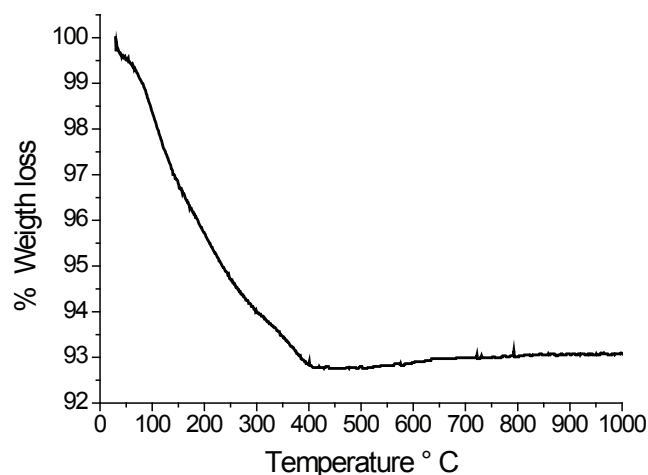


Figure II.29. TGA analysis of naked TiO<sub>2</sub> nanopowders

This results fit with literature TiO<sub>2</sub> surface investigated<sup>146,293</sup>. Bezrodna et al<sup>146</sup> was studied spectra of H-bonded from H<sub>2</sub>O on the surface of pure anatase and rutile nanocrystalline samples by IR spectroscopy. They proposed the surface structure in Figure II.30. TiO<sub>2</sub> surface bend with adsorbed water molecules by weak hydrogen bonds (Figure II.30-a), easily removed when temperature increases, until 180 °C. Some surface structures are additionally stabilized by the hydrogen bonds with neighboring anions of TiO<sub>2</sub> lattice and adjacent bridge OH-groups (Figure II.30-b,c) and can be removed at higher temperatures.

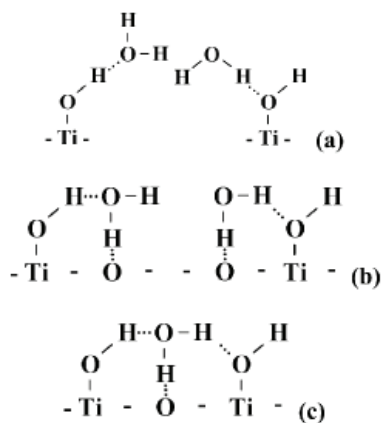
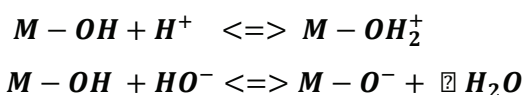


Figure II.30. Surface structures of the hydrated particles of TiO<sub>2</sub>

### 3.4.3 Colloidal stability

Suspensions of these particles are stable several months at the pH of the synthesis (pH 2) and can be destabilized in neutral solution. The particles are not sufficiently charged at these conditions. Titanium oxide particles create, in aqueous solution, a bi-phasic system with a solid/liquid interface.

The charge of this interface influences stability of nanoparticles. The layer of water chemisorbed forms hydroxyl (OH) groups on the surface. Other water molecules are physisorbed. The hydroxyl groups at the surface have acid-base properties that will bring charge on the surface of the particles<sup>294</sup> and have a role of reactive sites for the grafting reaction. Basically, at alkaline conditions, Ti-OH reacts with OH<sup>-</sup> ions and particles are negatively charged and at acid conditions, they react with protons and are positively charged.



Behavior of the colloidal suspension of the particles was examined by zeta potential and result is shown in Figure II.31. Because of the acid-base properties of the surface, Zeta potential versus pH curve of these particles is high and positive at low pH and lower and negative at high pH. it can be seen that if pH is below 4.5 or above 10 there is sufficient charge to confer stability to the suspension.

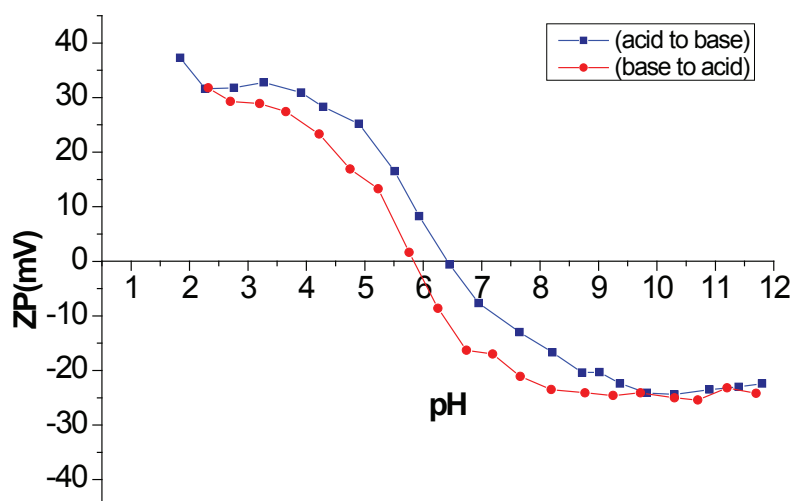


Figure II.31. Cyclic measurement of pH versus zeta potential of TiO<sub>2</sub> nanoparticles: (Blue) acid to alkaline measurement and (red) reverse measurement, alkaline to acid

However when pH is in range 4.5-10, the colloidal suspension is unstable. This charge phenomena and particles stability is reversible for these TiO<sub>2</sub> particles, with a little shift of IEP from 6.4 to 5.8 mV. At the naked form, these particles are not stable at neutral pH 7, suited for biological applications.

### 3.4.4 Conclusion

Titanium oxide particles were synthesized by hydrolysis of titanium isopropoxide. The resulting particles were treated under reflux or under hydrothermal conditions. Particles have spheroidal shape with around 10 nm in diameter. They are made of 86 % of anatase phase and 14 % of brookite phase. Hydrothermal treatment leads to more crystalline particles. Surfaces of the particles are hydrated and they are stable only in the very acidic or basic conditions. Thus they have to be further functionalized to ensure their stability in physiological conditions.

### 3.5 Characterizations of the pegylated particles

In the previous section we characterized three types of naked particles:  $GdF_3$ ,  $GdPO_4$  and  $TiO_2$ , which will correspond respectively to isotropic, anisotropic and core-shell systems after surface functionalization. To finish the realization of these particles as contrast agent, the first two systems made of magnetic cores ( $GdF_3$  and  $GdPO_4$ ) were be pegylated and the third consists of a diamagnetic core ( $TiO_2$ ), will be modified by grafting of a paramagnetic organic shell. We will first investigate the pegylation of isotropic and anisotropic systems. The implementation of the core-shell system will be investigated further.

Beyond stabilization in physiological conditions, pegylation will enhance circulation times of the particles in the blood stream and improve biocompatibility. Hereafter the pegylation of the systems is investigated via characterization of the surface, by highlighting presence of PEG on the surface and the anchoring mode.

#### 3.5.1 Characterizations of the isotropic system: $GdF_3@PEG$

For clarity and similarity of results, only results of the pegylated particles from reflux method are presented here. Surface of the as-prepared particles is studied with spectroscopic methods and TGA.

First of all, infra-red and nuclear magnetic resonance spectroscopy were performed to evidence presence of PEG molecules and the bending modes of bisphosphonate group on the particles surfaces. The P-O stretching region between 1300 and 800  $cm^{-1}$  is examined for this particle. In Figure II.32, the FTIR spectra of free bisphosphonate-PEG- $CH_3$  (BP-PEG- $CH_3$ ) and pegylated  $GdF_3$  ( $GdF_3@PEG$ ) are compared. This FTIR spectrum shows that BP-PEG- $CH_3$  is efficiently grafted on the particles. New bands from the grafted molecule appear on the  $GdF_3@PEG$  spectrum. The broadness and complexity of the peaks in this region make it difficult to interpret, however the large changes observed show that a strong interaction of the bisphosphonate head group with the  $GdF_3$  surface is present.

In the BP-PEG-CH<sub>3</sub> spectra we can observe bands from CH<sub>2</sub> at 2875 cm<sup>-1</sup> for stretching mode and at 1452 and 1348 cm<sup>-1</sup> for bending mode. Peak from C-O-C is visible at 1100 cm<sup>-1</sup>. In this spectrum, three important bands can be observed. The P=O double bond valence vibration occurs at 1246 cm<sup>-1</sup>, the absorption band at 1064 cm<sup>-1</sup> is attributed to the P-O bond and the absorption band at 923 cm<sup>-1</sup> come from the P-OH bond<sup>227,295,252</sup>.

In the GdF<sub>3</sub>@PEG spectrum we observe the appearance of the bands from BP-PEG-CH<sub>3</sub>. Band from P-O shifted from 1064 to 1105 cm<sup>-1</sup> with a relatively constant intensity, while band from P-OH is shifted from 923 to 945 cm<sup>-1</sup> with a strong decline in intensity. Peak assigned to P=O at 1246 cm<sup>-1</sup> has almost disappeared. These observations highlight the implication of P-OH bonds in the attachment on the particles. Disappearance of the peaks at 1200 and 950 cm<sup>-1</sup> assigned to the P=O and P-O-H groups was observed in the study of phenylphosphonic acid on ZrO<sub>2</sub><sup>227</sup>, and was interpreted as evidence for a tridentate chelating bonding mode or a tridentate bridging mode.

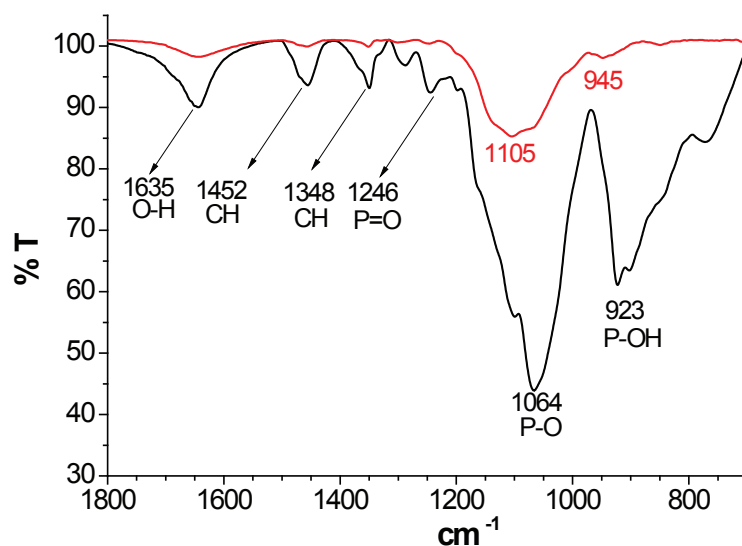
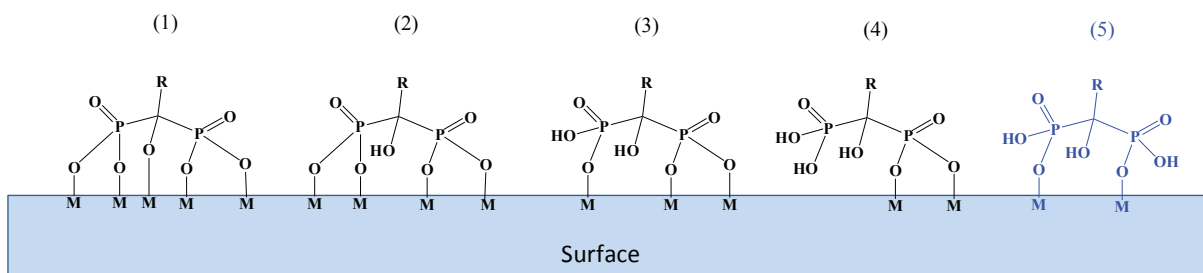


Figure II.32. FTIR spectra of free bisphosphonate-PEG-CH<sub>3</sub> (black) and GdF<sub>3</sub>@PEG (red)

Concerning bisphosphonate, each molecule have four P-OH functions and two P=O functions capable to react. Presence of P=O bond in very low intensity without shift suggests that they do not all participate in the reaction of grafting on the surface of the particles. Presence of P-OH function on the coated particles in low intensity with shift indicates that they did not all react. It appears therefore that some P-OH is involved in grafting reaction. It is difficult to determine the binding mode. Bidentate mode, involving each phosphonate group in monodentate mode is probably the more represented mode (Scheme II.7-(5)).



**Scheme II.7: Schematic representation of the possible bending modes of bisphosphonate molecules on  $GdF_3$  surface: bidentate mode (5) involving each phosphonate group in monodentate mode are the more probable bending mode.**

Since gadolinium fluoride is a paramagnetic particle and can disturb NMR measurement, an equivalent diamagnetic compound, lutetium fluoride ( $LuF_3$ ) was analyzed with  $^{31}P$  NMR after pegylation using the same method as for gadolinium particles. The obtained  $LuF_3@PEG$  particle is supposed to have a similar structure that  $GdF_3@PEG$ .  $^{31}P$  solid-state NMR spectra of  $LuF_3@PEG$  was taken (Figure II.33) and compared to the spectra of free BP-PEG- $CH_3$  (Figure II.34).

Free BP-PEG- $CH_3$  analyzed with  $^{31}P$  NMR indicates a uniform phosphorus peaks at 18.3 ppm, characteristic of a homogenous bisphosphonate groups<sup>296</sup>. The signals of bisphosphonate groups are broadened, probably due to the influence of polymer surrounding (PEG chain). Band at 3.4 ppm has too lower chemical shift to be assigned to one of the phosphorous from bisphosphonate witch should appears close to 20 ppm. This compound was indicated as 85 % of purity, thus this band comes certainly from phosphate ( $PO_4$  sites) derivatives species.

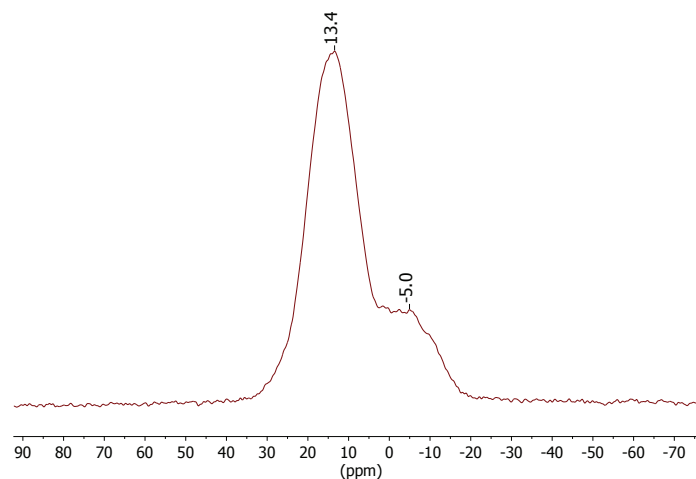


**Figure II.33.  $^{31}P$  NMR spectra of  $LuF_3@PEG$**

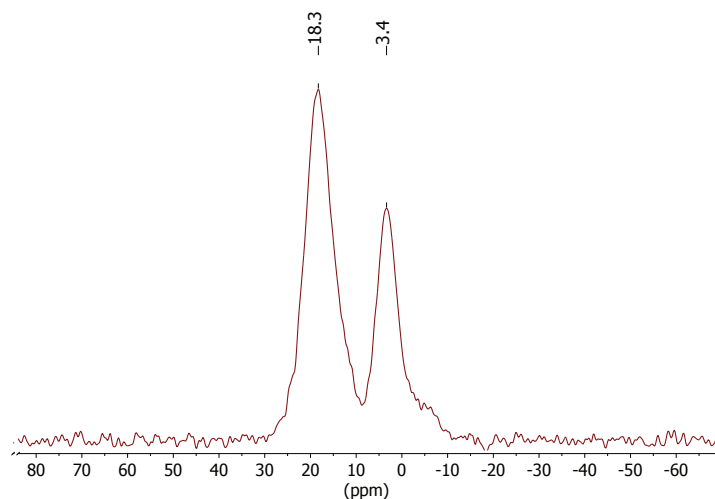


Figure II.34. <sup>31</sup>P NMR spectra of BP-PEG-CH<sub>3</sub>

Signal of LuF<sub>3</sub>@PEG is more broadened and shifted from 18.3 to 13.4 ppm compared to free BP-PEG-CH<sub>3</sub>. Width at half maximum has been enlarged from 7.5 to 14 ppm. These spectra indicate that the phosphonate group has reacted at the surface of the particles with formation of P-O-Lu bonds. The broadened weak peak centered at 5 ppm can be due to the anchoring of phosphate derivatives species on the particles. The peak at 13.4 ppm is symmetrical, suggesting a symmetric chemistry environment for phosphorus atom. Usually asymmetry of the peak is due to different environment of phosphorus on the surface of the particles, thus to different coordination modes. Here this asymmetry is not clearly evidenced, may be because of the broadening, observed also in case of phosphonate by Richard<sup>254</sup>, or because phosphorus atoms have really a symmetric chemistry environment. In this case, since the symmetrical mode (1) and (2) in Scheme II.7 are less probable due to residual P-OH (evidenced by IR analysis) and mode (3) and (4) are asymmetry, the symmetric monodentate mode (5) corresponds to these observations.

Also, this slight shift of 5 ppm (from 18.3 to 13.4 ppm) indicates a covalent bond in monodentate mode for each phosphonate head group, therefore an incomplete deprotonation of the phosphonate head group, highlighted also by the broaden band. This observation is in agreement with FTIR analysis. The absence of a clear asymmetry indicates probably the absence of an additional resonance. All phosphorus would be identical and anchored on the particles in identical bending mode.

TGA is presented in Figure II.35 and shows profiles of GdF<sub>3</sub>@PEG sample. The initial weight loss of 1.5 % from room-temperature to about 260°C can be assigned to desorption of the adsorbed water. The weight loss of 4 % from 260 to 1000 °C, can be attributed to dehydration of the lattice waters and decomposition of the organic species, BP-PEG-CH<sub>3</sub> and probably some trace of NMP.

Residual mass is around 94.5 % corresponding to the unfunctionalized and dehydrated inorganic particles core.

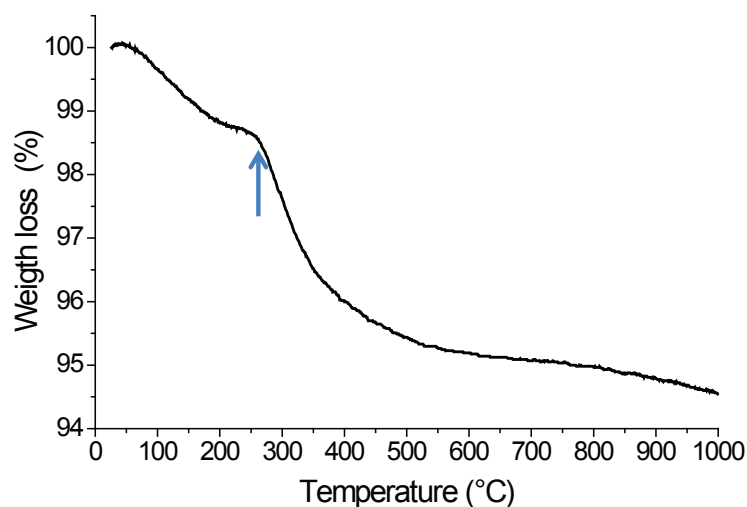


Figure II.35. TGA analysis of GdF<sub>3</sub>@PEG nanopowders

Presence of bands from PEG and bisphosphonate group is revealed by IR and NMR analysis. The results indicate that there is a covalent bond between PEG and particle. The anchoring involves mainly two phosphonate head group within one bisphosphonate molecule in monodentate mode (bidentate considering whole bisphosphonate group). TGA analysis shows two weight loss related to water and PEG molecules loss. These results evidence pegylation of gadolinium fluoride nanoparticles.

### 3.5.2 Characterizations of the anisotropic system: GdPO<sub>4</sub>@PEG

For clarity and similarity of results, only IR results of the pegylated particles from reflux method are presented here. Particles from hydrothermal with different sizes are examined by TGA.

Infrared spectra of the naked gadolinium phosphate particles were analyzed in previous section. The main bands were found at 1000 cm<sup>-1</sup> for stretching mode of P-O, 619 cm<sup>-1</sup> for bending vibration mode of O-P=O. The sharp band at 1618 cm<sup>-1</sup> was associated with the deformation vibration of H-O-H bonds of the water molecules and the broad band at 3460 cm<sup>-1</sup> was associated with the stretching vibration O-H.

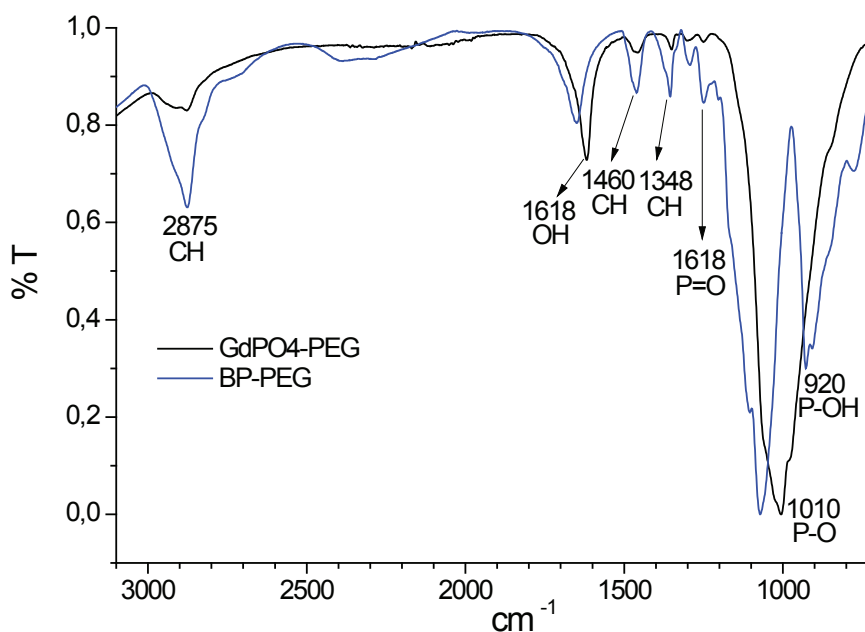


Figure II.36. FTIR spectra of naked  $\text{GdPO}_4$  (black) and  $\text{GdPO}_4@$ PEG (blue)

Since phosphate groups are present in the particle, it is difficult to study the anchoring mode of bisphosphonate on the particles by IR. Binding of phosphonate to the surface of  $\text{GdPO}_4$  nanoparticles were already demonstrated by confocal laser scanning microscopy<sup>139</sup> using fluorescent molecules. The result showed that coordinated covalent bonds can be formed between the phosphonate group and  $\text{Gd(III)}$  ions at the surface. In fact,  $\text{Gd(III)}$  surface free sites are bound to oxide and hydroxide groups, and the phosphonate group can displace the oxides and hydroxides on the surface. Here bands from PEG on the surface of the particles are needed to evidence the grafting efficiency. In the BP-PEG- $\text{CH}_3$  spectra,  $\text{CH}_3$  bands at  $2875 \text{ cm}^{-1}$  for stretching mode and at  $1452$  and  $1348 \text{ cm}^{-1}$  for binding mode are present in  $\text{GdPO}_4@$ PEG spectra and shifted at  $2880$ ,  $1460$  and  $1350 \text{ cm}^{-1}$  respectively (Figure II.36). This functionalization was also evidenced thanks to its capacity to allow dispersion of large amounts of particles in water. Samples containing as much as  $700 \text{ mg}$  of pegylated particles per mL of water were prepared by my colleagues and did not show any trace of irreversible aggregation<sup>297</sup>.

Thermal analysis of the pegylated nanorods, from hydrothermal methods were performed and compared to the naked  $\text{GdPO}_4$  nanorod (Figure II.37). It can be seen that weight loss depends strongly on surface functionalization and hydration of the core particles.

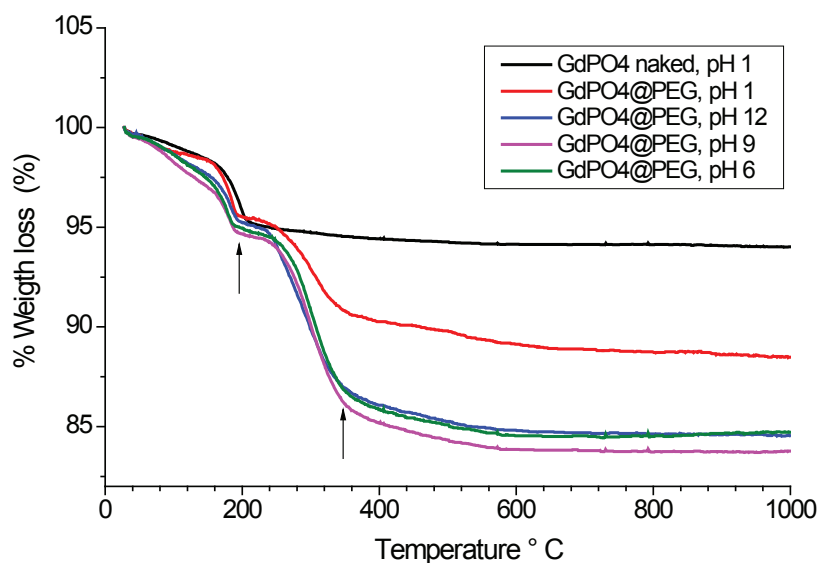


Figure II.37. TGA analysis of naked GdPO<sub>4</sub> (black) and various GdPO<sub>4</sub>@PEG nanopowders, with indicated pH of the synthesis

We observe three levels corresponding to the weight loss related to the evaporation of the adsorbed water (RT-200°C), dehydration of lattice waters (200-350 °C) and decomposition of PEG (350-600 °C). Both naked and pegylated particles loss 5 % of weight from RT to 200 °C, assigned essentially to adsorbed water evaporation. The naked particles synthesized at pH 1 (black) is hydrated with one water molecule per GdPO<sub>4</sub> molecule (GdPO<sub>4</sub>:1 H<sub>2</sub>O), loss only 1 % of weight from 200 °C to 350 °C due to dehydration of lattice waters; while the pegylated version (red) loss 5 % of weight at the same temperature range (200-350 °C), probably due to dehydration of lattice waters and dehydration of the grafted PEG molecules. PEG is a hydrophilic molecule that can contain water bound via hydrogen bonds. This pegylated version (green) loss 2.5 % of weight at 350-1000 °C related to PEG decomposition.

The pegylated particles whose inorganic cores are synthesized at pH 6, 9 and 12 (respectively red, pink and blue) are more hydrated (GdPO<sub>4</sub>: 1.5 H<sub>2</sub>O). Thus the weight loss assigned to dehydration of lattice waters is more important, 10 % at 200-350 °C.

The weight loss related to PEG decomposition is almost identical for all pegylated particles, 2.5 % at 350-1000 °C.

Bands from PEG revealed in IR analysis and weight losses assigned to PEG decomposition confirm definitively pegylation of these nanorods. Since weight loss corresponding to PEG decomposition is identical for all particles, it seems that these particles are identically functionalized with the same amount of PEG. Grafting rate of this particle will be discussed later.

### 3.5.3 Conclusion on pegylation of the particles $GdF_3$ and $GdPO_4$

Pegylation of the particles is definitively evidenced by TGA, IR and NMR spectroscopies. Groups from BP-PEG- $CH_3$  were successfully identified in IR and NMR. TGA curves comparison shows clearly weight loss at high temperature (350 – 1000°C) only for pegylated particles, attributed to PEG decomposition. From IR and NMR spectroscopies, the binding mode informations of phosphonic acids within bisphosphonate onto metal ions is not easy to obtain. In literature the developed investigations do not discuss the binding mode of bisphosphonate<sup>298,299,300,301</sup> contrary to phosphonate. A few studies of long-chain phosphonic acid (from phosphonated molecules) forming self-assembled monolayers on oxide materials were carried out<sup>252,254,301,302,303,304,305</sup>. However, the exact nature of the binding mode of phosphonic acids on metal ions has not been clearly revealed. Some studies show that phosphonic acid monolayer formation on oxide surface took place predominantly via bidentate and tridentate binding involving P-O-M bonds. In this work, presence of residual P=O and P-O-H in IR spectrum and the slight shift of 5 ppm indicating a covalent bond in monodentate mode (for each phosphonate head group), discarded the possibility of tridentate binding mode. Hypothesis of a bidentate anchoring mode for whole bisphosphonate involving each phosphonate group in monodentate binding mode is privileged as presented in the proposed structures in Scheme II.7-5.

The obtained systems can be schematically represented as pegylated spherical and rod shape particles corresponding to the isotropic and anisotropic systems (Figure II.38). Their behavior in aqueous solution including stability and capacity to enhance relaxivity of proton as contrast agent will be investigated.

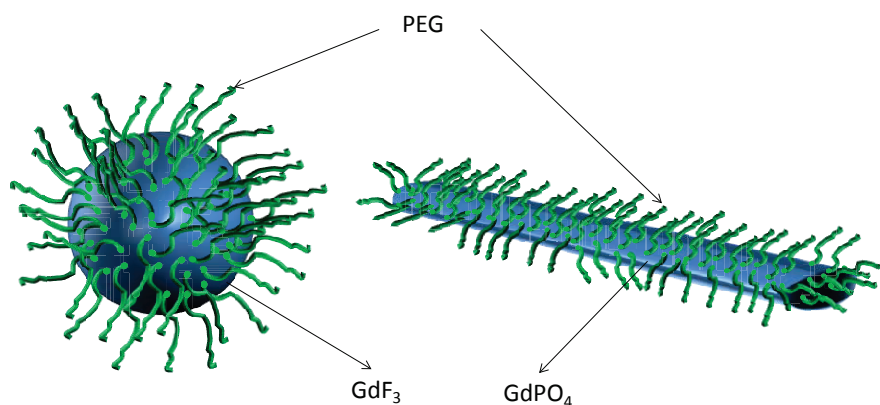


Figure II.38. Schematic representation of isotropic and anisotropic system:  
 $GdF_3@PEG$  (left) and  $GdPO_4@PEG$  (right)

### 3.6 Characterizations of the core-shell system: TiO<sub>2</sub>@DOTA-Gd(III)

In this part, the modified TiO<sub>2</sub> will be studied step by step, from pegylation, DOTA conjugation, to gadolinium chelating. We are interested in the characterizations of the surfaces in order to identify functions present at different stages of the modification. Only particles from reflux method were used to develop the core-shell system. Samples were collected at each stage of the preparation.

#### 3.6.1 Surface analysis

##### ✓ Pegylated TiO<sub>2</sub> (TiO<sub>2</sub>@PEG)

The first step in TiO<sub>2</sub> modification is pegylation. TiO<sub>2</sub> particles are pegylated for the similar reasons given for the previous particles, with the difference that here the used PEG is an amino-PEG, to allow conjugation of DOTA-NHS by peptide coupling. The pegylated particles were characterized by IR and NMR, in order to highlight the presence of PEG and NH<sub>2</sub> group. Amine group must be free for peptide coupling.

In the BP-PEG-NH<sub>2</sub> spectra (Figure II.39), bands at 2874 and 2919 cm<sup>-1</sup> and at 1453 and 1351 cm<sup>-1</sup> are assigned respectively to stretching mode and bending mode of CH<sub>2</sub>. The P=O double bond valence vibration is visible at 1246 cm<sup>-1</sup>, the broad absorption band at 1068 cm<sup>-1</sup> is attributed to the P-O bond, overlapped the C-O-C band expected around 1100 cm<sup>-1</sup> and the absorption band at 909 cm<sup>-1</sup> come from the P-OH bond<sup>227,295,252</sup>. The broad band from 3658 to around 3000 cm<sup>-1</sup> is assigned to O-H groups involved in hydrogen bonds. This band is too broadened and intense that it overlaps with the bands of the stretching mode of NH expected around 3300 cm<sup>-1</sup>, less intense in some cases<sup>266</sup>. We can see band due to binding mode of NH<sub>2</sub> at 1515 cm<sup>-1</sup>.

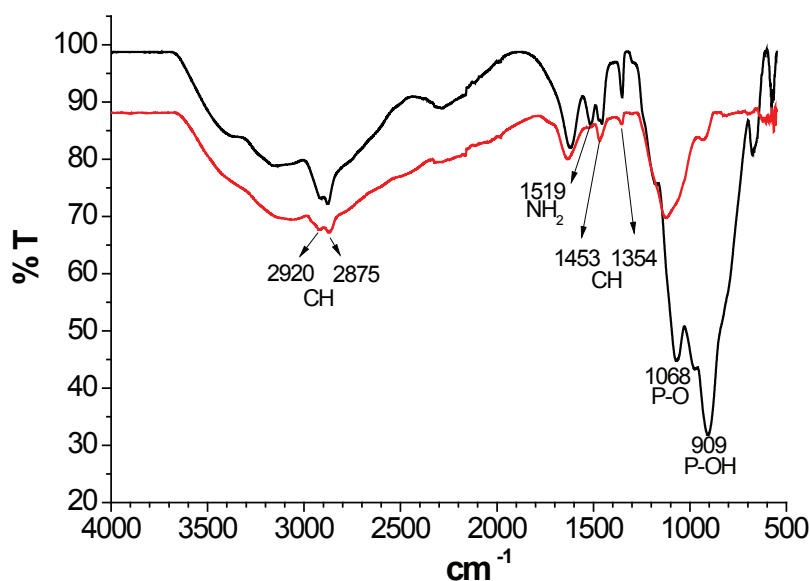


Figure II.39. FTIR spectra of free BP-PEG-NH<sub>2</sub> (black) and TiO<sub>2</sub>@PEG (red)

TiO<sub>2</sub>@PEG spectrum (Figure II.39) shows appearance of the bands at 2875, 2920 cm<sup>-1</sup> and at 1453 and 1354 cm<sup>-1</sup> assigned to CH<sub>2</sub>. As for GdF<sub>3</sub>@PEG, band due to P-O shifted from 1068 to 1125 cm<sup>-1</sup> with a relatively constant intensity, while band from P-OH is shifted from 909 to 929 cm<sup>-1</sup> with a strong decline in intensity. Peak assigned to P=O at 1245 cm<sup>-1</sup> has also almost disappeared, maintaining the identical frequency without shift. BP-PEG-CH<sub>3</sub> and BP-PEG-NH<sub>2</sub> seems to react identically on GdF<sub>3</sub> and TiO<sub>2</sub> respectively. Presence of broad band from 3658 to around 3000 cm<sup>-1</sup> (O-H, N-H) and band from binding mode of NH<sub>2</sub> at 1519 cm<sup>-1</sup> suggests that only phosphonate groups react on the particle and NH<sub>2</sub> groups remain free. The previously bidentate anchoring mode, proposed for GdF<sub>3</sub>@PEG and GdPO<sub>4</sub>@PEG (Scheme II.7-5), seems valid for TiO<sub>2</sub>@PEG particles.

<sup>31</sup>P NMP spectrum of TiO<sub>2</sub>@PEG (Figure II.40) is similar to that of LuF<sub>3</sub>@PEG (Figure II.33) suggesting a similar anchoring structure. Also <sup>13</sup>C NMR spectrum (Figure II.41) shows a unique band at 70 ppm assigned to CH<sub>2</sub> from PEG. These results confirm anchoring of bisphosphonate and presence of PEG on TiO<sub>2</sub> and then evidence pegylation of the particles.

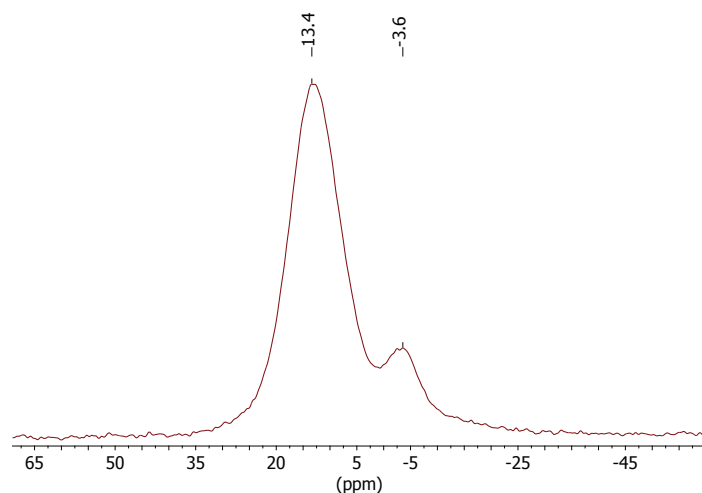


Figure II.40. <sup>31</sup>P NMR spectra of TiO<sub>2</sub> sample modified BP-PEG-NH<sub>2</sub> (TiO<sub>2</sub>@PEG)

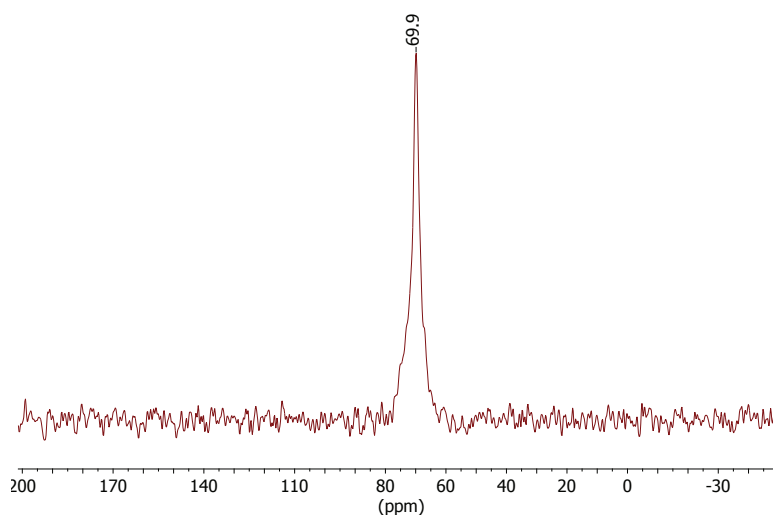


Figure II.41. <sup>13</sup>C NMR spectra of TiO<sub>2</sub> sample modified BP-PEG-NH<sub>2</sub> (TiO<sub>2</sub>@PEG)

✓ **DOTA coated TiO<sub>2</sub> (TiO<sub>2</sub>@PEG-DOTA)**

NHS ester is spontaneously reactive with primary amines (–NH<sub>2</sub>). Thus DOTA were conjugated with amino pegylated TiO<sub>2</sub> nanoparticles by reacting *N*-hydroxysuccinimide (NHS) ester within DOTA-NHS and the free NH<sub>2</sub> group present on the particles. Samples were collected and analyzed. IR spectrum of the obtained particles TiO<sub>2</sub>@PEG-DOTA (not shown) is complicate to examine because of the overlapping of several bands. Some new peaks of TiO<sub>2</sub>@PEG-DOTA spectrum (1385, 1325 cm<sup>-1</sup>) fit with peaks from DOTA-NHS and band at 1719 cm<sup>-1</sup> can be identifies as C=O stretching mode. <sup>13</sup>C NMR spectra has performed and presented here (Figure II.42). CH<sub>2</sub> band at 70 ppm assigned to PEG is identified and bands assigned to C=O and CH<sub>2</sub> from DOTA were clearly identified respectively at 170 and 50 ppm. These bands confirm conjugation of DOTA with the particle.

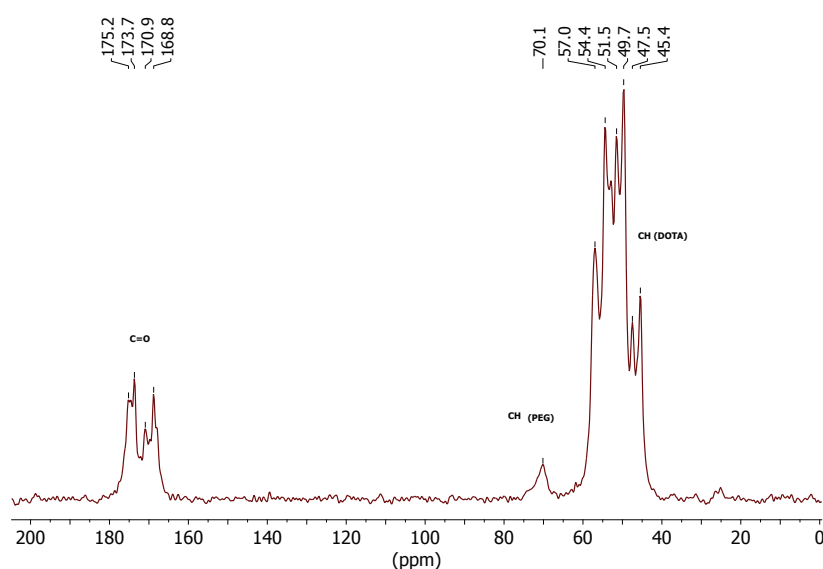


Figure II.42. <sup>13</sup>C NMR spectra of TiO<sub>2</sub>@PEG-DOTA

✓ **DOTA-Gd(III) coated TiO<sub>2</sub> particles (TiO<sub>2</sub>@PEG-DOTA-Gd(III))**

Because of the paramagnetic propriety of Gd(III), we synthesize TiO<sub>2</sub>@PEG-DOTA-Lu(III) for NMR purpose. The obtained particle has a similar structure with TiO<sub>2</sub>@PEG-DOTA-Gd(III) because of the capacity of DOTA to chelate lanthanide ions. Infrared spectra of TiO<sub>2</sub>@PEG-DOTA-Gd(III) and TiO<sub>2</sub>@PEG-DOTA-Lu(III) are generally unchanged compared to that of TiO<sub>2</sub>@PEG-DOTA one. <sup>31</sup>P NMR spectrum of TiO<sub>2</sub>@PEG-DOTA-Lu(III) (Figure II.44) is broadened compared to that of TiO<sub>2</sub>@BP-PEG-NH-DOTA one (Figure II.43), due to Gd(III) chelation and shift remains unchanged at 13.4 ppm. Presence of Gd(III) was also evidenced by ICP analysis.

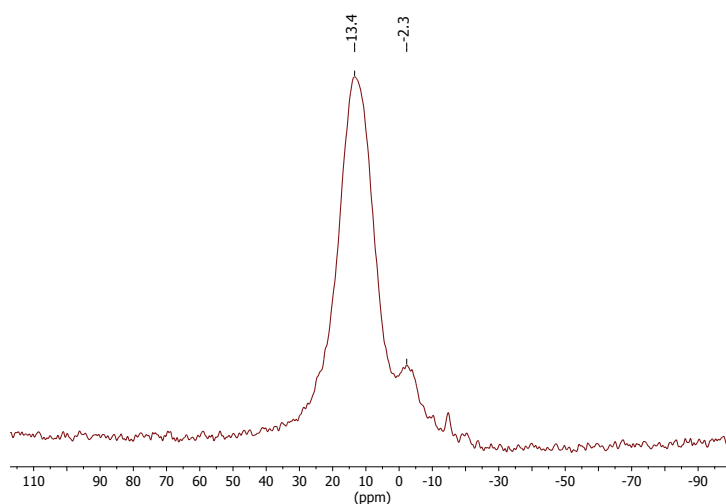


Figure II.43.  $^{31}\text{P}$  NMR spectra of  $\text{TiO}_2\text{@PEG-DOTA}$

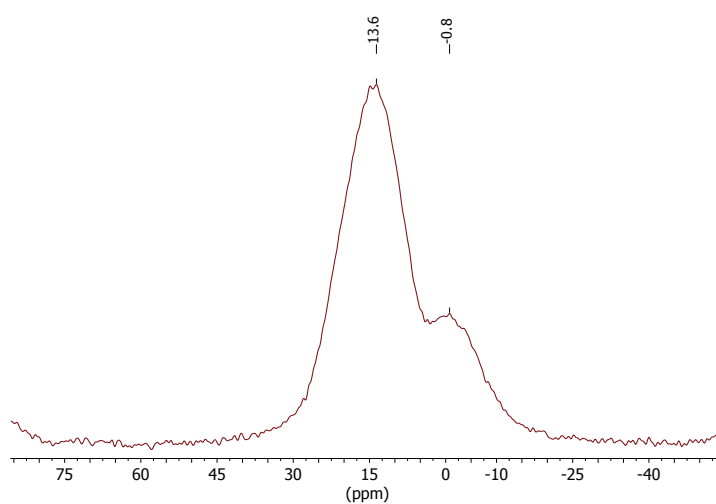


Figure II.44.  $^{31}\text{P}$  NMR spectra of  $\text{TiO}_2\text{@PEG-DOTA-Lu(III)}$

TGA profiles of the naked and modified  $\text{TiO}_2$  nanoparticles are presented in Figure II.45. The naked  $\text{TiO}_2$  has a unique weight loss of 7 % from RT to 400 °C, corresponding mainly to evaporation of the adsorbed water and dehydration of lattice waters.

$\text{TiO}_2\text{@PEG}$  loss 11 % of weight from RT to 300 °C, assigned to water evaporation and dehydration of lattice waters; and 4 % from 300°C to 600 °C, assigned to PEG decomposition.

The weight loss profile of  $\text{TiO}_2\text{@PEG-DOTA}$  can be divided in four parts. The first one with a 6 % loss from RT to 120 °C (water evaporation), the second part with a 24 % loss in temperature range 120-250 °C assigned to dehydration of lattice waters and dehydration of water bound to PEG-NH-DOTA molecules. We can see the third and the fourth parts with respectively the weight loss of 15 % (250-380°C) and 15 % (380-600°C) assigned to BP-PEG-NH<sub>2</sub> and DOTA decomposition.

It can be seen the total weight loss of about 18 % in the range RT-1000 °C for TiO<sub>2</sub>@PEG-DOTA-Gd(III), lower than that of TiO<sub>2</sub>@PEG-DOTA (60 %) in the same temperature range; because the weight related to gadolinium ion can't not be lost (gadolinium ion can't be decomposed and evaporated), minimizing the total weight loss. This observation confirms gadolinium chelation by DOTA.

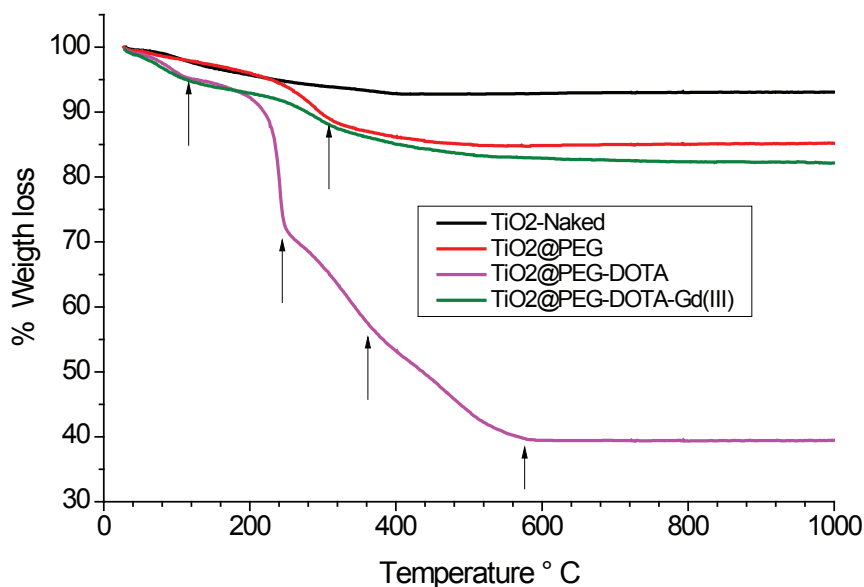


Figure II.45. TGA analysis of naked TiO<sub>2</sub> (black) and various modified TiO<sub>2</sub> nanopowders

Figure II.46 and Figure II.47 show TGA-DTA analysis of TiO<sub>2</sub>@PEG and TiO<sub>2</sub>@PEG-DOTA particles. TiO<sub>2</sub>@PEG presents the first weight loss, with an 11 % loss in the range from RT to 300 °C, assigned to water evaporation. The second part, with a total weight loss of about 4 % in the temperature range 300-800 °C, assigned to the dehydration of lattice waters and decomposition of PEG molecule is confirmed by the exotherm in at about 300 °C on the DTA profile.

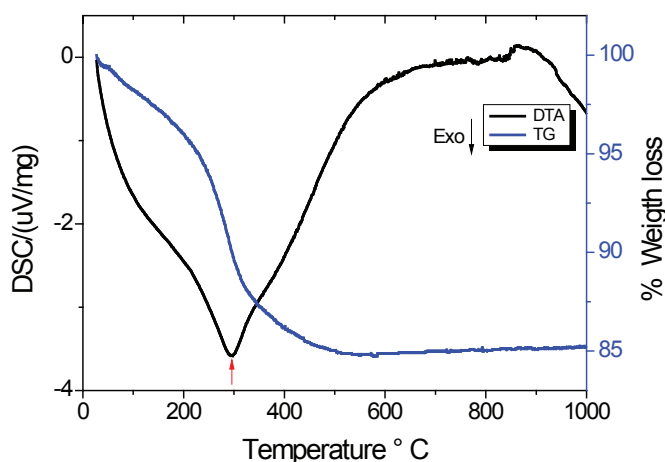


Figure II.46. TGA and TG analysis of TiO<sub>2</sub>@PEG nanopowders

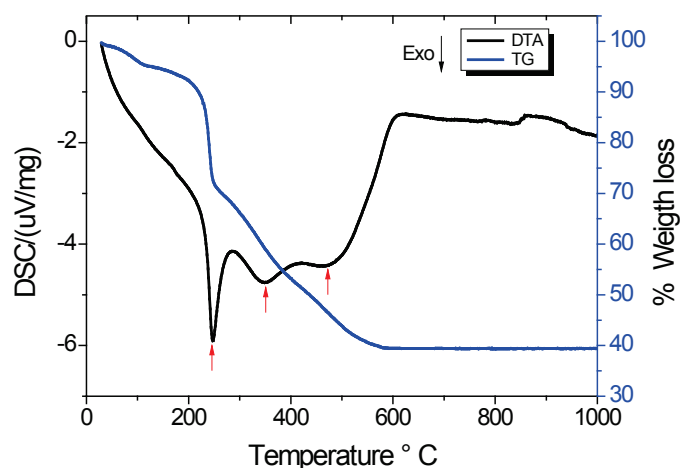


Figure II.47. TGA and TG analysis of  $\text{TiO}_2$ @PEG-DOTA nanopowders

In the  $\text{TiO}_2$ @PEG-DOTA profile, we can distinguish, weight loss due to water evaporation (6 %, RT-120 °C) and dehydration of lattice waters and certainly water from DOTA complex (24 %, 120-250°C) confirmed by exotherm at about 250 °C. Weight loss due to decomposition of PEG (15 %, 250-380 °C) and DOTA (15 %, 250-800°C) are confirmed respectively by exotherms at about 380 °C and 500 °C on the DTA profile. This observation confirms the grafting of the PEG-NH-DOTA moiety.

### 3.6.2 Conclusion on DOTA-Gd(III) modified $\text{TiO}_2$

In conclusion, we have developed a core-shell particle made of the diamagnetic titanium oxide core and a paramagnetic organic shell (Figure II.48). It was achieved using the highly metal-complexing agent (DOTA) containing a bisphosphonate group as the anchoring group. Gd(III) was chelated to this hybrid nanomaterial. Hence, a stable core-shell magnetic particle was obtained and may serve as a magnetic resonance contrast agent for MRI. Preparation was monitored step by step and the final structure of the particles was definitively evidenced by TGA, IR and NMR spectroscopies.

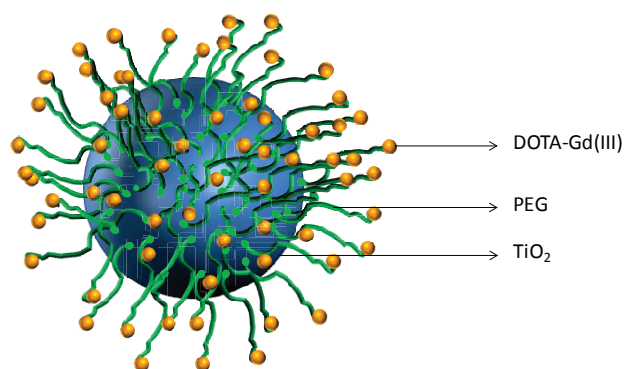


Figure II.48. Schematic representation of core-shell system:  $\text{TiO}_2$ @PEG-DOTA-Gd(III)

The structural characterizations of all three systems are performed. Hereafter we will see the grafting density (number of organic molecules/nm<sup>2</sup>) for each system, and we will study their behavior in aqueous solution. I.e. their colloidal stability and their ability to accelerate proton relaxation rate as a magnetic contrast agent.

### 3.7 Grafting density study

It is crucial to determine grafting density to evaluate relaxivity potential of the particles. The amount of molecules on the surface, forming organic layer, directly affects the particle-bulk water interaction and therefore the relaxivity. Moreover high grafting density is needed to properly ensure the stability of particles by steric repulsion. For core-shell system, number of PEG per particle is also related to number of gadolinium ions supported by particle. Also nanoparticles have a large surface area/volume ratio and tend to adsorb plasma proteins and are quickly cleared by macrophages before they can reach the target. Then a high grafting density will guard against proteins adsorption and thus increase circulation time of nanoparticles in the blood stream. Two methods were used for grafting density estimation and are detailed below.

#### ✓ TGA method

We observe in TGA curves different loss weight. The first one,  $\Delta m_1$  (mg) attributed mainly to the solvent evaporation and the second one,  $\Delta m_2$  (mg) corresponds mainly to decomposition of the organic moieties. Grafting density in mole of molecule per gram of particles can be estimate by this formula:

$$r_1 = \frac{\Delta m_2}{(m_{sample} - \Delta m_1) \times M_{grafting}}$$

$m_{sample}$  is the initial masse of the analyzed sample (mg)

$M_{grafting}$  is molar mass of the grafted molecule (g.mol<sup>-1</sup>)

For a particle with density ( $d$ ), volume ( $V_{NP}$ ), surface area ( $S_{NP}$ ); number of grafted molecule per particle and per nm<sup>2</sup> respectively  $\tau_1$  and  $\tau_2$  are given by:

$$\tau_1 = \frac{r_1 m \times V_{NP} \times N_A}{d}$$

$$\tau_2 = \frac{\tau_1}{S_{NP}}$$

✓ **ICP method**

ICP analysis provides metal (gadolinium or titanium) and phosphorus atoms concentration of the samples. Grafting molecules concentration (per particle and per nm<sup>2</sup>) was estimate for modified gadolinium fluoride and titanium oxide particles. This estimation is more complicate for phosphate gadolinium particle because this particle contain phosphorus atom before and after surface modification contrary to GdF<sub>3</sub> and TiO<sub>2</sub>. (ICP analysis should be done before and after grafting, which we have not done right now). Concentration of bisphosphonate grafted on particle surface were calculated assuming a perfectly spherical uniform particles, with unique crystalline phase, orthorhombic, space group Pnma (JCPDS, Card No. 00-012-07-88) for GdF<sub>3</sub> and anatase, tetragonal space groupe I41/amd (JCPDS, Card No. 00-021-1272) for TiO<sub>2</sub>. The diameter core size used is 15 and 10 nm respectively.

For a particle with diameter (D), volume ( $V_{NP}$ ), volume of cell ( $V_{cell}$ ) and number of metallic atom per cell (Z); number of metal atom per particle ( $N_{Metal}$ ) and number of mole of metal atom per particle ( $N_{m Metal}$ ) are given by:

$$N_{Metal} = \frac{Z \times V_{NP}}{V_{cell}} = \frac{2 \pi D^3}{3 V_{cell}}$$

Then,

$$N_{m Metal} = \frac{2 \pi D^3}{3 V_{cell} N_A}, \text{ NA is Avogadro constant}$$

For  $C_M$  and  $C_P$  respectively concentration (mg/mg of sample) of metal and phosphorus atom from ICP, number of PEG per particle and per nm<sup>2</sup>  $\tau_1$  and  $\tau_2$  are given by:

$$\tau_1 = \frac{C_P \times 0.5 \times N_{Metal} \times M_{m Metal} \times N_A}{M_P \times C_M}$$

and

$$\tau_2 = \frac{\tau_1}{S_{NP}}$$

The estimation result from TGA and ICP analysis is summarized in Table II.5

**Table II.5. Grafting density of the particles modified by bisphosphonate molecule**

Nanoparticle	Grafting density			
	ICP		TGA	
	Nber PEG/NP	Nber PEG /nm <sup>2</sup>	Nber PEG /NP	Nber PEG /nm <sup>2</sup>
GdF <sub>3</sub> @PEG	1294	1,83	637	0,68
GdPO <sub>4</sub> @PEG-pH 1	-	-	19897	0,63
GdPO <sub>4</sub> @PEG-pH 6	-	-	4667	0,80
GdPO <sub>4</sub> @PEG-pH 9	-	-	524	0,58
GdPO <sub>4</sub> @PEG-pH 12	-	-	498	0,55
TiO <sub>2</sub> @PEG	872	2,78	321	1,02
TiO <sub>2</sub> @PEG-DOTA	676	2,15	324	1,03

Grafting density depends on the reactivity of the particles surface, related to their structure (chemical composition, crystallinity, morphology ...). According to TGA method, grafting density is similar for GdF<sub>3</sub> and GdPO<sub>4</sub> particles, probably due to the presence of gadolinium ions. Contrary to what we may expect, nanorods shape GdPO<sub>4</sub> particles seem to not influence the grafting density, suggesting that all surfaces of the nanorods have a similar reactivity regarding bisphosphonate. Also, number of PEG chains per particle increases when pH of the synthesis decreases (from 19 897 to 498 PEG/NP). That is number of PEG chains per particle increases with the particle size while the grafting density remains almost constant. Then all particles surface is covered with PEG chains, not only the ends, which are supposed to be more reactive.

Grafting density of TiO<sub>2</sub>@PEG and TiO<sub>2</sub>@PEG-DOTA particles are similar and higher to that of GdF<sub>3</sub> and GdPO<sub>4</sub>. Probably due to the density of active site on the TiO<sub>2</sub> particles or a best reactivity of TiO<sub>2</sub> compare to GdF<sub>3</sub> and GdPO<sub>4</sub>. The grafting density values (0.55-2.7 PEG chains per nm<sup>2</sup>) are close to those found for gold particles coated Thiol-Terminated “long” polystyrene (PS<sub>125</sub> – SH), 0.9-1.2 chains per nm<sup>2</sup> and lower than those of gold particles coated Thiol-Terminated “short” polystyrene (PS<sub>19</sub> – SH), 3-4 chains per nm<sup>2</sup>, according to Muriel et al.<sup>230</sup>. Grafting density depends also on the size of the grafting molecule and the anchoring group. Guerrero et al.<sup>252</sup> have used a similar method to graft various phosphonate-terminated molecules on TiO<sub>2</sub> particles and have find grafting density around 1.3-4.7 molecules per nm<sup>2</sup>. Phosphonate and other simple molecules have a footprint around 20-25 Å<sup>2</sup><sup>252,230,306</sup>. Using bisphosphonate in our case, the footprint of the molecule can be double due to the restrictions imposed by the neighboring phosphonate, leading to a slight decrease of grafting density.

Also, the grafting density from TGA method could be underestimated, because residual mass of the particles is assumed to be mass of the core particles. And grafting density was estimated using density of particles (from crystallographic data), theoretical volume and surface area. However residual mass can be made of core particles and some un-evaporated phosphorus species, then PEG molecule mass could be underestimated and core particles mass overestimated, leading to the underestimating grafting density.

Using bisphosphonate we probably strengthen interaction between the particle and the grafted molecule without losing grafting density despite a larger foot-print. Also, these grafting densities indicate a high degree of self-assembly in the monolayer on surface of the particles.

### 3.8 Colloidal stability study of the developed hybrid particles

All modified particles can be easily dispersed in water, physiological water (0.9 % NaCl) and PBS. Concentration can be high for  $GdF_3@PEG$  and  $GdPO_4@PEG$ . Concentrated solutions were obtained by slowly adding weighed amounts (400–700 mg) in 1 mL of water<sup>297</sup>.

Size distribution of the particles dispersed in PBS was investigated with DLS (Figure II.49). It can be seen a shift of the hydrodynamic diameter, compared to naked particles, mainly due to the presence of PEG on the surfaces of the particles. Hydrodynamic diameter shifts from 30 to 60 nm, from 120 to 180 nm and from 8 to 20 nm respectively for  $GdF_3@PEG$ ,  $GdPO_4@PEG$  and  $TiO_2@PEG-DOTA-Gd(III)$ . Diameters of isotropic and core-shell systems were doubled after functionalization, which is consistent with literature<sup>230</sup>, in cases of functionalization with highly water-soluble molecules such as PEG. Diameter shift is lower for  $GdPO_4@PEG$  particles, certainly due to its anisotropic shape. However, these different particles present one single peak, suggesting that there is not aggregation leading to larger particles.

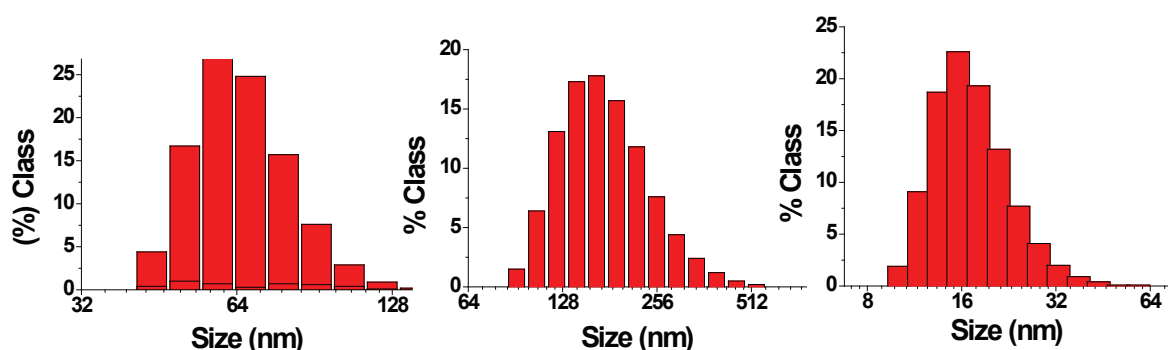


Figure II.49. Size distribution of the modified particles in PBS solution  $GdF_3@PEG$  (left),  $GdPO_4@PEG$  (middle) and  $TiO_2@PEG-DOTA-Gd(III)$  (right)

Zeta potential versus pH results (Figure II.50) show similar profile curve compared to those of the naked particles. Also potential fall abruptly with pH and IEP shifts to acidic pH, from 12 to 5; from 7 to 6.5 and from 7 to 5.5 respectively for  $GdF_3@PEG$ ,  $GdPO_4@PEG$  and  $TiO_2@PEG-DOTA-Gd(III)$ .

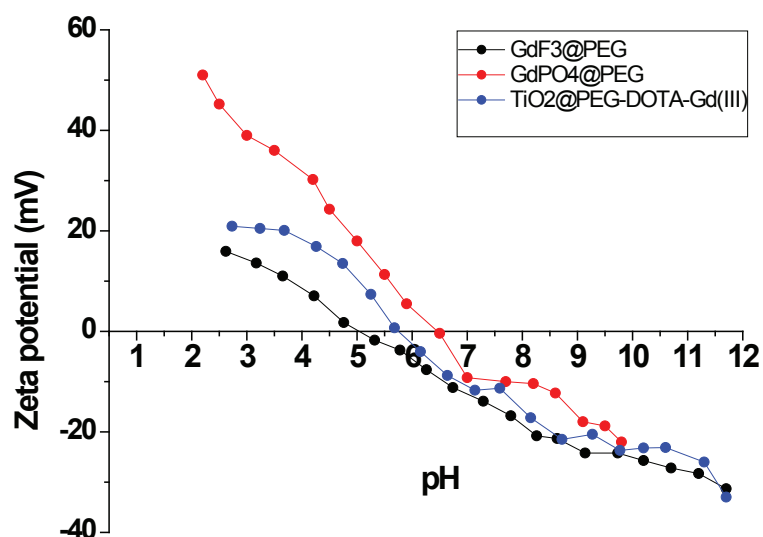


Figure II.50. Zeta potential versus pH curve of modified nanoparticles

IEP is around 15-20 mV at pH 7 for all particles, normally insufficient for only electrostatic stabilization. Contrary to the naked particles (except  $GdF_3$ ) which are stable in extreme pH (acidic or alkaline), and less stable in neutral pH, these functionalized particles are stable and for several days, without aggregation in a broad range of pH (4–12). That is this stability is due to electrostatic repulsion and steric strain.

### 3.9 Conclusion on surface modification

Original nanoproboscopes for MR imaging were prepared. Magnetic particles  $GdF_3$  and variant of  $GdPO_4$  particles were functionalized with polyethylene glycol with methyl and bisphosphonate groups at opposite ends.  $TiO_2$  particle was functionalized with polyethylene glycol with amine and bisphosphonate groups at opposite ends.  $TiO_2$  is a diamagnetic core particle, thus DOTA-Gd(III) complex was coated on the surface via amine groups. ICP, TGA, IR and NMR spectroscopies investigations evidenced the functionalization and bisphosphonate anchoring. Grafting density was estimated around 0.7-1.8; 0.5-0.8 and 1-2.8 PEG chains per  $nm^2$  respectively for  $GdF_3@PEG$ ,  $GdPO_4@PEG$  and  $TiO_2@PEG-DOTA$  particles with ICP and TGA method. Contrary to the naked particles, all the functionalized particles are stable in physiological conditions. These particles meet our initial criteria as magnetic contrast agent particles and we will investigate their MR signal enhancement effects.

### 3.10 Magnetic signal enhancement effects of the developed particles

Potential application of the developed systems in MRI was investigated. MRI contrast agent efficiency is measured by determination of their relaxivities ( $r$  [ $\text{mM}^{-1}\text{s}^{-1}$ ]), i.e. their ability to accelerate relaxation of magnetization and thereby improving MR image contrast. Measurements were performed for  $\text{GdF}_3@PEG$ ,  $\text{TiO}_2@PEG\text{-DOTA-Gd(III)}$  and  $\text{GdPO}_4@PEG$  with the variant ones (different composition). Experiments were performed by Marius Widerøe (MD), Else Marie Huuse (PhD), Marte Thuen (PhD) and Kristine Skårdal from Pr. Olav Haraldseth's team in MR-Center of Department of Circulation and Medical Imaging (Norwegian University of Science and Technology Trondheim).

#### 3.10.1 Experimental process and samples preparation

Relaxation time  $T_1$  and  $T_2$  of the colloidal solution was measured in different concentration. Then  $1/T_1$  and  $1/T_2$  was plotted versus gadolinium concentration (mM of Gd) from ICP. The slope of the curve gives respectively  $r_1$  and  $r_2$  relaxivity. Samples were diluted in saline (physiological water) into five different concentrations and filled in 2 mL tubes. These diluted concentrations were used for relaxivity measurements at all different strength.

##### ✓ Measurements of relaxation times at 7T magnetic field strength

The measurements at 7T field strength were performed at a Bruker Biospec horizontal bore magnet (Bruker Biospin, Ettlingen, Germany). The prepared tubes with five different concentrations of the same particles were placed in a dedicated holder (Figure II.51) together with a reference tube filled with saline. The holder was filled with distilled water and placed in the center of the magnet.  $T_1$  and  $T_2$  values were calculated from the signal intensities in the tubes using MATLAB. A map of the calculated  $T_1$  values of tubes with different concentrations of  $\text{TiO}_2@PEG\text{-DOTA-Gd(III)}$  is shown in Figure II.51.

##### ✓ Measurements of relaxation times at 3T magnetic field strength

The relaxivity measurements at 3T field strength were performed at Siemens 3T scanner (TrioTim, Siemens, Germany) with an 8 channels surface coil. The prepared tubes with five different concentrations of the same magnetic particles were placed in a dedicated holder together with a reference tube filled with saline. The holder was placed in the center of the magnet together with a 0.5 litre bottle filled with distilled water. The water bottle is needed to provide automatic pulse angle measurements, since the 3T scanner are optimized for humans containing a lot of water.  $T_1$  and  $T_2$  values were calculated using MATLAB.

✓ **Measurements of relaxation times at 0.5T magnetic field strength**

The relaxivity measurements at 0.5T field strength were performed at a Bruker 20 MHz Minispec (Bruker, Ettlingen, Germany). The diluted magnetic nanoparticles solutions from the 2 mL tubes were transferred to test tubes.  $T_1$  and  $T_2$  values were calculated for each samples in dedicated software at the Minispec (Bruker).

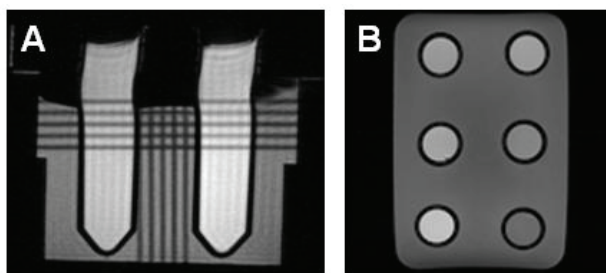


Figure II.51. Illustration showing the tubes placed in the holder (A) and  $T_1$  map of the tubes containing five different concentrations of  $TiO_2@PEG-DOTA-Gd(III)$  sample and one tube with saline for reference (B).

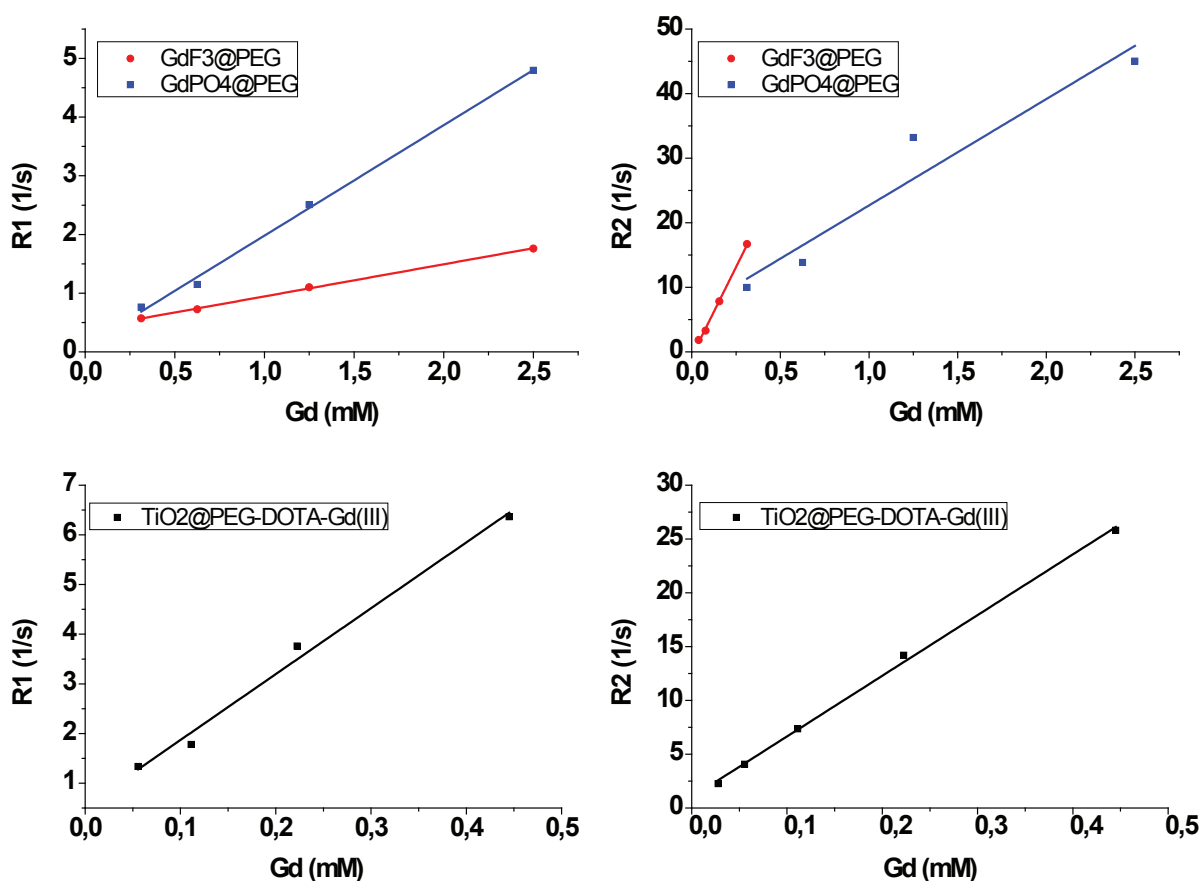


Figure II.52. The inverse  $T_1$  and  $T_2$  values ( $R_1$  and  $R_2$ ) for the particles containing tubes measured in the  $T_1$  and  $T_2$  map plotted as function of Gd concentration in mM. The relaxivity  $r_1$  and  $r_2$  are given by the slope of the linear fit.

During the relaxivity experiments, no aggregation or precipitation of the particles was observed. The relaxation time versus gadolinium concentration is represented in Figure II.52. These results from the three systems show clearly that  $R_1$  and  $R_2$  follow a linear relationship versus the gadolinium concentration. Table II.6 summarises the relaxivity results at different field strength and compared with relaxivity of some commercial and in development contrast agent. As discussed previously, in this study we aim to develop and design an alternative Gd based contrast agent for MRI examination. The developed particles present high relaxivity values and are discussed individually hereafter.

**Table II.6. Relaxivity at 3 different field strength: 7T, 3T and 0.5 T of our particles (blue), other particles and commercial product (black)**

Particle	Core size (nm)	Relaxivity ( $\text{mM}^{-1}\text{s}^{-1}$ )								
		$r_1$			$r_2$			$r_2/r_1$		
		7T	3 T	0.5T	7T	3T	0.5T	7T	3T	0.5 T
TiO <sub>2</sub> @PEG-DOTA-Gd(III)	10	13.5	27	-	56.4	61	-	4.2	2.6	-
GdF <sub>3</sub> @PEG	30	0.6	0.7	0.6	55	11	0.9	92	16	1.5
GdPO <sub>4</sub> @PEG	120	1.8	1.7	1.7	11	6.3	1.9	6.1	3.7	1.1
DOTA-Gd (Dotarem)	-	4.1			4.9			1.2		
Gd <sub>2</sub> O <sub>3</sub> @PEG <sup>226</sup>	4.6	4.4			28.9					
Gd <sub>2</sub> O <sub>3</sub> @PEG <sup>307</sup>	1.3	10.9		16.2	15.9		17	1.5		1.04
Fe <sub>2</sub> O <sub>3</sub> -Dextran (Endorem)	120-180	2.2		24	182		107	83		4.5

### 3.10.2 Core-shell system: TiO<sub>2</sub>@DOTA-Gd(III)

Core-shell particles have been previously developed to improve the longitudinal relaxivity of the paramagnetic Gd(III) complexes<sup>228,273,308</sup>. Few of these studies deal with transverse relaxivity. Here both longitudinal and transverse relaxivity will be presented. The advantage of the DOTA-Gd(III) coated particles versus the DOTA molecular complex is the possibility to load thousands of magnetic ions and thus enhance Gd(III) local concentration and ensure a large relaxation effect. The founded relaxivities of TiO<sub>2</sub>-DOTA-Gd(III) particle is higher than clinical small molecule contrast agents such as Dotarem. This core-shell particle yielded per Gd(III) ion longitudinal relaxivity ( $r_1$ ) of 13.5 and 27  $\text{mM}^{-1}\text{s}^{-1}$  respectively at 7T and 3T; transversal relaxivity ( $r_2$ ) of 56 and 61  $\text{mM}^{-1}\text{s}^{-1}$  at respectively 7 and 3T.

Also relaxivity of this particle is favorably compared with those obtained for Gd(III) chelate<sup>108,309</sup>, Gd(III) aggregates consisting of dendrimer cores<sup>310</sup> or zeolite shells used to sequester Gd(III)<sup>311</sup>. Relaxivity of this particle is higher than those of commercial products and those found in

literature using  $\text{Ag}^{245}$  or  $\text{SiO}_2^{312}$  as Gd(III)-complex carrier. Using silica hybrid particle ( $\text{SiO}_2$ -DTAA-Gd) William J. et al.<sup>312</sup> found lower relaxivities for multilayer shell particles. Endres et al.<sup>228</sup> have prepared DNA- $\text{TiO}_2$  nanoconjugates labeled with DOTA-Gd(III), and the nanoconjugates yielded a  $r_1$  relaxivity of  $3.5 \text{ mM}^{-1}\text{s}^{-1}$  per Gd(III) ion, similar to clinical small molecule contrast agents but lower than our particle. The particularity of this  $\text{TiO}_2$ @PEG-DOTA-Gd(III) particle is to have both longitudinal and transversal relaxivities values higher. This performance can be explained in three points. (1) A significant number of Gd(III) ions by particle due to the high grafting density, thus high Gd(III) local concentration; (2) the accessibility of the paramagnetic sites due to the hydrophilic environment of the particle. These two points can influence as well as longitudinal and transversal relaxivities. (3) Finally a decrease of trembling rate of the magnetic moiety due to the fact that the magnetic moiety is attached to the particle. When the paramagnetic trembling rates match the proton Larmor frequency, energy exchange is efficiency. This last point influences especially longitudinal relaxivity. However the high  $r_2$  relaxivity can results in relatively long residency time of the water molecule in the complex<sup>313</sup>.

More interesting, with these high relaxivities and low  $r_2/r_1$  ratio (2.6 and 4 respectively at 7T and 3 T), this particle is suited for both positive and negative contrast agent and at both low and high field strength. Preliminaries ex-vivo imaging using these particles will be discussed in chapter IV.

### 3.10.3 Isotropic system: $\text{GdF}_3$ @PEG

$\text{GdF}_3$ @PEG particle has a high transverse relaxivity  $r_2$  value  $55 \text{ mM}^{-1}\text{s}^{-1}$  at 7T. Due to magnetization effect,  $r_2$  values increase with field strength<sup>314,95</sup> from  $0.9 \text{ mM}^{-1}\text{s}^{-1}$  at 0.5 T to  $55 \text{ mM}^{-1}\text{s}^{-1}$  at 7T. This particle is clearly interesting to be used at high field strength. Moreover  $r_2/r_1$  ratio is 91 at 7T, suggesting that particles are negative contrast agent suited ( $T_2$ ), contrary to the recent developed smaller particles Gd(III) based, ( $\text{Gd}_2\text{O}_3$ )<sup>315,265</sup> and Mn(II) based ( $\text{MnO}$ )<sup>316</sup>.  $\text{GdF}_3$ @PEG is sufficiently larger and is strongly magnetizable at high field, leading to magnetic field inhomogeneity; in which water molecules will diffuse. This homogeneity of field makes change the magnetic field in space, leading to difference in the Larmor frequencies of the protons. The diffusion of water protons between different magnetic environments reduces their phase coherence and, consequently, causes this effective  $T_2$ -shortening.

This value is higher than those of gadolinium oxide<sup>226, 307</sup> or fluoride<sup>317</sup> and as high as some of USPIO<sup>318</sup> that can be found in the literature. This paramagnetic particle has lower transverse relaxivity than some iron oxide mainly because iron oxide nanoparticles is ferromagnetic at body temperature ( $T_{\text{Néel}} 37 \text{ }^\circ\text{C}$ ) and is in superparamagnetic regime ( $T_B < 37 \text{ }^\circ\text{C}$ )<sup>319</sup>. Paramagnetic particles such as  $\text{GdF}_3$  have a curie temperature ( $T_C$ ) below to room temperature. Hence, at this temperature,

they are paramagnetic behavior and their magnetization increases with the strength field, but the magnetic saturation is not reached at the magnetic fields used for MRI. Their magnetic moment is indeed not maximal contrary to the superparamagnetic particles, which are fully magnetized by 1 T<sup>313</sup>. However, its paramagnetic moment is enough at strong fields; to create contrast and be used as contrast agent.

However, the longitudinal relaxivity  $r_1$  value of GdF<sub>3</sub>@PEG at 0.6 mM<sup>-1</sup>s<sup>-1</sup> in different strength field is lower than that of DOTA-Gd(III) and smaller particles Gd<sub>2</sub>O<sub>2</sub><sup>318</sup>, NaGdF<sub>4</sub><sup>125,320</sup> as expected. Longitudinal relaxivity is closely related to direct contact with water. It is limited by the distance between water molecule to Gd<sup>3+</sup> ion, and the water exchange between Gd<sup>3+</sup> ion and the bulk water molecule. Thus water molecules must be close to Gd<sup>3+</sup> ion. Because PEG is sufficiently water-soluble for allowing water circulation from solution to the surface of the particles, PEG can't prevent Gd(III) in the surface of the particles to exert their influence on the water protons. Also the  $r_1$  evolution with core size indicates that the effect on  $r_1$  is mainly result from the Gd<sup>3+</sup> ions present at the surface of the particle<sup>226</sup>, thus because of the surface-to-volume ratio, larger particles have lower  $r_1$  relaxivity<sup>125</sup>. Also  $r_1$  relaxivity is independent on strength field, probably because of water exchange rate limitation on the surface of the particle, since the rotational correlation time must be low because of size and mass of the particle.

This particle represents an alternative T<sub>2</sub> contrast agent, especially for high magnetic fields. Preliminaries ex-vivo imaging using these particles will be discussed in chapter IV.

#### 3.10.4 Anisotropic system: GdPO<sub>4</sub>@PEG

The relaxivity of the particles depends also on the morphology and particle size. This dependence is more important for these particles because of their anisotropy. With very high aspect ratio (much higher length than width) the particles leads to very high  $r_2/r_1$  ratio<sup>139</sup>, which gives them the features of the T<sub>2</sub> contrast agent. In return, with a moderate aspect ratio,  $r_2/r_1$  is moderate<sup>123</sup> and particles are T<sub>1</sub> contrast agent suited. That is why; we prepared these nanorods in different sizes and chemistry composition to study the influence on the relaxivity. Unfortunately, at present, only relaxivities of particles with large aspect ratio and different chemical compositions have been evaluated. Those of particles in different sizes (synthesized at different pH) are not yet available.

From Table II.6, the observations and discussions on isotropic particles remain valid for anisotropic ones. That is the longitudinal relaxivity very low and independent on the field strength, unlike the relatively high transverse relaxivity which increases with the field strength. Contrary to the isotropic particle, the values of  $r_2$  are much lower, 11 mM<sup>-1</sup>s<sup>-1</sup> at 7T (55 Mm for isotropic particle). Nevertheless this is in agreement with the literature for the same particle at similar aspect ratio<sup>139</sup>.

The difference compared to isotropic particle is due to the difference in magnetization. The magnetism of rare-earth based particles is mainly depending on the type of paramagnetic ion. It was show that for a given volume, a spherical shape induces higher relaxation rate and is thus more efficient from the relaxation point of view<sup>95,321</sup>. Because of its high aspect ratio (120 nm length and 20 nm width) due to its morphology (nanorod), this particle is less magnetisable than spherical particles and thus less efficient. Also, according to literature<sup>322,123</sup>, particles with low aspect ratio (30 nm length and 10 nm width) leads to higher relaxivities up to 14 and 15 mM<sup>-1</sup>S<sup>-1</sup> respectively for r1 and r2 .

Table II.7 shows relaxivity at different field strength of the nanorods with different chemical compositions. Gd(III) intrinsic concentration in the particles is diluted by adding La(III) ion; in order to minimize the interaction between Gd(III) sites by increasing distance between two neighboring Gd(III) ions. Increase this distance would influence the Gd-Gd interaction and therefore their electronic relaxation times, which would have a direct impact on proton nuclear relaxation. As we can see, relaxivities remains proportional to the per particle Gd(III) ratio (Figure II.53), and decrease with Gd(III) dilution, because the number of Gd(III) that interact with water molecules decreases. This dilution therefore has a negative impact on the relaxivity. In conclusion this particle must be preferred in low aspect ratio, without Gd(III) dilution, to be used as positive contrast agent.

**Table II.7. Relaxivity of the Gd(III) diluted GdPO<sub>4</sub> systems particles at different field strength**

Particle	Relaxivity (mM <sup>-1</sup> s <sup>-1</sup> )								
	r <sub>1</sub>			r <sub>2</sub>			r <sub>2</sub> / r <sub>1</sub>		
	7T	3 T	0.5T	7T	3T	0.5T	7T	3T	0.5T
Gd <sub>1.00</sub> La <sub>0.00</sub> PO <sub>4</sub> @PEG	2.1	3.0	2.0	11	6.5	2.4	5,2	2,2	1,2
Gd <sub>0.75</sub> La <sub>0.25</sub> PO <sub>4</sub> @PEG	1.7	2.0	2.1	9.7	5.9	2.4	5,7	3,0	1,1
Gd <sub>0.50</sub> La <sub>0.50</sub> PO <sub>4</sub> @PEG	1.0	1.6	2.0	6.5	4.9	2.4	6,5	3,1	1,2
Gd <sub>0.25</sub> La <sub>0.75</sub> PO <sub>4</sub> @PEG	0.39	0.59	1.6	3.0	3.2	1.8	7,7	5,4	1,1
Gd <sub>0.00</sub> La <sub>1.00</sub> PO <sub>4</sub> @PEG	No Gd no sense with relaxation per Gd								

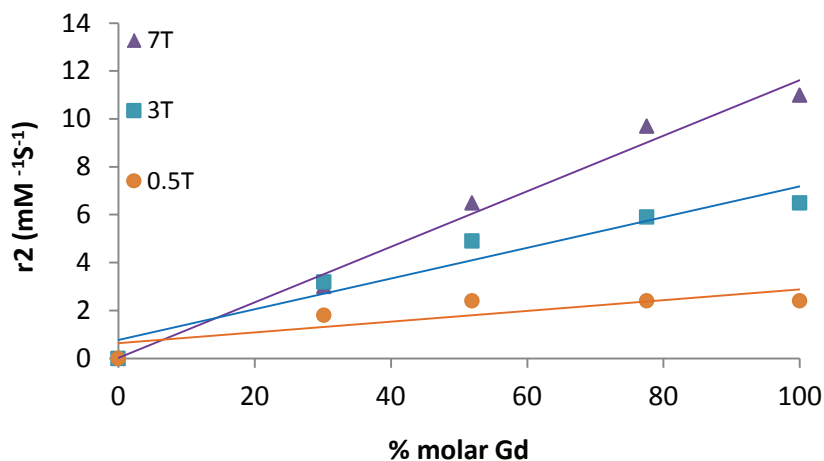


Figure II.53. Transverse relaxivity  $r_2$  versus % molar Gd(III). Concentration from ICP analysis

### 3.10.5 Comparison of the developed systems

The advantage of  $\text{TiO}_2@\text{DOTA-Gd(III)}$  particle is that all Gd(III) sites are fully accessible and in relatively high local concentrations. It has high longitudinal relaxivity compared to the Gd(III) complexes and transverse relaxivity comparable to that of paramagnetic particles. This is a significant advantage since it allows achieving bimodal imaging (both T1 and T2). This particle has the same disadvantage that have all agents made of chelated Gd(III), related to a possible gadolinium release, which would increase the toxicity of the agent, even though these complexes already used clinically offers significant guarantees. The other disadvantage may come from the eventual desorption of molecules from the particle. In this case, the most important consequence would be the decline in the efficiency. Because phosphonate, PEG and DOTA are already used clinically; therefore the toxic consequences could be weakened. Also achieving a bi-functionalization on this particle, i.e. grafting of fluorescent molecules for example, can lead to a decrease in performance since the surface of the particle will be shared (by PEG-DOTA-Gd<sup>3+</sup> and fluorescence molecules) and the colloidal stability of the particle could be affected due to the interactions of these molecules on the surface.

GdF<sub>3</sub>@PEG particle could be an alternative to T2 iron oxide agents, thanks to its high T2 relaxivity. The other advantage is to contain the Gd(III) ion in a crystalline core, with theoretically less possibility of release, although more study should be achieved about. Unlike the core-shell system, the surface of this particle is occupied by only simple PEG that can be coupled with fluorescent molecules or share the surface of the particles with. The main disadvantage of this system is that it can be used as only T2 contrast agent and is suited for high field strength contrary to core-shell system.

GdPO<sub>4</sub>@PEG nanorod has medium relaxivities. Low aspect ratio particles should lead to higher relaxivities at least as high as those of the literature. However, these particles have high and modest r<sub>2</sub>/r<sub>1</sub> ratio leading to T1 contrast agent. Beyond availability of surface for functionalization as the isotropic system, this system is original by its little conventional shape and is particularly interesting on the comparative study of penetration to the tissue and especially in the study of blood brain barrier crossing.

#### **4 Conclusion on nanoparticles synthesis and surface modification**

In this chapter three kinds of particles were developed. According to their structure and morphology. There are (1) system made of pegylated sphere-shaped gadolinium fluoride, (2) system made of pegylated rod-shaped gadolinium phosphate and (3) core-shell system made of DOTA-Gd(III) coated titanium oxide. First all, naked inorganic core particles were synthesized and characterized. They were obtained highly crystallized and their stability were investigated. It was found that gadolinium fluoride excepted, electrostatic stabilization was not enough in pH close to that of physiological media. Pegylation and DOTA-Gd(III) coating were achieved.

Stability of the particles was improved at physiological conditions thanks to steric repulsion, and no aggregation was observed. The pegylation and coating was studied and confirmed by IR, NMR, TGA and ICP. A magnetic signal enhancement effect of the particles was evaluated. The core-shell system is an excellent bimodal magnetic contrast agent, able to enhance both T1 and T2 relaxation time. While the isotropic system appears as a great alternative for iron oxide agent, thanks to its high T2 relaxation enhancing. The anisotropic system appears more efficient at low aspect ratio version, and is probably T1 suited. These results proved that the prepared particles can be used for MRI. The ex-vivo MRI preliminary tests with these particles will be discussed in chapter IV.

Hereafter, chapter III is devoted to the development of the multifunctional agents. The as-prepared particles will be coupled with polythiophene oligomers to achieve both magnetic and fluorescence smart contrast agent, able to target A $\beta$  plaques.



# CHAPTER III



# CHAPTER III DEVELOPMENT OF MULTIMODAL CONTRAST AGENTS

In this chapter we develop the smart multifunctional agents, which are particles able to target specifically  $\beta$ -amyloid ( $A\beta$ ) peptide and create contrast in both magnetic resonance and two photon fluorescence imaging. In this purpose, the previously prepared magnetic contrast agents are coupled with luminescent conjugated polythiophenes (LCPs). As mentioned in chapter I, LCPs are polythiophenes molecules which bind to  $A\beta$  and emit a specific fluorescent signal once bound to  $A\beta$ . These molecules are synthesized by Peter Nilsson, Per Hammarström, Andreas Åslund et al<sup>83</sup>, from department of chemistry of Linköping University (Sweden). A water-soluble spacer (WSS) makes the link between LCPs and particle. The used WSS is a polyhydroxyethylacrylate (pHEA), synthesized in our laboratory by Cyrille monnereau and Vinu Krishnan Appukuttan. Gadolinium fluoride particle ( $GdF_3$ ) was used to be coupled with LCPs. This particle was selected due to its conventional shape (spherical) and its high transverse relaxivity. Also it was preferred to DOTA-Gd(III) coated titanium oxide because of the availability of its surface to receive LCPs without decrease the performance of the agent in term of relaxivity and stability.

Hereafter, we will introduce the schematic synthesis of the used LCPs, WSS and the click chemistry to attach WSS into the LCPs during the preparation of LCP-spacer moiety (LCP-WWS). Then we will discuss the coupling method of nanoparticles with the LCP-WSS moiety. The obtained LCP labeled nanoparticles will be characterized and the results discussed herein.

## 1 MULTIMODAL CONTRAST AGENTS

### 1.1 Multimodal contrast agent in diagnosis applications

As mentioned previously, several imaging techniques are commonly employed for clinical diagnostics including MRI, PET, single-photon emission computed tomography (SPECT) and x-ray computed tomography (CT)<sup>323</sup>. These methods differ from another in terms of spatial and temporal resolution, anatomical and molecular details, imaging depth, and material properties of contrast agents. For faster and more accurate diagnosis, multimodal imaging is needed. Also, the use of multimodal contrast agent can reduce costs and enhance safety by limiting the number of contrast agent administrations. Several nonspecific multimodal contrast agents are in development for the diagnosis of various diseases; and in the most cases MRI is involved<sup>324</sup>. MRI is powerful tool allowing obtaining anatomical information in high resolution.

Obtaining information on the molecular scale requires a biopsy of the diseased tissue to perform ex-vivo molecular analysis, such as histopathology and immunochemistry. Then MRI is usually coupled to fluorescence imaging to combine anatomic and molecular imaging<sup>325,324,326</sup>.

In order to reduce cytotoxicity, side effects and improve efficiency of the agents, the current contrast agent in development, can target specific biomarkers of diseases. The most advanced results can be found in cancer therapy and diagnostic<sup>327</sup>. The development of these non-invasive *in vivo* imaging techniques of specific biomarkers of various diseases should greatly improve the diagnosis and treatment, (1) by providing an early molecular information on the disease; (2) adapting the treatment according to the "personal" characteristics of the disease; (3) by selecting the appropriate clinical trial patient populations.

There are some investigations on development of specific multimodal contrast agent, for tumors targeting in cancer diagnosis<sup>328,329</sup> for example, and few work for Alzheimer disease<sup>127</sup>, restricted to the studies of A $\beta$  binding selectivity *in vitro*. Nano-platforms for multimodal imaging are generally made of three structures<sup>330,331</sup>: (1) MRI contrast agent made of functionalized magnetic nanoparticles, (2) an optical contrast agent and (3) antibodies against specific targets, attached to nanoparticles. Today, these investigations used the current rhodamine, Congo red and A $\beta$  peptide fragments as chromophore and targeting agent, while as discussed in chapter I, we introduce a new compound, more efficiency, the polythiophene as both optical contrast agent and A $\beta$  targeting agent.

## 1.2 Polythiophene and applications

Polythiophenes have received much attention in recent years, because of their chemical, optical and electrochemical properties easily adjustable. The applications of these polymers are rather numerous, in fields as varied as the anti-static protection, light-emitting diodes, flat screens or energy storage<sup>332</sup>. The insulating properties of polythiophenes at neutral state as well as their excellent properties of resistance to temperature made of good materials for antistatic coatings as well as for the electromagnetic shielding<sup>333</sup>. Their semiconductor properties are also investigated in different systems<sup>332,334</sup>. The amounts of electricity that they can incorporate in their doping state are interesting for energy storage systems. They are thus studied as cathode in lithium systems<sup>332,335,336</sup>. Another application considered for polythiophenes is their use as active ingredients in electrodes of supercapacitors<sup>337,338,339</sup>. The application of the electroluminescence properties of polythiophenes is much studied in systems of light-emitting diodes and photovoltaic systems<sup>334,340</sup>. The optical properties are interesting for applications in electrochromic systems (flat screens, photosensitive glass,...)<sup>333,341</sup>.

Recently, it was used for biological applications as new chromophore for fluorescence microscopy and for selective identification of protein aggregates such as A $\beta$ <sup>80,83</sup>. It showed a greater efficiency compared to conventional amyloid stain including Congo red and thioflavin T. For the first time it is coupled with magnetic particles to achieve new two-in-one nanomaterials multimodal contrast agent for the development of novel diagnostic tools. We expected to perform efficiency multimodal probes able to cross the BBB thanks to presence of LCPs on the surface. In this purpose, the probe should be mono-disperse; as small as possible, water dispersible without losing hydrophobic interactions of LCPs allowing the BBB crossing and conformation sensitivity of LCPs allowing specific staining.

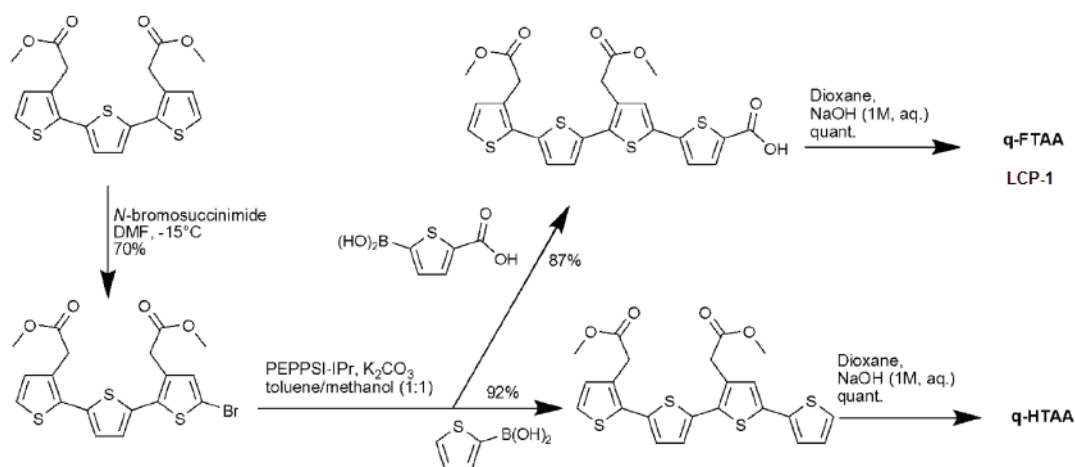
## 2 PREPARATION OF MULTIMODAL CONTRAST AGENTS

### 2.1 Production of two luminescent conjugated polythiophene

Several types of oligothiophenes are used as probes for fluorescent microscopy of A $\beta$  and other proteins aggregates. Generally from trimer to heptamer, with different amounts of carboxyl groups and in different positions<sup>80,83</sup>. In this work, two kinds of oligothiophenes were used, the tetrameric (qFTAA) and the pentameric (pFTAA) ones (Scheme III.1 and Scheme III.2).

#### ✓ Carboxyl group-terminated tetrameric oligothiophenes

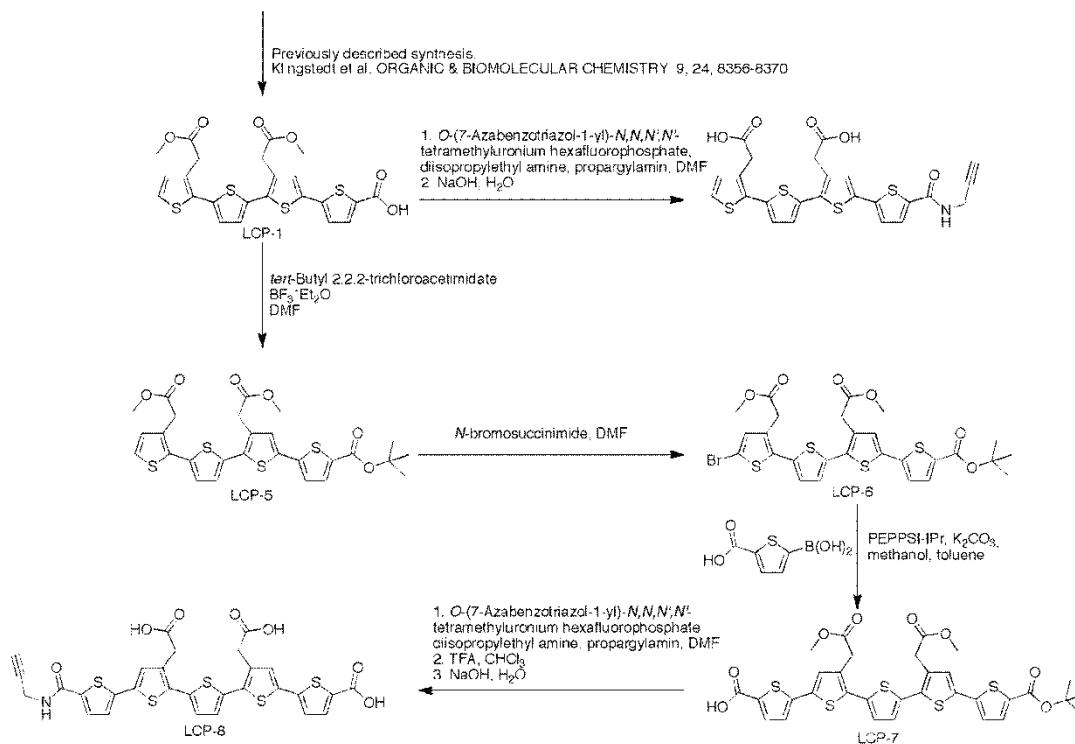
The synthesis method of the tetrameric LCP (LCP-1 in Scheme III.1 and Scheme III.2) performed by Andreas et al. is previously published<sup>80</sup>, following this schematic representation. The thiophene trimer is the starting point of this synthesis.



Scheme III.1. Preparation of carboxyl group-terminated tetrameric oligothiophenes (LCP-1)

✓ **Alkynyl group-terminated oligothiophenes: tetrameric and pentameric**

The synthesis method of the alkynyl group-terminated tetrameric and pentameric oligothiophene (respectively LCP-6 and LCP-7) performed by Andreas is shown in Scheme III.2. The carboxyl group-terminated tetrameric is the starting point of this synthesis. Description of the synthesis is detailed in Annex B.

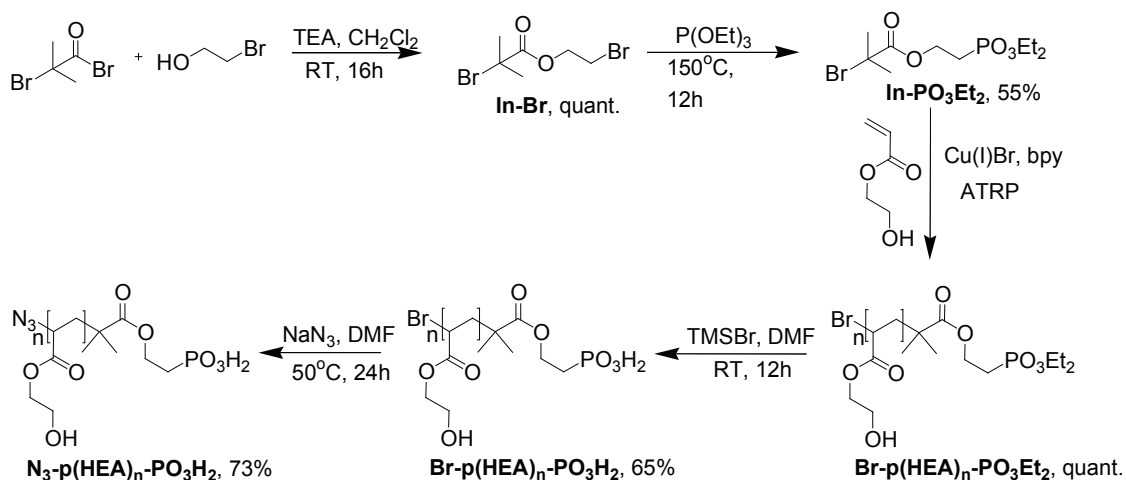


**Scheme III.2. Preparation of alkynyl group-terminated oligothiophenes: tetrameric and pentameric**

## 2.2 Production of water soluble spacer: polyhydroxyethylacrylate

The WSS used in this work is polyhydroxyethylacrylate. We used two different lengths of this polymer, 14 and 26 units. The strategy consisted in synthesizing linkers of various lengths. This was achieved using ATRP polymerization strategy. This polymerization strategy was used for three main reasons. (1) It allows obtaining, with a minimum synthetic efforts, objects with various and very defined lengths. (2) It allows obtaining objects functionalized on both  $\alpha$  and  $\omega$  ends, with groups allowing further coupling to the fluorescent probe (N<sub>3</sub>), and anchoring to the nanoparticles (PO<sub>3</sub>H<sub>2</sub>). (3) It allows possibility varying the composition of the linker, by varying the nature of the starting monomer material, and therefore achieving control over some crucial properties of the linker (water solubility, biocompatibility, BBB crossing ability). These spacers were prepared in our laboratory by Cyrille Monnereau and Vinukrishnan appukuttan.

This is a multistage synthesis. The five stages of the synthesis are briefly described in Annex C and shown schematically in Scheme III.3.



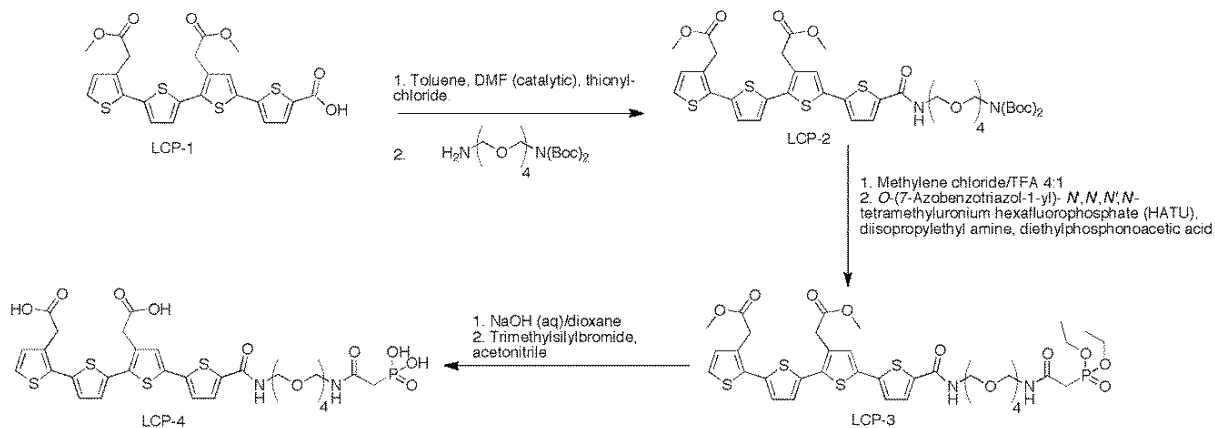
Scheme III.3. Preparation of water-soluble spacer (polyHydroxyethylacrylate)

## 2.3 Attachment of the spacers with luminescent conjugated polythiophene

Three length of the spacer was used. The shorter with 4 units of ethylene glycol (TEG) and the medium with 14 units of pHEA were clicked with the tetrameric LCP (qFTAA). The longer with 26 units of pHEA is clicked with the pentameric LCP (pFTAA). The clicking process is schematically shown here after.

### ✓ Clicking of the short spacer with tetrameric LCP

The qFTAA-(PEG)<sub>4</sub>-PO<sub>3</sub>H<sub>2</sub> moiety was prepared by Andreas according to the chemistry shown in Scheme III.4 and describe in Annex D.

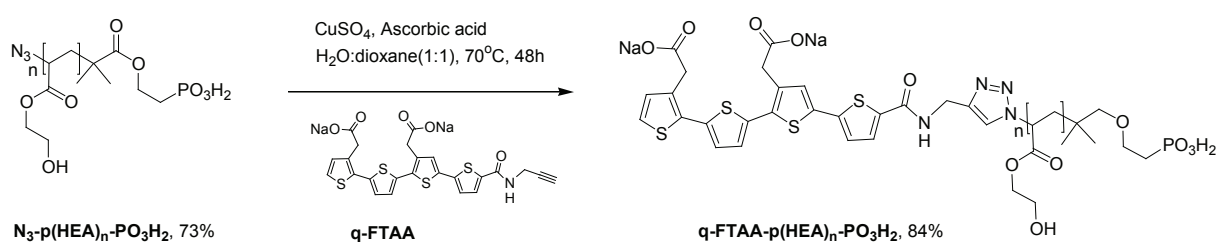


Scheme III.4. Synthetic route of qFTAA-(PEG)<sub>4</sub>-PO<sub>3</sub>H<sub>2</sub> synthesis

The attachment of medium and longer spacer to LCPs was carried out by Vinu Krishnan Appukuttan using the same chemistry. They were coupled respectively to tetrameric and to pentameric LCPs.

✓ **Clicking of the medium spacer with tetrameric LCP**

The qFTAA-p(HEA)<sub>14</sub>-PO<sub>3</sub>H<sub>2</sub> moiety was prepared according to the chemistry shown in Scheme III.5 and describe in Annex D.



Scheme III.5. Clicking of water-soluble spacer (p(HEA)<sub>14</sub>-PO<sub>3</sub>H<sub>2</sub>) with LCP (qFTAA)

✓ **Clicking of the longer spacer with pentameric LCP**

The preparation procedure of pFTAA-p(HEA)<sub>26</sub>-PO<sub>3</sub>H<sub>2</sub> is similar to that of qFTAA-p(HEA)<sub>14</sub>-PO<sub>3</sub>H<sub>2</sub>, using longer spacer instead the medium one and attached to the pentameric LCP (pFTAA) instead tetrameric one (qFTAA). The different obtained compounds are shown in these following figures.

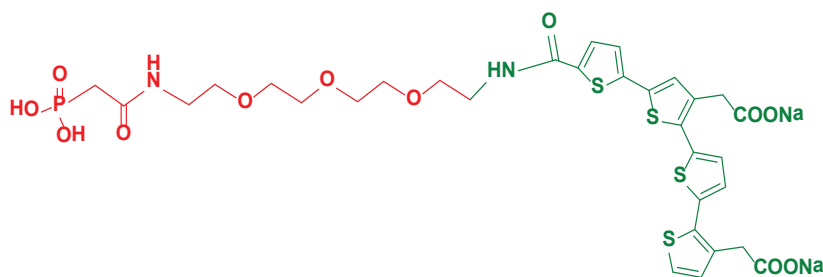


Figure III.1. qFTAA-(TEG)<sub>4</sub>-PO<sub>3</sub>H<sub>2</sub> (tetrameric probe with short spacer)

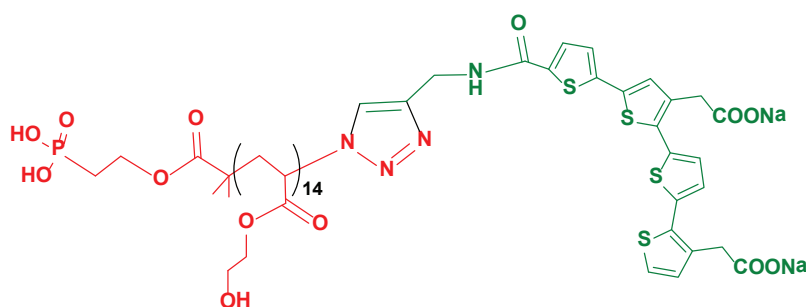


Figure III.2. qFTAA-p(HEA)<sub>14</sub>-PO<sub>3</sub>H<sub>2</sub> (tetrameric probe with medium spacer)

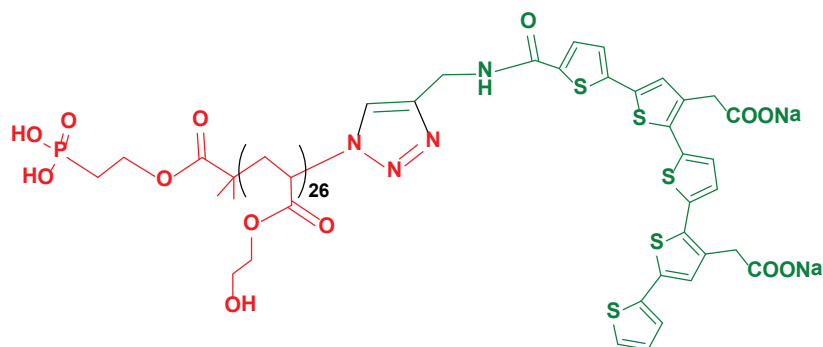


Figure III.3. pFTAA-p(HEA)<sub>26</sub>-PO<sub>3</sub>H<sub>2</sub> (pentameric probe with longer spacer)

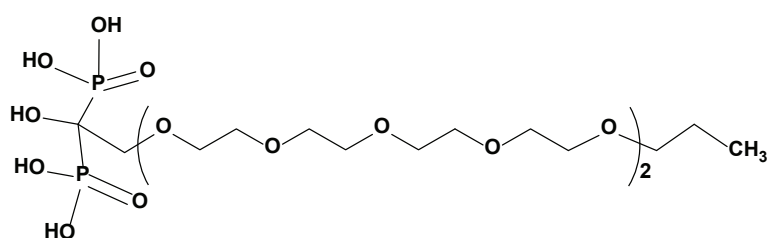


Figure III.4. Bisphosphonate-PEG-CH<sub>3</sub> (BP-PEG-CH<sub>3</sub>)

## 2.4 Preparation of LCP labeled nanoparticles

### 2.4.1 Preparation strategy

LCPs were coupled to gadolinium fluoride (GdF<sub>3</sub>) to be used as model nanoparticle. Whole surface of the particles do not need full covering by LCPs. Low LCP local concentration is supposed to be sufficient to provide targeting. In addition the stability of colloidal solutions could be compromise with high concentrations of LCPs. We have therefore decided to cover the surface with from 2 to 10 % of LCP, with from 98 to 90% of BP-PEG-CH<sub>3</sub>. The polyethylene will ensure biocompatibility and stability of the new particles. Other crucial parameter is that the oligothiophenes support two carboxylate groups per molecule which can anchor to the surface of the particles. This anchoring would disturb the LCPs properties; by limiting their conformation freedom and their availability to bind to Aβ.

The use of spacer with phosphonate group allows keeping the LCPs free, relatively far to the particle and presence of PEG will create a steric repulsion to disadvantage the anchoring of the LCPs via the carboxyl groups. In addition the use of phosphonate and bisphosphonate as anchoring group for respectively LCP and PEG, with stronger coupling constants than carboxylate group will tend to

prevent the attachment of the latter on the surface of the particles. The obtained particle; using the tetrameric LCP with the medium spacer is schematically shown in Figure III.5

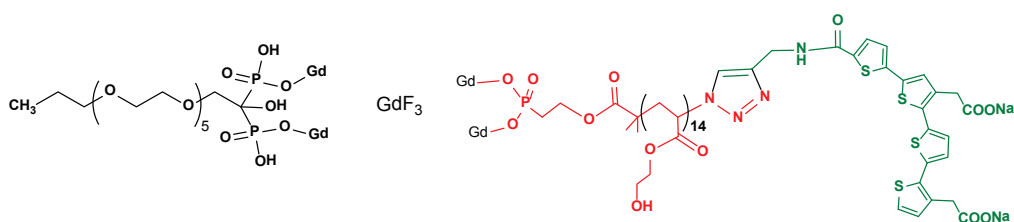


Figure III.5.  $GdF_3@(pHEA)_{14}$ -qFTAA (2%)

## 2.4.2 Coupling of LCP-spacer moieties with $GdF_3$ nanoparticles

First of all the desired amount of PEG is dissolved in water at room temperature. Then the solution with the desired amount of LCP is added to the PEG solution. The resulting mixture is a clear yellow solution. The mixture is done in the container in which the reaction will take place (schlenk) and is previously heated at 70 ° C. Under a strong agitation the solution containing the desired amount of particle is added. Then the solution is sonicated to avoid aggregation and precipitation of particles. The mixture is usually clear yellow and transparent. It is heated at 70 ° C for 5 H. The solution is stable and particles well dispersed throughout the grafting reaction.

After 5 H, agitation and heating are stopped. The solution is then transferred into dialysis tubes which will be immersed in a large volume of water (30 L), with two daily water changes. Presence of free LCP in dialysis water is checked by fluorescence spectroscopy.

Samples were prepared using a total of 0.5 mmol of coupling molecules (BP-PEG-CH<sub>3</sub> and LCPs-spacer at desired ratio) for 1 mmol (Gd<sup>3+</sup> concentration) of naked  $GdF_3$  nanoparticles (1:2 ratio). This ratio corresponds to excess relative to the amount needed for a full surface coverage. Coupling was carried out with BP-PEG-CH<sub>3</sub>/LCP-spacer moiety ratio of 98:2, 95:5 and 90:10.

In a typical experiment, such as for 95:5 ratio, BP-PEG-CH<sub>3</sub> (0.475 mmol) is dissolved in 5 mL of water and mixed with a solution of 0.025 mmol of LCPs-spacer in 0.5 mL of water. The mixing is previously heated at 70 °C. A suspension of 1 mmol (gadolinium theoretical concentration) of naked  $GdF_3$  nanoparticles in 2 mL of water is added to this mixing, under vigorous stirring. The mixture is immediately sonicated to prevent aggregation and heated by reflux at 70 °C for 5H. The resulting suspension is purified to remove unreacted coupling molecules, through dialysis during 10 days. The purification is stopped only when the presence of LCP is no longer detected in water from dialysis by

fluorescence spectroscopy. Then solution is freeze-dried and kept in solid state. Table III.1 shows the prepared particles.

**Table III.1. Compositions of the studied particles**

Compound	Core particle	Spacer		LCP	
		Nature	Length	%	Length
GdF <sub>3</sub> @p(HEA) <sub>14</sub> -qFTAA(2%)	GdF <sub>3</sub>	p(HEA)	14	2	Tetrameric
GdF <sub>3</sub> @TEG-qFTAA(5%)	GdF <sub>3</sub>	PEG	4	5	Tetrameric
GdF <sub>3</sub> @p(HEA) <sub>26</sub> -pFTAA(2%)	GdF <sub>3</sub>	p(HEA)	26	2	Pentameric
GdF <sub>3</sub> @p(HEA) <sub>26</sub> -pFTAA(10%)	GdF <sub>3</sub>	p(HEA)	26	10	Pentameric

### 3 CHARACTERIZATIONS OF LCP LABELED NANOPARTICLES

We characterized the as-prepared particles for the effectiveness of both PEG and LCP grafting, through analysis of the particle surfaces with IR, TGA and elemental analysis for the estimation of the grafting density. We are also interested in the behavior of these particles in solution, their size distribution and their stability in colloidal suspension. Finally we will analyze the photophysics properties and their ability to accelerate the relaxation of protons in solution. Biological evaluation is investigated in the next chapter.

#### 3.1 Evaluation of the labeling by surface characterizations

##### 3.1.1 Infrared analysis

Infrared analyses allow identifying different molecules present on the surface of the functionalized particles. We will first examine the clicking of LCPs with the spacer by comparison of their spectra. Then we will analyze the different groups attesting the coating of LCP on the surface of the LCPs labeled particles.

##### 3.1.1.1 LCP-spacer moieties

Infrared spectra of free LCP (p-FTAA) were compared to that of LCP-spacer moieties, qFTAA-(TEG)<sub>4</sub>-PO<sub>3</sub>H<sub>2</sub> and pFTAA-p(HEA)<sub>26</sub>-PO<sub>3</sub>H<sub>2</sub>. qFTAA and pFTAA (Figure III.6) have a similar infrared feature. In Figure III.7 and Figure III.8, spectrums of pFTAA are compared to those of the LCP-spacer moieties and the main bands are assigned to the related groups.

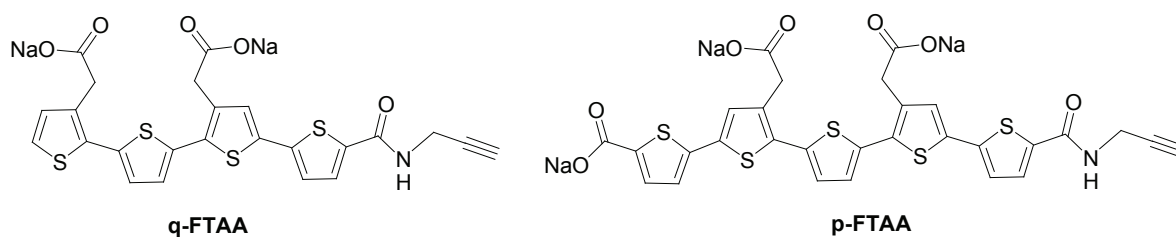


Figure III.6. Free LCPs: tetrameric LCP (q-FTAA) and pentameric LCP (p-FTAA)

### ✓ pFTAA

In pFTAA spectrum in Figure III.7, the two single bands at 1530 and 1445  $\text{cm}^{-1}$  are assigned respectively to the aromatic C=C anti-symmetric stretching mode ( $\nu_{\text{anti}}$ ) and the aromatic symmetric stretching mode ( $\nu_{\text{sym}}$ ), respectively<sup>342</sup>. The peak at 1368 is assigned to the anti-symmetric  $\nu_{\text{(C-C) ring}}$  mode<sup>342</sup>. The weak absorption at 1266  $\text{cm}^{-1}$  is assigned to the anti-symmetric in-plane C-H deformations<sup>342,343,344</sup>. The bands at 1034  $\text{cm}^{-1}$  have been assigned to the symmetric in-plane C-H deformations<sup>342,343,344</sup>. The multiplets: 1206 and 1186  $\text{cm}^{-1}$  mainly from the inter-ring C-C stretching vibration. The multiplets of bands at 840 and 867  $\text{cm}^{-1}$  are due to the symmetric and anti-symmetric aromatic C-S stretching modes, and the C-H out-of-plane bending vibration is observed at 773  $\text{cm}^{-1}$ . Bands from the alkyl group and the C-H aromatic stretching mode expected respectively at around 3300 and 3070  $\text{cm}^{-1}$  are not visible, they are overlapped by the broad band centered at 3350  $\text{cm}^{-1}$  from OH.

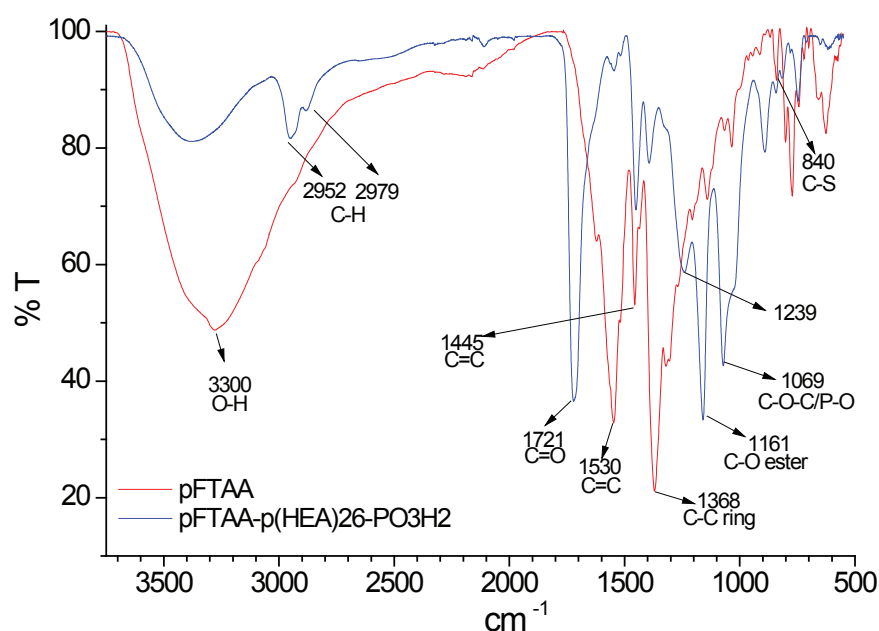


Figure III.7. IR spectra of pFTAA and pFTAA-p(HEA)<sub>26</sub>-PO<sub>3</sub>H<sub>2</sub>

✓ **pFTAA-p(HEA)<sub>26</sub>-PO<sub>3</sub>H<sub>2</sub>**

In IR spectrum of pFTAA-p(HEA)<sub>26</sub>-PO<sub>3</sub>H<sub>2</sub> (Figure III.7), the intense bands from p(HEA) appear. C=O bond stretching appears at 1721 cm<sup>-1</sup> and the aliphatic C-H anti-symmetric and symmetric stretching was observed at 2952 and 2879 cm<sup>-1</sup>. The aliphatic C-H bending mode can be seen at 1449 cm<sup>-1</sup>. The broad peak centered at 3399 cm<sup>-1</sup> corresponds to O-H bond stretching and O-H bending can be seen at 1390 cm<sup>-1</sup>. The ester peak (C-O stretching) of polymer was observed at 1161 cm<sup>-1</sup>. The plenty of p(HEA) chain hides signal from pFTAA. We can identify two bands at 1446 and 840 cm<sup>-1</sup> which can be assigned to the aromatic C=C anti-symmetric stretching mode and to the symmetric aromatic C-S stretching modes. Also bands from phosphonate are hardly visible. They are overlapped by the intense bands from p(HEA) at 1300-800 cm<sup>-1</sup> region such as bands at 1069 and 1021 cm<sup>-1</sup> from C-O-C overlapping certainly bands from P-O (around 1060 cm<sup>-1</sup>).

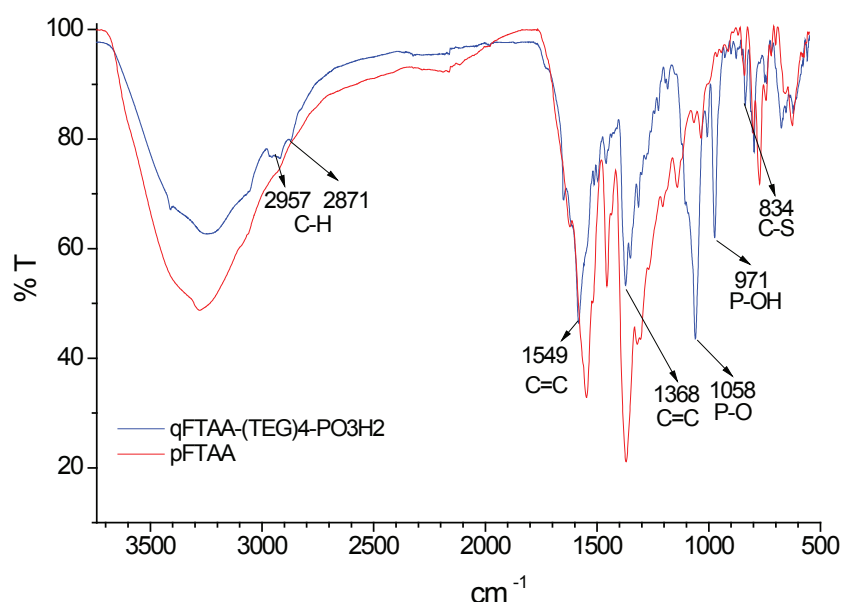


Figure III.8. IR spectra of pFTAA and qFTAA-TEG-PO<sub>3</sub>H<sub>2</sub>

✓ **qFTAA-TEG-PO<sub>3</sub>H<sub>2</sub>**

In IR spectrum of qFTAA-TEG-PO<sub>3</sub>H<sub>2</sub>, in Figure III.8 bands from qFTAA can be identified at 1549, 1368 and 834 cm<sup>-1</sup> respectively from aromatic C=C anti-symmetric and symmetric stretching mode and the symmetric aromatic C-S stretching modes. It can be seen bands from PEG at 2957-2871 cm<sup>-1</sup> for anti-symmetric and symmetric stretching mode of CH. Bands from phosphonate are visible at 1225, 1058 and 971 cm<sup>-1</sup> assigned respectively to P=O, P-O and P-OH.

### 3.1.1.2 LCP labeled particles

#### ✓ **GdF<sub>3</sub>@TEG-qFTAA(5%)**

IR spectrum of the particle is compared to that of GdF<sub>3</sub>@PEG in Figure III.9. Spectral feature of GdF<sub>3</sub>@TEG-qFTAA(5%) is dominated by bands from BP-PEG-CH<sub>3</sub> due to its high ratio compared to that of qFTAA-TEG-PO<sub>3</sub>H<sub>2</sub> on the particles surfaces and the fact that the used spacer is a PEG (tetraethylene glycol), hence the similarity to the GdF<sub>3</sub>@PEG spectrum discussed in chapter II. However, presence of qFTAA is evidenced by the peak at 1549 cm<sup>-1</sup> from the aromatic C=C anti-symmetric stretching mode (Figure III.9-right). This spectrum evidenced co-functionalization of this particle with PEG and qFTAA-TEG-PO<sub>3</sub>H<sub>2</sub>.

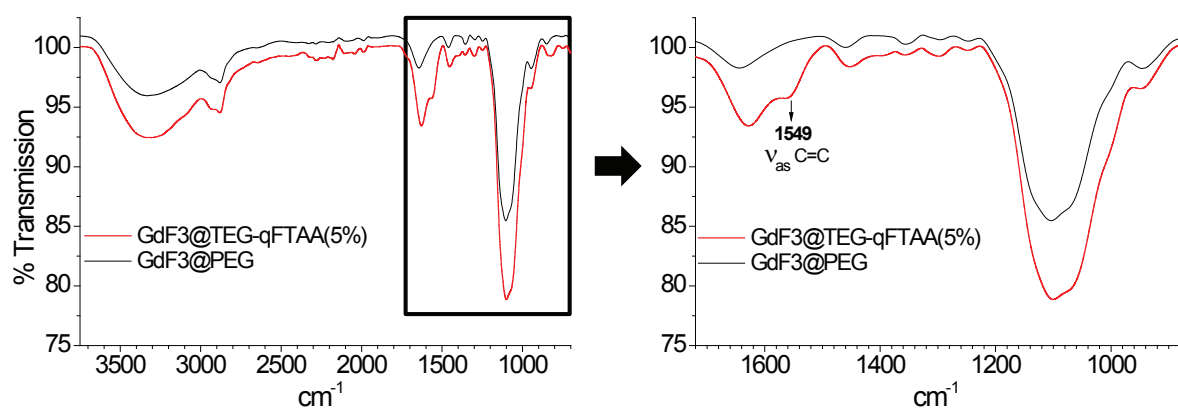


Figure III.9. IR spectra of particle GdF<sub>3</sub>@TEG-qFTAA(5%) compared to that of GdF<sub>3</sub>@PEG (left) and magnification of 1800-700 cm<sup>-1</sup> zone (right)

#### ✓ **GdF<sub>3</sub>@p(HEA)<sub>14</sub>-qFTAA(2%); GdF<sub>3</sub>@p(HEA)<sub>26</sub>-pFTAA(2%) and GdF<sub>3</sub>@p(HEA)<sub>26</sub>-pFTAA(10%)**

Compared to GdF<sub>3</sub>@p(HEA)<sub>26</sub>-pFTAA(2%) and GdF<sub>3</sub>@p(HEA)<sub>26</sub>-pFTAA(10%), GdF<sub>3</sub>@p(HEA)<sub>14</sub>-qFTAA(2%) is functionalized with the same spacer molecule; different in length (14 instead 26 units) and with qFTAA instead pFTAA. That is the only difference in IR is the peaks intensity. Thus for clarity and simplicity, we discuss only spectra of GdF<sub>3</sub>@p(HEA)<sub>26</sub>-pFTAA(2%) and GdF<sub>3</sub>@p(HEA)<sub>26</sub>-pFTAA(10%), particles where some differences are also observed.

IR spectra of these particles are compared to that of pFTAA-p(HEA)<sub>26</sub>-PO<sub>3</sub>H<sub>2</sub> (Figure III.10). These IR spectra show definitively an efficiency co-functionalization of both pFTAA-p(HEA)<sub>26</sub>-PO<sub>3</sub>H<sub>2</sub> and BP-PEG-CH<sub>3</sub> on surface of the GdF<sub>3</sub> particles. Intensities of peaks from pFTAA-p(HEA)<sub>26</sub>-PO<sub>3</sub>H<sub>2</sub> discussed previously dominate those of from BP-PEG-CH<sub>3</sub>. Particle GdF<sub>3</sub>@p(HEA)<sub>26</sub>-pFTAA(10%) theoretically made of 90 % of BP-PEG-CH<sub>3</sub> and 10 % of pFTAA-p(HEA)<sub>26</sub>-PO<sub>3</sub>H<sub>2</sub> has an IR spectral feature close to that of pFTAA-p(HEA)<sub>26</sub>-PO<sub>3</sub>H<sub>2</sub>.

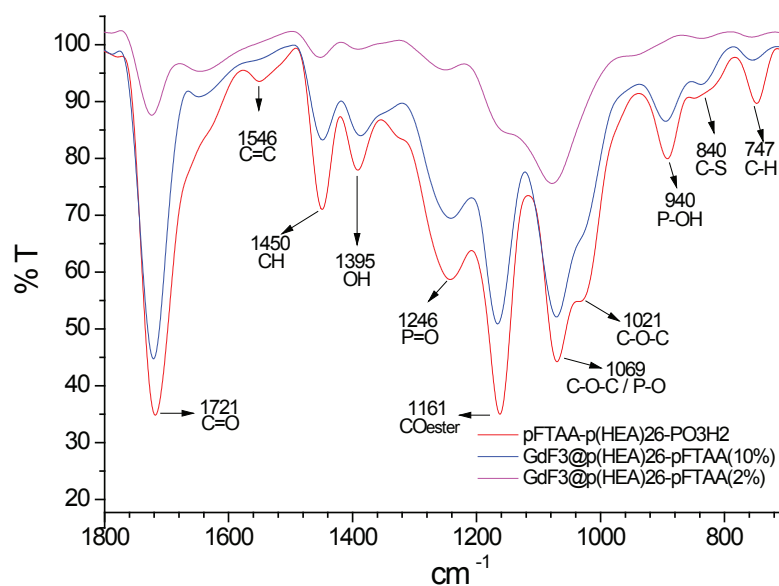


Figure III.10. IR spectra of particles GdF<sub>3</sub>@p(HEA)<sub>26</sub>-pFTAA(2%) and GdF<sub>3</sub>@p(HEA)<sub>26</sub>-pFTAA(10%) compared to those of pFTAA-p(HEA)<sub>26</sub>-PO<sub>3</sub>H<sub>2</sub>

All bands can be easily identified. When BP-PEG-CH<sub>3</sub>/ pFTAA-p(HEA)<sub>26</sub>-PO<sub>3</sub>H<sub>2</sub> ratio increases, this is the case of particle GdF<sub>3</sub>@p(HEA)<sub>26</sub>-pFTAA(2%) (respectively 95 and 5 %), IR spectral feature comes close to that of BP-PEG-CH<sub>3</sub>. Presence of pFTAA-p(HEA)<sub>26</sub>-PO<sub>3</sub>H<sub>2</sub> can be identified thanks to several bands such as at 1721 cm<sup>-1</sup> assigned to the carboxyl groups. The grafting density of the particles and then the exact ratio of BP-PEG-CH<sub>3</sub>/ pFTAA-p(HEA)<sub>26</sub>-PO<sub>3</sub>H<sub>2</sub> for particle GdF<sub>3</sub>@p(HEA)<sub>26</sub>-pFTAA(2%) and GdF<sub>3</sub>@p(HEA)<sub>26</sub>-pFTAA(10%) will be determined and discussed below.

### 3.1.2 Grafting density

#### 3.1.2.1 Thermal analysis

Thermal analyses were performed to analyze the weight loss related to organic compound grafted on the particles. The weight loss is analyzed qualitatively here and quantitatively in the estimation of grafting density. TGA was performed on the LCP coated particles and compared to that of GdF<sub>3</sub>@PEG. Figure III.11 shows the TGA profile of the particles GdF<sub>3</sub>@p(HEA)<sub>26</sub>-pFTAA(10%), GdF<sub>3</sub>@p(HEA)<sub>26</sub>-pFTAA(2%), GdF<sub>3</sub>@TEG-qFTAA(5%) and GdF<sub>3</sub>@PEG. Particles GdF<sub>3</sub>@TEG-qFTAA(5%) and GdF<sub>3</sub>@PEG have a simple curve profile, resulting in dehydration and loss of one type of organic molecule (PEG). Particle GdF<sub>3</sub>@TEG-qFTAA(5%) is modified with 95 % of BP-PEG-CH<sub>3</sub> and 5 % of tetrameric LCP with a short PEG as spacer (qFTAA-TEG-PO<sub>3</sub>H<sub>2</sub>). These two compounds are chemically close and decompose probably at identical temperature. However LCP-spacer moiety has a slightly higher mass than the used BP-PEG-CH<sub>3</sub> (720 versus 544 g/mol), thus the weight loss of this particle is slightly higher than that of GdF<sub>3</sub>@PEG.

The weight loss of particles  $GdF_3@p(HEA)_{26}$ -pFTAA(2%) and  $GdF_3@p(HEA)_{26}$ -pFTAA(10%) show clearly decomposition of two molecules.

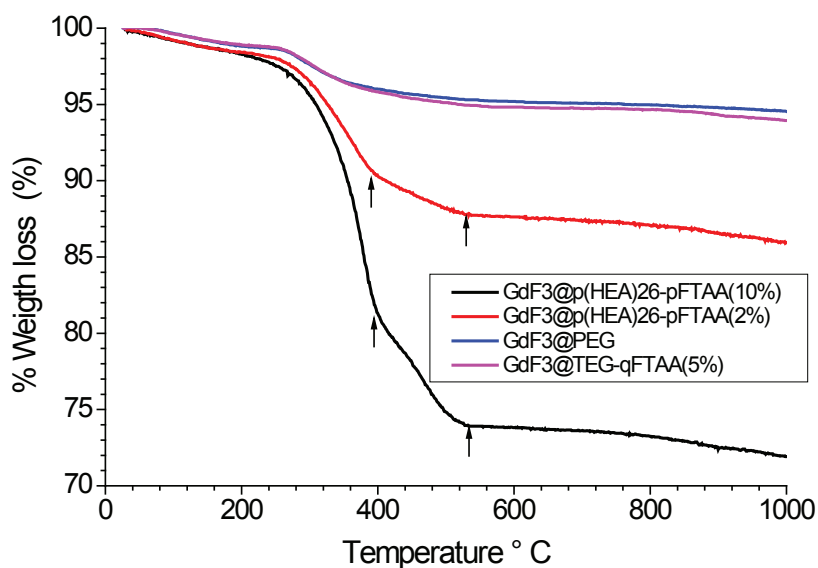


Figure III.11. TGA of pegylated and LCP coated nanoparticles

These particles are modified with BP-PEG-CH<sub>3</sub> and pentameric LCPs with longer spacer pHEA (pFTAA-p(HEA)<sub>26</sub>-PO<sub>3</sub>H<sub>2</sub>) and have similar profile. Here pFTAA-p(HEA)<sub>26</sub>-PO<sub>3</sub>H<sub>2</sub> is chemically different to BP-PEG-CH<sub>3</sub> and decompose probably in different temperature. TGA and DTA analysis of  $GdF_3@p(HEA)_{26}$ -pFTAA(2%) and  $GdF_3@p(HEA)_{26}$ -pFTAA(10%) are shown in Figure III.12. The weight loss profile can be divided into three parts. The first one, with a 2.5% loss in the range room temperature to 260 °C, corresponds to the evaporation of water molecules bound to the surface of the nanoparticles and to the grafted molecules.

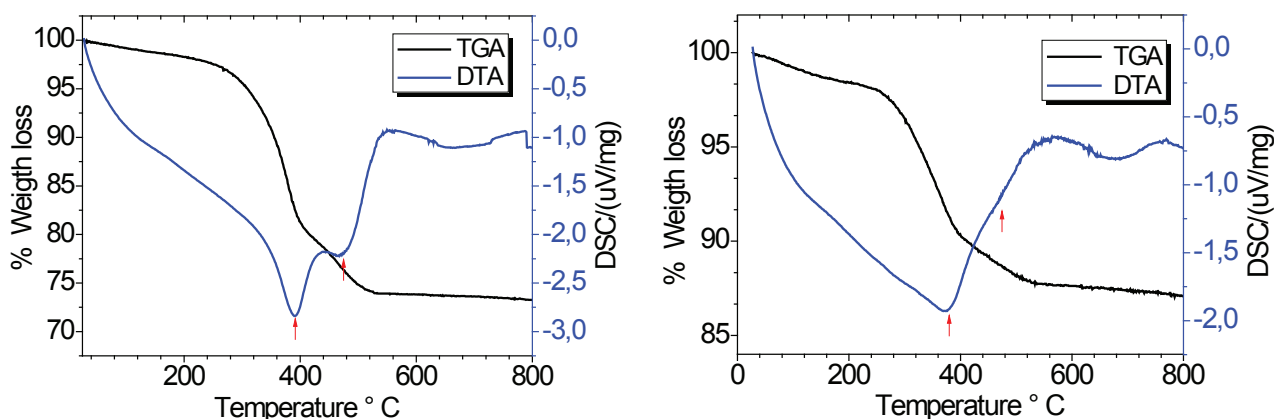


Figure III.12. TGA and DTA curves of particles  $GdF_3@p(HEA)_{26}$ -pFTAA(10%) (left) and  $GdF_3@p(HEA)_{26}$ -pFTAA(2%) (right)

The second part, with a weight loss of about 17.5 and 7.5 % respectively for  $GdF_3@p(HEA)_{26}-pFTAA(2\%)$  and  $GdF_3@p(HEA)_{26}-pFTAA(10\%)$ , in the range 260-400 °C, corresponds to the dehydration of the lattice waters and decomposition of PEG (exotherm at 400°C). The last weight loss in range ~400-800 °C, corresponds to  $pFTAA-p(HEA)_{26}-PO_3H_2$  decomposition. This is confirmed by exotherm at about 480 °C on the DTA profile. We observed clearly the decomposition of two kinds of molecule, assigned to PEG and LCP-spacer. This result confirms the LCP labeling of the particles.

### 3.1.2.2 Grafting density estimation

The grafting density of the particles  $GdF_3@p(HEA)_{26}-pFTAA(2\%)$  and  $GdF_3@p(HEA)_{26}-pFTAA(10\%)$  was calculated from ICP analysis and weight loss of organic moiety from TGA, like in chapter II. The first table (Table III.2) shows grafting density of BP-PEG-CH<sub>3</sub> on particles  $GdF_3@p(HEA)_{26}-pFTAA(2\%)$  and  $GdF_3@p(HEA)_{26}-pFTAA(10\%)$ , assuming that all phosphorus come from BP-PEG-CH<sub>3</sub> molecules for method using ICP concentration and all weight loss is due to BP-PEG-CH<sub>3</sub> molecules decomposition for method using TGA. Here, presence of LCP is discarded at the first time.

We can see that with this assumption, the grafting density of the particles  $GdF_3@p(HEA)_{26}-pFTAA(2\%)$  and  $GdF_3@p(HEA)_{26}-pFTAA(10\%)$  is higher than that of  $GdF_3@PEG$ . This is due to the fact that LCP-spacer moiety has a phosphonate instead bisphosphonate as anchoring group. Thus it has a smaller footprint<sup>252</sup>, probably around 24 Å<sup>2</sup>, and occupies smaller area (compared to bisphosphonate). The restriction imposed by the neighboring phosphonate is weaker, leading to the high grafting density. That is, the occupation of the surface area is different to the surface particles functionalized only by BP-PEG-CH<sub>3</sub>.

**Table III.2. Grafting density of BP-PEG-CH<sub>3</sub>, assuming that all phosphorus come from BP-PEG-CH<sub>3</sub> and all weight loss is due to BP-PEG-CH<sub>3</sub> decomposition**

Nanoparticle	Grafting density			
	ICP-AES		ATG	
	Nber PEG /NP	Nber PEG/nm <sup>2</sup>	Nber PEG/NP	Nber PEG/nm <sup>2</sup>
$GdF_3@PEG$	1294,26	1,83	637	0,68
$GdF_3@p(HEA)_{26}-pFTAA(2\%)$	1442,54	2,04	2021	1,20
$GdF_3@p(HEA)_{26}-pFTAA(10\%)$	1559,58	2,21	4285	1,80

Table III.3. Effective grafting density of BP-PEG-CH<sub>3</sub> compared to that of LCP

Nanoparticle	Grafting density		PEG/LCP ratio	
	ICP- AES		Theoretical	Experimental
	Nber PEG/nm <sup>2</sup>	Nber LCP/nm <sup>2</sup>		
GdF <sub>3</sub> @PEG	1,83	-	-	-
GdF <sub>3</sub> @p(HEA) <sub>26</sub> -pFTAA(2%)	1,81	0,47	49	3.85
GdF <sub>3</sub> @p(HEA) <sub>26</sub> -pFTAA(10%)	1,64	1,14	9	1.44

Taking into account the presence of LCPs at the surface, the second table (Table III.3) shows the grafting density of BP-PEG-CH<sub>3</sub> and LCP from ICP method. When we use 2 % of pFTAA-p(HEA)<sub>26</sub>-PO<sub>3</sub>H<sub>2</sub> and 98 % of BP-PEG-CH<sub>3</sub> as coupling molecules, grafting density of BP-PEG-CH<sub>3</sub> is unchanged compared to that of GdF<sub>3</sub>@PEG particles. In fact, bisphosphonate is more reactive and has a better coupling constant than phosphonate. Bisphosphonate can react first, and when steric restriction avoids grafting of other bisphosphonate molecules, phosphonate molecules with its smaller footprint can react and insert between bisphosphonate.

When we use 10 % of pFTAA-p(HEA)<sub>26</sub>-PO<sub>3</sub>H<sub>2</sub> and 90 % of BP-PEG-CH<sub>3</sub> as coupling molecules, grafting density of BP-PEG-CH<sub>3</sub> is lower compared to that of GdF<sub>3</sub>@PEG particles. This is probably due to increasing of reactivity of pFTAA-p(HEA)<sub>26</sub>-PO<sub>3</sub>H<sub>2</sub> molecules due to the concentration effect. The use of 10% of pFTAA-p(HEA)<sub>26</sub>-PO<sub>3</sub>H<sub>2</sub> instead 2 % increases grafting density of LCP from 0.47 to 1.14 molecules per nm<sup>2</sup> (142 %) and decrease the PEG/LCP ratio from 3.85 to 1.44 (62 %). Then with this process, preparation with initial ratio of 10% of pFTAA-p(HEA)<sub>26</sub>-PO<sub>3</sub>H<sub>2</sub> is enough to occupy third of the surface particles. The PEG/LCP theoretical ratios are higher than the experimental ratios, because PEG (with bisphosphonate as anchoring group) is used in large excess compared to LCP-spacer moiety (with phosphonate as anchoring group), and cannot react all because of the steric saturation of the surface and its higher footprint related to bisphosphonate.

This result confirms the co-functionalization of PEG and LCP on the surface of the particles. However this coupling should not negatively affect the fluorescent properties of the LCPs and the magnetic properties of the nanoparticles. Hereafter we discuss these properties using photo-physical and relaxivity measurements.

### 3.2 LCP labeled particles behavior in solution

It is crucial to evaluate the behavior of these particles in solution, particularly in terms of size distribution and colloidal stability. The objective is to prepare particles less than 100 nm of hydrodynamic diameter and stable in physiological environments, which means particles relatively

small, well dispersed and stable in solution to promote the blood circulation times and the BBB crossing after *in vivo* injection.

### 3.2.1 Size distribution in aqueous solution

Figure III.13 shows size distribution of the LCP conjugated GdF<sub>3</sub> nanoparticles in PBS. It can be seen a unique population for each particle. Particles GdF<sub>3</sub>@p(HEA)14-qFTAA(2%) and GdF<sub>3</sub>@TEG-qFTAA(5%) with the shorter and the medium spacer have the same diameter than the pegylated particle (GdF<sub>3</sub>@PEG), at 60 nm. Probably because spacer is not sufficiently long to increase significantly the hydrodynamic size. Particles GdF<sub>3</sub>@p(HEA)26-pFTAA(2%) and GdF<sub>3</sub>@p(HEA)26-pFTAA(10%) with the longer spacer change the size to the smaller (50 nm) after grafting. It can be explain by a different interaction on the particles surface due to the presence of the long p(HEA) units leading to the more compact shell or avoiding the possible aggregation of some particles during grafting, contrary to the functionalization with BP-PEG-CH<sub>3</sub> or with the shorter and medium spacer. However this observed phenomenon with longer spacer is not clear.

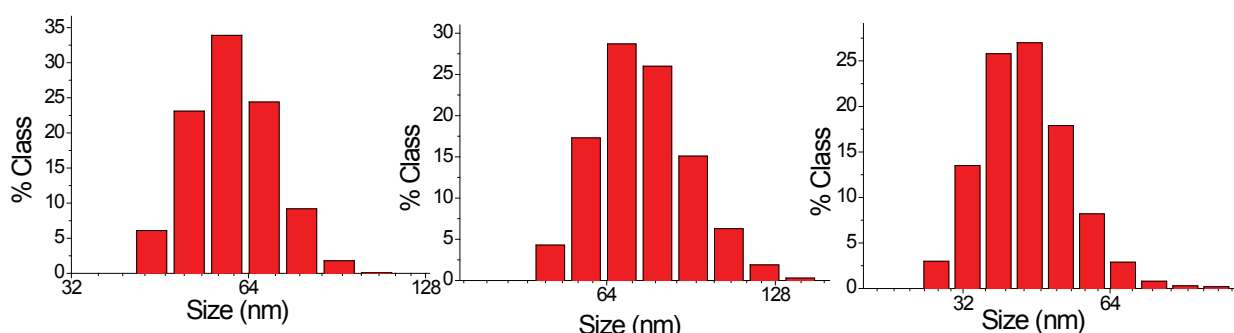


Figure III.13. Size distribution of the LCP conjugated GdF<sub>3</sub> particles in PBS solution. GdF<sub>3</sub>@TEG-qFTAA(5%) (left), GdF<sub>3</sub>@p(HEA)14-qFTAA(2%) (middle) and GdF<sub>3</sub>@p(HEA)26-pFTAA(10%) (right)

### 3.2.2 Stability in aqueous solution

A crucial requirement for biomedical application of different nanomaterials is, besides a low toxicity, a sufficient stability in physiological environments. For this purpose, evolution of zeta potential and size versus pH of the LCP labeled particles was investigated (Figure III.14 and Figure III.15).

Zeta potential and particles size are stable in the pH range from 12 to 5 for particles GdF<sub>3</sub>@p(HEA)26-pFTAA(2%), GdF<sub>3</sub>@p(HEA)26-pFTAA(10%) and less stable with a constant increase in size from pH 5 and 4 to more acidic pH. Zeta potential and size of particles GdF<sub>3</sub>@p(HEA)14-qFTAA(2%) and GdF<sub>3</sub>@TEG-qFTAA(5%) is stable in the pH range from 12 to respectively 5 and 6.5. The evolution of the size follows that of zeta potential, it is almost constant when zeta potential is around -20 mV and increase when zeta potential go to zero.

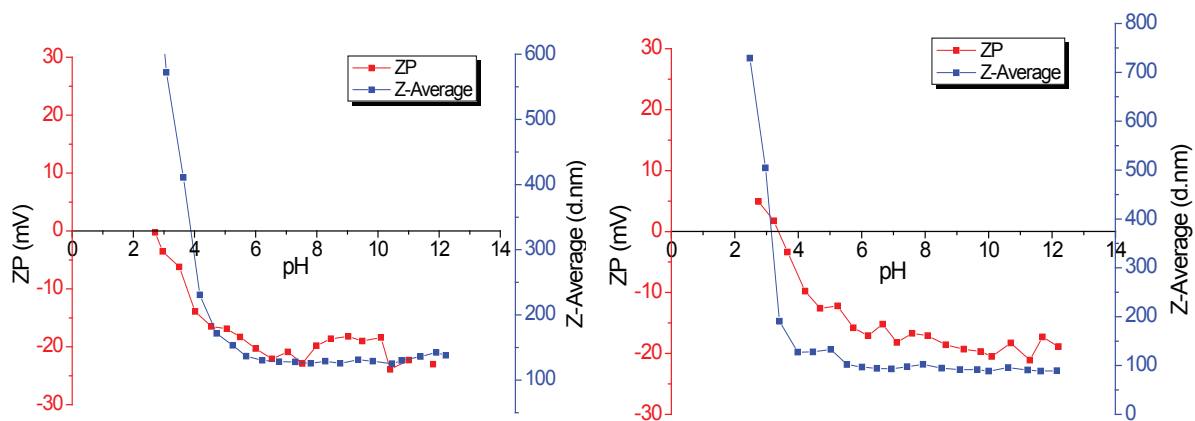


Figure III.14. Zeta potential and size versus pH of nanoparticles GdF<sub>3</sub>@p(HEA)26-pFTAA(10%) (left) and GdF<sub>3</sub>@p(HEA)26-pFTAA(2%) (right)

Zeta potential around -20 mV seems to be the minimum for the stability of the particles. Change compared to the pegylated particle which has an isoelectric point (IEP) at pH 5, with a zeta potential almost proportional to the pH, is the appearance of a plateau of zeta at -25/-30 mV from pH 12 to around 4-5. This reflected better stabilization of the particles compared to the pegylated particle. This stabilization is due to the presence of the LCPs-spacer moieties, larger than BP-PEG-CH<sub>3</sub> and the presence of deprotonated carboxyl group within LCPs, negatively charged in alkaline pH. IEP is shifted from pH 5 to pH 2.8; 3.1; 4.8 and 3.8 for respectively particles GdF<sub>3</sub>@p(HEA)26-pFTAA(10%), GdF<sub>3</sub>@p(HEA)26-pFTAA(2%), GdF<sub>3</sub>@TEG-qFTAA(5%) and GdF<sub>3</sub>@p(HEA)14-qFTAA(2%). Zeta potential is in range -30 and -25 mV at pH 7; and particles size at pH 7 is close to the minimum value (excepted particles GdF<sub>3</sub>@TEG-qFTAA(5%)), suggesting a strong stability of the suspension at this pH.

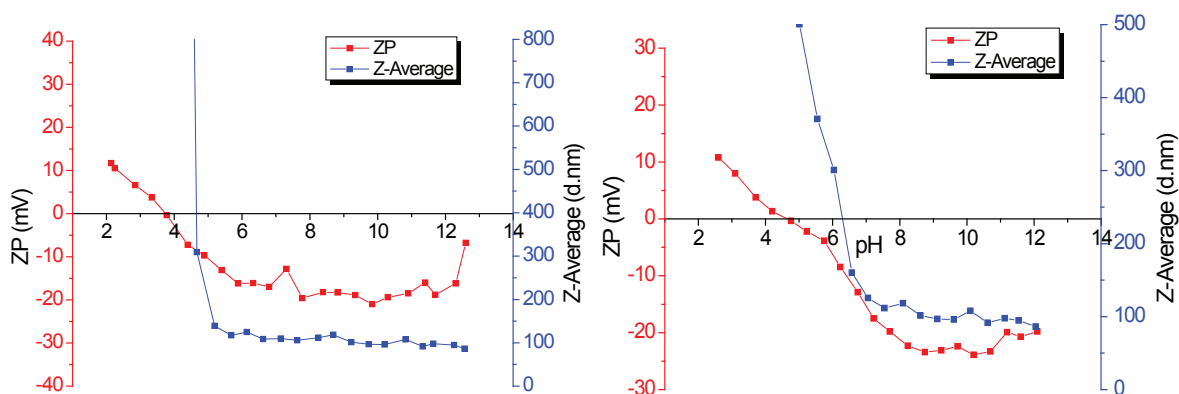


Figure III.15. Zeta potential and size versus pH of nanoparticles GdF<sub>3</sub>@p(HEA)14-qFTAA(2%) (left) and GdF<sub>3</sub>@TEG-qFTAA(5%) (right)

Particle GdF<sub>3</sub>@TEG-qFTAA(5%) seems less stable probably because the used spacer is too short. However, dispersion of all these LCP labeled particles in water or PBS solution lead to the very stable

colloidal solution and no aggregation was observed for several months. LCPs labeling does not affect the stability of the particles, on the contrary, presence of very water soluble spacer, larger than the BP-PEG-CH<sub>3</sub> and charged LCPs contribute to improvement of steric and electrostatic stabilization.

### 3.3 Photo-physic and relaxation properties in solution

#### 3.3.1 Quantum efficiency evaluation in aqueous solution

Photo-physics characterizations were carried out in order to evaluate the influence of the LCP labeling on the absorption, fluorescence emission and quantum efficiency. The absorption and emission spectra of free LCPs and LCP labeled particles were recorded. The spectral properties of the LCP labeled particles are similar to those of their respective free LCP and LCP-spacer moieties (Figure III.16 and Figure III.17). The spectral properties of the LCP are not affected by the particles. This indicates that they are not bound to the particles through their carboxylic functions. The maximum absorption is at 420 nm and 390 nm respectively for compounds attached to the tetrameric LCP (qFTAA) and attached to the pentameric LCP (pFTAA). The maximum emission is at 550 and 525 nm.

Quantum efficiency (QE) was measured, using Demasa and Crosby method<sup>345</sup>. It can be seen that particles with both pentameric LCP and the longer spacer (GdF<sub>3</sub>@p(HEA)26-pFTAA(2%), GdF<sub>3</sub>@p(HEA)26-pFTAA(10%)) have the same QE (0.085 and 0.086) independently to LCP ratio, suggesting that making pFTAA come too close to each other in this case do not quenches fluorescence signal.

However this QE is inferior to that of related free LCP, with is consistent because of the conformation freedom loss when bound to the particles. The obtained values are consistent to literature for various chromophores attached to nanoparticles<sup>346,347</sup>. QE of the particles with tetrameric LCP (GdF<sub>3</sub>@p(HEA)14-qFTAA(2%) and GdF<sub>3</sub>@TEG-qFTAA(5%)) depends on the spacer length. It is higher in the case of medium spacer (0.136) and lower for short spacer (0.057). The shorter spacer (GdF<sub>3</sub>@TEG-qFTAA(5%)) has a dramatical decrease in QE when attached to the nanoparticles. With the shorter spacer, the proximity of LCP-spacer moiety when bound to the particle seems make the chromophores come too close to the particles and may be also too close to each other and quenches each other by various mechanisms. It is difficult to give account on the mechanism without a systematic study of variations of spacer length.

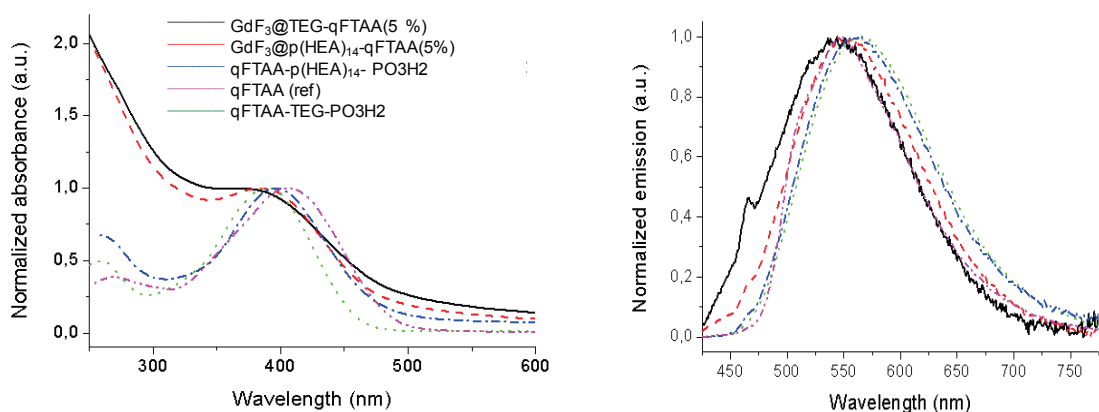


Figure III.16. Absorbance and fluorescence emission of free LCP and LCP coated nanoparticles ( $GdF_3@p(HEA)_{14}$ -qFTAA(2%) and  $GdF_3@TEG$ -qFTAA(5%))

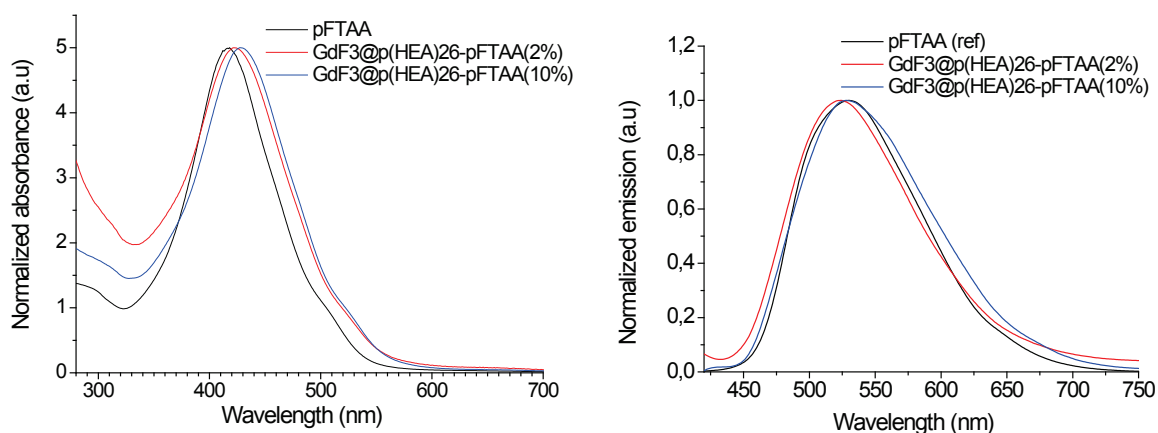


Figure III.17. Absorbance and fluorescence emission of free pFTAA and LCP coated nanoparticles ( $GdF_3@p(HEA)_{26}$ -pFTAA(2%) and  $GdF_3@p(HEA)_{26}$ -pFTAA(10%))

Table III.4. Quantum efficiency of different compounds

Compounds	LCP	QE
pFTAA (Ref)	pentameric	0.220
$GdF_3@p(HEA)_{14}$ -qFTAA(2%)	Tetrameric 2%	0.136
$GdF_3@TEG$ -qFTAA(5%)	Tetrameric 5%	0.057
$GdF_3@p(HEA)_{26}$ -pFTAA(2%)	Pentameric 2%	0.085
$GdF_3@p(HEA)_{26}$ -pFTAA(10%)	Pentameric 10%	0.084

These results indicate that the photo-physics properties of the LCPs are not altered after coupling with the particles. Despite the observation of the slight shifts of few nanometers and

decreasing of quantum yield, absorption and emission spectra after coupling remain close to those of free LCPs.

### 3.3.2 Relaxivity measurements in aqueous solution

Relaxivity properties of the as-prepared LCP labeled nanoparticles were performed to evaluate the influence of the LCP labeling on the relaxivity properties of the particles. The measurements were performed at 7T, according to the process described in chapter II and in PBS solution. The results (Table III.5) show that the relaxivity  $r_1$  remains constant or undergo a minor reduction, whereas relaxivity  $r_2$  change from  $55 \text{ mM}^{-1}\text{s}^{-1}$  to  $71\text{-}158 \text{ mM}^{-1}\text{s}^{-1}$  after LCP grafting. We observe the enhancement of transverse relaxivity after labeling, to reach relaxivity values comparable to those of super-paramagnetic iron particles<sup>319</sup>.

**Table III.5. Relaxivity of the particles conjugated to different LCPs with different linkers**

Particle	Per ion Relaxivity ( $\text{mM}^{-1}\text{s}^{-1}$ )		Per particle relaxivity ( $\mu\text{M}^{-1}\text{s}^{-1}$ )	
	$r_1$	$r_2$	$r_1$	$r_2$
GdF <sub>3</sub> @p(HEA) <sub>14</sub> -qFTAA(2%)	0.53	158.2	185	54192
GdF <sub>3</sub> @TEG-qFTAA(5%)	0.40	148.9	137	51641
GdF <sub>3</sub> @p(HEA) <sub>26</sub> -pFTAA(2%)	0.37	71.4	127	24776
GdF <sub>3</sub> @p(HEA) <sub>26</sub> -pFTAA(10%)	0.45	87.4	155	30331

These values can be divided into two groups. First, those higher than  $100 \text{ mM}^{-1}\text{s}^{-1}$ ; related to particles combined with tetrameric LCP; at  $158$  and  $148 \text{ mM}^{-1}\text{s}^{-1}$  respectively for particles GdF<sub>3</sub>@p(HEA)<sub>14</sub>-qFTAA(2%) and GdF<sub>3</sub>@TEG-qFTAA(5%). Second those less than  $100 \text{ mM}^{-1}\text{s}^{-1}$ ; related to particles combined with pentameric LCP; at  $71$  and  $87 \text{ mM}^{-1}\text{s}^{-1}$  respectively for particles GdF<sub>3</sub>@p(HEA)<sub>26</sub>-pFTAA(2%) and GdF<sub>3</sub>@p(HEA)<sub>26</sub>-pFTAA(10%). We can point out the fact that particles with tetrameric LCP were made with short and medium spacer (4 and 14 units) unlike particles with pentameric one (26 units).

Usually, the relaxivities are related to four key characteristic of the magnetic nanoparticles: (i) chemical composition, (ii) size of the particle, (iii) shape of the particle and (iv) surface properties<sup>348</sup>. Here the major changes from unlabeled particles that can influence relaxivity are (i) size of the particle, the degree of their aggregation, and (ii) surface properties. Here we observed no aggregation after conjugation with LCP, and the increase in size is not significant. However, change in mass is ineluctable. Thus this  $r_2$  enhancement can be due to the reducing of particle tumbling rate.

The difference observed in enhancement of  $r_2$  between the labeled particles is also probably due to the surface state; because of the presence of different spacer-LCP moieties.

First of all, the longitudinal relaxivity  $r_1$  is based on the exchange of energy which occurs primarily in contact to the surface of the particle (short distance); thus it is less affected by conjugation of the particle with LCP. The observed slight decrease could be due to a slight decrease in diffusion and exchange of proton near the surface of the particle because of the presence of the spacer (pHEA) which can lead to more hindrance or water molecules retention by hydrogen bond. Transverse relaxivity  $r_2$  is based on field inhomogeneity due to presence of magnetic entities, thus it occurs in relatively high scale (large distance). Labeling can affect transverse relaxation by diffusion, hydration and hydrogen binding. These parameters depend mainly on nature of coating molecules and thickness of the coating. Here we see clearly that the relaxivity depends strongly on nature of LCP, spacer and is higher for the tetramer one.

Duan et al have shown that hydrophilicity of the coated surface contributes greatly to the enhancement of relaxivity<sup>349</sup>. They demonstrated that particles coated with the hydrophilic ligand yield the highest proton relaxivity. Tong et al have shown that relaxivity depend on thickness of the coating<sup>350</sup>. The  $r_2$  relaxivity values can increase with the coating thickness until reaches a maximum value before going down. As difference in thickness of our coating shell is not clear, the difference in relaxivity of the particles can be due to the difference in hydrophilicity of the spacer-LCP moieties. However, a systematic study of the influence of nature and length of spacer and LCP is needed to clarify the influence of each parameter.

### **3.4 Conclusion**

These results show that LCPs were successfully coated on gadolinium fluoride particles with different LCP ratio and spacer length. The resulting particles present a unique population in colloidal solution and a strong stability in physiological environment. Moreover no aggregation was observed after several days. Coating efficiency was confirmed by different technique and grafting density was estimated from 1.68 to 1.83 PEG/nm<sup>2</sup> and from 0.47 to 1.14 LCP/nm<sup>2</sup>. Fluorescence properties of LCPs were conserved after coating, even if decrease of quantum efficiency is observed. Surprisingly, magnetic properties of gadolinium fluoride particles are enhanced after coating resulting in high T2 relaxation, making it a great negative contrast agent. Requirements of the coating are met and preliminaries biological evaluation of the obtained particles can be carried out.

# CHAPTER IV



# CHAPTER IV BIOLOGICAL EVALUATION OF THE PARTICLES

Pegylated gadolinium fluoride ( $\text{GdF}_3\text{@PEG}$ ), pegylated gadolinium phosphate ( $\text{GdPO}_4\text{@PEG}$ ) and titanium oxide coated DOTA- $\text{Gd}^{3+}$  ( $\text{TiO}_2\text{@DOTA-Gd}^{3+}$ ) were prepared in this project. In chapter III we showed the conjugation between  $\text{GdF}_3$  particles and LCPs to perform multimodal contrast agent. This chapter is devoted to biological evaluation of the prepared particles:  $\text{GdF}_3\text{@PEG}$ ,  $\text{TiO}_2\text{@DOTA-Gd}^{3+}$  and the LCP coated  $\text{GdF}_3$  particles presented in Table III.1 are investigated.

First all, Ex-vivo MRI experiments are performed to evaluate capacity of  $\text{GdF}_3\text{@PEG}$  and  $\text{TiO}_2\text{@DOTA-Gd}^{3+}$  particles to create contrast in mice brain tissues. Then *in vitro* and *in vivo* experiments are carried out with LCPs coated  $\text{GdF}_3$  particles. In these studies we investigate the capacity of the particles to cross the blood brain barrier, bind and stain A $\beta$  plaques *in vitro* and *in vivo*.

## 1 EX VIVO MRI EVALUATION OF PEGYLATED NANOPARTICLES

Efficiency of the prepared particles was studied *ex vivo*. Images were obtained from *ex vivo* wild type mice brains. The brains have been frozen, causing deformation and loss of pronounced structures. The observed contrast is due to direct injection of 2  $\mu\text{l}$  of 0.2225 mM (gadolinium concentration) of the particles solution into *ex vivo* brains which had been thawed before injections. These *ex vivo* experiments were performed in Trondheim University by Else Marie Huuse, Marius Widerøe, Marte Thuen, Kristine Skårdal and Olav Haraldseth.

### 1.1 Gadolinium fluoride as negative contrast agent

Magnetic properties of the pegylated gadolinium fluoride ( $\text{GdF}_3\text{@PEG}$ ) are investigated and discussed in chapter II. Particles have relaxivity values of 0.55 and 55  $\text{mM}^{-1}\text{s}^{-1}$  respectively for  $r_1$  and  $r_2$ . Its  $r_2/r_1$  ratio of 100 suggests that particles are suited for T2 contrast. The particles are tested *ex vivo* brains (Figure IV.1 and Figure IV.2). We can observe a high dark contrast in T2-weighted spin echo sequence as expected (Figure IV.1). Because of the higher  $r_2$  compared to  $r_1$ , dark contrast in T1-weighted gradient echo images is observed due to T2\* effects (Figure IV.2 –right-). In T1-weighted spin echo sequence (Figure IV.2-left-), contrast is weak and image is blurred. These observations show that these particles are definitively suited as negative contrast agent with capacity to provide high contrast.

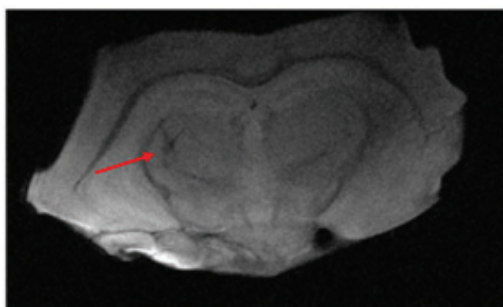


Figure IV.1. *Ex vivo* MRI image of wild type mice brains using GdF<sub>3</sub>@PEG as contrast agent: T2-weighted spin echo MRI– dark contrast. Direct injections of the particles into *ex vivo* brains

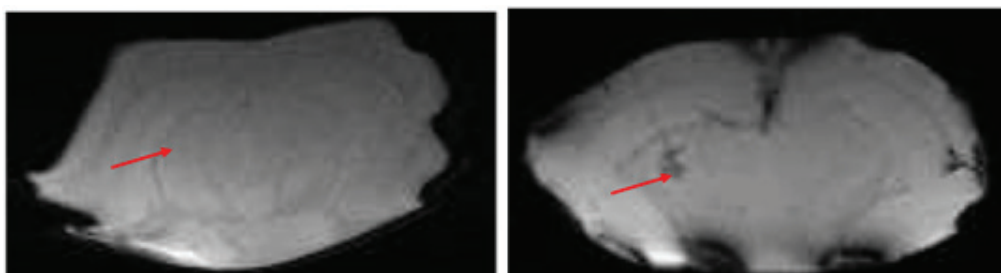


Figure IV.2. *Ex vivo* MRI image of wild type mice brains using GdF<sub>3</sub>@PEG as contrast agent: T1-weighted spin echo MRI (left) and T1-weighted gradient echo MRI– dark contrast (right). Direct injections of the particles into *ex vivo* brains

## 1.2 TiO<sub>2</sub> coated DOTA-Gd(III) as negative and positive contrast agent

TiO<sub>2</sub>@DOTA-Gd(III) particles were also investigated and discussed in chapter II. They have relaxivity value of 13.5 and 56.4 mM<sup>-1</sup>s<sup>-1</sup> respectively for r<sub>1</sub> and r<sub>2</sub> and a lower r<sub>2</sub>/r<sub>1</sub> ratio of 4.2 suggesting that they are suited for both positive and negative contrast. Figure IV.3 shows that TiO<sub>2</sub>@DOTA-Gd(III) are visible in MR images as both positive and negative contrast depending on the imaging sequence used for acquisition. In a T1 weighted spin echo image (Figure IV.3-A) the particles appear as positive contrast while the same particles appears as negative contrast in a T1-weighted gradient-echo image (Figure IV.3-B) due to T<sub>2</sub>\* effects. Due to the high r<sub>2</sub> the signal are negative in both T2-weighted gradient echo (Figure IV.1-C) and T2-weighted spin echo (Figure IV.1-D).

Because of the natural content of iron in the brain, black spots might appear in T2 weighted images without any paramagnetic or super paramagnetic particles. For Alzheimer's plaque imaging it would be an advantage to use this kind of particles which can shorten both T<sub>1</sub> and T<sub>2</sub> relaxation time. These particles induce positive (bright) contrast in T<sub>1</sub> weighted images and negative (dark) contrast in T<sub>2</sub> weighted images, contrary to particles with very high r<sub>2</sub> compared to r<sub>1</sub>, such as iron or GdF<sub>3</sub>@PEG particles with witch the contrast in the images becomes absent or dark in T<sub>1</sub> weighted images due to T<sub>2</sub>\* effects.

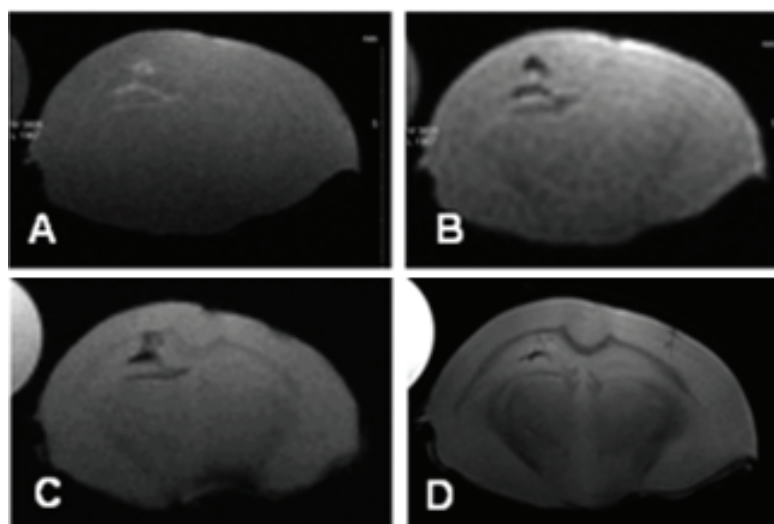


Figure IV.3. *Ex vivo* MRI image of wild type mice brains using  $\text{TiO}_2\text{@DOTA-Gd(III)}$ . T1 weighted spin echo image (A), T1-weighted gradient-echo image (B), T2-weighted gradient echo image (C), T2-weighted spin echo image (D). Direct injections of the particles into *ex vivo* brains

These *ex vivo* MR image experiments allow the validation of these two particles,  $\text{GdF}_3\text{@PEG}$  and  $\text{TiO}_2\text{@DOTA-Gd(III)}$  as respectively negative contrast agent and both positive and negative contrast agent. In the next section, we will evaluate the LCP labelled  $\text{GdF}_3$  particles. The *in vitro* and *in vivo* evaluation of their capacity to labeled  $\text{A}\beta$  plaques will be determined by fluorescence microscopy, and then *in vivo* evaluation of their capacity to short T2 relaxation in brain tissue after *in vivo* injection will be discussed.

## 2 IN VITRO EVALUATION OF THE LCP LABELED NANOPARTICLES

Previously we mentioned the interesting properties of LCPs to specifically and efficiently stain  $\text{A}\beta$  and its ability to emit a specific fluorescence signal, feature of  $\text{A}\beta$  binding. In this section, we are interested in capacity of the LCP labeled  $\text{GdF}_3$  particles to stain and image  $\text{A}\beta$  plaques. These *in vitro* experiments were performed by Andreas Åslund, Sofie Nyström, Therése Klingstedt and Mikael Lindgren at Linköping University.

### 2.1 Selectivity of the LCP labeled particles to $\beta$ -amyloid fibrils cells

In order to evaluate the selective binding of the LCPs labeled particle to  $\text{A}\beta$  aggregates, *in vitro* test was performed with the LCP labeled particle ( $\text{GdF}_3\text{@TEG-qFTAA}(5\%)$ ) and free LCP particles as control ( $\text{GdF}_3\text{@PEG}$ ), on two cells:  $\text{A}\beta$  positive and  $\text{A}\beta$  negative (Figure IV.4). It can be seen that only the association of  $\text{GdF}_3\text{@TEG-qFTAA}(5\%)$  and the  $\text{A}\beta$  positive cells results in fluorescence emission, characteristic of the binding of  $\text{GdF}_3\text{@TEG-qFTAA}(5\%)$  to  $\text{A}\beta$  fibrils in cells.

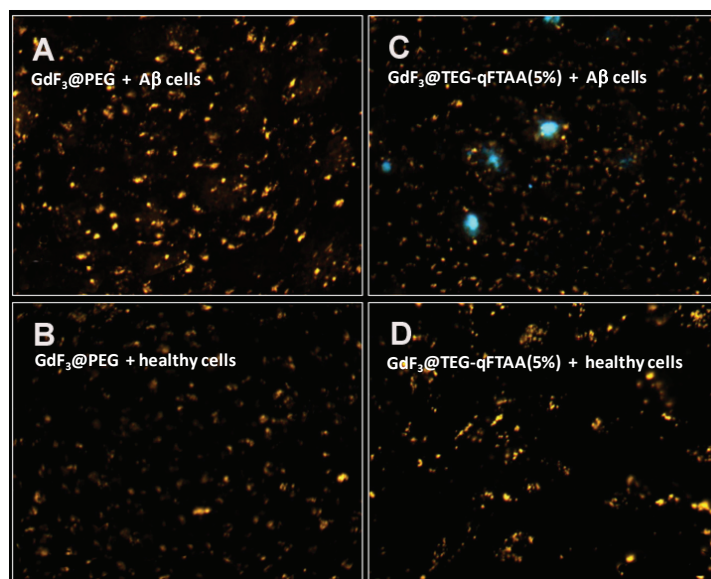


Figure IV.4. Fluorescence microscope images of positive (A, C) and negative (B, D) A $\beta$  cells stained by GdF<sub>3</sub>@TEG-qFTAA(5%) (C, D); and GdF<sub>3</sub>@PEG (A, B) nanoparticles

Thus, by adding the GdF<sub>3</sub>@TEG-qFTAA(5%) nanoparticles to the A $\beta$  cells, A $\beta$  are stained with fluorescence. Suggesting that, by attaching LCP to the particles, LCPs don't lost these staining properties, and the staining remains specific since fluorescence signal is observable only on positive cells with particles GdF<sub>3</sub>@TEG-qFTAA(5%), while no signal can be seen both in positive and negative cells with particle GdF<sub>3</sub>@PEG. This result confirms the selective staining of the LCP conjugated nanoparticles, assuming that there is no free LCP in the cells, released from GdF<sub>3</sub>@TEG-qFTAA(5%) particles. To confirm this staining, this binding can be visualized with TEM.

## 2.2 TEM visualization of the binding to $\beta$ -amyloid fibrils

TEM was performed to visualize the selective binding of the LCPs labeled particle to A $\beta$  aggregates. We associated on one hand free LCP particles (GdF<sub>3</sub>@PEG) and on the other hand LCP labeled particle (GdF<sub>3</sub>@TEG-qFTAA(5%)) with amyloid fibrils made from recombinant A $\beta$ -42 peptide<sup>80</sup>. Figure IV.5 and Figure IV.6 show TEM images of respectively A $\beta$  fibrils/GdF<sub>3</sub>@PEG and A $\beta$  fibrils/GdF<sub>3</sub>@TEG-qFTAA(5%) nanoparticles assemblies. The GdF<sub>3</sub>@PEG particles bind only partially to the A $\beta$  fibrils (electrostatic interaction) and it can be seen many free unassociated particles beside the A $\beta$  fibrils, as observed in case of A $\beta$  fibrillation in presence of free  $\gamma$ -Fe<sub>2</sub>O<sub>3</sub> nanoparticles<sup>127</sup>. The interaction of unlabeled particles with A $\beta$  is not specific contrary to that of particles GdF<sub>3</sub>@TEG-qFTAA(5%) with A $\beta$  fibrils. All GdF<sub>3</sub>@TEG-qFTAA(5%) particles are bind specifically to fibrils because no free unassociated GdF<sub>3</sub>@TEG-qFTAA(5%) particles can be observed. This specific bind was also observed in case of A $\beta$ -40 labeled  $\gamma$ -Fe<sub>2</sub>O<sub>3</sub> nanoparticles<sup>220</sup>.

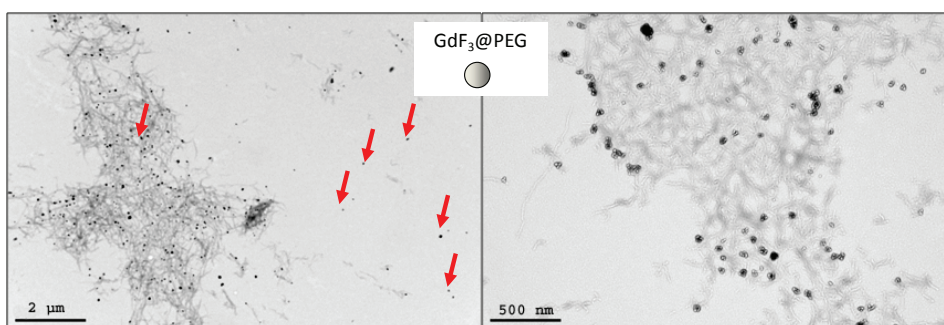


Figure IV.5. TEM images of the A $\beta$  fibrils bind to free particle (GdF<sub>3</sub>@PEG): non-specific binding

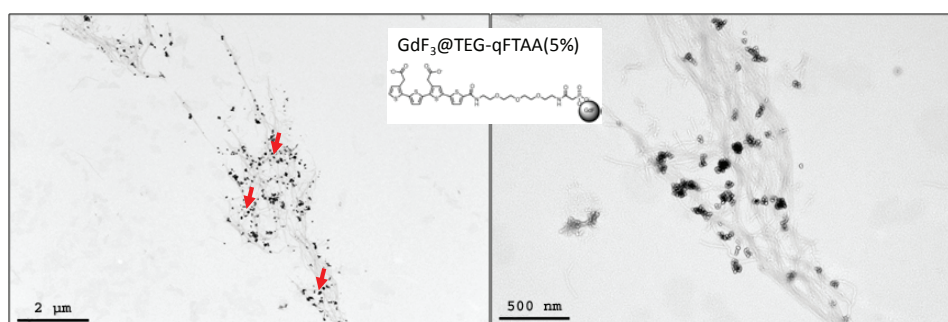


Figure IV.6. TEM images of the A $\beta$  fibrils bind to LCP labeled particle GdF<sub>3</sub>@TEG-qFTAA(5%): specific binding

This important result shows clearly that this specific binding is due to the presence of LCP on the particles surface, suggesting that LCPs remain active against A $\beta$  when located at the surface of the particles. Its capacity to bind and stain A $\beta$  is not altered and can bind to A $\beta$  fibrils as well as A $\beta$  labeled particles. This observation demonstrates the interest of these particles. They can create double contrast (MRI and fluorescence), and have a strong affinity to A $\beta$ . Also, there is probably no risk to induce A $\beta$  peptides aggregation enhancement in the brain<sup>80</sup>, contrary to A $\beta$  labeled particles.

### 2.3 *In vitro* binding of the particles to A $\beta$ in tissue samples

In order to study the *in vitro* staining for amyloid deposits detection, transgenic mice with A $\beta$  aggregated pathological species are needed. APP23 and APP/PS1 mice overexpressing human APP are used to evaluate the staining of A $\beta$  plaques. Two LCP labeled particles, GdF<sub>3</sub>@p(HEA)14-qFTAA(2%) and GdF<sub>3</sub>@TEG-qFTAA(5%) were used to visualize amyloid plaques in tissue slides from 16-18-month transgenic mice (APP23 and APP/PS1), and compared to the related free LCPs and free LCP-spacer moieties. (Figure IV.7 and Figure IV.8).

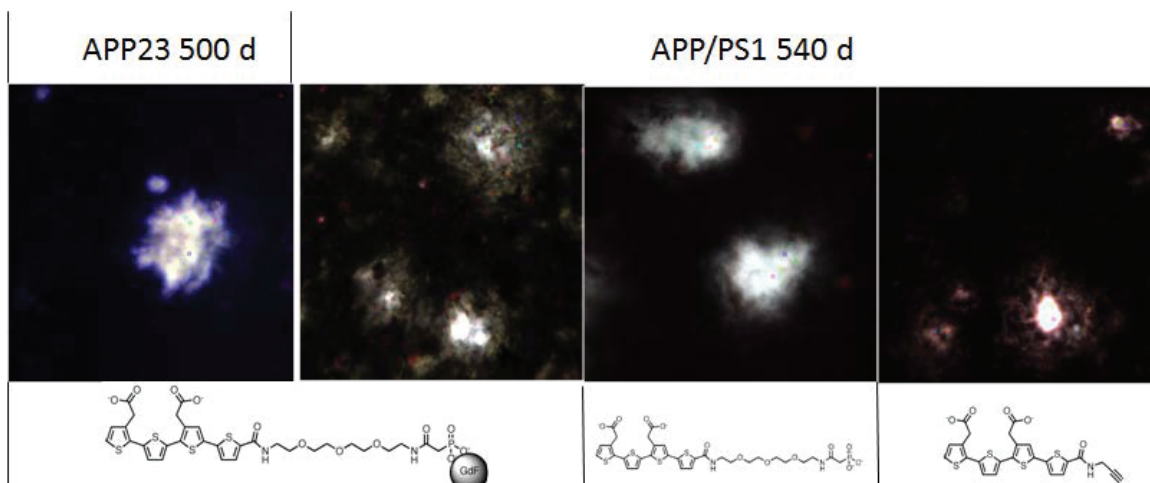


Figure IV.7. Spectral image of *in vitro* staining of APP23 500 days mice and APP/PS1 540 days mice with GdF<sub>3</sub>@TEG-qFTAA(5%), qFTAA-TEG-PO<sub>3</sub>H<sub>2</sub> and qFTAA

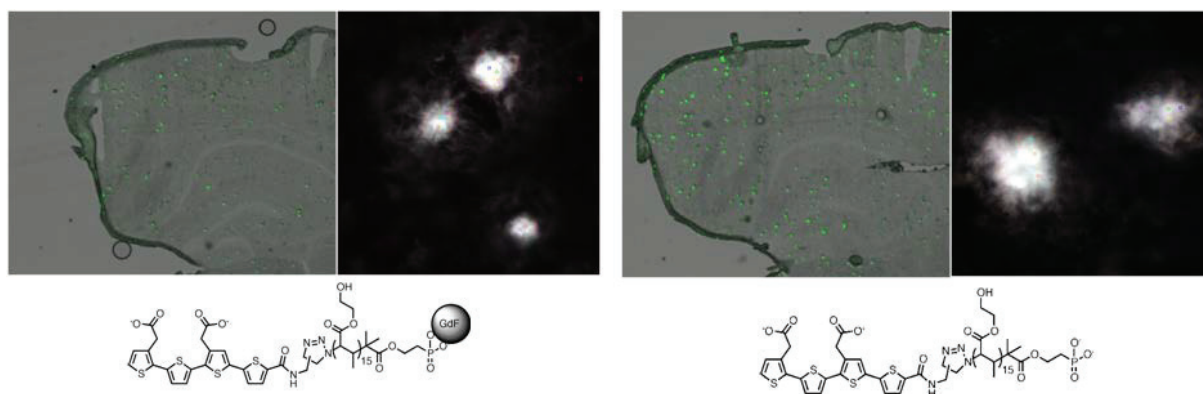


Figure IV.8. Overview and spectral image of *in vitro* staining of APP/PS1 540 days mice with GdF<sub>3</sub>@p(HEA)14-qFTAA(2%) and qFTAA-TEG-PO<sub>3</sub>H<sub>2</sub>

We can see that these compounds stain both APP23 and APPPS1 mice tissues. The detected plaques in the tissues are seen as green spots in the overview images and as a bright blue clear signal in spectral image. The observed signal come from fluorescence of LCP bound to A $\beta$  plaques. It can be seen that spectral signal of free LCPs and free LCP-spacer moiety, with medium or short spacers are similar to those of LCP labeled particles GdF<sub>3</sub>@p(HEA)14-qFTAA(2%) and GdF<sub>3</sub>@TEG-qFTAA(5%). This is the confirmation of the preservation of the *in vitro* fluorescence and staining properties of the conjugated particles.

On the basis of this successful *in vitro* experiment on the mice brain tissues, we hypothesized that these LCP conjugated particles could be used as efficient targeted probes able to cross the BBB and stain A $\beta$  plaques *in vivo*. Thus, the crucial questions arise; will these probes survive *in vivo*? Will the probes pass the blood-brain-barrier? Indeed these particles must have appropriate physico-chemical properties in the plasma after *in vivo* injection to conserve their activities and their

efficiency. Among others, they must remain intact and dispersed, i.e. neither break-ups (desorption of grafted molecules) nor aggregation. They must have a long enough blood circulation time, therefore a minimum uptake into endothelial cells. And the most important, despite their large size and complex structure compared to the free LCPs, they must still pass the BBB before to bind to A $\beta$  plaques.

### **3 IN VIVO EVALUATION OF THE LCP LABELED NANOPARTICLES**

The *in vitro* binding and specificity of the tetrameric LCP labeled particles, GdF<sub>3</sub>@p(HEA)14-qFTAA(2%) and GdF<sub>3</sub>@TEG-qFTAA(5%) towards amyloid was previously well established. We therefore assume that there is highly probable that this is also valid for the pentameric LCP labeled particles GdF<sub>3</sub>@p(HEA)26-pFTAA(2%) and GdF<sub>3</sub>@p(HEA)26-pFTAA(10%) in regard to the efficiency of free pentameric LCPs. Thus in this section, all these particles are tested *in vivo*. The solution of the particles are injected in APP/PS1 mice, and imaged *in vivo* over time in the case of staining kinetic studies, or sacrificed several days after in case of histological staining studies. In this case, brains sections were collected and analyzed by both fluorescence and MR imaging. Difficulties are related in the particles stability in the plasma, in the BBB passage and in the *in vivo* A $\beta$  binding. Also, once bound to the A $\beta$ , they must be able to create both fluorescence and magnetic contrast.

The aims of these experiments are to evaluate the capacity of the particles to cross the BBB, to bind to A $\beta$  and emit fluorescence signal and enhance MRI signal. In these purpose, fluorescence imaging with one and two photons excitation were carried out on the *in vivo* injected brains sections. Then the relaxation rate change of the sections was investigated. These *in vivo* experiments were performed in collaboration with Charité University (Susann Handrick, Stefan Prokop and Frank Heppner); Tübingen University (Bettina Wegenast-Braun, Jasmin Mahler and Mathias Jucker) and Trondheim Universities (Nina Kristine Reitan, Mikael Lindgren).

#### **3.1 Single photon fluorescence imaging of plaques in APP/PS1 mice brain**

##### **3.1.1 Tetrameric LCP labeled nanoparticles**

The tetrameric labeled particles (GdF<sub>3</sub>@p(HEA)14-qFTAA(2%) and GdF<sub>3</sub>@TEG-qFTAA(5%)) were dispersed in aqueous PBS (10 mg/ml). As references, we used free pFTAA in PBS, 10 mg of molecule per ml and no stained mice (PBS injection) as control. The 581 days old mice were injected in the tail vein. 100  $\mu$ l of probe solution was injected in two consecutive injections within 48h. Mice were sacrificed one week after second injection. No perfusion was used. One brain hemisphere was stored at -80°C (for other experiments including MRI) and other hemisphere were used for

cryosections (unfixed) and imaged by fluorescence microscopy, with excitation at 489 nm and emission at 509 nm. Here after fluorescence images of the slides (Figure IV.9).

The fluorescence intensity of plaques *in vivo* injected APP/PS1 mice with pFTAA,  $GdF_3@p(HEA)_{14}$ -qFTAA(2%) and  $GdF_3@TEG$ -qFTAA(5%) compared to PBS injected mice are higher in this one photon excitation microscopy. However, at this wavelength excitation (489 nm), the auto-fluorescence from amyloid plaque (PBS control) is visible even if it remains lower than signal from probes.

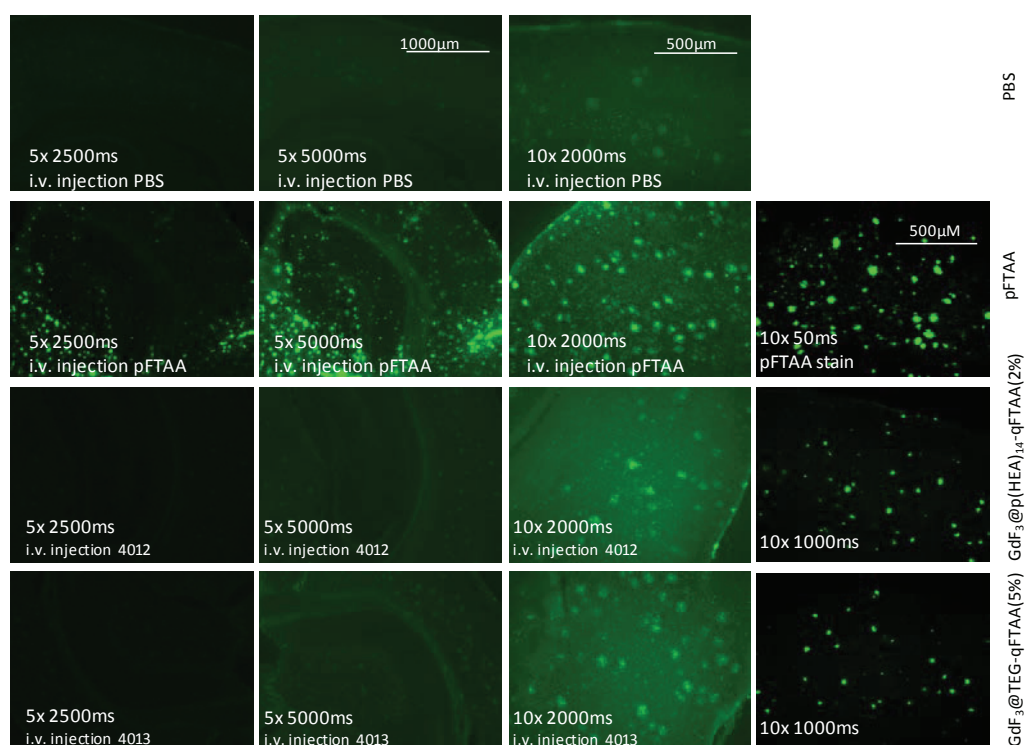


**Figure IV.9. Fluorescence image of plaque *in vivo* injected APP/PS1 mice with PBS, pFTAA,  $GdF_3@p(HEA)_{14}$ -qFTAA(2%) and  $GdF_3@TEG$ -qFTAA(5%)**

Despite this strong auto-fluorescence, these images show that  $GdF_3@p(HEA)_{14}$ -qFTAA(2%) and  $GdF_3@TEG$ -qFTAA(5%) probes bind to  $A\beta$  deposits with a signal intensity comparable to that of pFTAA which is more concentrated. As the auto-fluorescence is too strong in this wavelength excitation, two-photon excitation with higher wavelength excitation (around 800 nm) should minimize auto-fluorescence from plaques and revealed efficiently the  $A\beta$  plaques staining. Also, it has been demonstrated that the free tetrameric LCP (qFTAA) bind almost exclusively to core parts of mature plaques. Hence in young APP/PS1 mice for example it shows rather low binding to plaque compared to what is detected with pFTAA. Then the pentameric LCP conjugated particles will most likely improve staining.

### 3.1.2 Pentameric LCP labeled nanoparticles

The procedure is identical to that used for particles  $GdF_3@p(HEA)_{14}\text{-qFTAA}(2\%)$  and  $GdF_3@TEG\text{-qFTAA}(5\%)$ . The pentameric labeled particles ( $GdF_3@p(HEA)_{26}\text{-pFTAA}(2\%)$  and  $GdF_3@p(HEA)_{26}\text{-pFTAA}(10\%)$ ) were dispersed in aqueous PBS (10 mg/ml); pFTAA in PBS solution (10 mg/ml) and no stained mice (PBS injection) are used as control. The aged mice were injected in the tail vein. 100  $\mu\text{l}$  of probe solution was injected in two consecutive injections within 48h. Mice were sacrificed one week after second injection. No perfusion was used. One brain hemisphere was stored at  $-80^\circ\text{C}$  (for other experiments including MRI) and other hemisphere were used for cryosections (unfixed) and imaged by fluorescence microscopy. Imaging was performed with excitation at 489 nm and emission at 509 nm. Here after fluorescence images of the brains sections (Figure IV.10).

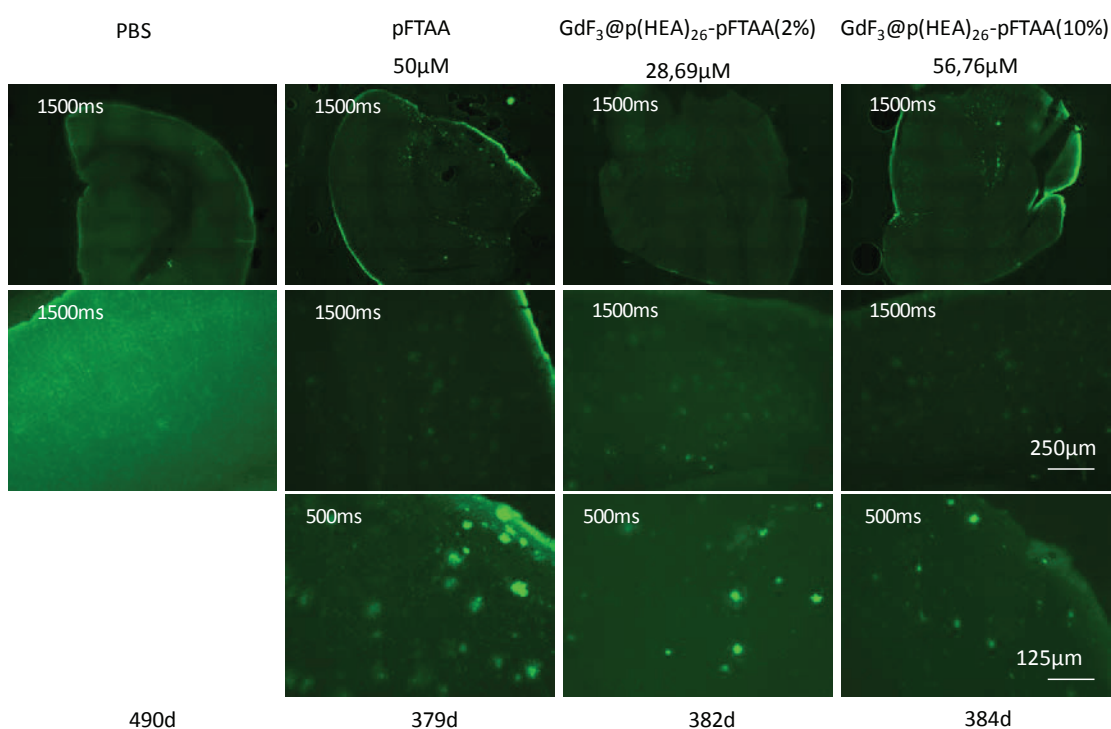


**Figure IV.10. Fluorescence image of plaque *in vivo* injected APP/PS1 mice with PBS, pFTAA,  $GdF_3@p(HEA)_{26}\text{-pFTAA}(2\%)$  and  $GdF_3@p(HEA)_{26}\text{-pFTAA}(10\%)$  (LCP concentration given in  $\mu\text{M}$  and mouse age in days (d))**

It can be seen in these images that binding of the probes  $GdF_3@p(HEA)_{26}\text{-pFTAA}(2\%)$  and  $GdF_3@p(HEA)_{26}\text{-pFTAA}(10\%)$  to amyloid revealed a stronger fluorescence signal than  $GdF_3@p(HEA)_{14}\text{-qFTAA}(2\%)$  and  $GdF_3@TEG\text{-qFTAA}(5\%)$  probes. Probes emit green light upon binding to the amyloid deposits, and the deposits can easily be discriminated from the rest of the tissue compared to control (PBS injection). Beyond the possible influence of spacer length, the higher specific feature and selectivity of the pentameric LCP compared to the tetrameric one were

explained by a strong hydrophobic interaction with A $\beta$  due to presence of five thiophene rings<sup>80,87</sup>. LCPs are designed in such a way that the backbone is exposed for maximum hydrophobic interaction with fibrillar protein, while the side chain must remain hydrophilic to ensure water solubility as well as reducing the interaction with non amyloidic protein<sup>87</sup>. It is interesting to note that after conjugations, LCPs properties are preserved in such a way that differences in properties between the tetrameric and the pentameric are also preserved.

In the following section, we are interested in two-photon absorption microscopy (TPA) to eliminate the auto-fluorescence problem of A $\beta$  and other biomolecules. Also TPA allows enhancing spatial resolution and depth penetration of tissue, suited for live animal imaging.

### 3.2 Two photon fluorescence imaging of plaque in APP/PS1 mice brain

In order to avoid the auto-fluorescence, two-photon excitation imaging was performed in the Zeiss-LSM-Meta with 780, 800 and 830 nm excitation wavelengths. At these excitation wavelengths auto-fluorescence from amyloid plaque is much lower compared to that from LCP as shown in Figure IV.11. Experiments were performed by Nina Reitan and Mikael Lindgren from physic department of Trondheim University.

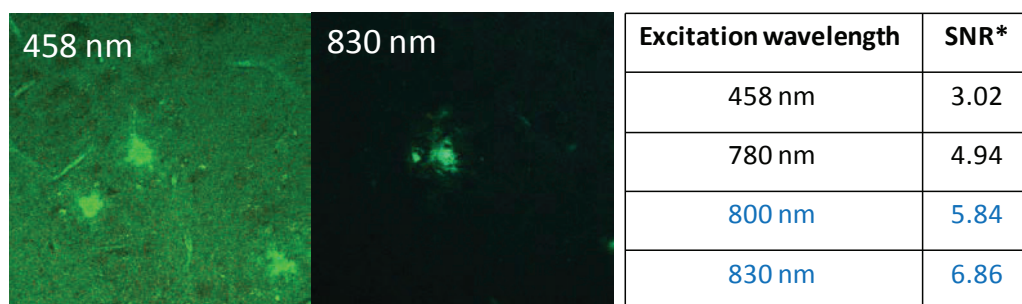


Figure IV.11. Fluorescence images and signal to noise ratio (SNR) of *in vivo* injected APP/PS1 mice with free pFTAA.

\*The SNRs was calculated as the maximum plaque intensity relative to the maximum background intensity

The imaged samples are brain tissue sections of APP/PS1 mouse sampled after *in vivo* injection of free pFTAA. The SNR is based on the spectra of averages intensity values of several ROIs. The plaque and background intensities for each excitation wavelength are normalized to the maximum intensity of the respective plaque spectrum. At 458 nm, it is one-photon absorption. The SNR value is only 3 and the auto-fluorescence is relatively high in the corresponding image, making difficult the interpretation of the image. From 780 nm, it is two-photon absorption and we can see that the SNR increases regularly with the excitation wavelength, reaching the maximum of 6.86 at 830 nm. On the corresponding image, the auto-fluorescence disappeared and we can clearly see the stained plaques thanks to the green signal on a black background. Increase the excitation wavelength allows

deviating from the wavelength absorption of biomolecules, including A $\beta$ . The latter absorbs less and cannot absorb at two-photon, their fluorescence signal turns off gradually, hence increase of SNR. TPA gives a higher signal-to-noise ratio (SNR) in brain sections than one photon absorption (OPA).

### 3.2.1 Tetrameric LCP labeled nanoparticles

TPA image of brain tissue sections of APPPS1 mouse sampled after *in vivo* injection of probe GdF<sub>3</sub>@TEG-qFTAA(5%) was carried out at 780 nm (Figure IV.12-left). A clear separation from the autofluorescence is observed, however the later remains relatively high. Probably because of the used concentration of the particles solutions, 1 mg/ml, lower than previously in OPA (10 mg/ml).

An unmixed spectral analyze was performed in order to better resolve GdF<sub>3</sub>@TEG-qFTAA(5%) binding. Figure IV.12 shows TPA fluorescence image (left), unmixing fluorescence image (middle) and spectral separation of signal (right) from GdF<sub>3</sub>@TEG-qFTAA(5%) and that from the auto-fluorescence. Fluorescence spectra were acquired at the center of plaques of a control sample (PBS injection) and of a sample stained with GdF<sub>3</sub>@TEG-qFTAA(5%).

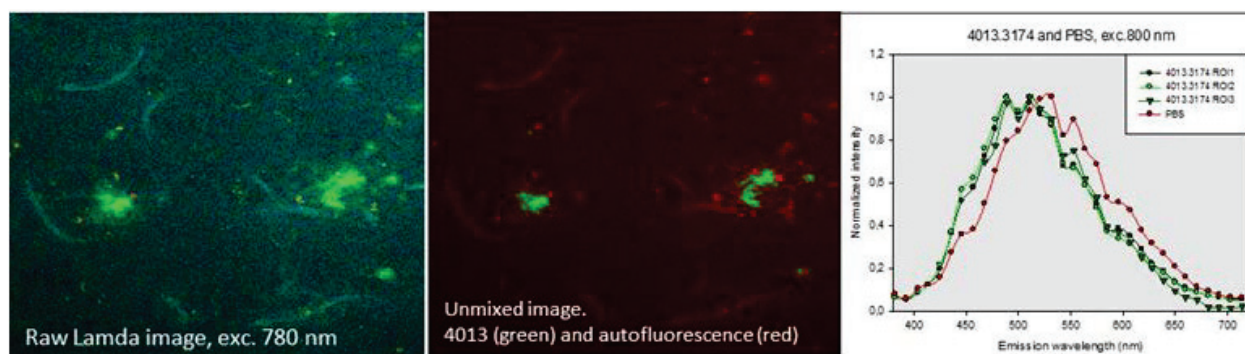


**Figure IV.12. TPA fluorescence (left), unmixing fluorescence image (middle) and spectral separation of GdF<sub>3</sub>@TEG-qFTAA(5%) signal from the autofluorescence (right). Fluorescence from GdF<sub>3</sub>@TEG-qFTAA(5%) (green), from autofluorescence (red)**

Because of the low signal intensity, separation from autofluorescence is not highly efficiency (Figure IV.12-middle), higher concentrations are needed. However, we can clearly distinguish signal from background to signal from probe. The auto-fluorescence from amyloid plaque is definitively lower at 780, (TPA) than at 480 nm (OPA). The auto-fluorescence from the amyloid plaques (red traces) and fluorescence from GdF<sub>3</sub>@TEG-qFTAA(5%) (green traces) are shown in above spectra (Figure IV.12-right). The GdF<sub>3</sub>@TEG-qFTAA(5%) spectrum is red shifted compared to the auto-fluorescence and has two maximum peaks, characteristic of A $\beta$  binding<sup>80,83</sup>. Thus we can distinguish signal from background to signal from probe that confirms A $\beta$  plaques binding.

### 3.2.2 Pentameric LCP labeled nanoparticles

We have also imaged with TPA, samples stained with particles  $GdF_3@p(HEA)26-pFTAA(2\%)$  and  $GdF_3@p(HEA)26-pFTAA(10\%)$ , which were more efficiency than particles  $GdF_3@p(HEA)14-qFTAA(2\%)$  and  $GdF_3@TEG-qFTAA(5\%)$  in OPA. First images of whole brain were performed in order to study the binding and signal separation from the autofluorescence, then, we looked at the difference in staining of some brain region.

#### 3.2.2.1 Whole brain staining with pentameric LCP labeled particles

TPA image of brain tissue sections of APP/PS1 mouse sampled after *in vivo* injection of probe  $GdF_3@p(HEA)26-pFTAA(2\%)$ ,  $GdF_3@p(HEA)26-pFTAA(10\%)$  and PBS were carried out at 780, 800 and 830 nm. Figure IV.13 shows fluorescence image with  $GdF_3@p(HEA)26-pFTAA(2\%)$ (left) and  $GdF_3@p(HEA)26-pFTAA(10\%)$ (middle) and normalized average spectra of 10 plaques with  $GdF_3@p(HEA)26-pFTAA(2\%)$ ,  $GdF_3@p(HEA)26-pFTAA(10\%)$  and PBS (right), with indicated standard deviation. (Samples excited at 800 nm wavelengths). Plaques are clearly stained (green light in the fluorescence image) and autofluorescence is almost disappeared. Also probes spectra are definitively different to that of PBS. A second maximum peak appears at 550 nm for  $GdF_3@p(HEA)26-pFTAA(2\%)$  and  $GdF_3@p(HEA)26-pFTAA(10\%)$  probes and not in the PBS spectra.

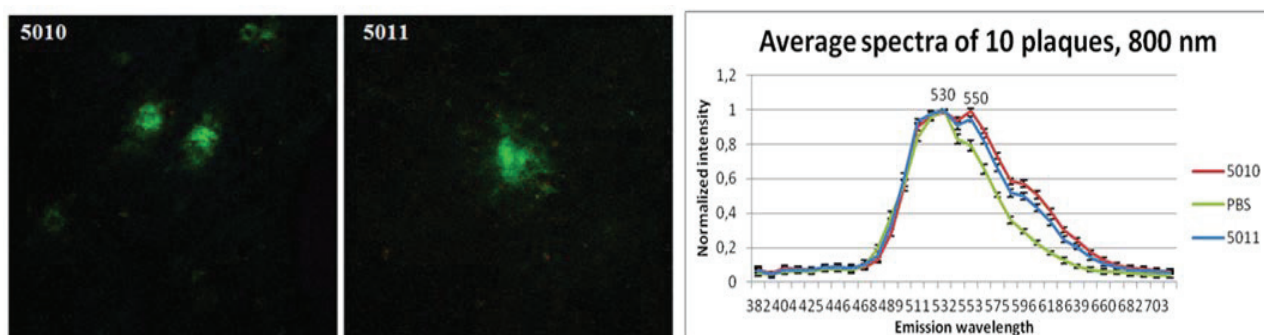


Figure IV.13. Fluorescence image of plaque *in vivo* injected APP/PS1 mice with  $GdF_3@p(HEA)26-pFTAA(2\%)$  (left) and  $GdF_3@p(HEA)26-pFTAA(10\%)$  (middle). Spectra of stained plaque compared with PBS

This observation shows definitively the staining of  $A\beta$  deposits after *in vivo* injection. Results are more convincing compared to the observation from  $GdF_3@p(HEA)14-qFTAA(2\%)$  and  $GdF_3@TEG-qFTAA(5\%)$  particles. Staining is clearly shown in the fluorescence images and the obtained spectra are close to those observed with free LCPs stained plaques, suggesting that our probes can cross the BBB and efficiently stained  $A\beta$  plaques *in vivo*.

### 3.2.2.2 Regional staining with GdF<sub>3</sub>@p(HEA)26-pFTAA(10%)

The stored cryo-section from the previously injected mice (two consecutive injections of 100  $\mu$ l of GdF<sub>3</sub>@p(HEA)26-pFTAA(2%) and GdF<sub>3</sub>@p(HEA)26-pFTAA(10%) probes solution of 10 mg/ml) were analyzed. Before analyze, they were first fixed in ethanol, buffered in PBS and mounted with Dako fluorescence mounting medium. All spectral images were collected with the same acquisition settings and exposure times. GdF<sub>3</sub>@p(HEA)26-pFTAA(10%) has a LCP coating ratio higher than that of particle GdF<sub>3</sub>@p(HEA)26-pFTAA(2%). Hence it is expected to find higher fluorescence from GdF<sub>3</sub>@p(HEA)26-pFTAA(10%) than from GdF<sub>3</sub>@p(HEA)26-pFTAA(2%).

Figure IV.14 and Figure IV.15 show respectively tissues in the hippocampus and close to ventricle, stained by the probes. It can be seen that fluorescence intensity from tissue close to ventricle (Figure IV.15) is higher and decreases when we move away from the ventricle. This fluorescence is higher also on the outmost part of the cortex (not shown). Spectral profile of GdF<sub>3</sub>@p(HEA)26-pFTAA(2%) and GdF<sub>3</sub>@p(HEA)26-pFTAA(10%) are identical in all plaques and distinctly different from the auto-fluorescence from PBS injected control animal. We can see in Figure IV.16 that spectral profile from bright plaques (close to ventricle) and faint plaques (hippocampus) are identical, suggesting an identical staining of the same kind of plaques.

The brain is supplied with blood through arteries and capillary in the subarachnoid cavity. The brain's ventricle is also supplied with blood to produce cerebrospinal fluid. The endothelial cells in the ventricle, acting as a filter, are the anatomical part of the blood-brain barrier<sup>351</sup>. Probes are transported from the blood stream to the brain, by crossing blood brain barrier.

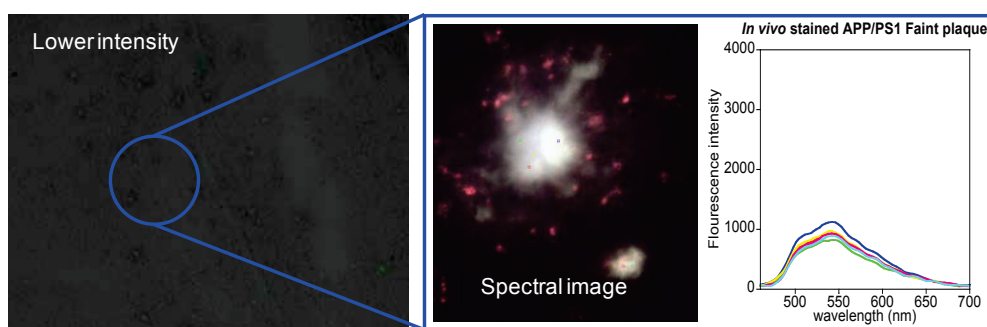


Figure IV.14. Fluorescence (left), spectral image (middle) and spectra (right) of plaque *in vivo* injected APP/PS1 mice with GdF<sub>3</sub>@p(HEA)26-pFTAA(10%). Tissue in the middle of hippocampus

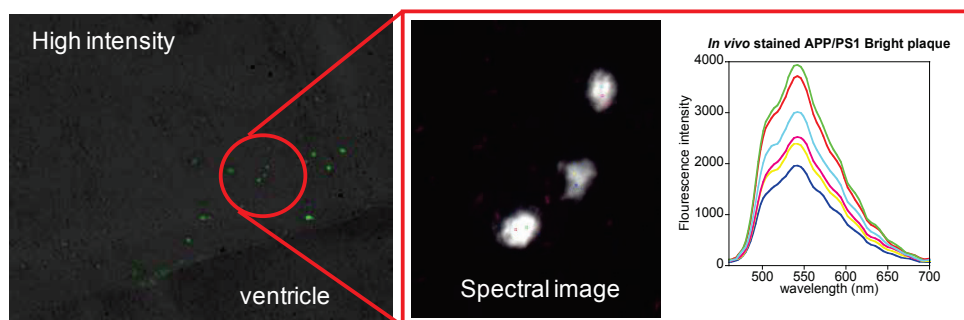


Figure IV.15. Fluorescence (left), spectral (middle) image and spectra (right) of plaque *in vivo* injected APP/PS1 mice with GdF<sub>3</sub>@p(HEA)26-pFTAA(10%). Tissue close to ventricle

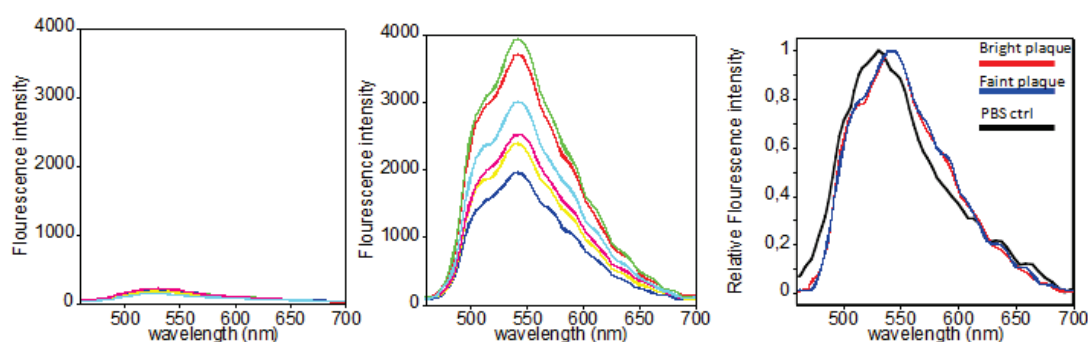


Figure IV.16. Spectra of *in vivo* stained APP/PS1 with PBS (left), GdF<sub>3</sub>@p(HEA)26-pFTAA(10%) (middle and right)

Plaques in close vicinity of the main arteries, thus close to the ventricles, have the most intense stained, because these plaques bind large portions of the probes before it gets a chance to penetrate further into the brain. It is also clear that the fluorescence is significantly lower in the GdF<sub>3</sub>@p(HEA)26-pFTAA(2%) injected brain than in the GdF<sub>3</sub>@p(HEA)26-pFTAA(10%) case.

It is quite clear that we see an excellent *in vivo* staining of plaques using the GdF<sub>3</sub>@p(HEA)26-pFTAA(2%) and GdF<sub>3</sub>@p(HEA)26-pFTAA(10%) probes. May be the lower amount of LCO coating is beneficial for deeper penetrance into the brain since these particles in theory should have lower affinity for the plaques and hence diffuse past a larger number of plaques before it is bound. These results are very interesting, proving the *in vivo* staining of plaques by fluorescence after *in vivo* injection. The staining kinetic of the mice brains was followed hereafter, using TPA microscopy in living animal.

### 3.2.3 *In vivo* staining kinetics of the particle

*In vivo* visualization of amyloid plaques over time was carried out in order to analyze the short-term staining kinetic of the probes. A round cranial window was installed on the mice head (Figure IV.17). The skin and the bone were removed without disturb or puncture the dura mater (the outermost of the membranes which envelops the brain).

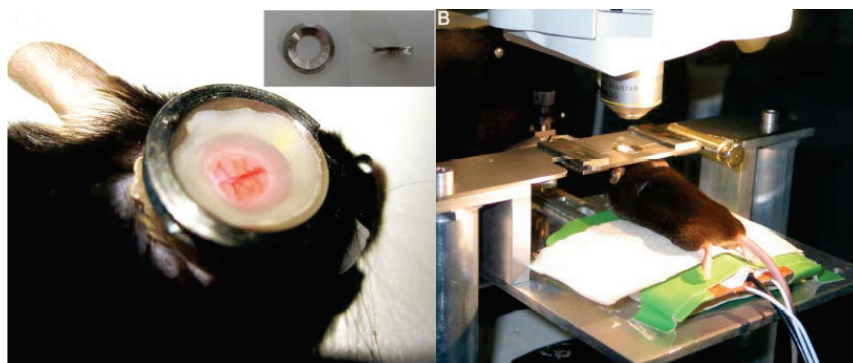


**Figure IV.17. Custom-made head fixation system for long-term *in vivo* imaging: Image of a mouse carrying a cranial window (left) and the ring fits into a fixed holder on the microscope (right). (Adapted from<sup>352</sup>)**

Then, a sterile, custom-made glass coverslip (thickness, 0.13 mm) was installed. After surgery, the animals were allowed to recover for 1 week before starting the imaging process.

*In vivo* imaging of two APPPS1 mice (11 month of age) following a single *in vivo* injection of the probes GdF<sub>3</sub>@p(HEA)26-pFTAA(2%) and GdF<sub>3</sub>@p(HEA)26-pFTAA(10%) (100µl of 20mg/ml solution) was performed. Aβ plaques imaging were carried out over time, on live animal from base line (before injection) and until 21 days (after injection). Three cortical areas were imaged per mouse. Details about the procedure of TPA imaging of live animal can be found in Wegenast-Braun et al. work<sup>352</sup>. Images and curves showing fluorescence from brain versus times after probes injection are shown in Annex E. An example of Aβ plaque imaged 5 and 24 h after probes injection is shown in Figure IV.18. Experiments were performed by Jasmin Mahler, from Tuebingen University. As a first analysis, it can be seen clearly the difference between base line and 5 and 24 h after injection. In base line the probe signal is not detected, while probe signal increases with time after injection. Over the entire observation time, in Annex E we can see that the probe signal is immediately detectable in the blood vessels and faded from the vasculature within 3 hours. First plaque staining was clearly visible at 3 hours after injection. Then the signal increases only in plaques and reach a maximum after 10-14 days. We clearly observe specific staining of amyloid plaques in both GdF<sub>3</sub>@p(HEA)26-pFTAA(2%) and GdF<sub>3</sub>@p(HEA)26-pFTAA(10%) particles. We can notice that signal of plaques stained with GdF<sub>3</sub>@p(HEA)26-pFTAA(10%) (higher LCP concentration) is more intense that plaques stained with GdF<sub>3</sub>@p(HEA)26-pFTAA(2%). Also, the maximum intensity for GdF<sub>3</sub>@p(HEA)26-pFTAA(10%) is shifted a few days later, compared to the maximum intensity observed for GdF<sub>3</sub>@p(HEA)26-pFTAA(2%), probably because of the LCP concentration.

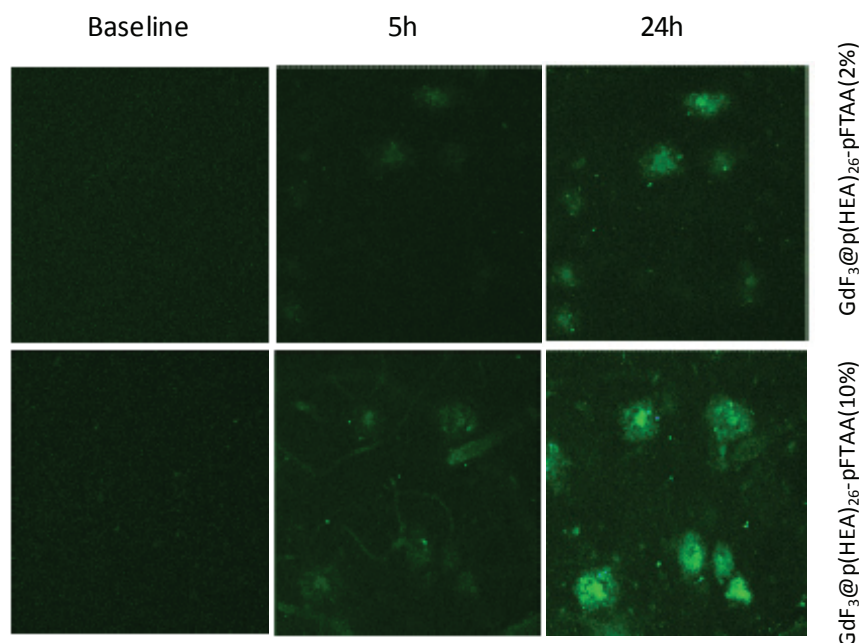


**Figure IV.18. Fluorescence image evolution in time of plaque *in vivo* injected two APP/PS1 mice (12 months of age) with GdF<sub>3</sub>@p(HEA)26-pFTAA(2%) and GdF<sub>3</sub>@p(HEA)26-pFTAA(10%)**

This improvement of the staining over time may be linked to a good circulation time of the particles, suggesting a strong stability, if the observed fluorescence comes not from free LCPs, released by the particles. This point will be discussed later. Thus specific *in vivo* binding of GdF<sub>3</sub>@p(HEA)26-pFTAA(2%) and GdF<sub>3</sub>@p(HEA)26-pFTAA(10%) to the amyloid deposits after *in vivo* injection was achieved successfully. With GdF<sub>3</sub>@p(HEA)26-pFTAA(2%) and GdF<sub>3</sub>@p(HEA)26-pFTAA(10%) probes, signal/noise ratio is higher compared to GdF<sub>3</sub>@p(HEA)14-qFTAA(2%) and GdF<sub>3</sub>@TEG-qFTAA(5%) particles. This is related to the high activity of pentameric LCP (pFTAA) compared to tetrameric one (qFTAA).

These results prove that LCP cross the BBB, bind and stained A $\beta$  plaques. However, the crucial question is to prove that particles are still intact and the observed fluorescence signal is not due to the break-up of the particles, leading to free LCPs release that pass the BBB in free form, without particles. Relaxation rate changes in plaques after *in vivo* injection and elementary dosage of gadolinium in the brain should provide more information about the BBB crossing.

### **3.3 Relaxation rate change and gadolinium concentration in brain tissues**

A suitable MRI process for detection of the particles *in vivo* requires images with sufficient spatial resolution and signal to noise obtained within a time period that the animals can be safely

kept anesthetized. Signal intensity in MR images does not only depend on the MR imaging process, and also on varying factors, such as animal size, placement in scanner, position of the coil, accuracy of pulse angles, field homogeneity, temperature and tissue physiological factors among others. Therefore comparison of images between animals is challenging, and the contrast created by the probes must be enough large in order to be detectable. Since the magnetic contrast agents create image contrast by changing the tissue relaxation properties (T1 and T2) by reducing or increasing the signal in a given image; the best way to detect the presence of our probes is to look at the resulting change in tissue relaxation.

It was therefore decided to focus on quantification of tissue relaxation times, in order to reduce measurement variation between individual animals, thereby improving the chance of detecting changes in relaxation times caused by the probes. Thus T2 mapping was chosen to enable quantification of the changes in tissue relaxation time in regions of interest due to LCP labeled particles bound in tissue. Experiments were done with wild type and APP/PS1 mice at Trondheim University.

### 3.3.1 Relaxation rate change of *in vivo* injected brain hemispheres

The previously injected mice were used for T2 measurements in the hemispheres brains. 100  $\mu$ l of probe solution was injected in the tail vein in two consecutive injections within 48h. Mice were sacrificed one week after second injection and no perfusion was used. We used the second brain hemisphere stored at  $-80^{\circ}\text{C}$  for these MRI experiments. Two groups (genotypes) of mice were used: APP/PS1, the transgenic one expressing A $\beta$  deposits and WT (wild type), without A $\beta$  deposits expression. APP/PS1 mice (n= 11) were injected with free pFTAA and nanoparticles probes GdF<sub>3</sub>@p(HEA)14-qFTAA(2%), GdF<sub>3</sub>@TEG-qFTAA(5%), GdF<sub>3</sub>@p(HEA)26-pFTAA(2%), GdF<sub>3</sub>@p(HEA)26-pFTAA(10%). For clarity and simplicity, the particles probes are respectively labeled in the following figures as 4012; 4013; 5010 and 5011.

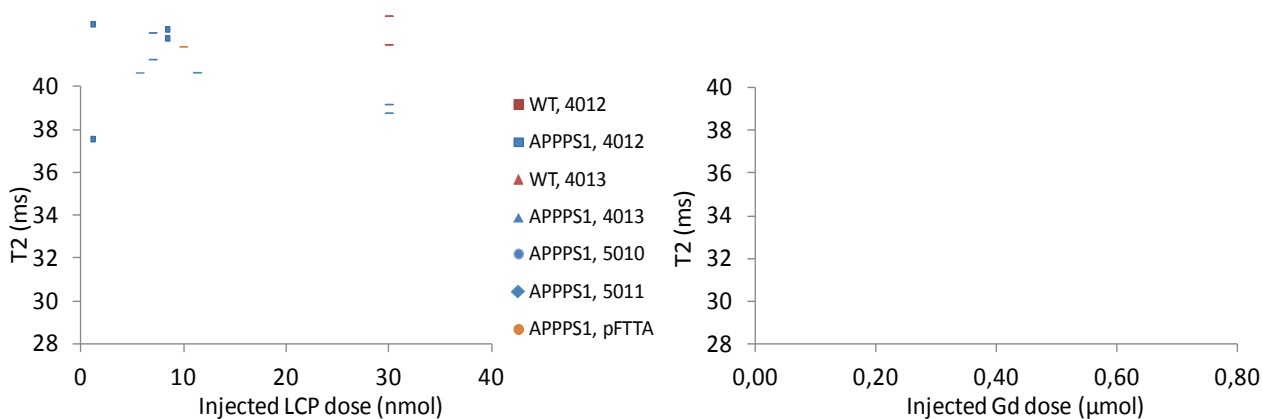


Figure IV.19. T2 measurements of APPPS1 and WT injected probes

GdF<sub>3</sub>@p(HEA)14-qFTAA(2%) and GdF<sub>3</sub>@TEG-qFTAA(5%) were injected in two different doses. WT mice (n=3) were injected with probes GdF<sub>3</sub>@p(HEA)14-qFTAA(2%) and GdF<sub>3</sub>@TEG-qFTAA(5%). The frozen hemispheres were thawed at room temperature, and then T2-map and T2 measures in ROI in cortex were performed. Results are shown in Figure IV.19 as T2 versus injected probes in different dose.

It can be seen a small T2 difference between WT and APP/PS1 injected mice with probes GdF<sub>3</sub>@p(HEA)14-qFTAA(2%) and GdF<sub>3</sub>@TEG-qFTAA(5%): from 39 ms (WT) to 35 ms (APP/PS1) with GdF<sub>3</sub>@p(HEA)14-qFTAA(2%) at 0.3 μmol Gd(III). And from 37 ms (WT) to 32 ms (APP/PS1) with GdF<sub>3</sub>@TEG-qFTAA(5%) at 0.6 μmol Gd(III). There is a decrease of 4 and 5 ms respectively, or 10.3 and 13.5 % of T2 change. Regarding others APP/PS1 mice injected with probes GdF<sub>3</sub>@p(HEA)26-pFTAA(2%) and GdF<sub>3</sub>@p(HEA)26-pFTAA(10%), the average T2 is approximately 34-35 ms. Unfortunately T2 relaxation of all injected magnetic probes samples is close to that of control sample, that is free pFTAA injected mice (35 ms). And increase of probes dose, in the case of GdF<sub>3</sub>@p(HEA)14-qFTAA(2%) and GdF<sub>3</sub>@TEG-qFTAA(5%) particles do not result in a strong decrease in T2 as expected. Also individual variance can be observed; that is T2 can be different between one type of mice with the same probe injection and in same dose. 3-5 ms of difference can be seen.

In summary the measured T2 variation is not sufficient because it is in order of magnitude of individual variation and two mice type variation. Therefore it involves several assumptions regarding the presence of particles in the brain and the passage of the BBB. Either the particles have not passed the BBB, in this case, desorption of the LCP would be the cause of fluorescence staining. Either the particles are passed the BBB, but their magnetic properties, thus relaxation are impaired under these *in vivo* conditions; or the amount of particles that have passed the BBB is not sufficient to cause a significant drop in the transverse T2 relaxation. Beyond this T2 analyze, uncertainty in T2 measurements can be due to different parameters such as change of temperature or water content of the analyzed hemispheres. These results need to be complemented with gadolinium ion dosage.

### 3.3.2 Gadolinium dosage of *in vivo* injected brain hemispheres

Gadolinium concentration in the brain of *in vivo* injected GdF<sub>3</sub>@p(HEA)14-qFTAA(2%), GdF<sub>3</sub>@TEG-qFTAA(5%), pFTAA and PBS were measured using ICP. The results expressed as gadolinium masse per tissue mass (left) and percentage of gadolinium that reaches the brain, compared to the injected dose (right) are shown in Figure IV.20. The assumption is that gadolinium dose has been equally distributed in both hemispheres. Gadolinium concentration from ICP measurements is given as Gd mass per mass of the analyzed sample. Therefore the total amount of Gd in the brain is given by: Gd concentration in wet brain hemisphere tissue × 2 × brain hemisphere



post mortem brains, probably because T2 change with these concentrations is too low, in order of 0.1 ms and is easily confused to the individual variance. This result seems indicate insufficient Gd concentration in brain which can be related to insufficient crossing of blood brain barrier or an efficiently brain cleaning one week after injection.

### 3.4 Blood brain barrier crossing discussion

MRI signal was not significantly enhanced in the different part of the brain, and between brains with plaques and brains without plaques. The reduction in average T2 is in the order of the individual variance and natural difference between WT and APP/PS1. These observations lead us naturally to wonder why this little detectable T2 change. Several hypotheses exist to answer this question. First of all, the used MRI sequences may be inappropriate and therefore need to be optimized. Also time of imaging after particles injection (7 days) can be questioned. This time would be too late; compared to the residence time of particles in the brain (may be rapidly cleared from the brain). Moreover, LCP staining was seen by fluorescence microscopy at these time-points with same injection protocol suggesting an altered relaxivity or release of LCP *in vivo*, that can bound to A $\beta$  several days later.

Another and certainly the most likely explanation is the too low concentration of particles in the brain, due to the too low used dose and or an insufficient blood brain barrier crossing. Indeed, relaxivity values of the probes would change upon the interaction of contrast agents to macromolecules, like A $\beta$  plaques, due to the reduction in tumbling rate for example<sup>353</sup>. Thus, we can need higher probes concentration than planned to see T2 change.

In future work, these questions should be studied. Also biodistribution and clearance of the particles in the mice body will be investigated to determine presence of particles in different organisms including brain, and determine the best time to image. Also stability of the particles *in vivo* would be investigated.

### 3.5 Conclusion

In this section, particles were evaluated in biological media. Among the synthesized nanoparticles, GdF<sub>3</sub>@PEG and TiO<sub>2</sub>@DOTA-Gd(III) were tested *ex vivo* as magnetic contrast agents. As expected, thanks to its high r<sub>2</sub>/r<sub>1</sub> ratio, GdF<sub>3</sub>@PEG leads to high dark contrast, confirming its capacity to be used as negative agent. TiO<sub>2</sub>@DOTA-Gd(III) with a moderate r<sub>2</sub>/r<sub>1</sub> ratio is suited for both positive and negative contrast agent.

LCP labeled GdF<sub>3</sub> particles were tested *in vitro* and *in vivo*. Ability of these particles to bind to A $\beta$  fibers was revealed *in vitro* by transmission electronic and fluorescence microscopies. *In vivo*

staining of A $\beta$  plaques with these particles were showed by fluorescence microscopy after *in vivo* injection of the particles. The *in vivo* A $\beta$  staining has not yet confirmed by magnetic resonance imaging, which do not show a significant T2 decrease in post-mortem *in vivo* injected particles. More investigations are needed on biodistribution of the particles and *in vivo* stability. Results of these investigations would provide decisive information for determination of the suited particles concentration and optimization of MRI experiments, including imaging time after injection.



**GENERAL  
CONCLUSION  
AND  
FUTURE WORKS**



## GENERAL CONCLUSION

In this work, we developed multifunctional nanoparticles for *in vitro* and *in vivo* detection of  $\beta$ -amyloid ( $A\beta$ ) plaques in biological samples, simultaneously by enhancing magnetic resonance imaging (MRI) and fluorescent contrast.

First of all, different types of magnetic nanoparticles have been prepared. These particles have been studied in terms of size, stability, magnetic behavior and they finally shown excellent magnetic properties for this application. The first one, an isotropic system, consists of spheroidal gadolinium fluoride ( $GdF_3$ ). They have been synthesized with narrow size distribution, high crystallinity and interesting magnetic properties. The surface of these nanoparticles has been modified, with polyethylene glycol, which allows biocompatibility, and to be dispersed in aqueous media. These particles show excellent relaxivity properties (high  $r_2/r_1$  ratio) and great contrast enhancement in T2 weighted MRI. *Ex-vivo* experiments proved that they can be used as negative MRI contrast agent.

A second nanoparticle is an anisotropic system, made of gadolinium phosphate ( $GdPO_4$ ) nanorods. The size of these nanorods was tailored from 40 to 450 nm of length by varying synthesis parameters, such as pH, temperature and pressure. These particles have been also synthesized with high crystallinity and interesting magnetic properties. They have been functionalized with polyethylene glycol and have moderate  $r_2/r_1$  ratio, varying according to the particles size and can have great contrast enhancement both in T1 and T2 weighted MRI.

A third type of nanoparticles is a core shell system, made of spherical titanium oxide ( $TiO_2$ ) nanoparticles coated DOTA-Gd(III). These nanoparticles, with excellent T1 and T2 contrast enhancement, were tested *ex vivo* and shown great contrast enhancement both in T1 and T2 weighted magnetic resonance imaging.

Then gadolinium fluoride nanoparticles were successfully conjugated with different luminescent conjugated polythiophene (LCPs); conserving both magnetic proprieties of the particles and fluorescence properties of the LCPs. These multifunctional nanoparticles can target specifically  $A\beta$  thanks to LCPs on the surface of the particles and can be visualized by fluorescence microscopy (due to the LCPs photoemission) and MRI (gadolinium fluoride T2 contrast).

Finally, these LCP labeled nanoparticles were used for detection of  $A\beta$  fibrils *in vitro* and  $A\beta$  plaques *in vivo* in APP/PS1 mice. Transmission electronic and fluorescence microscopies have shown the properties of these particles to bind specifically to  $A\beta$  fibrils *in vitro*. Then One- and Two-photon fluorescence microscopies revealed the staining of  $A\beta$  plaques on APP/PS1 mice after *in vivo* injection

of the particles, suggesting that these particles can naturally cross the blood brain barrier (BBB), diffuse into the brain tissue and labeled amyloid plaques.

The fluorescence sensing system was able to detect the changes of the fluorescence properties of the LCPs labeled nanoparticles in biological samples, allowing fast and sensitive A $\beta$  detection that allow to distinguish between infected and non-infected animals. The magnetic properties of these LCPs conjugated nanoparticles are not altered, but rather exalted after conjugation with LCPs. However at this stage, the *in vitro* magnetic properties of the particles when bound to A $\beta$  is not investigated and no significant change in relaxivity rate was observed at *in vivo* injected mice, which is at variance with the fact that particles pass the BBB. The results of gadolinium concentration determination in the brains samples show that the amount of the probes that crosses the blood brain barrier is insufficient for MRI.

Based on these results, this work is an important contribution to the development of multifunctional nanomaterials that will allow early diagnosis of Alzheimer disease and achieve more efficient diagnosis not available today. Several future works should lead to the best understanding of the *in vivo* behavior of the optimized particles and improve magnetic resonance imaging observation.

## FUTURE WORKS

According to fluorescence microscopy observation, these LCPs conjugated nanoparticles can cross the BBB and stain A $\beta$  plaques while this *in vivo* A $\beta$  staining is not yet confirmed by MRI observation. Then the main future works will aim to understand the *in vivo* behavior of the particles, to ensure a sufficient amount of particles that can reach the brain and improve A $\beta$  MRI.

The first main work will be the study of the A $\beta$  plaques fluorescence staining. Are they stained by free LCPs or by LCPs conjugated nanoparticles? That is, the study of biodistribution, stability and integrity of the probes in physiological media. One of the important experiments is the use of LCPs labeled europium doped gadolinium particles. Then fluorescence from europium and from LCPs can be compared to localize particles in the brain tissue.

The second main question is the absence of T2 reduction in MRI experiments. In this question, the capacity of these particles to cross the BBB and stain A $\beta$  in live animal arises. First of all, TEM images of *in vivo* injected brain tissues can be carried out; to confirm presence of nanoparticles in the *in vivo* stained tissue, thus the BBB crossing. Secondly, investigation on *in vitro* relaxivity of the particles when bound to A $\beta$  fibrils would be carried out. It is necessary to know how relaxivity is affected when probes bound to A $\beta$  fibrils.

Also biodistribution and pharmacokinetic studies of the particles can help to improve the MRI sequence in term of injection dose of probes and time to perform MRI after probes injection.

Others trails would be the use of smaller particles such as LCPs labeled  $\text{TiO}_2$  coated DOTA-Gd(III); studies of the influence of some changes such as homogenization of the anchoring group for PEG and LCPs (one type of anchoring group for both PEG and LCPs), the use of the same molecule as both stabilizer and spacer. Also, even if mice survive several days after particles injection without problems, a rigorous toxicity study will be necessary.



# **ANNEX**



# ANNEX

## ANNEX A MAGNETIC RESONANCE IMAGING BACKGROUND

The existence of the nuclear magnetic resonance (NMR) phenomenon was first demonstrated in 1946 by two American scientists, Felix Bloch and Edward Purcell<sup>354,355</sup>, who jointly received the Nobel Prize for Physics in 1952 for their discovery. NMR is a physical phenomenon in which magnetic nuclei in a magnetic field absorbs and re-emits electromagnetic radiation. Today several techniques employ NMR phenomena to study chemical and physical properties of materials and molecules. NMR is also used in medical imaging techniques, such as magnetic resonance imaging (MRI). MRI is an excellent diagnostic imaging modality that captures the interest of the medical profession because it employs radiowaves and magnetic fields rather ionizing radiation. In addition to provide excellent spatial resolution, the technique uses differences in the density and the molecular environment of different substances to provide excellent tissue contrast.

Here we are interested in the application of NMR in MRI. Then this section aims to remind briefly NMR theory and MRI mechanism.

### A Magnetic resonance phenomenon

#### ❖ Quantum approach of magnetic resonance

##### ■ State of equilibrium: the main magnetic field application

Protons in the  $\vec{B}_0$  field have magnetic moments that can have only two orientations and quantified values: parallel (up) or anti-parallel (down). These orientations correspond to two energy levels.  $E_1 = -\gamma\hbar B_0/2$  corresponds to the Up spins and  $E_2 = +\gamma\hbar B_0/2$  corresponds to the Dow spin. There is more anti-parallel spins than parallel spins and  $\Delta E = E_2 - E_1$  is proportional to  $\vec{B}_0$ . The transverse magnetization  $\vec{M}_{xy}$  is zero at equilibrium because there is dephasing spins due to the molecular environment inducing small local magnetic fields that will slightly change the precession frequency of protons.

##### ■ Disturbance of equilibrium by the rotating magnetic field

At equilibrium, the difference of energy  $\Delta E = E_2 - E_1$ . When an RF equal to  $\Delta E = h\nu$  is applied, transitions  $E_1 \rightarrow E_2$  are induced. Thus  $\vec{M}$  is oriented. There is rephasing of spins and appearance of  $\vec{M}_{xy}$ . Indeed, when protons change in energy level (from  $E_1$  to  $E_2$ ), they put himself in phase with each other, making appear  $\vec{M}_{xy}$ . During the transition, when half of excess protons pass from  $E_1$  to  $E_2$ ,

there is equalization of population on the two energy levels,  $\vec{M}_z$  disappears (90 ° pulse) and  $\vec{M}_{xy}$  is at maximum (spins are all in phase). When all the excess protons are passed from  $E_1$  to  $E_2$  there is inversion of the longitudinal component  $\vec{M}_z = -\vec{M}_{z0}$  (180 ° pulse). At the end of the excitation (RF), there is the gradual return to equilibrium state: reverse phenomenon. Fast dephasing of spin,  $\vec{M}_{xy}$  decreases rapidly (T2 relaxation) and there is gradually  $E_2 \rightarrow E_1$  transition.  $\vec{M}_z$  grows back gradually (T1 relaxation). Thus  $\vec{M}_z$  corresponds to transitions of protons between two energy levels and  $\vec{M}_{xy}$  to the phasing and rephasing of the spins (Figure - A-1).

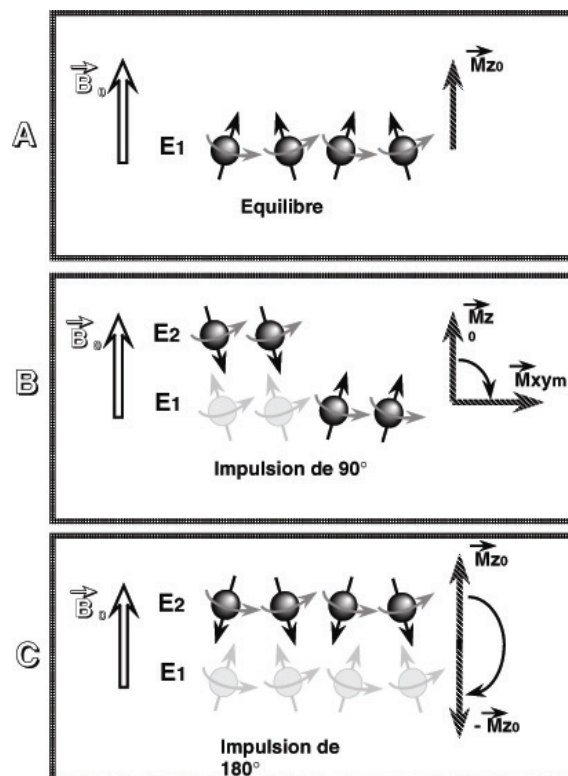


Figure - A-1. Effect of RF pulses on the macroscopic magnetization vector  $\vec{M}$

In summary,  $\vec{M}_z$  is at maximum at equilibrium, under  $\vec{B}_0$ . That is all the excess protons are at  $E_1$  level.  $\vec{M}_{xy}$  is at the maximum after  $\vec{B}_1 = \Delta E = h\nu$  application, that causes transition  $E_1 \rightarrow E_2$  of the excess protons. When half is passed to  $E_2$ , there is the "perfect" equilibrium, up and down spins cancel each other out, thus  $\vec{M}_z$  is zero. As the transition is accompanied by the spin rephasing,  $\vec{M}_{xy}$  is at maximum. When all the excess protons move from  $E_1 \rightarrow E_2$ , there is the inversion of  $\vec{M}_z$ .

## ❖ Relaxation processes

Relaxation is the process of the return of  $\vec{M}$  to equilibrium state (direction of  $\vec{B}_0$ ) after RF pulse. There are three factors that influence the decay of  $\vec{M}$ : magnetic field inhomogeneity, longitudinal T1 relaxation (spin-lattice relaxation) and transverse T2 relaxation (spin-spin relaxation). T1 relaxation is the realignment of spins with the external magnetic field  $\vec{B}_0$  (z-axis). T2 relaxation is the decrease in the xy plan component of magnetization.

### ■ T1 relaxation

After RF pulse, nuclei will dissipate their excess energy as heat to the surrounding environment (lattice) and revert to their equilibrium position. Realignment of the nuclei along  $\vec{B}_0$ , through a process known as recovery, leads to a gradual increase in the longitudinal magnetization. The time taken for a nucleus to relax back to its equilibrium state depends on the rate that excess energy is dissipated to the lattice. If  $M_{z(0)}$  is the amount of magnetization parallel with  $\vec{B}_0$  before the RF pulse is applied, and  $M_z$  the z component of M at time t, following a 90 degree pulse at time t = 0. It can be shown that the process of equilibrium restoration is described by the following equation:

$$M_z = M_{z(0)}(1 - e^{-t/T_1}) \quad \text{Equation A.1}$$

Where, T1 is the time taken for approximately 63% of the longitudinal magnetization to be restored following a 90 degree pulse.

### ■ T2 relaxation

While nuclei dissipate their excess energy to the lattice following an RF pulse, the magnetic moments interact with each other causing spin dephasing, thus a decrease in transverse magnetization. This effect is similar to that produced by magnet inhomogeneity, but on a smaller scale. The decrease in transverse magnetization does not involve the emission of energy. The rate of decay is described by a time constant, T2\*, that is the time takes for the transverse magnetization to decay to 37% of its original magnitude. T2\* characterizes dephasing due to both  $\vec{B}_0$  inhomogeneity and transverse relaxation. If  $M_{xy(0)}$  is the amount of transverse magnetization immediately following an RF pulse and  $M_{xy}$  the amount of transverse magnetization at time t, following a 90 degree pulse at time t = 0. It can be shown that:

$$M_{xy} = M_{xy(0)} \times e^{-t/T_2^*}$$

Equation A.2

### ■ Contrast in MRI

In MRI, contrast is due to differences in the MR signal, which depend on T1, T2 and proton density ( $\rho$ ) of the tissues and sequence parameters. MR signal is expressed in grey level, bright for high signal and dark for low signal. Then the higher the signal is, the brighter it will appear on the MR image. Interpretation is based on analysis of tissue contrast, for given signal weightings (T1, T2 or  $\rho$ ). When “natural” contrast is not sufficient, contrast agents are used. There are magnetic compounds. Usually super-paramagnetic iron oxide nanoparticles or paramagnetic compounds such as complex or nanoparticles made of gadolinium.

## B Paramagnetic relaxation enhancement

### ❖ Relaxation mechanisms

There are several different mechanisms responsible for relaxation. Because the relaxation rate constants ( $R_i = 1/T_i$ ,  $T =$  relaxation time and  $i = 1, 2$ ), are additive magnitudes, the global relaxation rate is equal to the sum of the relaxation rates of each contribution.

$$\frac{1}{T_i} = \sum m \frac{1}{T_1^m}$$

Equation A.3

Where  $1/T_i^m$  is the relaxation time of the mechanism  $m$ . The contribution of these mechanisms differs and depends on the type of the nucleus, the chemical environment and the magnetic field strength. The main and more influencing mechanisms are dipolar interaction and scalar relaxation. Relaxation time can arise from the interaction between two magnetic dipoles, known as the dipole-dipole or dipolar coupling. Due to alignment of the spins along the magnetic field, the local dipolar field of a neighboring spin experienced by a nucleus depends on the orientation of the molecule. For proton spins in a liquid at the field intensities employed in most MRI; the dipolar mechanism is the main contribution to the relaxation<sup>356</sup>.

When the probability of finding an electron at the nucleus is considerable as non-zero, paramagnetic systems offer a new pathway for nuclear relaxation. This interaction, known as the scalar interaction, occurs at shorter nucleus-electron distance, around the nuclear radius ( $\sim 10$  fm). Both longitudinal and transverse nuclear relaxation rates are increased by the presence of paramagnetic species in solution. This phenomenon, known as the Paramagnetic Relaxation

Enhancement (PRE), arises from the interaction of the nucleus with the magnetic moment of electron spins.

### ❖ Relaxivity

The observed relaxation rates  $1/T_i^{obs}$  are the sums of the diamagnetic and paramagnetic contributions,  $1/T_i^d$  and  $1/T_i^p$  respectively<sup>280</sup>. The paramagnetic relaxation is caused mainly by dipole-dipole interaction (nucleus-electron interaction) and the scalar interaction.

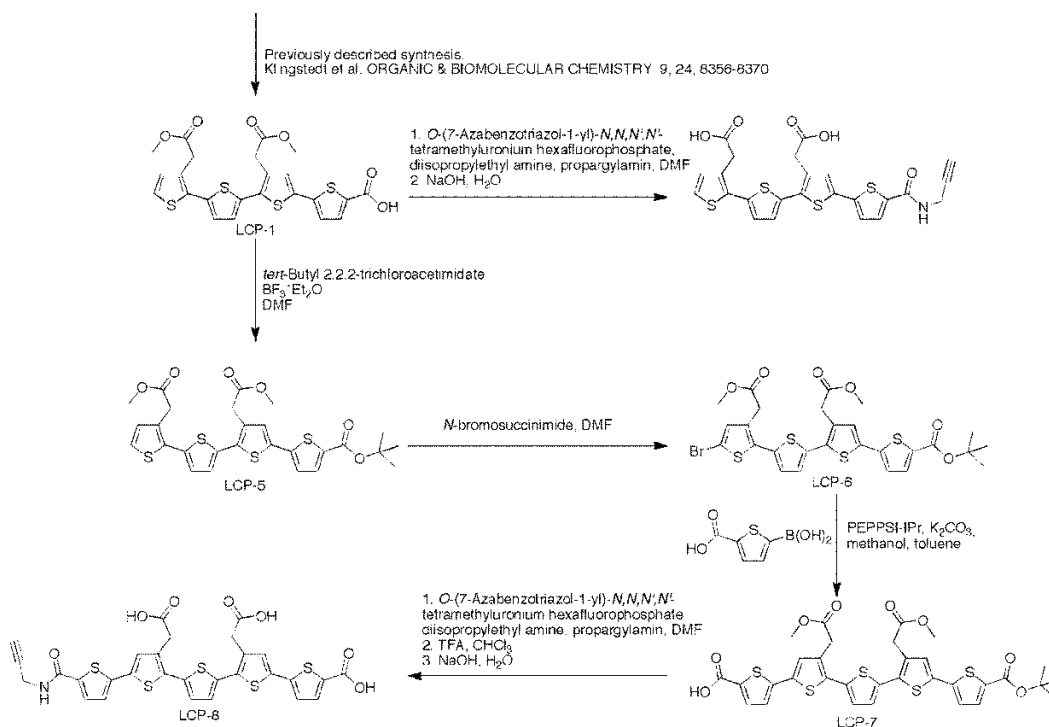
$$\frac{1}{T_i^{obs}} = \frac{1}{T_i^d} + \frac{1}{T_i^p}; i = 1, 2 \quad \text{Equation A.4}$$

The paramagnetic relaxation rate is proportional to the concentration of the paramagnetic species<sup>280,357</sup>. To refer their efficiency to enhance the relaxation rate, the notion of relaxivity  $r_i$ , in units of  $\text{mM}^{-1} \text{s}^{-1}$ , has been introduced. The observed relaxation rate in terms of relaxivity and concentration of the paramagnetic species  $[M]$  is given by the follow Equation.

$$\frac{1}{T_i^{obs}} = \frac{1}{T_i^d} + r_i [M] \quad ; i = 1, 2 \quad \text{Equation A.5}$$

## ANNEX B ALKYNYL GROUP-TERMINATED OLIGOTHIOPHENES SYNTHESIS

The synthesis method of the alkynyl group-terminated tetrameric and pentameric oligothiophene (respectively LCP-6 and LCP-7) is showed in Scheme - B-1. The carboxyl group-terminated tetrameric is the starting point of the synthesis, described below. This work was performed in Linköping University by Andreas Åslund.



**Scheme - B-1. Preparation of alkynyl group-terminated oligothiophenes: tetrameric and pentameric**

**LCP-1** (1 mmol) was dissolved in DMF (5 mL). *Tert*-Butyl 2,2,2-trichloroacetimidate (2 mmol) and BF<sub>3</sub>·Et<sub>2</sub>O (0.30 mmol) were added. After 30 min the reaction was concentrated in vacuum and purified on reversed phase chromatography (acetonitrile/water 4:1 to 9:1) to give the product quantitatively (**LCP-5**).

**LCP-5** (1 mmol) was dissolved in DMF (5 mL) and cooled to -15 °C. *N*-bromosuccinimide (1 mmol) was added slowly and the reaction mixture were allowed to reach room temperature. After 2 h the solution was diluted with toluene and washed with brine to give LCP-6 quantitatively (**LCP-6**).

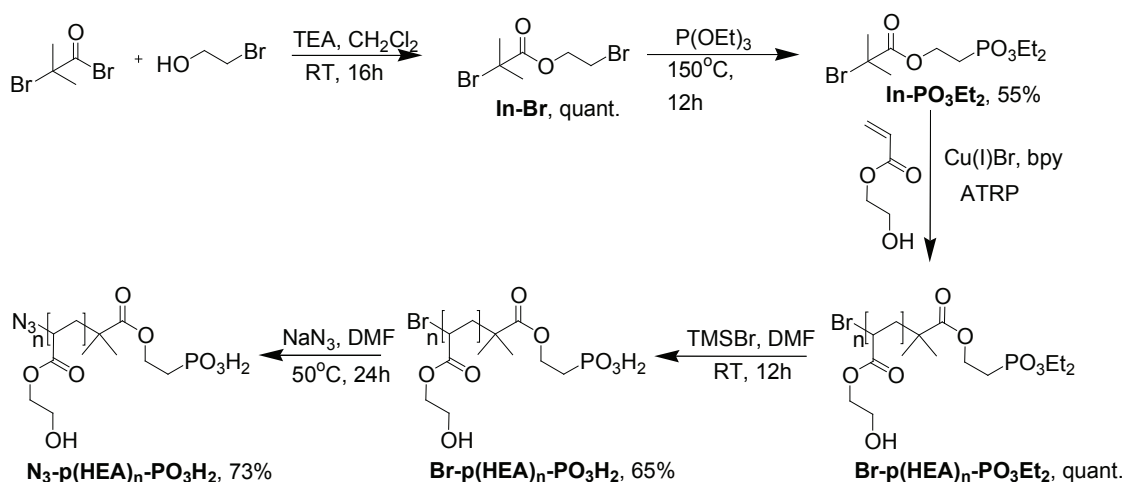
**LCP-6** (1 mmol) K<sub>2</sub>CO<sub>3</sub> (6 mmol), 5-Carboxythiophene-2-boronic acid (3 mmol) and PEPSSI-IPr (0.05 mmol) were dissolved in 5 mL toluene/methanol (1:1) and heated to 80 °C. After 20 minutes

the reaction mixture were diluted with acetic acid and ethyl acetate and washed with Brine several times to give **LCP-7** in 67 % yield.

**LCP-7** (1 mmol), diisopropylethylamine (3 mmol), propargylamine (2 mmol) and HATU (1.2 mmol) were dissolved in DMF. After two hours the reaction mixture were diluted with chloroform and washed with Brine 3 times. The product was purified on flash chromatography using toluene/ethyl acetate/chloroform (80:7:7) as the eluent to give the protected product in 66% yield. The protected product was dissolved in chloroform/TFA (4:1). After 1 h the solvents were removed in vacuum and the product was dissolved in water and NaOH (3 mmol). After 3 h the solution was lyophilized to give **LCP-8** in 66% yield over three steps.

## ANNEX C      SYNTHESIS      OF      PHOSPHONATE      TERMINATED POLYHYDROXYETHYLACRYLATE

This synthesis was performed in our laboratory, Laboratoire de chimie de l'ENS de Lyon, by Cyrille Monnereau and Vinu Krishnan Appukuttan. The five stages of the synthesis are briefly described here and shown schematically in Scheme - C-1.



**Scheme - C-1. Preparation of water-soluble spacer (polyHydroxyethylacrylate)**

### Synthesis of In-Br

To 1.7 ml of bromoethanol (24 mmol) and 3.5 mL of triethylamine (24 mmol) in 100mL dichloromethane in ice bath, slowly added bromo-isobutyryl bromide (3.5 mL, 29 mmol). The solution was allowed to warm to room temperature and kept under agitation overnight. The reaction was stopped after 18 h and the solution was washed with 1M hydrochloric acid several times and one time with distilled water. Dried over  $\text{Na}_2\text{SO}_4$  and solvent was removed by evaporation. Clear oil consistent with **In-Br** by NMR ( $^1\text{H}$  and  $^{13}\text{C}$ ) was used further without any purification (6.04 g, 92 %).

### Synthesis of Initiator (In- $\text{PO}_3\text{Et}_2$ )

Compound **In-Br** and triethylphosphate (9.5 mL, 55 mmol) were heated at 150 °C in a round bottom flask equipped with condenser under inert atmosphere. After 16h the reaction was stopped and excess triethylphosphate was evaporated under high vacuum. The residue was purified by column chromatography using silica gel eluting with dichloromethane/ethyl acetate mixture (1:1) to give light yellow oil of **In- $\text{PO}_3\text{Et}_2$**  (3.98 g, 54 %).

### **Polymerization of Hydroxyethylacrylate (HEA) by In-PO<sub>3</sub>Et<sub>2</sub> (Br-p(HEA)<sub>n</sub>-PO<sub>3</sub>Et<sub>2</sub>)**

In a typical example, initiator (In-PO<sub>3</sub>Et<sub>2</sub>) (0.71 g, 2.15 mmol) and HEA (12.5 g, 107.5 mmol) and bpy ligand (0.67 g, 4.3 mmol) were mixed and degassed for 10 minutes. CuBr catalyst (0.31 g, 2.15 mmol) were added to this degassed solution, and stirred at 85 °C, affording a dark brown solution. Polymerization occurred immediately, leading to an increase in viscosity of the solution. The polymerization was quenched in liq. N<sub>2</sub> after 11 min, the solution was diluted with deionized water and then transferred to dialysis membrane (spectra/por membrane, MWCO=1000) for dialysis. The outer phase was replaced at 6-h intervals with fresh water during dialysis (2 days). The polymer solution was filtered and lyophilized to yield Br-p(HEA)<sub>n</sub>-PO<sub>3</sub>Et<sub>2</sub>.

### **Deprotection reaction of phosphonate ester (Br-p(HEA)<sub>n</sub>-PO<sub>3</sub>H<sub>2</sub>)**

In a typical reaction, a solution of 0.70 g of polymer (*M<sub>n</sub>* = 3400) in anhydrous DMF (10mL) at 0 °C, added excess amount of trimethylsilyl bromide (2.4 mL, 18.0 mmol) drop-wise and the solution was slowly warmed to room temperature. After 6 h the mixture was kept in ice and bath and methanol (10 mL) was added to it. After 10 min of stirring, the solution transferred to a dialysis tube and dialyzed against deionized water (same way as before) for 2 days to remove organic part. The solution was filtered and lyophilized get the polymer.

### **Synthesis of azide terminated polymer (N<sub>3</sub>-p(HEA)<sub>n</sub>-PO<sub>3</sub>H<sub>2</sub>)**

In a 100mL flask, 0.40 g of the polymer was dissolved in DMF (5mL) and NaN<sub>3</sub> (0.04 g, 0.61 mmol) was added to it. The mixture was kept stirring for 24 h at 50 °C. After cooling to room temperature, the mixture diluted with water and the performed dialysis (same way as before) followed by free-drying to yield the compound.

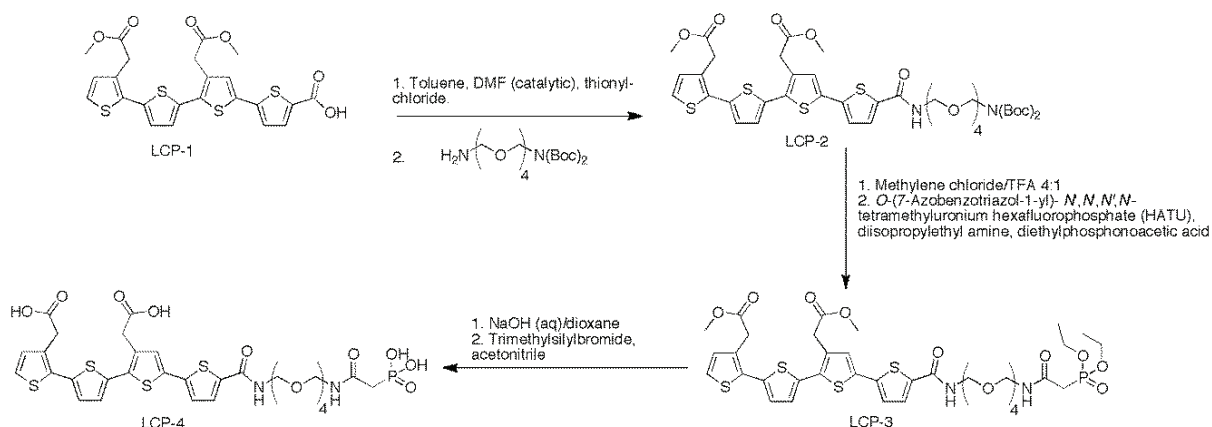
## ANNEX D CLICKING OF SPACER WITH POLYTHIOPHENE

This synthesis was performed in our laboratory, Laboratoire de chimie de l'ENS de Lyon, by Cyrille Monnereau and Vinu Krishnan Appukkuttan.

The qFTAA-(PEG)<sub>4</sub>-PO<sub>3</sub>H<sub>2</sub> moiety was prepared according to the chemistry shown in Scheme - D-1 and describe above. To a solution of **LCP-1** (1 mmol) and DMF (0.15 mmol) in toluene (5 mL) thionylchloride (1.3 mmol) was added. The reaction was refluxed for 1 h followed by concentration to dryness. The acid chloride and diisopropylethylamine was dissolved in DMF and the amine (1,1 mmol) was added to the solution. After 2 hours the reaction mixture was diluted with toluene and washed with HCl (1M, aq) and brine. The crude product was purified by flash chromatography (toluene/ethyl acetate 4:1 to 2:1 to 1:1) to give **LCP-2** in 92% yield.

**LCP-2** (1 mmol) was dissolved in methylene chlorid/trifluoroacetic acid (TFA, 4:1, 5 mL). After 1 h the solution was concentrated in vacuo and dissolved in DMF. Diisopropylamine was added until basic whereupon dethylphosphonoacetic acid (1.1 mmol) and HATU (1.1 mmol) were added. After 4 h the reaction mixture was concentrated and purified on flash chromatography methylene chloride/methanol (30:1) to give product **LCP-3** in 74 % yield.

**LCP-3** (1 mmol) was dissolved and dioxane (5 mL) and NaOH (1 M, aq., 3 mmol) was added. After 2h the mixture were evaporated in vacuum. The product was dissolved in acetonitrile and trimethylsilylbromide (3 mmol) was added. When no starting material was seen on HPLC the solvents were evaporated and the product was dialyzed in water with a cutoff of 500 D to give **LCP 4** in 96% yield.

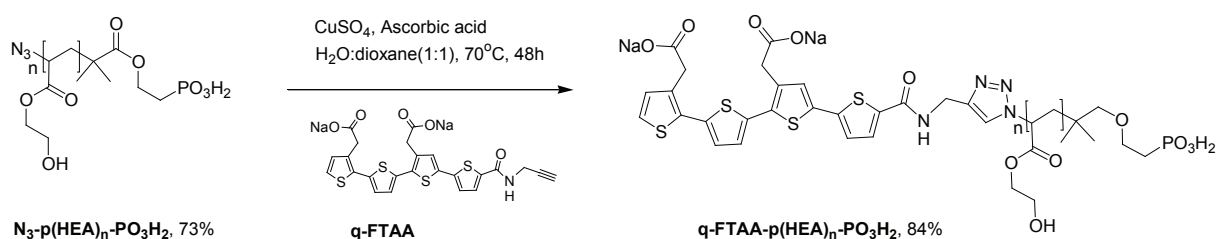


Scheme - D-1. Synthetic route of qFTAA-(PEG)<sub>4</sub>-PO<sub>3</sub>H<sub>2</sub> synthesis

✓ **Clicking of the medium spacer with tetrameric LCP**

The qFTAA-p(HEA)<sub>14</sub>-PO<sub>3</sub>H<sub>2</sub> moiety was prepared according to the chemistry shown in Scheme - D-2 and describe above.

0.2 g of polymer (**N<sub>3</sub>-p(HEA)<sub>14</sub>-PO<sub>3</sub>H<sub>2</sub>**) and **q-FTAA** (0.053 g, 0.067 mmol) were dissolved in a 10 mL mixture of water/ dioxane (1:1, v/v) containing in flask fitted with a rubber septum. The solution was degassed by bubbling argon, and then CuSO<sub>4</sub> (0.033 g, 0.134 mmol) and ascorbic acid (0.35 g, 2.0 mmol) were added. The mixture was stirred at 70 °C for 48 h under argon atmosphere. Then the mixture was cooled to room temperature and transferred to dialysis tube (MWCO=2000). Dialysis was performed for 3 days against water to completely remove the excess **q-FTAA** molecule, Cu and the organic part. The solution was then filtered though a celite plug and lyophilized to get the **q-FTAA-p(HEA)<sub>n</sub>-PO<sub>3</sub>H<sub>2</sub>**.



**Scheme - D-2. Clicking of water-soluble spacer (p(HEA)<sub>14</sub>-PO<sub>3</sub>H<sub>2</sub>) with LCP (qFTAA)**

## ANNEX E IN VIVO STAINING KINETICS OF A $\beta$ PLAQUES WITH PROBES

The kinetics staining of GdF<sub>3</sub>@p(HEA)26-pFTAA(2%) and GdF<sub>3</sub>@p(HEA)26-pFTAA(10%) were performed in Tuebingen University by Jasmin Mahler as a part of master thesis "*Ex vivo* and *in vivo* analysis of protein aggregates in transgenic mouse models of cerebral amyloidosis using luminescent conjugated oligothiophenes" submitted in 2012.

### ■ GdF<sub>3</sub>@p(HEA)26-pFTAA(2%)

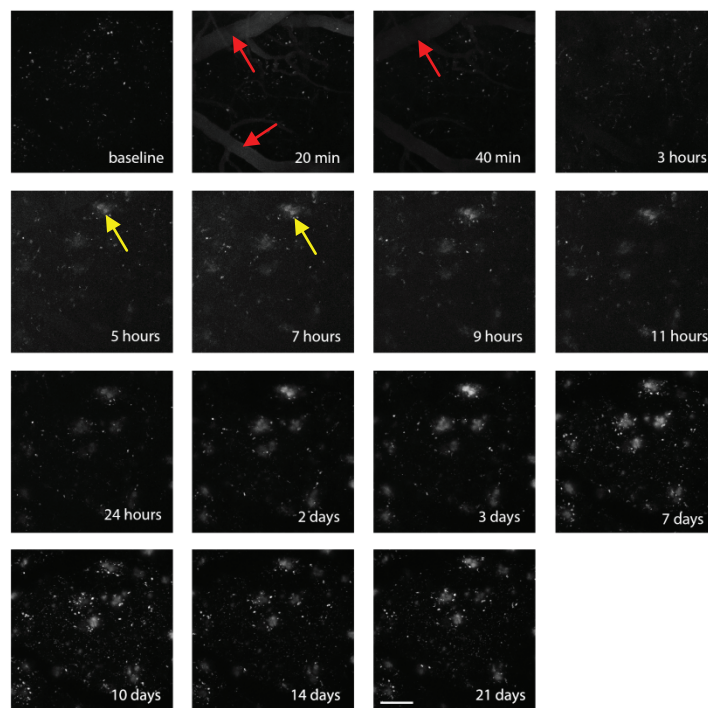
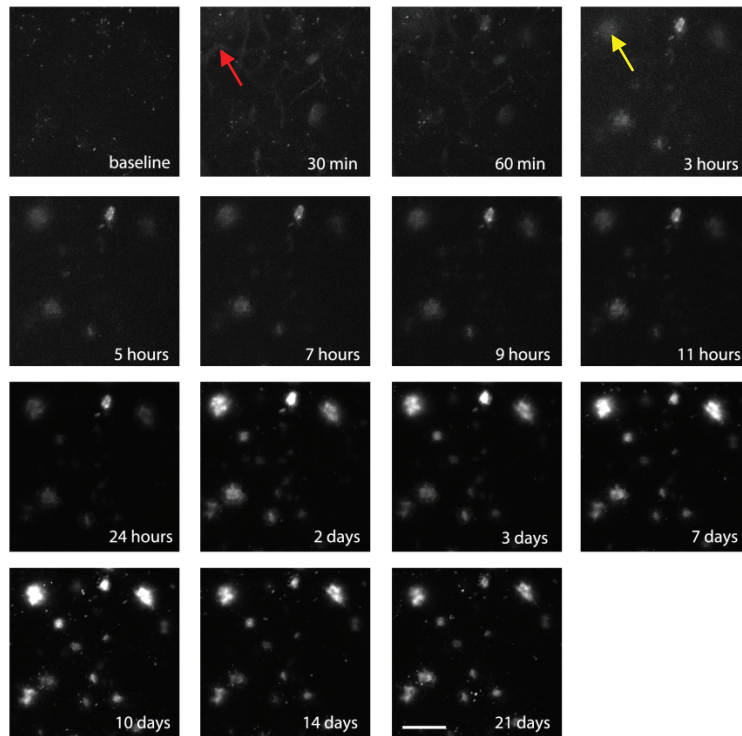


Figure - E-1. Staining kinetic with particle GdF<sub>3</sub>@p(HEA)26-pFTAA(2%), area 1. Two-photon imaging of an APP/PS1 mouse (female, 11 month) after a single i.v. injection



**Figure - E-2. Staining kinetic with particle GdF<sub>3</sub>@p(HEA)26-pFTAA(2%), area 2. Two-photon imaging of an APP/PS1 mouse (female, 11 month) after a single i.v. injection**

The dye is immediately detectable in the blood vessels (red arrows) and faded from the vasculature within 3 hours. First plaque staining was clearly visible at 3 hours after injection (yellow arrows) and remained stable until the last imaging point, which was three weeks after injection.

The first image shows the baseline scan, i.e. the selected area imaged before the injection of the probe. Within the first 24 hours, the brain region of the mouse was imaged eight times, in order to investigate the short-term kinetics of the dye. Then, the mouse was imaged in regular intervals, in order to analyze the staining stability over time. After 30 min, the probe was detected as diffuse staining in the blood vessels. From 3 hours onwards, a distinct staining of plaques became visible. The maximum staining intensity was observed between 7 and 10 days after the injection (also depending on the respective imaging depth). Until the last imaging session, three weeks after injection, the staining intensity remained stable.

■  $GdF_3@p(HEA)26-pFTAA(10\%)$

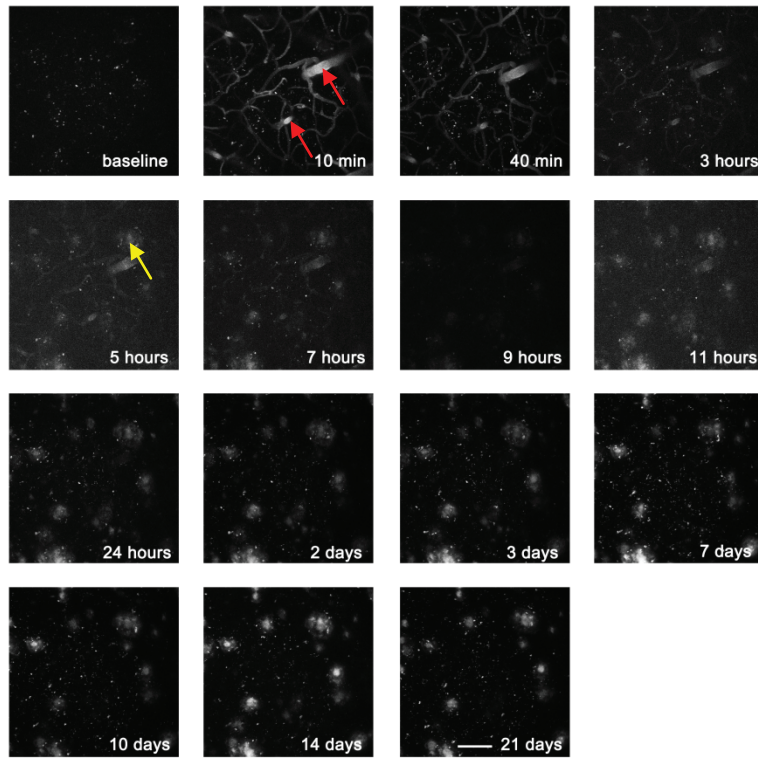


Figure - E-3. Staining kinetic with particle  $GdF_3@p(HEA)26-pFTAA(10\%)$ , area 1

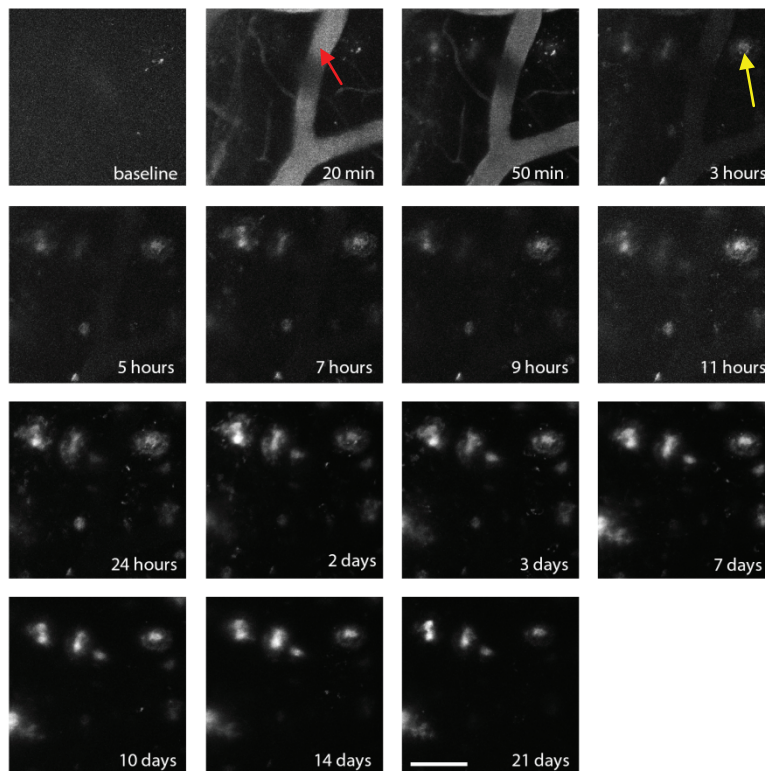


Figure - E-4. Staining kinetic with particle  $GdF_3@p(HEA)26-pFTAA(10\%)$ , area 2

At the first imaging time-point, 20 min after injection, a strong signal of the diffusing probes was detected in the vasculature. This signal was detectable up to 3 hours after injection. The first distinct plaque staining appeared around 3 hours post-injection. The specific plaque staining was maximal at 7 to 14 days after the injection. The signal remained stable until the last imaging session, three weeks post-injection.

### ■ Evolution of signal intensity in different brain area

A signal of the diffusing dye was detected in the vessels (green), directly after the injection. This signal faded within the first 2 hours after injection and finally stabilized close to baseline. Starting around 2-3 hours after injection, the dye began to specifically bind to amyloid plaques (red). Up to 10 days after injection, an increasing  $GdF_3@p(HEA)26-pFTAA(2\%)$  signal was detected.

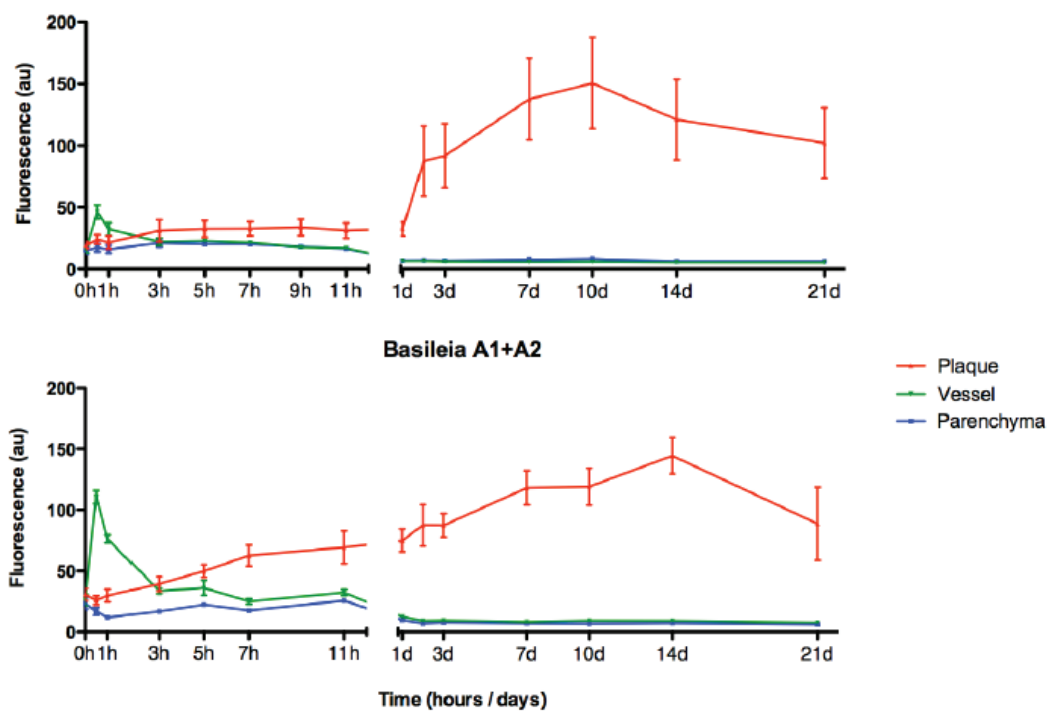


Figure - E-5. *In vivo* staining kinetic of  $GdF_3@p(HEA)26-pFTAA(2\%)$  (top) and  $GdF_3@p(HEA)26-pFTAA(10\%)$  (bottom) in plaque, vessel and parenchyma kinetics are depicted in an APP/PS1 mouse. The mean fluorescence intensities of ROIs drawn within the parenchyma (blue, n=4), vessels (green, n=3) and within plaques (red, n=3) are plotted for each time-point, up to 21 days post-injection.

After the specific fluorescent signal reached its maximum (10 days post-injection) it decreased, but the dye was still detectable until the last imaging session, three weeks after injection. In the

parenchyma a very weak signal of the diffusing dye was visible directly after injection (from 0-5 hours, blue line), before this signal faded.

Directly after injection of  $\text{GdF}_3@p(\text{HEA})26\text{-pFTAA}(10\%)$ , a strong signal of the diffusing dye was detected in the vessels (green). While the dye began to specifically bind to plaques (red from 2-3 hours) the signal in the vessels started to decrease. The maximum intensity of plaque staining was around 15 days post-injection. Afterwards, the signal faded, but it was still detectable until the last imaging time-point.

In conclusion, the graphs of  $\text{GdF}_3@p(\text{HEA})26\text{-pFTAA}(2\%)$  and  $\text{GdF}_3@p(\text{HEA})26\text{-pFTAA}(10\%)$ , showed that the kinetics of both dyes were very similar. However, for  $\text{GdF}_3@p(\text{HEA})26\text{-pFTAA}(10\%)$ , the signal detected in the vessels in the beginning is clearly stronger than for  $\text{GdF}_3@p(\text{HEA})26\text{-pFTAA}(2\%)$ . The maximum intensity for  $\text{GdF}_3@p(\text{HEA})26\text{-pFTAA}(10\%)$ , is shifted a few days later, compared to the maximum intensity observed for  $\text{GdF}_3@p(\text{HEA})26\text{-pFTAA}(2\%)$ .

# **BIBLIOGRAPHY**



## BIBLIOGRAPHY

1. Maurer, K.; Volk, S.; Gerbaldo, H. "Auguste D and Alzheimer's disease." *Lancet* **1997**, *349*, 1546–9.
2. Masters, C. L.; Simms, G.; Weinman, N. a; Multhaup, G.; McDonald, B. L.; Beyreuther, K. "Amyloid plaque core protein in Alzheimer disease and Down syndrome." *Proc. Natl. Acad. Sci. USA* **1985**, *82*, 4245–9.
3. Wischik, C. M.; Novak, M.; Thøgersen, H. C.; Edwards, P. C.; Runswick, M. J.; Jakes, R.; Walker, J. E.; Milstein, C.; Roth, M.; Klug, A. "Isolation of a fragment of tau derived from the core of the paired helical filament of Alzheimer disease." *Proc. Natl. Acad. Sci. USA* **1988**, *85*, 4506–10.
4. Wimo, A.; Prince, M. *World Alzheimer Report 2010*; 2010.
5. Lowndes, G.; G. S. "Early detection of memory impairment in Alzheimer's disease: a neurocognitive perspective on assessment." *Neuropsychol Rev* **2007**, *17*, 193–202.
6. Perry, R.; Hodges, J. "Attention and executive deficits in Alzheimer's disease A critical review." *Brain* **1999**, *122*, 383–404.
7. Mickes, L.; Wixted, J. T.; Fennema-Notestine, C.; Galasko, D.; Bondi, M. W.; Thal, L. J.; Salmon, D. P. "Progressive impairment on neuropsychological tasks in a longitudinal study of preclinical Alzheimer's disease." *Neuropsychology* **2007**, *21*, 696–705.
8. Busciglio, J.; Gabuzdat, D. H.; Matsudairat, P.; Yankner, B. A. "Generation of beta-amyloid in the secretory pathway in neuronal and nonneuronal cells." *Proc. Natl. Acad. Sci. USA* **1993**, *90*, 2092–2096.
9. Greenberg, S. M.; Koo, E. H.; Selkoe, D. J.; Qiu, W. Q.; Kosik, K. S. "Secreted beta-amyloid precursor protein stimulates mitogen-activated protein kinase and enhances tau phosphorylation." *Proc. Natl. Acad. Sci. USA* **1994**, *91*, 7104–8.
10. Kibbey, M. C.; Juckert, M.; Weeks, B. S.; Neve, R. L.; Nostrand, W. E. V. A. N.; Kleinman, H. K. "Beta-amyloid precursor protein binds to the neurite-promoting IKVAV site of laminin CeH Biology :." *Proc. Natl. Acad. Sci. USA* **1993**, *90*, 10150–10153.
11. Haass, C. "Take five--BACE and the gamma-secretase quartet conduct Alzheimer's amyloid beta-peptide generation." *The EMBO journal* **2004**, *23*, 483–8.
12. Zou, K.; Gong, J.-S.; Yanagisawa, K.; Michikawa, M. "A novel function of monomeric amyloid beta-protein serving as an antioxidant molecule against metal-induced oxidative damage." *J. Neurosci.* **2002**, *22*, 4833–41.
13. Baruch-Suchodolsky, R.; Fischer, B. "Abeta40, either soluble or aggregated, is a remarkably potent antioxidant in cell-free oxidative systems." *Biochemistry* **2009**, *48*, 4354–70.

14. Yao, Z.-X.; Papadopoulos, V. "Function of beta-amyloid in cholesterol transport: a lead to neurotoxicity." *FASEB journal* **2002**, *16*, 1677–9.
15. Soscia, S. J.; Kirby, J. E.; Washicosky, K. J.; Tucker, S. M.; Ingelsson, M.; Hyman, B.; Burton, M. A.; Goldstein, L. E.; Duong, S.; Tanzi, R. E.; Moir, R. D. "The Alzheimer's disease-associated amyloid beta-protein is an antimicrobial peptide." *PloS one* **2010**, *5*, e9505.
16. Citron, M.; Diehl, T. S.; Gordon, G.; Biere, A. L.; Seubert, P.; Selkoe, D. J. "Evidence that the 42- and 40-amino acid forms of amyloid beta protein are generated from the beta-amyloid precursor protein by different protease activities." *Proc. Natl. Acad. Sci. USA* **1996**, *93*, 13170–5.
17. Jarrett, J. T.; Berger, E. P.; Lansbury, P. T. "The carboxy terminus of the beta-amyloid protein is critical for the seeding of amyloid formation: Implications for the pathogenesis of Alzheimer's disease." *Biochemistry* **1993**, *32*, 4693–4697.
18. Brion, J.; Passareiro, H. "Mise en evidence immunologique de la proteine tau au niveau des lesions de degenerescence neurofibrillaire de la maladie d'Alzheimer." *Arch. Biol.* **1985**, *95*, 229–235.
19. J. Gotz, F. Chen, J. van D. and R. M. N. "Formation of neurofibrillary tangles in P301l tau transgenic mice induced by A $\beta$ 42 fibrils." *Science* **2001**, *293*, 1491–1495.
20. Oddo, S.; Caccamo, A.; Shepherd, J. "Triple-transgenic model of Alzheimer's disease with plaques and tangles: intracellular beta-amyloid and synaptic dysfunction." *Neuron* **2003**, *39*, 409–421.
21. Schmechel, D. E.; Saunders, A. M.; Strittmatter, W. J.; Crain, B. J.; Hulette, C. M.; Joo, S. H.; Pericak-Vance, M. A.; Goldgaber, D.; Roses, A. D. "Increased amyloid beta-peptide deposition in cerebral cortex as a consequence of apolipoprotein E genotype in late-onset Alzheimer disease." *Proc. Natl. Acad. Sci. USA* **1993**, *90*, 9649–53.
22. Higgins, J. H. and G. A. "Alzheimer's disease: the amyloid cascade hypothesis." *Science* **1992**, *256*, 184–185.
23. Johnson, K. a; Fox, N. C.; Sperling, R. a; Klunk, W. E. "Brain imaging in Alzheimer disease." *Cold Spring Harb Perspect Med* **2012**, *2*, a006213.
24. Mckhann, G.; Drachman, D.; Folstein, M. "views & reviews Clinical diagnosis of Alzheimer ' s disease : " *Neurology* **1984**, *34*, 939.
25. Hampel, H.; Mitchell, A.; Blennow, K.; Frank, R. A.; Brettschneider, S.; Weller, L.; Möller, H.-J. "Core biological marker candidates of Alzheimer's disease - perspectives for diagnosis, prediction of outcome and reflection of biological activity." *J .Neural. Transm.* **2004**, *111*, 247–72.
26. Oskar Hansson, Henrik Zetterberg, Peder Buchhave, Elisabet Londos, Prof Kaj Blennow, L. M. "Association between CSF biomarkers and incipient Alzheimer's disease in patients with mild cognitive impairment: a follow-up study." *Lancet Neurol* **2006**, *5*, 228–234.

27. Brys, M.; Pirraglia, E.; Rich, K.; Rolstad, S. "Prediction and longitudinal study of CSF biomarkers in mild cognitive impairment." *Neurobiol Aging*. **2009**, *30*, 682–690.
28. Boland, K.; Behrens, M.; Choi, D.; Manias, K.; Perlmutter, D. H. "The serpin-enzyme complex receptor recognizes soluble, nontoxic amyloid-beta peptide but not aggregated, cytotoxic amyloid-beta peptide." *J. Biol. Chem.* **1996**, *271*, 18032–44.
29. Dubois, B., H. H. Feldman, et al. "Research criteria for the diagnosis of Alzheimer's disease: revising the NINCDS-ADRDA criteria." *Lancet Neurol* **2007**, *6*, 734–746.
30. Metropolitan, T.; Hospital, M. "A computed tomography study of Alzheimer ' s disease." *J. Neurol.* **1983**, *229*, 69–77.
31. Creasey, H.; Schwartz, M.; Frederickson, H.; Haxby, JV. & Rapoport, S. "Quantitative computed tomography in dementia of the Alzheimer type." *Neurology* **1986**, *36*, 1563–1568.
32. Brenner, D. J.; Hall, E. J. "Computed tomography-an increasing source of radiation exposure." *N. Engl. J. Med.* **2007**, *357*, 2277–84.
33. New, T. H. E.; Journal, E.; Medicine, O. F. "Preclinical evidence of alzheimer's disease in persons homozygous for the." *N. Engl. J. Med.* **1996**, *34*, 752–758.
34. Minoshima, S.; Giordani, B.; Berent, S.; Frey, K. A.; Foster, N. L.; Kuhl, D. E. "Metabolic reduction in the posterior cingulate cortex in very early Alzheimer's disease." *Annals of neurology* **1997**, *42*, 85–94.
35. Leon, M. J. De; Convit, A.; Wolf, O. T.; Tarshish, C. Y.; Desanti, S.; Rusinek, H.; Tsui, W.; Kandil, E.; Scherer, A. J.; Roche, A.; Imossi, A.; Thorn, E.; Bobinski, M.; Caraos, C.; Lesbre, P.; Schlyer, D.; Poirier, J.; Reisberg, B.; Fowler, J. "Prediction of cognitive decline in normal elderly subjects with 2- [ 18 F ] fluoro-2-deoxy- D -glucose/positron-emission tomography ( FDG/PET )." *Proc. Natl. Acad. Sci. USA* **2001**, *98*, 10966–10971.
36. Kenneth K. et al. "Dynamic magnetic resonance imaging of human brain activity during primary sensory stimulation." *Proc. Natl. Acad. Sci. USA* **1992**, *89*, 5675–5679.
37. Landau, S. M.; Harvey, D.; Madison, C. M.; Reiman, E. M.; Foster, N. L.; Aisen, P. S.; Petersen, R. C.; Shaw, L. M.; Trojanowski, J. Q.; Jack, C. R.; Weiner, M. W.; Jagust, W. J. "Comparing predictors of conversion and decline in mild cognitive impairment." *Neurology* **2010**, *75*, 230–8.
38. Hoffman, J. "FDG PET imaging in patients with pathologically verified dementia." *J. Nucl. Med.* **2000**, *41*, 1920–1928.
39. Klunk, W. E.; Engler, H.; Nordberg, A.; Wang, Y.; Blomqvist, G.; Holt, D. P.; Bergstro, M.; Savitcheva, I.; Debnath, M. L.; Barletta, J.; Price, J. C.; Sandell, J.; Lopresti, B. J.; Wall, A.; Koivisto, P.; Antoni, G.; Mathis, C. A.; Långstro, B. "Imaging brain amyloid in Alzheimer's disease with Pittsburgh Compound- $\beta$ ." *Annals of Neurology* **2004**, *55*, 306–319.
40. Nordberg, A. "Amyloid imaging in Alzheimer's disease." *Neuropsychologia* **2008**, *46*, 1636–41.

41. Ikonovic, M. D.; Klunk, W. E.; Abrahamson, E. E.; Mathis, C. A.; Price, J. C.; Tsopelas, N. D.; Lopresti, B. J.; Ziolkowski, S.; Bi, W.; Paljug, W. R.; Debnath, M. L.; Hope, C. E.; Isanski, B. A.; Hamilton, R. L.; DeKosky, S. T. "Post-mortem correlates of in vivo PiB-PET amyloid imaging in a typical case of Alzheimer's disease." *Brain* **2008**, *131*, 1630–45.
42. Acer, N.; Turgut, A.; Özsunar, Y.; Turgut, M. "Quantification of Volumetric Changes of Brain in Neurodegenerative Diseases Using Magnetic Resonance Imaging and Stereology." *intechopen.com* **2002**.
43. Gosche, K. M.; Mortimer, J. A.; Smith, C. D.; Markesbery, W. R.; Snowdon, D. A. "Hippocampal volume as an index of Alzheimer neuropathology: findings from the Nun Study." *Neurology* **2002**, *58*, 1476–82.
44. Jack, C.; Dickson, D.; Parisi, J.; Xu, Y. "Antemortem MRI findings correlate with hippocampal neuropathology in typical aging and dementia." *Neurology* **2002**, *58*, 750–757.
45. Colliot, O.; Chupin, M.; Sarazin, M.; Habert, M.-O.; Dormont, D.; Lehericy, S. "L'apport de la neuro-imagerie dans la maladie d'Alzheimer." *Psychiatr. Sci. Hum. Neurosci.* **2008**, *6*, 68–75.
46. Klöppel, S.; Stonnington, C. M.; Chu, C.; Draganski, B.; Scahill, I.; Rohrer, J. D.; Fox, N. C.; Jr, C. R. J.; Ashburner, J.; Frackowiak, R. S. J. "UKPMC Funders Group Automatic classification of MR scans in Alzheimer's disease." *Brain* **2008**, *131*, 681–689.
47. Misra, C.; Fan, Y.; Davatzikos, C. "Baseline and longitudinal patterns of brain atrophy in MCI patients, and their use in prediction of short-term conversion to AD: results from ADNI." *NeuroImage* **2009**, *44*, 1415–22.
48. Paolo Vitali, Raffaella Migliaccio, Federica Agosta, Howard J. Rosen, and M. D. G. "Neuroimaging in dementia." *Neurologic clinics* **2000**, *28*, 467–483.
49. Holcomb, L.; Gordon, M.; McGowan, E. "Accelerated Alzheimer-type phenotype in transgenic mice carrying both mutant amyloid precursor protein and presenilin 1 transgenes." *Nature medicine* **1998**, *4*, 97–100.
50. Nilsson, K. P. R. "Small organic probes as amyloid specific ligands--past and recent molecular scaffolds." *FEBS letters* **2009**, *583*, 2593–9.
51. Nordberg, A. "Reviews PET imaging of amyloid in Alzheimer's disease." *Lancet Neurol* **2004**, *3*, 519–527.
52. Maggio, J.; Stimson, E. "Reversible in vitro growth of Alzheimer disease beta-amyloid plaques by deposition of labeled amyloid peptide." *Proc. Natl. Acad. Sci. USA* **1992**, *89*, 5462–6.
53. Lee, H. J.; Zhang, Y.; Zhu, C.; Duff, K.; Pardridge, W. M. "Imaging brain amyloid of Alzheimer disease in vivo in transgenic mice with an beta-amyloid peptide radiopharmaceutical." *J. Cereb. Blood Flow Metab.* **2002**, *22*, 223–31.
54. Mathis, C. A.; Wang, Y.; Holt, D. P.; Huang, G.; Debnath, M. L.; Klunk, W. E. "Synthesis and Evaluation of Amyloid Imaging Agents 6-Substituted 2-Arylbenzothiazoles as." *J. Med. Chem.* **2003**, *46*, 2740–2754.

55. Zhuang, Z.-P.; Kung, M.-P.; Wilson, A.; Lee, C.-W.; Plössl, K.; Hou, C.; Holtzman, D. M.; Kung, H. F. "Structure-activity relationship of imidazo[1,2-a]pyridines as ligands for detecting beta-amyloid plaques in the brain." *J. Med. Chem.* **2003**, *46*, 237–43.
56. Poduslo, J. F.; Wengenack, T. M.; Curran, G. L.; Wisniewski, T.; Sigurdsson, E. M.; Macura, S. I.; Borowski, B. J.; Jack, C. R. "Molecular Targeting of Alzheimer's Amyloid Plaques for Contrast-Enhanced Magnetic Resonance Imaging." *Neurobiology of Disease* **2002**, *11*, 315–329.
57. Wadghiri, Y. Z.; Sigurdsson, E. M.; Sadowski, M.; Elliott, J. I.; Li, Y.; Scholtzova, H.; Tang, C. Y.; Aguinaldo, G.; Pappolla, M.; Duff, K.; Wisniewski, T.; Turnbull, D. H. "Detection of Alzheimer's amyloid in transgenic mice using magnetic resonance microimaging." *Magn. Reson. Med.* **2003**, *50*, 293–302.
58. Mathis, C. A.; Bacskai, B. J.; Kajdasz, S. T.; McLellan, M. E.; Frosch, M. P.; Hyman, B. T.; Holt, D. P.; Wang, Y.; Huang, G.-F.; Debnath, M. L.; Klunk, W. E. "A lipophilic thioflavin-T derivative for positron emission tomography (PET) imaging of amyloid in brain." *Bioorg. Med. Chem. Lett.* **2002**, *12*, 295–8.
59. Bacskai, B. J.; Kajdasz, S. T.; Christie, R. H.; Carter, C.; Games, D.; Seubert, P.; Schenk, D.; Hyman, B. T. "Imaging of amyloid-beta deposits in brains of living mice permits direct observation of clearance of plaques with immunotherapy." *Nature medicine* **2001**, *7*, 369–72.
60. Bacskai, B. J.; Hickey, G. A.; Skoch, J.; Kajdasz, S. T.; Wang, Y.; Huang, G.-F.; Mathis, C. A.; Klunk, W. E.; Hyman, B. T. "Four-dimensional multiphoton imaging of brain entry, amyloid binding, and clearance of an amyloid-beta ligand in transgenic mice." *Proc. Natl. Acad. Sci. USA* **2003**, *100*, 12462–7.
61. Klunk, W. E.; Wang, Y.; Huang, G.; Debnath, M. L.; Holt, D. P.; Shao, L.; Hamilton, R. L.; Ikonovic, M. D.; DeKosky, S. T.; Mathis, C. A. "The binding of 2-(4'-methylaminophenyl)benzothiazole to postmortem brain homogenates is dominated by the amyloid component." *J. Neurosci.* **2003**, *23*, 2086–92.
62. Laforce, R. J. *Amyloid imaging*; 2012.
63. Faber, C.; Zahneisen, B.; Tippmann, F.; Schroeder, A.; Fahrenholz, F. "Gradient-echo and CRAZED imaging for minute detection of Alzheimer plaques in an APPV717I x ADAM10-dn mouse model." *Magn. Reson. Med.* **2007**, *57*, 696–703.
64. House, M. J.; St Pierre, T. G.; McLean, C. "1.4T study of proton magnetic relaxation rates, iron concentrations, and plaque burden in Alzheimer's disease and control postmortem brain tissue." *Magn. Reson. Med.* **2008**, *60*, 41–52.
65. Jack, C. R.; Garwood, M.; Wengenack, T. M.; Borowski, B.; Curran, G. L.; Lin, J.; Adriany, G.; Gröhn, O. H. J.; Grimm, R.; Poduslo, J. F. "In vivo visualization of Alzheimer's amyloid plaques by magnetic resonance imaging in transgenic mice without a contrast agent." *Magn. Reson. Med.* **2004**, *52*, 1263–71.
66. Wengenack, T.; Reyes, D.; Curran, G. "Regional differences in MRI detection of amyloid plaques in AD transgenic mouse brain." *Neuroimage* **2011**, *54*, 113–122.

67. Chamberlain, R.; Reyes, D.; Curran, G. L.; Marjanska, M.; Wengenack, T. M.; Poduslo, J. F.; Garwood, M.; Jack, C. R. "Comparison of amyloid plaque contrast generated by T2-weighted, T2\*-weighted, and susceptibility-weighted imaging methods in transgenic mouse models of Alzheimer's disease." *Magn. Reson. Med.* **2009**, *61*, 1158–64.
68. Meadowcroft, M. D.; Connor, J. R.; Smith, M. B.; Yang, Q. X. "MRI and histological analysis of beta-amyloid plaques in both human Alzheimer's disease and APP/PS1 transgenic mice." *J. Magn. Reson. Imaging* **2009**, *29*, 997–1007.
69. Falangola, M.; Dyakin, V.; Lee, S. "Quantitative MRI reveals aging-associated T2 changes in mouse models of Alzheimer's disease." *NMR Biomed* **2007**, *20*, 343–351.
70. Benveniste, H.; Einstein, G. "Detection of neuritic plaques in Alzheimer's disease by magnetic resonance microscopy." *Proc. Natl. Acad. Sci. USA* **1999**, *96*, 14079–14084.
71. Dhenain, M.; Privat, N.; Duyckaerts, C.; Jacobs, R. E. "Senile plaques do not induce susceptibility effects in T2\*-weighted MR microscopic images." *NMR in biomedicine* **2002**, *15*, 197–203.
72. Nakada, T.; Matsuzawa, H.; Igarashi, H.; Fujii, Y.; Kwee, I. L. "In vivo visualization of senile-plaque-like pathology in Alzheimer's disease patients by MR microscopy on a 7T system." *J. neuroimaging* **2008**, *18*, 125–9.
73. Higuchi, M.; Iwata, N.; Matsuba, Y.; Sato, K.; Sasamoto, K.; Saido, T. C. "19F and 1H MRI detection of amyloid beta plaques in vivo." *Nature neuroscience* **2005**, *8*, 527–33.
74. Li, S.; He, H.; Cui, W.; Gu, B.; Li, J.; Qi, Z.; Zhou, G.; Liang, C.-M.; Feng, X.-Y. "Detection of A $\beta$  plaques by a novel specific MRI probe precursor CR-BSA-(Gd-DTPA)<sub>n</sub> in APP/PS1 transgenic mice." *Anatomical record* **2010**, *293*, 2136–43.
75. Yang, J.; Wadghiri, Y. Z.; Hoang, D. M. "Detection of amyloid plaques targeted by USPIO-A $\beta$ 1–42 in Alzheimer's disease transgenic mice using magnetic resonance microimaging." *Neuroimage* **2011**, *55*, 1600–1609.
76. Crystal, A. S.; Giasson, B. I.; Crowe, A.; Kung, M.-P.; Zhuang, Z.-P.; Trojanowski, J. Q.; Lee, V. M.-Y. "A comparison of amyloid fibrillogenesis using the novel fluorescent compound K114." *J. Neurochem.* **2003**, *86*, 1359–1368.
77. LeVine, H. "Mechanism of A beta(1-40) fibril-induced fluorescence of (trans,trans)-1-bromo-2,5-bis(4-hydroxystyryl)benzene (K114)." *Biochemistry* **2005**, *44*, 15937–43.
78. Nilsson, K. P. R.; Rydberg, J.; Baltzer, L.; Inganäs, O. "Self-assembly of synthetic peptides control conformation and optical properties of a zwitterionic polythiophene derivative." *Proc. Natl. Acad. Sci. USA* **2003**, *100*, 10170–4.
79. Nilsson, K. P. R.; Rydberg, J.; Baltzer, L.; Inganäs, O. "Twisting macromolecular chains: self-assembly of a chiral supermolecule from nonchiral polythiophene polyanions and random-coil synthetic peptides." *Proc. Natl. Acad. Sci. USA* **2004**, *101*, 11197–202.
80. Klingstedt, T.; Aslund, A.; Simon, R. a; Johansson, L. B. G.; Mason, J. J.; Nyström, S.; Hammarström, P.; Nilsson, K. P. R. "Synthesis of a library of oligothiophenes and their

- utilization as fluorescent ligands for spectral assignment of protein aggregates." *Org. Biomol. Chem.* **2011**, *9*, 8356–70.
81. McCullough, R. D.; Ewbank, P. C.; Loewe, R. S. "Self-Assembly and Disassembly of Regioregular, Water Soluble Polythiophenes: Chemoselective Ionchromatic Sensing in Water." *J. Am.Chem.Soc* **1997**, *119*, 633–634.
  82. Chen, L.; Osada, Y. "Titration Behavior and Spectral Transitions of Water-Soluble Polythiophene Carboxylic Acids." *Macromolecules* **1999**, *32*, 3964–3969.
  83. Aslund, A.; Sigurdson, C. J.; Klingstedt, T.; Grathwohl, S.; Bolmont, T.; Dickstein, D. L.; Glimsdal, E.; Prokop, S.; Lindgren, M.; Konradsson, P.; Holtzman, D. M.; Hof, P. R.; Heppner, F. L.; Gandy, S.; Jucker, M.; Aguzzi, A.; Hammarström, P.; Nilsson, K. P. R. "Novel pentameric thiophene derivatives for in vitro and in vivo optical imaging of a plethora of protein aggregates in cerebral amyloidoses." *ACS chemical biology* **2009**, *4*, 673–84.
  84. Herland, A.; Nilsson, K. P. R.; Olsson, J. D. M.; Hammarström, P.; Konradsson, P.; Inganäs, O. "Synthesis of a regioregular zwitterionic conjugated oligoelectrolyte, usable as an optical probe for detection of amyloid fibril formation at acidic pH." *J. Am.Chem.Soc* **2005**, *127*, 2317–23.
  85. Nilsson, K. P. R.; Hammarström, P.; Ahlgren, F.; Herland, A.; Schnell, E. A.; Lindgren, M.; Westermark, G. T.; Inganäs, O. "Conjugated polyelectrolytes--conformation-sensitive optical probes for staining and characterization of amyloid deposits." *Chembiochem* **2006**, *7*, 1096–104.
  86. Almstedt, K.; Nyström, S.; Nilsson, K. P. R.; Hammarström, P. "Amyloid fibrils of human prion protein are spun and woven from morphologically disordered aggregates." *Prion* **2009**, *3*, 224–35.
  87. Aslund, A.; Herland, A.; Hammarström, P.; Nilsson, K. P. R.; Jonsson, B.-H.; Inganäs, O.; Konradsson, P. "Studies of luminescent conjugated polythiophene derivatives: enhanced spectral discrimination of protein conformational states." *Bioconjugate Chem.* **2007**, *18*, 1860–8.
  88. Oheim, M.; Michael, D. J.; Geisbauer, M.; Madsen, D.; Chow, R. H. "Principles of two-photon excitation fluorescence microscopy and other nonlinear imaging approaches." *Adv. Drug Deliv. Rev.* **2006**, *58*, 788–808.
  89. G.J. Brakenhoff, M. M. and R. I. G. "Analysis of efficiency of two-photon versus single-photon absorption for fluorescence generation in biological objects." *Journal of Microscopy* **1996**, *183*, 140–144.
  90. Centonze, V. E.; White, J. G. "Multiphoton excitation provides optical sections from deeper within scattering specimens than confocal imaging." *Biophys. J.* **1998**, *75*, 2015–24.
  91. Hillman, E. M. C. "Optical brain imaging in vivo: techniques and applications from animal to man." *J. Biomed. Opt.* **2007**, *12*, 051402.
  92. Xu, W.; Kattel, K.; Park, J. Y.; Chang, Y.; Kim, T. J.; Lee, G. H. "Paramagnetic nanoparticle T1 and T2 MRI contrast agents." *Phys. Chem. Chem. Phys.* **2012**, *14*, 12687–700.

93. Na, H. Bin; Hyeon, T. "Nanostructured T1 MRI contrast agents." *J.Mater.Chem* **2009**, *19*, 6267.
94. Na, H. Bin; Song, I. C.; Hyeon, T. "Inorganic Nanoparticles for MRI Contrast Agents." *Adv. Mater.* **2009**, *21*, 2133–2148.
95. Vuong, Q. L.; Van Doorslaer, S.; Bridot, J.-L.; Argante, C.; Alejandro, G.; Hermann, R.; Disch, S.; Mattea, C.; Stapf, S.; Gossuin, Y. "Paramagnetic nanoparticles as potential MRI contrast agents: characterization, NMR relaxation, simulations and theory." *Magma* **2012**.
96. Ben-david, Y.; Leitun, G.; Cohen, H.; Vilan, A.; Degani, H.; Milstein, D. "Water-Soluble Contrast Agents Targeted at the Estrogen Receptor for Molecular." *Bioconjugate Chem.* **2007**, *18*, 1362–1365.
97. Villaraza, A. J. L.; Bumb, A.; Brechbiel, M. W. "Macromolecules, dendrimers, and nanomaterials in magnetic resonance imaging: the interplay between size, function, and pharmacokinetics." *Chem.rev.* **2010**, *110*, 2921–59.
98. Bloembergen, N.; Morgan, L. O. "Proton Relaxation Times in Paramagnetic Solutions. Effects of Electron Spin Relaxation." *J. Phys. Chem.* **1961**, *34*, 842.
99. Mornet, S.; Vasseur, S.; Grasset, F.; Duguet, E. "Magnetic nanoparticle design for medical diagnosis and therapy." *J.Mater.Chem* **2004**, *14*, 2161.
100. Tóth, É.; Pubanz, D.; Vauthey, S.; Helm, L.; Merbach, A. E. "The Role of Water Exchange in Attaining Maximum Relaxivities for Dendrimeric MRI Contrast Agents." *Chem. Eur. J.* **1996**, *2*, 1607–1615.
101. Yerly, F.; Hardcastle, K. I.; Helm, L.; Aime, S.; Botta, M.; Merbach, A. E. "Molecular dynamics simulation of [Gd(egta)(H<sub>2</sub>O)](-) in aqueous solution: internal motions of the poly(amino carboxylate) and water ligands, and rotational correlation times." *Chem. Eur. J.* **2002**, *8*, 1031–9.
102. Zhang, Z.; Greenfield, M. T.; Spiller, M.; McMurry, T. J.; Lauffer, R. B.; Caravan, P. "Multilocus binding increases the relaxivity of protein-bound MRI contrast agents." *Angew. Chem. Int. Ed.* **2005**, *44*, 6766–9.
103. Fulton, D. A.; O'Halloran, M.; Parker, D.; Senanayake, K.; Botta, M.; Aime, S. "Efficient relaxivity enhancement in dendritic gadolinium complexes: effective motional coupling in medium molecular weight conjugates." *Chem. Commun.* **2005**, 474–6.
104. Werner, E. J.; Avedano, S.; Botta, M.; Hay, B. P.; Moore, E. G.; Aime, S.; Raymond, K. N. "Highly soluble tris-hydroxypyridonate Gd(III) complexes with increased hydration number, fast water exchange, slow electronic relaxation, and high relaxivity." *J. Am.Chem.Soc* **2007**, *129*, 1870–1.
105. Terreno, E.; Castelli, D. D.; Viale, A.; Aime, S. "Challenges for molecular magnetic resonance imaging." *Chem.rev.* **2010**, *110*, 3019–42.
106. Aime, S.; Fasano, M.; Terreno, E. "Lanthanide (III) chelates for NMR biomedical applications." *Chem. Soc. Rev.* **1998**, 27.

107. Aime, S.; Cabella, C.; Colombatto, S.; Geninatti Crich, S.; Gianolio, E.; Maggioni, F. "Insights into the use of paramagnetic Gd(III) complexes in MR-molecular imaging investigations." *J. Magn. Reson. Imaging* **2002**, *16*, 394–406.
108. Caravan, P. "Resonance Imaging ( MRI ) Contrast Agents : Design and Mechanism of Action." *Acc. Chem. Res.* **2009**, *42*, 851–862.
109. Laurent, S.; Forge, D.; Port, M.; Roch, A.; Robic, C.; Vander Elst, L.; Muller, R. N. "Magnetic iron oxide nanoparticles: synthesis, stabilization, vectorization, physicochemical characterizations, and biological applications." *Chem.rev.* **2008**, *108*, 2064–110.
110. Basly, B.; Felder-Flesch, D.; Perriat, P.; Billotey, C.; Taleb, J.; Pourroy, G.; Begin-Colin, S. "Dendronized iron oxide nanoparticles as contrast agents for MRI." *Chem. Commun.* **2010**, *46*, 985–7.
111. Răcuciu, M.; Creangă, D. E.; Airinei, A. "Citric-acid-coated magnetite nanoparticles for biological applications." *Eur. Phys. J. E* **2006**, *21*, 117–21.
112. Lee, H.; Lim, N.; Seo, J. "Preparation and magnetic resonance imaging effect of polyvinylpyrrolidone-coated iron oxide nanoparticles." *J Biomed Mater Res B Appl Biomater* **2006**, *79B*, 142–150.
113. Barrera, C.; Herrera, A. P.; Rinaldi, C. "Colloidal dispersions of monodisperse magnetite nanoparticles modified with poly(ethylene glycol)." *J. Coll. Int. Sci.* **2009**, *329*, 107–13.
114. Gupta, A. K.; Gupta, M. "Synthesis and surface engineering of iron oxide nanoparticles for biomedical applications." *Biomaterials* **2005**, *26*, 3995–4021.
115. Iida, H.; Takayanagi, K.; Nakanishi, T.; Osaka, T. "Synthesis of Fe<sub>3</sub>O<sub>4</sub> nanoparticles with various sizes and magnetic properties by controlled hydrolysis." *J. Coll. Int. Sci.* **2007**, *314*, 274–80.
116. Arrais, A.; Botta, M.; Avedano, S.; Giovenzana, G. B.; Gianolio, E.; Boccaleri, E.; Stanghellini, P. L.; Aime, S. "Carbon coated microshells containing nanosized Gd(III) oxidic phases for multiple bio-medical applications." *Chem. Commun.* **2008**, 5936–8.
117. Norek, M.; Pereira, G. A.; Geraldies, C. F. G. C.; Denkova, A.; Zhou, W.; Peters, J. a. "NMR Transversal Relaxivity of Suspensions of Lanthanide Oxide Nanoparticles." *J.Phys.Chem.C* **2007**, *111*, 10240–10246.
118. Fortin, Marc-André; Petoral Jr., Rodrigo M.; Söderlind, F. K.; A.; Engstöm, Maria; Veres, Teodor; Käll, Per-Olof; Uvdal, K.; Us, C. "PEG-covered ultra-small Gd<sub>2</sub>O<sub>3</sub> nanoparticles for positive contrast.pdf." *Nanotechnology* **2007**, *18*, 395501.
119. Norek, M.; Kampert, E.; Zeitler, U.; Peters, J. A. "Tuning of the size of Dy<sub>2</sub>O<sub>3</sub> nanoparticles for optimal performance as an MRI contrast agent." *J. Am.Chem.Soc* **2008**, *130*, 5335–40.
120. Na, H. Bin; Lee, J. H.; An, K.; Park, Y. Il; Park, M.; Lee, I. S.; Nam, D.-H.; Kim, S. T.; Kim, S.-H.; Kim, S.-W.; Lim, K.-H.; Kim, K.-S.; Kim, S.-O.; Hyeon, T. "Development of a T1 contrast agent for magnetic resonance imaging using MnO nanoparticles." *Angew. Chem. Int. Ed.* **2007**, *46*, 5397–401.

121. Pan, D.; Senpan, A.; Caruthers, S. D.; Williams, T. A.; Scott, M. J.; Gaffney, P. J.; Wickline, S. a; Lanza, G. M. "Sensitive and efficient detection of thrombus with fibrin-specific manganese nanocolloids." *Chem. Commun.* **2009**, 3234–6.
122. Létourneau, M.; Tremblay, M.; Faucher, L.; Rojas, D.; Chevallier, P.; Gossuin, Y.; Lagueux, J.; Fortin, M.-A. "MnO-Labeled Cells: Positive Contrast Enhancement in MRI." *J. Phys. Chem. B* **2012**.
123. Hifumi, H.; Yamaoka, S.; Tanimoto, A.; Akatsu, T.; Shindo, Y.; Honda, A.; Citterio, D.; Oka, K.; Kuribayashi, S.; Suzuki, K. "Dextran Coated Gadolinium Phosphate Nanoparticles for Magnetic Resonance Tumor Imaging." *J. Biol. Chem.* **2009**, *19*, 6393.
124. Hifumi, H.; Yamaoka, S.; Tanimoto, A.; Citterio, D.; Suzuki, K. "Gadolinium-based hybrid nanoparticles as a positive MR contrast agent." *J. Am.Chem.Soc* **2006**, *128*, 15090–1.
125. Cheung, E. N. M.; Alvares, R. D. A.; Oakden, W.; Chaudhary, R.; Hill, M. L.; Pichaandi, J.; Mo, G. C. H.; Yip, C.; Macdonald, P. M.; Stanisz, G. J.; Van Veggel, F. C. J. M.; Prosser, R. S. "Polymer-Stabilized Lanthanide Fluoride Nanoparticle Aggregates as Contrast Agents for Magnetic Resonance Imaging and Computed Tomography." *Chem. Mater.* **2010**, *22*, 4728–4739.
126. Evanics, F.; Diamente, P. R.; Veggel, F. C. J. M. Van; Stanisz, G. J.; Prosser, R. S. "Characterization and NMR Relaxation Properties." *Chem. Mater.* **2006**, *18*, 2499–2505.
127. Skaat, H.; Margel, S. "Synthesis of fluorescent-maghemite nanoparticles as multimodal imaging agents for amyloid-beta fibrils detection and removal by a magnetic field." *Biochem. Biophys. Res. Commun.* **2009**, *386*, 645–9.
128. Prasad Yadav, T.; Manohar Yadav, R.; Pratap Singh, D. "Mechanical Milling: a Top Down Approach for the Synthesis of Nanomaterials and Nanocomposites." *Nanoscience and Nanotechnology* **2012**, *2*, 22–48.
129. Giri, P. K.; Bhattacharyya, S.; Singh, D. K.; Kesavamoorthy, R.; Panigrahi, B. K.; Nair, K. G. M. "Correlation between microstructure and optical properties of ZnO nanoparticles synthesized by ball milling." *J. Applied. Physics.* **2007**, *102*, 093515.
130. Wang, Y.; Li, Y.; Rong, C.; Liu, J. P. "Sm-Co hard magnetic nanoparticles prepared by surfactant-assisted ball milling." *Nanotechnology* **2007**, *18*, 465701.
131. Chakka, V. M.; Altuncevahir, B.; Jin, Z. Q.; Li, Y.; Liu, J. P. "Magnetic nanoparticles produced by surfactant-assisted ball milling." *J. Applied. Physics.* **2006**, *99*, 08E912.
132. Kong, L. B.; Zhu, W.; Tan, O. K. "Preparation and characterization of Pb(Zr<sub>0.52</sub> Ti<sub>0.48</sub>)O<sub>3</sub> ceramics from high-energy ball milling powders." *Materials Letters* **2000**, *42*, 232–239.
133. Behari, J. "Principles of nanoscience: an overview." *Indian J. Exp. Biol.* **2010**, *48*, 1008–19.
134. Sugimoto, T. "Preparation of monodispersed colloidal particles." *Adv. Colloid interf. Sci.* **1987**, *28*, 65–108.
135. Wang, X.; Gao, M. "A facile route for preparing rhabdophane rare earth phosphate nanorods." *J. Mater. Chem.* **2006**, *16*, 1360.

136. Hikichi, Y.; Hukuo, K.; Shiokawa, J. "Syntheses of rare earth orthophosphates." *Bull. Chem. Soc. Jap.* **1978**, *51*, 3645–3646.
137. Kim, K. Do; Kim, S. H.; Kim, H. T. "Applying the Taguchi method to the optimization for the synthesis of TiO<sub>2</sub> nanoparticles by hydrolysis of TEOT in micelles." *Coll. Surf. A: Physicochem. Eng. Aspects.* **2005**, *254*, 99–105.
138. Nakashima, T.; Kimizuka, N. "Interfacial synthesis of hollow TiO<sub>2</sub> microspheres in ionic liquids." *J. Am. Chem. Soc.* **2003**, *125*, 6386–7.
139. Dumont, M. F.; Baligand, C.; Li, Y.; Knowles, E. S.; Meisel, M. W.; Walter, G. A.; Talham, D. R. "DNA Surface Modified Gadolinium Phosphate Nanoparticles as MRI Contrast Agents." *Bioconjugate Chem.* **2012**, *23*, 951.
140. Lu, A.-H.; Salabas, E. L.; Schüth, F. "Magnetic nanoparticles: synthesis, protection, functionalization, and application." *Angew. Chem. Int. Ed.* **2007**, *46*, 1222–44.
141. Salavati-Niasari, M.; Davar, F.; Mazaheri, M. "Synthesis of Mn<sub>3</sub>O<sub>4</sub> nanoparticles by thermal decomposition of a [bis(salicylidiminato)manganese(II)] complex." *Polyhedron* **2008**, *27*, 3467–3471.
142. Seo, W. S.; Jo, H. H.; Lee, K.; Kim, B.; Oh, S. J.; Park, J. T. "Size-dependent magnetic properties of colloidal Mn(3)O(4) and MnO nanoparticles." *Angew. Chem. Int. Ed.* **2004**, *43*, 1115–7.
143. Zheng, J.; Yuan, X.; Ikezawa, M.; Jing, P.; Liu, X.; Zheng, Z.; Kong, X.; Zhao, J.; Masumoto, Y. "Efficient Photoluminescence of Mn<sup>2+</sup> Ions in MnS/ZnS Core/Shell Quantum Dots." *J. Phys. Chem. C* **2009**, *113*, 16969–16974.
144. Wang, S.; Jarrett, B. R.; Kauzlarich, S. M.; Louie, A. Y. "Core/shell quantum dots with high relaxivity and photoluminescence for multimodality imaging." *J. Am. Chem. Soc.* **2007**, *129*, 3848–56.
145. Nian, J.-N.; Teng, H. "Hydrothermal synthesis of single-crystalline anatase TiO<sub>2</sub> nanorods with nanotubes as the precursor." *J. Phys. Chem. B* **2006**, *110*, 4193–8.
146. Bezrodna, T.; Puchkovska, G.; Shymanovska, V.; Baran, J.; Ratajczak, H. "IR-analysis of H-bonded H<sub>2</sub>O on the pure TiO<sub>2</sub> surface." *J. Mol. Struct.* **2004**, *700*, 175–181.
147. Jungowska, W. "Phase equilibria in the system La<sub>2</sub>O<sub>3</sub>.K<sub>2</sub>O.P<sub>2</sub>O<sub>5</sub>." *J. Am. Ceram. Soc.* **2000**, *60*, 193–197.
148. Zeng, S.; Ren, G.; Yang, Q. "Fabrication, formation mechanism and optical properties of novel single-crystal Er<sup>3+</sup> doped NaYbF<sub>4</sub> micro-tubes." *J. Mater. Chem.* **2010**, *20*, 2152.
149. Yan, R. X.; Li, Y. D. "Down/Up Conversion in Ln<sup>3+</sup>-Doped YF<sub>3</sub> Nanocrystals." *Adv. Funct. Mater.* **2005**, *15*, 763–770.
150. Wang, H.; Li, G.; Guan, X.; Li, L. "Synthesis and conductivity of GdPO<sub>4</sub> nanorods: Impacts of particle size and Ca<sup>2+</sup> doping." *J. Alloy. Comp.* **2011**, *509*, 4160–4166.

151. Komarneni, S.; Katsuki, H. "Nanophase materials by a novel microwave-hydrothermal process." *Pure Appl. Chem.* **2002**, *74*, 1537–1543.
152. Kim, J. "Developing a Testing Method for Antimicrobial Efficacy on TiO<sub>2</sub> Photocatalytic Products." *Environ. Eng. Res.* **2008**, *13*, 136–140.
153. Maneerat, C.; Hayata, Y. "Antifungal activity of TiO<sub>2</sub> photocatalysis against *Penicillium expansum* in vitro and in fruit tests." *International journal of food microbiology* **2006**, *107*, 99–103.
154. Euvananont, C.; Junin, C.; Inpor, K.; Limthongkul, P.; Thanachayanont, C. "TiO<sub>2</sub> optical coating layers for self-cleaning applications." *Ceramics International* **2008**, *34*, 1067–1071.
155. Mellott, N. P.; Durucan, C.; Pantano, C. G.; Guglielmi, M. "Commercial and laboratory prepared titanium dioxide thin films for self-cleaning glasses: Photocatalytic performance and chemical durability." *Thin Solid Films* **2006**, *502*, 112–120.
156. Savage, N. O.; Akbar, S. A.; Dutta, P. K. "Titanium dioxide based high temperature carbon monoxide selective sensor." *Sens. Actuator B-Chem.* **2001**, *72*, 239–248.
157. Benkstein, K. D.; Kopidakis, N.; Van de Lagemaat, J.; Frank, A. J. "Influence of the Percolation Network Geometry on Electron Transport in Dye-Sensitized Titanium Dioxide Solar Cells." *J. Phys. Chem. B* **2003**, *107*, 7759–7767.
158. Cameron, P. J.; Peter, L. M. "Characterization of Titanium Dioxide Blocking Layers in Dye-Sensitized Nanocrystalline Solar Cells." *J. Phys. Chem. B* **2003**, *107*, 14394–14400.
159. Nagaveni, K.; Hegde, M. S.; Ravishankar, N.; Subbanna, G. N.; Madras, G. "Synthesis and structure of nanocrystalline TiO<sub>2</sub> with lower band gap showing high photocatalytic activity." *Langmuir* **2004**, *20*, 2900–7.
160. Tang, Y.; Wee, P.; Lai, Y.; Wang, X. "Hierarchical TiO<sub>2</sub> nanoflakes and nanoparticles hybrid structure for improved photocatalytic activity." *J. Phys. Chem. C* **2012**, *116*, 2772–2780.
161. Nagaveni, K.; Sivalingam, G.; Hegde, M. .; Madras, G. "Solar photocatalytic degradation of dyes: high activity of combustion synthesized nano TiO<sub>2</sub>." *Appl. Catal. B* **2004**, *48*, 83–93.
162. Cheng, H.; Ma, J.; Zhao, Z. "Hydrothermal preparation of uniform nanosize rutile and anatase particles." *Chem. Mater.* **1995**, *03*, 663–671.
163. Lim, K. T.; Hwang, H. S.; Ryoo, W.; Johnston, K. P. "Synthesis of TiO<sub>2</sub> nanoparticles utilizing hydrated reverse micelles in CO<sub>2</sub>." *Langmuir* **2004**, *20*, 2466–71.
164. Schneider, M. "High-surface-area titania aerogels: preparation and structural properties." *J. Mater. Chem.* **1992**, *2*, 587–589.
165. Yang, J.; Mei, S. "Hydrothermal synthesis of TiO<sub>2</sub> nanopowders from tetraalkylammonium hydroxide peptized sols." *Mater. Sci. Eng.: C* **2001**, 183–185.

166. Kolen'ko, Y. V.; Churagulov, B. R.; Kunst, M.; Mazerolles, L.; Colbeau-Justin, C. "Photocatalytic properties of titania powders prepared by hydrothermal method." *Appl. Catal. B* **2004**, *54*, 51–58.
167. Hachani, S.; Moine, B.; El-akrmi, A.; Férid, M. "Luminescent properties of some ortho- and pentaphosphates doped with Gd<sup>3+</sup>–Eu<sup>3+</sup>: Potential phosphors for vacuum ultraviolet excitation." *Optical Materials* **2009**, *31*, 678–684.
168. Chen, Y.; Wang, J.; Zhang, X.; Zhang, G.; Gong, M.; Su, Q. "An intense green emitting LiSrPO<sub>4</sub>:Eu<sup>2+</sup>, Tb<sup>3+</sup> for phosphor-converted LED." *Sens. Actuator B-Chem.* **2010**, *148*, 259–263.
169. Ekambaram, S.; Patil, K. C.; Maaza, M. "Synthesis of lamp phosphors: facile combustion approach." *J. Alloy. Comp.* **2005**, *393*, 81–92.
170. Hifumi, H.; Yamaoka, S.; Tanimoto, A.; Citterio, D.; Suzuki, K. "Gadolinium-based hybrid nanoparticles as a positive MR contrast agent." *J. Am.Chem.Soc* **2006**, *128*, 15090–1.
171. Zhang, L.; Yin, M.; You, H.; Yang, M.; Song, Y.; Huang, Y. "Mutifunctional GdPO<sub>4</sub>:Eu<sup>3+</sup> hollow spheres: synthesis and magnetic and luminescent properties." *Inorg. Chem.* **2011**, *50*, 10608–13.
172. Huang, C.; Lo, Y.; Kuo, W.; Hwu, J.; Su, W.; Shieh, D.; Yeh, C. "Facile Preparation of Self-Assembled Hydrogel-like GdPO<sub>4</sub> · H<sub>2</sub>O Nanorods." *Langmuir* **2008**, *24*, 8309–8313.
173. Xiu, Z.; Liu, S.; Lü, M.; Zhang, H.; Zhou, G. "Photoluminescence of Eu<sup>3+</sup> doped LaPO<sub>4</sub> nanocrystals synthesized by combustion method." *Mater. Res. Bull.* **2006**, *41*, 642–646.
174. Hezel, A. "X-ray powder data and cell dimensions of some rare earth orthophosphates." *J. inorg, nucl. Chem.* **1967**, *29*, 2085–2089.
175. Lessing, P. "Synthesis and characterization of gadolinium phosphate neutron absorber." *J. Eur. Ceram. Soc.* **2003**, *23*, 3049–3057.
176. Bregiroux, D.; Audubert, F.; Charpentier, T.; Sakellariou, D.; Bernache-Assollant, D. "Solid-state synthesis of monazite-type compounds LnPO<sub>4</sub> (Ln=La to Gd)." *Solid State Sci.* **2007**, *9*, 432–439.
177. Jung, K.; Lee, K.; Kang, Y. "Photoluminescence characteristics of spherical LnPO<sub>4</sub>:(Tb, Mn) phosphor particles under the UV and VUV illumination." *J. Mater. Sci. Lett* **2003**, *22*, 1527–1529.
178. Rajesh, K.; Shajesh, P.; Seidel, O.; Mukundan, P.; Warriar, K. G. K. "A Facile Sol–Gel Strategy for the Synthesis of Rod-Shaped Nanocrystalline High-Surface-Area Lanthanum Phosphate Powders and Nanocoatings." *Adv. Funct. Mater.* **2007**, *17*, 1682–1690.
179. Bo, L.; Liya, S.; Xiaozhen, L.; Shuihe, Z. "Sol-gel synthesis of monazite-type cerous phosphate for fiber coating." *J. Mater. Sci. Lett* **2001**, *20*, 1071–1075.
180. Gallini, S.; Jurado, J. R.; Colomer, M. T. "Synthesis and characterization of monazite-type Sr:LaPO<sub>4</sub> prepared through coprecipitation." *J. Mater. Sci. Lett* **2005**, *25*, 2003–2007.

181. Diaz-Guillén, J. a.; Fuentes, A. F.; Gallini, S.; Colomer, M. T. "A rapid method to obtain nanometric particles of rhabdophane LaPO<sub>4</sub>·nH<sub>2</sub>O by mechanical milling." *J. Alloy. Comp.* **2007**, *427*, 87–93.
182. Guan, H.; Zhang, Y. "Hydrothermal synthesis and characterization of hexagonal and monoclinic neodymium orthophosphate single-crystal nanowires." *J. solid. state. chem* **2004**, *177*, 781–785.
183. Fujishiro, Y.; Ito, H.; Sato, T.; Okuwaki, A. "Synthesis of monodispersed LaPO<sub>4</sub> particles using the hydrothermal reaction of an La (edta) chelate precursor and phosphate ions." *J. Alloy. Comp.* **1997**, *252*, 103–109.
184. Fang, Y.-P.; Xu, A.-W.; Song, R.-Q.; Zhang, H.-X.; You, L.-P.; Yu, J. C.; Liu, H.-Q. "Systematic synthesis and characterization of single-crystal lanthanide orthophosphate nanowires." *J. Am.Chem.Soc* **2003**, *125*, 16025–34.
185. Mooney, R. C. L. "X-ray diffraction study of cerous phosphate and related crystals. I. Hexagonal modification." *Acta Cryst.* **1950**, *3*, 337–340.
186. Murphy, K. E.; Altman, M. B.; Wunderlich, B. "The monoclinic-to-trigonal transformation in selenium." *J. Applied. Physics.* **1977**, *48*, 4122.
187. Peng, Z. "Mechanisms of the shape evolution of CdSe nanocrystals." *J. Am.Chem.Soc* **2001**, 1389–1395.
188. Peng, Z. A.; Peng, X. "Nearly monodisperse and shape-controlled CdSe nanocrystals via alternative routes: nucleation and growth." *J. Am.Chem.Soc* **2002**, *124*, 3343–53.
189. Yan, R.; Sun, X.; Wang, X.; Peng, Q.; Li, Y. "Crystal structures, anisotropic growth, and optical properties: controlled synthesis of lanthanide orthophosphate one-dimensional nanomaterials." *Chem. Eur. J.* **2005**, *11*, 2183–95.
190. Liu, Y.; Chen, W.; Wang, S.; Joly, A. G. "Investigation of water-soluble x-ray luminescence nanoparticles for photodynamic activation." *Appl. Phys. Lett.* **2008**, *92*, 043901.
191. Chatterjee, D. K.; Rufaihah, A. J.; Zhang, Y. "Upconversion fluorescence imaging of cells and small animals using lanthanide doped nanocrystals." *Biomaterials* **2008**, *29*, 937–43.
192. Yu, X.; Li, M.; Xie, M.; Chen, L.; Li, Y.; Wang, Q. "Dopant-controlled synthesis of water-soluble hexagonal NaYF<sub>4</sub> nanorods with efficient upconversion fluorescence for multicolor bioimaging." *Nano Res.* **2010**, *3*, 51–60.
193. Evanics, F.; Diamente, P. R.; Veggel, F. C. J. M. Van; Stanis, G. J.; Prosser, R. S. "Characterization and NMR Relaxation Properties." *Chem. Mater.* **2006**, 2499–2505.
194. Cheung, E. N. M.; Alvares, R. D. A.; Oakden, W.; Chaudhary, R.; Hill, M. L.; Pichaandi, J.; Mo, G. C. H.; Yip, C.; Macdonald, P. M.; Stanis, G. J.; Van Veggel, F. C. J. M.; Prosser, R. S. "Polymer-Stabilized Lanthanide Fluoride Nanoparticle Aggregates as Contrast Agents for Magnetic Resonance Imaging and Computed Tomography." *Chem. Mater.* **2010**, *22*, 4728–4739.

195. Tsuge, T. "Radiopacity of conventional, resin-modified glass ionomer, and resin-based luting materials." *J. Proteome Res.* **2009**, *51*, 223–30.
196. Nuñez, N. O.; Quintanilla, M.; Cantelar, E.; Cussó, F.; Ocaña, M. "Uniform YF<sub>3</sub>:Yb,Er up-conversion nanophosphors of various morphologies synthesized in polyol media through an ionic liquid." *J. Nanopart. Res.* **2009**, *12*, 2553–2565.
197. Chen, D.; Yu, Y.; Lin, H.; Huang, P.; Weng, F.; Shan, Z.; Wang, Y. "CeF<sub>3</sub>-based glass ceramic: a potential luminescent host for white-light-emitting diode." *Optics letters* **2009**, *34*, 2882–4.
198. Yoshikawa, A.; Yanagida, T.; Yokota, Y.; Kamada, K.; Kawaguchi, N.; Fukuda, K.; Yamazaki, A.; Watanabe, K.; Uritani, A.; Iguchi, T.; Boulon, G.; Nikl, M. "Development of novel rare earth doped fluoride and oxide scintillators for two-dimensional imaging." *Journal of Rare Earths* **2011**, *29*, 1178–1182.
199. Jacobsohn, L. G.; Kucera, C. J.; James, T. L.; Sprinkle, K. B.; DiMaio, J. R.; Kokuoz, B.; Yazgan-Kukouz, B.; DeVol, T. A.; Ballato, J. "Preparation and Characterization of Rare Earth Doped Fluoride Nanoparticles." *Materials* **2010**, *3*, 2053–2068.
200. Mishra, S.; Daniele, S.; Ledoux, G.; Jeanneau, E.; Joubert, M.-F. "Heterometallic Na-Y(Ln) trifluoroacetate diglyme complexes as novel single-source precursors for upconverting NaYF<sub>4</sub> nanocrystals co-doped with Yb and Er/Tm ions." *Chem. Commun.* **2010**, *46*, 3756–8.
201. Sun, X.; Zhang, Y.-W.; Du, Y.-P.; Yan, Z.-G.; Si, R.; You, L.-P.; Yan, C.-H. "From trifluoroacetate complex precursors to monodisperse rare-earth fluoride and oxyfluoride nanocrystals with diverse shapes through controlled fluorination in solution phase." *Chem. Eur. J.* **2007**, *13*, 2320–32.
202. Liang, L.; Xu, H.; Su, Q.; Konishi, H.; Jiang, Y.; Wu, M.; Wang, Y.; Xia, D. "Hydrothermal synthesis of prismatic NaHoF(4) microtubes and NaSmF(4) nanotubes." *Inorg. Chem.* **2004**, *43*, 1594–6.
203. Y, N. L.; Yb, D.; Zhuang, J.; Liang, L.; Sung, H. H. Y.; Yang, X.; Wu, M.; Williams, I. D. "Controlled Hydrothermal Growth and Up-Conversion Emission of." *Inorg. Chem.* **2007**, *46*, 2324–2329.
204. Liang, X.; Wang, X.; Zhuang, J. "Branched NaYF<sub>4</sub> nanocrystals with luminescent properties." *Inorg. Chem.* **2007**, *46*, 6050–6055.
205. Sun, Y.; Chen, Y.; Tian, L.; Yu, Y.; Kong, X.; Zhao, J.; Zhang, H. "Controlled synthesis and morphology dependent upconversion luminescence of NaYF<sub>4</sub>:Yb, Er nanocrystals." *Nanotechnology* **2007**, *18*, 275609.
206. Zhao, J.; Sun, Y.; Kong, X.; Tian, L.; Wang, Y.; Tu, L.; Zhao, J.; Zhang, H. "Controlled synthesis, formation mechanism, and great enhancement of red upconversion luminescence of NaYF<sub>4</sub>:Yb<sup>3+</sup>, Er<sup>3+</sup> nanocrystals/submicroplates at low doping level." *J. Phys. Chem. B* **2008**, *112*, 15666–72.
207. Li, C.; Yang, J.; Yang, P.; Lian, H.; Lin, J. "Hydrothermal synthesis of lanthanide fluorides LnF<sub>3</sub> (Ln= La to Lu) nano-/microcrystals with multiform structures and morphologies." *Chem. Mater.* **2008**, *3*, 4317–4326.

208. Zhang, T.; Guo, H.; Qiao, Y. "Facile synthesis, structural and optical characterization of LnF<sub>3</sub>:Re nanocrystals by ionic liquid-based hydrothermal process." *J. Lumin.* **2009**, *129*, 861–866.
209. Nuñez, N. O.; Ocaña, M. "An ionic liquid based synthesis method for uniform luminescent lanthanide fluoride nanoparticles." *Nanotechnology* **2007**, *18*, 455606.
210. Jacob, D.; Bitton, L.; Grinblat, J. "Are ionic liquids really a boon for the synthesis of inorganic materials? A general method for the fabrication of nanosized metal fluorides." *Chem. Mater.* **2006**, *299*, 3162–3168.
211. Wang, Z. L.; Quan, Z. W.; Jia, P. Y.; Lin, C. K.; Luo, Y.; Chen, Y.; Fang, J.; Zhou, W.; Connor, C. J. O.; Lin, J. "A Facile Synthesis and Photoluminescent Properties of Redispersible CeF<sub>3</sub>, CeF<sub>3</sub>:Tb<sup>3+</sup>, and CeF<sub>3</sub>:Tb<sup>3+</sup>/LaF<sub>3</sub> (Core/Shell) Nanoparticles." *Chem. Mater.* **2006**, *18*, 2030–2037.
212. Karbowski, M.; Mech, A.; Kępiński, L.; Mielcarek, W.; Hubert, S. "Effect of crystallite size on structural and luminescent properties of nanostructured Eu<sup>3+</sup>:KGdF<sub>4</sub> synthesised by co-precipitation method." *J. Alloy. Comp.* **2005**, *400*, 67–75.
213. Heer, S.; Kömpe, K.; Güdel, H.-U.; Haase, M. "Highly Efficient Multicolour Upconversion Emission in Transparent Colloids of Lanthanide-Doped NaYF<sub>4</sub> Nanocrystals." *Adv. Mater.* **2004**, *16*, 2102–2105.
214. Bednarkiewicz, A.; Mech, A.; Karbowski, M.; Stręk, W. "Spectral properties of Eu<sup>3+</sup> doped NaGdF<sub>4</sub> nanocrystals." *J. Lumin.* **2005**, *114*, 247–254.
215. Chaput, F.; Lerouge, F.; Tusseau-nenez, S.; Coulon, P.-E.; Dujardin, C.; Denis-Quanquin, S.; Mpambani, F.; Parola, S. "Rare Earth Fluoride Nanoparticles Obtained Using Charge Transfer Complexes: A Versatile and Efficient Route toward Colloidal Suspensions and Monolithic Transparent Xerogels." *Langmuir* **2011**, *27*, 5555–5561.
216. B.V. Derjaguin, L. L. "No Title." *Acta Physicochim. URSS.* **1941**, *14*, 633.
217. E.J.W Verwey, J. T. G. O. "Theory of stability of lyophobic colloids." *Elsevier, Amsterdam (1948)* **1948**.
218. Theodoor, J.; Overbeek, G. "Strong and weak points in the interpretation of colloid stability." *Adv. Colloid interf. Sci.* **1982**, *16*, 17–30.
219. Jolivet, J. . "De la solution à l'oxyde." *InterEditions/CNRS Editions, Paris* **1994**, InterEdition.
220. Skaat, H.; Shafir, G.; Margel, S. "Acceleration and inhibition of amyloid-beta fibril formation by peptide-conjugated fluorescent-maghemite nanoparticles." *J. Nanopart. Res.* **2011**, *13*, 3521–3534.
221. Lu, Y.; Yin, Y.; Mayers, B. T.; Xia, Y. "Modifying the Surface Properties of Superparamagnetic Iron Oxide Nanoparticles through A Sol-Gel Approach." *Nano lett.* **2002**, *2*, 183–186.
222. Lin, J.; Zhou, W.; Kumbhar, A.; Wiemann, J.; Fang, J.; Carpenter, E. E.; O'Connor, C. J. "Gold-Coated Iron (Fe@Au) Nanoparticles: Synthesis, Characterization, and Magnetic Field-Induced Self-Assembly." *J. solid. state. chem* **2001**, *159*, 26–31.

223. Schladt, T. D.; Koll, K.; Prüfer, S.; Bauer, H.; Natalio, F.; Dumele, O.; Raidoo, R.; Weber, S.; Wolfrum, U.; Schreiber, L. M.; Radsak, M. P.; Schild, H.; Tremel, W. "Multifunctional superparamagnetic MnO@SiO<sub>2</sub> core/shell nanoparticles and their application for optical and magnetic resonance imaging." *J.Mater.Chem* **2012**, *22*, 9253.
224. Kobayashi, Y.; Katakami, H.; Mine, E.; Nagao, D.; Konno, M.; Liz-Marzán, L. M. "Silica coating of silver nanoparticles using a modified Stober method." *J. Colloid Interface. Sci.* **2005**, *283*, 392–6.
225. Daou, T. J.; Grenèche, J. M.; Pourroy, G.; Buathong, S.; Derory, A.; Ulhaq-Bouillet, C.; Donnio, B.; Guillon, D.; Begin-Colin, S. "Coupling Agent Effect on Magnetic Properties of Functionalized Magnetite-Based Nanoparticles." *Chem. Mater.* **2008**, *20*, 5869–5875.
226. Bridot, J.-L.; Faure, A.-C.; Laurent, S.; Rivière, C.; Billotey, C.; Hiba, B.; Janier, M.; Josserand, V.; Coll, J.-L.; Elst, L. Vander; Muller, R.; Roux, S.; Perriat, P.; Tillement, O. "Hybrid gadolinium oxide nanoparticles: multimodal contrast agents for in vivo imaging." *J.Am.Chem.Soc* **2007**, *129*, 5076–84.
227. Randon, J.; Blanc, P.; Paterson, R. "Modification of ceramic membrane surfaces using phosphoric acid and alkyl phosphonic acids and its effects on ultrafiltration of BSA protein." *J. Membr. Sci.* **1995**, *98*, 119–129.
228. Endres, P. J.; Paunesku, T.; Vogt, S.; Meade, T. J.; Woloschak, G. E. "DNA-TiO<sub>2</sub> nanoconjugates labeled with magnetic resonance contrast agents." *J. Am.Chem.Soc* **2007**, *129*, 15760–1.
229. Shimmin, R. G.; Schoch, A. B.; Braun, P. V "Polymer size and concentration effects on the size of gold nanoparticles capped by polymeric thiols." *Langmuir* **2004**, *20*, 5613–20.
230. Corbierre, M. K.; Cameron, N. S.; Lennox, R. B. "Polymer-stabilized gold nanoparticles with high grafting densities." *Langmuir* **2004**, *20*, 2867–73.
231. Kang, K.; Choi, J.; Nam, J. H.; Lee, S. C.; Kim, K. J.; Lee, S.-W.; Chang, J. H. "Preparation and characterization of chemically functionalized silica-coated magnetic nanoparticles as a DNA separator." *J. Chem. Phys.B* **2009**, *113*, 536–43.
232. Liz-Marzán, L.; Giersig, M.; Mulvaney, P. "Synthesis of nanosized gold-silica core-shell particles." *Langmuir* **1996**, *7463*, 4329–4335.
233. Barreto, J. A.; O'Malley, W.; Kubeil, M.; Graham, B.; Stephan, H.; Spiccia, L. "Nanomaterials: applications in cancer imaging and therapy." *Adv. mater.* **2011**, *23*, H18–40.
234. Fujiwara, H.; Murakoshi, K. "Observation of Adsorbed N, N-Dimethylformamide Molecules on Colloidal ZnS Nanocrystallites. Effect of Coexistent Counteranion on Surface Structure." *Langmuir* **1998**, *7463*, 4070–4073.
235. Luo, K.; Zhou, S.; Wu, L.; Gu, G. "Dispersion and functionalization of nonaqueous synthesized zirconia nanocrystals via attachment of silane coupling agents." *Langmuir* **2008**, *24*, 11497–505.

236. Mansur, A.; Nascimento, O. "Chemical functionalization of ceramic tile surfaces by silane coupling agents: polymer modified mortar adhesion mechanism implications." *Materials Research* **2008**, *11*, 293–300.
237. Wang, C.; Mao, H.; Wang, C.; Fu, S. "Dispersibility and Hydrophobicity Analysis of Titanium Dioxide Nanoparticles Grafted with Silane Coupling Agent." *Ind. Eng. Chem. Res.* **2011**, *50*, 11930–11934.
238. Colorado, R.; Villazana, R. J.; Lee, T. R. "Self-Assembled Monolayers on Gold Generated from Aliphatic Dithiocarboxylic Acids." *Langmuir* **1998**, 6337–6340.
239. Wuelfing, W.; Gross, S. "Nanometer gold clusters protected by surface-bound monolayers of thiolated poly (ethylene glycol) polymer electrolyte." *J. Am.Chem.Soc.* **1998**, 12696–12697.
240. Lafond, V.; Gervais, C.; Maquet, J.; Prochnow, D.; Babonneau, F.; Mutin, P. H. "17 O MAS NMR Study of the Bonding Mode of Phosphonate Coupling Molecules in a Titanium Oxo-Alkoxo-Phosphonate and in Titania-Based Hybrid Materials." *Chem. Mater.* **2003**, *15*, 4098–4103.
241. Mutin, P. H.; Lafond, V.; Popa, A. F.; Granier, M.; Markey, L.; Dereux, A.; Euge, P. "Selective Surface Modification of SiO<sub>2</sub>- TiO<sub>2</sub> Supports with Phosphonic Acids." *Chem. Mater.* **2004**, *16*, 5670–5675.
242. Sahoo, Y.; Pizem, H.; Fried, T.; Golodnitsky, D. "Alkyl phosphonate/phosphate coating on magnetite nanoparticles: a comparison with fatty acids." *Langmuir* **2001**, 7907–7911.
243. Zhang, B.; Kong, T.; Xu, W.; Su, R.; Gao, Y.; Cheng, G. "Surface functionalization of zinc oxide by carboxyalkylphosphonic acid self-assembled monolayers." *Langmuir* **2010**, *26*, 4514–22.
244. Zou, X.; Bao, H.; Guo, H.; Zhang, L.; Qi, L.; Jiang, J.; Niu, L.; Dong, S. "Mercaptoethane sulfonate protected, water-soluble gold and silver nanoparticles: Syntheses, characterization and their building multilayer films with polyaniline via ion-dipole interactions." *J. Coll. Int. Sci.* **2006**, *295*, 401–8.
245. Siddiqui, T. S.; Jani, A.; Williams, F.; Muller, R. N.; Vander Elst, L.; Laurent, S.; Yao, F.; Wadghiri, Y. Z.; Walters, M. a "Lanthanide complexes on Ag nanoparticles: designing contrast agents for magnetic resonance imaging." *J. Coll. Int. Sci.* **2009**, *337*, 88–96.
246. Schaaff, T.; Shafigullin, M. "Isolation of smaller nanocrystal Au molecules: Robust quantum effects in optical spectra." *J. Phys. Chem. B* **1997**, *5647*, 7885–7891.
247. Döllefeld, H.; Hoppe, K.; Kolny, J.; Schilling, K.; Weller, H.; Eychmüller, A. "Investigations on the stability of thiol stabilized semiconductor nanoparticles." *Phys. Chem. Chem. Phys.* **2002**, *4*, 4747–4753.
248. Friesen, H.; Optaczy, B.; Schneider, S.; Ax, W.; Enssle, K. H.; Kurrle, R.; Seiler, F. R.; Lahn, D.-M.; Bordet, I. J. "Hinge-Thiol Coupling." *Bioconjugate Chem.* **1990**, *1*, 411–418.
249. Maria Claesson, E.; Philipse, A. P. "Thiol-functionalized silica colloids, grains, and membranes for irreversible adsorption of metal(oxide) nanoparticles." *Coll. Surf. A: Physicochem. Eng. Aspects.* **2007**, *297*, 46–54.

250. Khaled, S. M.; Sui, R.; Charpentier, P. A.; Rizkalla, A. S. "Synthesis of TiO<sub>2</sub>-PMMA nanocomposite: using methacrylic acid as a coupling agent." *Langmuir* **2007**, *23*, 3988–95.
251. Vittadini, A.; Selloni, A. "Formic acid adsorption on dry and hydrated TiO<sub>2</sub> anatase (101) surfaces by DFT calculations." *J. Phys. Chem. B* **2000**, *6*, 1300–1306.
252. Guerrero, G.; Mutin, P. H.; Vioux, A. "Anchoring of Phosphonate and Phosphinate Coupling Molecules on Titania Particles." *Chem. Mater.* **2001**, *13*, 4367–4373.
253. Rafailovich, M.; Sokolov, J.; Gedanken, A. "Self-Assembled Monolayers of Alkanesulfonic and -phosphonic Acids on Amorphous Iron Oxide Nanoparticles." *Langmuir* **1999**, 7111–7115.
254. Frantz, R.; Granier, M.; Durand, J.-O.; Lanneau, G. F. "Phosphonate derivatives of pyridine grafted onto oxide nanoparticles." *Tetrahedron Lett.* **2002**, *43*, 9115–9117.
255. Lukd, I.; Borbaruah, M.; Quin, L. D. "Direct Reaction of Phosphorus Acids with Hydroxy of." *J. Am.Chem.Soc* **1994**, 1737–1741.
256. Mitchell, M.; Sheinker, V.; Mintz, E. "Adsorption and decomposition of dimethyl methylphosphonate on metal oxides." *J. Phys. Chem. B* **1997**, *101*, 11192–11203.
257. Jin, T. "A TPD/AES Study of the Interaction." *J.Phys.Chem.* **1986**, *2*, 4607–4611.
258. Guerrero, G.; Mutin, P. H.; Vioux, A. "Anchoring of Phosphonate and Phosphinate Coupling Molecules on Titania Particles." *Chem. Mater.* **2001**, *13*, 4367–4373.
259. Galoppini, E. "Linkers for anchoring sensitizers to semiconductor nanoparticles." *Coord. Chem. Rev.* **2004**, *248*, 1283–1297.
260. Gumienna-Kontecka, E.; Jezierska, J.; Lecouvey, M.; Leroux, Y.; Kozlowski, H. "Bisphosphonate chelating agents. Coordination ability of 1-phenyl-1-hydroxymethylene bisphosphonate towards Cu(2+) ions." *J. Inorg. Biochem.* **2002**, *89*, 13–7.
261. Lalatonne, Y.; Paris, C.; Serfaty, J. M.; Weinmann, P.; Lecouvey, M.; Motte, L. "Bisphosphonates-ultra small superparamagnetic iron oxide nanoparticles: a platform towards diagnosis and therapy." *Chem. Commun.* **2008**, 2553–5.
262. Knop, K.; Hoogenboom, R.; Fischer, D.; Schubert, U. S. "Poly(ethylene glycol) in drug delivery: pros and cons as well as potential alternatives." *Angew. Chem. Int. Ed.* **2010**, *49*, 6288–308.
263. Daou, T. J.; Li, L.; Reiss, P.; Josserand, V.; Texier, I. "Effect of poly(ethylene glycol) length on the in vivo behavior of coated quantum dots." *Langmuir* **2009**, *25*, 3040–4.
264. Villie, F.; Michot, L. J.; Bardot, F.; Cases, J. M.; Franc, M. "An Improved Derivative Isotherm Summation Method To Study Surface Heterogeneity of Clay Minerals." *Langmuir* **1997**, *7463*, 1104–1117.
265. Ahrén, M.; Selegård, L.; Klasson, A.; Söderlind, F.; Abrikossova, N.; Skoglund, C.; Bengtsson, T.; Engström, M.; Käll, P.-O.; Uvdal, K. "Synthesis and characterization of PEGylated Gd<sub>2</sub>O<sub>3</sub> nanoparticles for MRI contrast enhancement." *Langmuir* **2010**, *26*, 5753–62.

266. Carniato, F.; Tei, L.; Cossi, M.; Marchese, L.; Botta, M. "A chemical strategy for the relaxivity enhancement of Gd(III) chelates anchored on mesoporous silica nanoparticles." *Chem. Eur. J.* **2010**, *16*, 10727–34.
267. Andrade JD, Hlady V, J. S. "Poly(ethylene oxide) and protein resistance principles, problems, and possibilities." *Adv. Chem. Ser.* **1996**, *248*, 51–59.
268. Zhang M, Desai T, F. M. "Proteins and cells on PEG immobilized silicon." *Biomaterials* **1998**, *19*, 953–960.
269. Lecouvey, M.; Mallard, I.; Bailly, T.; Burgada, R.; Leroux, Y. "A mild and efficient one-pot synthesis of 1-hydroxymethylene-1,1-bisphosphonic acids. Preparation of new tripod ligands." *Tetrahedron Lett.* **2001**, *42*, 8475–8478.
270. Guenin, E.; Degache, E.; Liquier, J.; Lecouvey, M. "Synthesis of 1-Hydroxymethylene-1,1-bis(phosphonic acids) from Acid Anhydrides: Preparation of a New Cyclic 1-Acyloxymethylene-1,1-bis(phosphonic acid)." *Eur. J. Org. Chem.* **2004**, *2004*, 2983–2987.
271. Auernheimer, J.; Kessler, H. "Benzylprotected aromatic phosphonic acids for anchoring peptides on titanium." *Bioorg. Med. Chem. Lett.* **2006**, *16*, 271–3.
272. Ehrick, R. S.; Capaccio, M.; Puleo, D. a; Bachas, L. G. "Ligand-modified aminobisphosphonate for linking proteins to hydroxyapatite and bone surface." *Bioconjugate chem.* **2008**, *19*, 315–21.
273. Řehoř, I.; Kubíček, V.; Kotek, J.; Hermann, P.; Lukeš, I.; Száková, J.; Vander Elst, L.; Muller, R. N.; Peters, J. a. "1H NMR relaxivity of aqueous suspensions of titanium dioxide nanoparticles coated with a gadolinium(III) chelate of a DOTA-monoamide with a phenylphosphonate pendant arm." *J. Mater. Chem.* **2009**, *19*, 1494.
274. Oskam, G.; Nellore, A. "The growth kinetics of TiO<sub>2</sub> nanoparticles from titanium (IV) alkoxide at high water/titanium ratio." *J. Phys. Chem. B* **2003**, *107*, 1734–1738.
275. Cline, G.; Hanna, S. "The aminolysis of N-hydroxysuccinimide esters. A structure-reactivity study." *J. Am. Chem. Soc.* **1987**, 3087–3091.
276. Lapidot, Y.; Rappoport, S.; Wolman, Y. "Use of esters of N-hydroxysuccinimide in the synthesis of N-acylamino acids." *J. Lipid Res.* **1967**, *8*, 142–145.
277. Feshitan, J. A.; Vlachos, F.; Sirsi, S. R.; Konofagou, E. E.; Borden, M. A. "Theranostic Gd(III)-lipid microbubbles for MRI-guided focused ultrasound surgery." *Biomaterials* **2012**, *33*, 247–55.
278. Jankolovits, J. "Studying pH Dependence of a Peptide Modification with an N-hydroxysuccinimide Ester Using Mass Spectrometry." *Journal of Young Investigators* **2006**, *15*, October.
279. Nojima, Y.; Iguchi, K.; Suzuki, Y.; Sato, A. "The pH-dependent formation of PEGylated bovine lactoferrin by branched polyethylene glycol (PEG)-N-hydroxysuccinimide (NHS) active esters." *Biol. Pharm. Bull.* **2009**, *32*, 523–6.

280. Caravan, P.; Ellison, J. J.; McMurry, T. J.; Lauffer, R. B. "Gadolinium(III) Chelates as MRI Contrast Agents: Structure, Dynamics, and Applications." *Chem.rev.* **1999**, *99*, 2293–352.
281. Frullano, L.; Caravan, P. "Strategies for the preparation of bifunctional gadolinium (III) chelators." *Curr. Org. Synth.* **2011**, *8*, 535–565.
282. Kumar, K.; Chang, C. "Synthesis, stability, and structure of gadolinium (III) and yttrium (III) macrocyclic poly (amino carboxylates)." *Inorg. Chem.* **1994**, *33*, 3567–3575.
283. Desreux, J. "Nuclear magnetic resonance spectroscopy of lanthanide complexes with a tetraacetic tetraaza macrocycle. Unusual conformation properties." *Inorg. Chem.* **1980**, *19*, 1319–1324.
284. Mishra, S.; Hubert-Pfalzgraf, L. G.; Daniele, S.; Rolland, M.; Jeanneau, E.; Jouguet, B. "Thermal dehydration of Y(TFA)<sub>3</sub>(H<sub>2</sub>O)<sub>3</sub>: Synthesis and molecular structures of [Y(μ,η<sup>1</sup>:η<sup>1</sup>-TFA)<sub>3</sub>(THF)(H<sub>2</sub>O)]<sub>1∞</sub>·THF and [Y<sub>4</sub>(μ<sub>3</sub>-OH)<sub>4</sub>(μ,η<sup>1</sup>:η<sup>1</sup>-TFA)<sub>6</sub>(η<sup>1</sup>-TFA)(η<sup>2</sup>-TFA)(THF)<sub>3</sub>(DMSO)(H<sub>2</sub>O)]·6THF (TFA=trifluoroacetate)." *Inorg. Chem. Commun* **2009**, *12*, 97–100.
285. D. H. Templeton, C. H. D. "Lattice parameters of rare earth compounds." *Acta Cryst.* **1954**, *11*, 11–13.
286. Patra, C.; Alexandra, G.; Patra, S. "Microwave approach for the synthesis of rhabdophane-type lanthanide orthophosphate (Ln= La, Ce, Nd, Sm, Eu, Gd and Tb) nanorods under solvothermal conditions." *New J. Chem.* **2005**, *29*, 733–739.
287. Yan, B.; Xiao, X. "Hydrothermal Synthesis, Microstructure and Photoluminescence of Eu-Doped Mixed Rare Earth Nano-Orthophosphates." *Nanoscale Res Lett.* **2010**, *5*, 1962–1969.
288. Kijkowska, R.; Cholewka, E.; Duszak, B. "X-ray diffraction and Ir-absorption characteristics of lanthanide orthophosphates obtained by." *J.Mater.Sci* **2003**, *8*, 223–228.
289. Assaaoudi, H.; Ennaciri, a; Rulmont, a "Vibrational spectra of hydrated rare earth orthophosphates." *Vibrational Spectroscopy* **2001**, *25*, 81–90.
290. Kumar, K.-N. P.; Keizer, K.; Burggraaf, A. J.; Okubo, T.; Nagamoto, H. "Textural evolution and phase transformation in titania membranes: Part 2. Supported membranes." *J. Mater. Chem.* **1993**, *3*, 1151.
291. Yang, H.; Finlayson-Pitts, B. J. "Infrared Spectroscopic Studies of Binary Solutions of Nitric Acid and Water and Ternary Solutions of Nitric Acid, Sulfuric Acid, and Water at Room Temperature: Evidence for Molecular Nitric Acid at the Surface." *J. Phys. Chem. A* **2001**, *105*, 1890–1896.
292. Perrin, A. "Review article Recent progress in the analysis of HNO<sub>3</sub> spectra." **1998**, *54*, 375–393.
293. Barteau, M. A. "Organic Reactions at Well-Defined Oxide Surfaces II . What Is Different Between Metals and." *Chem.rev.* **1996**, *96*, 1413–1430.

294. Devis, J.; Yames, R. "Surface ionization and complexation at the oxide/water interface." *J. Colloid Interface Sci* **1978**, *63*.
295. Block, B. P. "Inorganic Chemistry O." *Inorg. Chem.* **1967**, *6*, 1439–1443.
296. Alferiev, I. S.; Vyavahare, N. R.; Song, C. X.; Levy, R. J. "Elastomeric Polyurethanes Modified with Geminal." *J. Polym. Sci., Part A: Polym. Chem.* **2001**, *39*, 105–116.
297. Abécassis, B.; Lerouge, F.; Bouquet, F.; Kachbi, S.; Monteil, M.; Davidson, P. "Aqueous Suspensions of GdPO(4) Nanorods: A Paramagnetic Mineral Liquid Crystal." *J. Phys. Chem. B* **2012**, *116*, 7590–5.
298. Alferiev, I.; Vyavahare, N.; Song, C.; Connolly, J.; Hinson, J. T.; Lu, Z.; Tallapragada, S.; Bianco, R.; Levy, R. "Bisphosphonate derivatized polyurethanes resist calcification." *Biomaterials* **2001**, *22*, 2683–93.
299. Mao, J.; Mukherjee, S.; Zhang, Y.; Cao, R.; Sanders, J. M.; Song, Y.; Zhang, Y.; Meints, G. a; Gao, Y. G.; Mukkamala, D.; Hudock, M. P.; Oldfield, E. "Solid-state NMR, crystallographic, and computational investigation of bisphosphonates and farnesyl diphosphate synthase-bisphosphonate complexes." *J. Am.Chem.Soc* **2006**, *128*, 14485–97.
300. Mukherjee, S.; Song, Y.; Oldfield, E. "NMR investigations of the static and dynamic structures of bisphosphonates on human bone: a molecular model." *J. Am.Chem.Soc* **2008**, *130*, 1264–73.
301. Řehoř, I.; Kubíček, V.; Kotek, J.; Hermann, P.; Száková, J.; Lukeš, I. "Modification of Nanocrystalline TiO<sub>2</sub> with Phosphonate- and Bis(phosphonate)-Bearing Macrocyclic Complexes: Sorption and Stability Studies." *Eur. J. Inorg. Chem.* **2011**, *2011*, 1981–1989.
302. Pawsey, S.; McCormick, M.; De Paul, S.; Graf, R.; Lee, Y. S.; Reven, L.; Spiess, H. W. "1H fast MAS NMR studies of hydrogen-bonding interactions in self-assembled monolayers." *J. Am.Chem.Soc* **2003**, *125*, 4174–84.
303. Lucas, N.; Hook, J.; McDonagh, A.; Colbran, S. "Titanium Dioxide Nanoparticles Functionalized with Pd and W Complexes of a Catecholphosphane Ligand." *Eur. J. Inorg. Chem.* **2005**, *2005*, 496–503.
304. Ma, T.-Y.; Zhang, X.-J.; Yuan, Z.-Y. "High selectivity for metal ion adsorption: from mesoporous phosphonated titanias to meso-/macroporous titanium phosphonates." *J. Mater. Chem.* **2009**, *44*, 6775–6785.
305. Maliakal, A.; Katz, H.; Cotts, P. M.; Subramoney, S.; Mirau, P. "Inorganic oxide core, polymer shell nanocomposite as a high K gate dielectric for flexible electronics applications." *J. Am.Chem.Soc* **2005**, *127*, 14655–62.
306. Strong, L.; Whitesides, G. M. "Structures of self-assembled monolayer films of organosulfur compounds adsorbed on gold single crystals: electron diffraction studies." *Langmuir* **1988**, *4*, 546–558.

307. Faucher, L.; Tremblay, M.; Lagueux, J.; Gossuin, Y.; Fortin, M.-A. "Rapid synthesis of PEGylated ultrasmall gadolinium oxide nanoparticles for cell labeling and tracking with MRI." *Appl. Mater. Interfaces* **2012**, *4*, 4506–15.
308. Tsotsalas, M.; Busby, M.; Gianolio, E.; Aime, S.; De Cola, L. "Functionalized Nanocontainers as Dual Magnetic and Optical Probes for Molecular Imaging Applications." *Chem. Mater.* **2008**, *20*, 5888–5893.
309. Strauch, R. C.; Mastarone, D. J.; Sukerkar, P. A.; Song, Y.; Ipsaro, J. J.; Meade, T. J. "Reporter protein-targeted probes for magnetic resonance imaging." *J. Neurosci.* **2011**, *133*, 16346–9.
310. Bottle; Guo-Ping Yan; Steven E.; Ren-Xi Zhuo Li Wei, M.-L. L. and L. L. "Evaluation of Dendritic Gadolinium Complexes as MRI Contrast Agents." *J. Bioact. Compat. Pol.* **2004**, *19*, 453–465.
311. Young, S. W.; Qing, F.; Rubin, D.; Balkus, K. J.; Engel, J. S.; Lang, J.; Dow, W. C.; Mutch, J. D.; Miller, R. A. "Magn. Reson. Imag." *Magn. Reson. Imag.* **1995**, *5*, 499.
312. Rieter, W. J.; Kim, J. S.; Taylor, K. M. L.; An, H.; Lin, W.; Tarrant, T.; Lin, W. "Hybrid silica nanoparticles for multimodal imaging." *Angew. Chem. Int. Ed.* **2007**, *46*, 3680–2.
313. Boxerman JL, Hamberg LM, Rosen BR, W. R. "Mr contrast due to intravascular magnetic susceptibility perturbations InterEditions/CNRS Editions, Paris, InterEditi." *Magn. Reson. Med.* **1995**, *34*, 555–566.
314. Norek, M.; Pereira, G. A.; Geraldés, C. F. G. C.; Denkova, A.; Zhou, W.; Peters, J. a. "NMR Transversal Relaxivity of Suspensions of Lanthanide Oxide Nanoparticles." *J. Phys. Chem. C* **2007**, *111*, 10240–10246.
315. Bridot, J.-L.; Faure, A.-C.; Laurent, S.; Rivière, C.; Billotey, C.; Hiba, B.; Janier, M.; Josserand, V.; Coll, J.-L.; Elst, L. Vander; Muller, R.; Roux, S.; Perriat, P.; Tillement, O. "Hybrid gadolinium oxide nanoparticles: multimodal contrast agents for in vivo imaging." *J. Am.Chem.Soc* **2007**, *129*, 5076–84.
316. Na, H. Bin; Lee, J. H.; An, K.; Park, Y. Il; Park, M.; Lee, I. S.; Nam, D.-H.; Kim, S. T.; Kim, S.-H.; Kim, S.-W.; Lim, K.-H.; Kim, K.-S.; Kim, S.-O.; Hyeon, T. "Development of a T1 contrast agent for magnetic resonance imaging using MnO nanoparticles." *Angew. Chem. Int. Ed.* **2007**, *46*, 5397–401.
317. Tiziana Passuello , Marco Pedroni , Fabio Piccinelli , Stefano Polizzi , Pasquina Marzola , Stefano Tambalo , Giamaica Conti , Donatella Benati , Fiorenzo Vetrone, M. B. and A. S. "PEG-capped, lanthanide doped GdF3 nanoparticles: luminescent and T2 contrast agents for optical and MRI multimodal imaging." *Nanoscale* **2012**, *4*, 7682–7689.
318. Hifumi, H.; Yamaoka, S.; Tanimoto, A.; Citterio, D.; Suzuki, K. "Gadolinium-based hybrid nanoparticles as a positive MR contrast agent." *J. Am.Chem.Soc* **2006**, *128*, 15090–1.
319. Gossuin, Y.; Disch, S.; Vuong, Q. L.; Gillis, P.; Hermann, R. P.; Park, J.-H.; Sailor, M. J. "NMR relaxation and magnetic properties of superparamagnetic nanoworms." *Contrast Media Mol. Imaging* **2010**, *5*, 318–22.

320. Hou, Y.; Qiao, R.; Fang, F.; Wang, X.; Dong, C.; Liu, K.; Liu, C.; Liu, Z.; Lei, H.; Wang, F.; Gao, M. "NaGdF(4) Nanoparticle-Based Molecular Probes for Magnetic Resonance Imaging of Intraperitoneal Tumor Xenografts in Vivo." *ACS nano* **2012**.
321. Vuong QL, Gillis P, G. Y. "Superparamagnetic particles are widely used in MRI as R2 contrast agents. In this last decade, different studies have focused on aggregation of superparamagnetic particles for important applications such as multimodal agents. A complete study – via simula." *J. Magn. Reson. Imaging* **2011**, *212*, 139–148.
322. Jun, Y.; Lee, J.-H.; Cheon, J. "Chemical design of nanoparticle probes for high-performance magnetic resonance imaging." *Angew. Chem. Int. Ed.* **2008**, *47*, 5122–35.
323. Rudin, M.; Weissleder, R. "Molecular imaging in drug discovery and development." *Nature reviews. Drug discovery* **2003**, *2*, 123–31.
324. Kim, J.; Piao, Y.; Hyeon, T. "Multifunctional nanostructured materials for multimodal imaging, and simultaneous imaging and therapy." *Chem. Soc. Rev.* **2009**, *38*, 372–90.
325. Corr, S.; Rakovich, Y.; Gun'ko, Y. "Multifunctional magnetic-fluorescent nanocomposites for biomedical applications." *Nanoscale Res Lett.* **2008**, *3*, 87–104.
326. Frullano, L.; Meade, T. J. "Multimodal MRI contrast agents." *JBIC* **2007**, *12*, 939–49.
327. Nie, S.; Xing, Y.; Kim, G. J.; Simons, J. W. "Nanotechnology applications in cancer." *Annu Rev Biomed Eng* **2007**, *9*, 257–88.
328. Huh, Y.-M.; Jun, Y.; Song, H.-T.; Kim, S.; Choi, J.; Lee, J.-H.; Yoon, S.; Kim, K.; Shin, J.-S.; Suh, J.-S.; Cheon, J. "In vivo magnetic resonance detection of cancer by using multifunctional magnetic nanocrystals." *J. Am. Chem. Soc.* **2005**, *127*, 12387–91.
329. Yang, J.; Lim, E.-K.; Lee, H. J.; Park, J.; Lee, S. C.; Lee, K.; Yoon, H.-G.; Suh, J.-S.; Huh, Y.-M.; Haam, S. "Fluorescent magnetic nanohybrids as multimodal imaging agents for human epithelial cancer detection." *Biomaterials* **2008**, *29*, 2548–55.
330. Cheon, J.; Lee, J.-H. "Synergistically integrated nanoparticles as multimodal probes for nanobiotechnology." *Acc. Chem. Res.* **2008**, *41*, 1630–40.
331. Veiseh, O.; Gunn, J. W.; Zhang, M. "Design and fabrication of magnetic nanoparticles for targeted drug delivery and imaging." *Adv. Drug Deliv. Rev.* **2010**, *62*, 284–304.
332. Roncali, J. "Conjugated poly (thiophenes): synthesis, functionalization, and applications." *Chem. rev.* **1992**, *92*, 711–739.
333. Inzelt, G.; Pineri, M.; Schultze, J. .; Vorotyntsev, M. . "Electron and proton conducting polymers: recent developments and prospects." *Electrochim. Acta* **2000**, *45*, 2403–2421.
334. Gurunathan, K.; Murugan, A. V.; Marimuthu, R.; Mulik, U. .; Amalnerkar, D. . "Electrochemically synthesised conducting polymeric materials for applications towards technology in electronics, optoelectronics and energy storage devices." *Mater. Chem. Phys.* **1999**, *61*, 173–191.

335. Novák, P.; Müller, K.; Santhanam, K. S. V.; Haas, O. "Electrochemically Active Polymers for Rechargeable Batteries." *Chem.rev.* **1997**, *97*, 207–282.
336. Panero, S.; Spila, E.; Scrosati, B. "On the use of ionically conducting membranes for the fabrication of laminated polymer-based redox capacitors." *J. Electroanal. Chem.* **1995**, *396*, 385–389.
337. Laforgue, A.; Simon, P.; Sarrazin, C.; Fauvarque, J.-F. "Polythiophene-based supercapacitors." *J. Power Sources* **1999**, *80*, 142–148.
338. Ferraris, J. P.; Eissa, M. M.; Brotherston, I. D.; Loveday, D. C.; Moxey, A. A. "Preparation and electrochemical evaluation of poly (3-phenylthiophene) derivatives: potential materials for electrochemical capacitors." *J. Electroanal. Chem.* **1998**, *459*, 57–69.
339. Rudge, A.; Davey, J.; Raistrick, I.; Gottesfeld, S.; Ferraris, J. P. "Conducting polymers as active materials in electrochemical capacitors." *J. Power Sources* **1994**, *47*, 89–107.
340. Bolognesi, B. A.; Bajo, G.; Paloheirno, J.; Osiergird, T.; Stubb, H. "ADVANCED Polarized Electroluminescence from." *Adv. Mater.* **1997**, *9*, 121–124.
341. Kumar, D.; Sharma, R. C. "Review article advances in conductive polymers." *Eur. Polym. J.* **1998**, *34*, 1053–1060.
342. Hernandez, V.; Ramirez, F. J.; Otero, T. F.; Lopez Navarrete, J. T. "An interpretation of the vibrational spectra of insulating and electrically conducting poly(3-methylthiophene) aided by a theoretical dynamical model." *J. Phys. Chem.* **1994**, *100*, 114.
343. Rico, M.; Orza, J.; Morcillo, J. "Fundamental vibrations of thiophene and its deuterated derivatives." *Spectrochimica Acta* **1965**, *21*, 689–719.
344. Hernández, V.; Casado, J.; Ramírez, F. J.; Zotti, G.; Hotta, S.; López Navarrete, J. T. "Efficient  $\pi$  electrons delocalization in  $\alpha,\alpha'$ -dimethyl end-capped oligothiophenes: A vibrational spectroscopic study." *J. Phys. Chem.* **1996**, *104*, 9271.
345. Demasa, J.; Crosby, G. "The Measurement of Photoluminescence Quantum Yields. 1 A Review2." *J. Chem. Phys* **1968**, *75*, 991–1024.
346. Resch-Genger, U.; Grabolle, M. "Quantum dots versus organic dyes as fluorescent labels." *Nature Methods* **2008**, *5*, 763–775.
347. Varaganti, S.; Gessesse, M.; Obare, S. O.; Ramakrishna, G. "Dynamics and Two-photon absorption properties of Chromophore Functionalized Semiconductor Nanoparticles." *Proc. of SPIE* **2009**, *7413-09*, 741309/1–741309/12.
348. Huang, J.; Zhong, X.; Wang, L.; Yang, L.; Mao, H. "Improving the magnetic resonance imaging contrast and detection methods with engineered magnetic nanoparticles." *Theranostics* **2012**, *2*, 86–102.
349. Hongwei Duan, Min Kuang, Xiaoxia Wang, Y. Andrew Wang, H. M. and S. N. "Reexamining the Effects of Particle Size and Surface Chemistry on the Magnetic Properties of Iron Oxide

- Nanocrystals: New Insights into Spin Disorder and Proton Relaxivity." *J. Phys. Chem. C* **2008**, *112*, 8127–8131.
350. Tong, S.; Hou, S.; Zheng, Z.; Zhou, J.; Bao, G. "Coating optimization of superparamagnetic iron oxide nanoparticles for high T2 relaxivity." *Nano lett.* **2010**, *10*, 4607–13.
351. Brown, P.; Davies, S.; Speake, T.; Millar, I. "Molecular mechanisms of cerebrospinal fluid production." *Neuroscience* **2004**, *129*, 957–970.
352. Hefendehl, J. K.; Wegenast-Braun, B. M.; Liebig, C.; Eicke, D.; Milford, D.; Calhoun, M. E.; Kohsaka, S.; Eichner, M.; Jucker, M. "Long-term in vivo imaging of  $\beta$ -amyloid plaque appearance and growth in a mouse model of cerebral  $\beta$ -amyloidosis." *J. Neurosci.* **2011**, *31*, 624–9.
353. Vithanarachchi, S. M.; Allen, M. J. "A multimodal,  $\beta$ -amyloid-targeted contrast agent." *Chem. Commun.* **2012**, DOI: 10.1039/c2cc36583a.
354. Bloch, F. "Nuclear induction." *Phys. Rev.* **1946**, *70*, 460.
355. Geva, T. "Magnetic Resonance Imaging: Historical Perspective." *J. Cardiovasc. Magn. Reson.* **2006**, *8*, 573–580.
356. Freeman, R.; Hill, H. "Dipolar contribution to NMR spin-lattice relaxation of protons." *J. Chem. Phys.* **1974**, *61*, 4466–4473.
357. Lauffer, R. "Paramagnetic metal complexes as water proton relaxation agents for NMR imaging: theory and design." *Chem.rev.* **1987**, *87*, 901.